A Study on Improvement of Dipole Estimation in MEG Measurement

Shinpei Okawa

Contents

1 Introduction **4**

1.1 Background: functional brain imaging 4

1.2 Overview of MEG measurement 5

1.3 Signal processing in MEG measurement 6

1.4 Inverse problem in MEG measurement 8

1.5 Proposals for solutions 12

2 Methods **15**

2.1 Electrophysiology in MEG measurement 15

2.2 Instrumentation in MEG measurement 16

2.3 Forward problem in MEG measurement 19

2.4 Reduction of noise from MEG data 21

2.4.1 Sensor noise reduction with Kalman filter 21

2.4.2 Estimation of noise covariances with factor analysis prior to Kalman filtering 24

2.4.3 Independent component analysis following the sensor noise reduction 25

2.5 Estimation of current density distribution 27

2.5.1 Spatial filters in MEG analysis 27

2.5.1.1 LCMV beamformer 27

2.5.1.2 SAM 28

2.5.2 Proposed spatial filter without temporal information 29

2.5.2.1 Concept of the proposed spatial filter 29

2.5.2.2 Derivation of the optimization problem of the spatial filter . . . 32
2.5.2.3 Effect of the fourth order cumulant . . . 34
2.5.2.4 Normalization of the spatial filter . . . 35
2.5.2.5 Spatial filter only with the second order cumulants . . . 37
2.5.3 Reconstruction of current distribution estimated by the spatial filters . . . 38

3 Numerical studies **41**
3.1 Reduction of noise from MEG data . . . 41
3.1.1 Experimental conditions . . . 41
3.1.2 FA-processed Kalman filter . . . 41
3.1.3 ICA followiong FA-processed Kalman filtering . . . 52
3.1.4 Discussion . . . 60
3.2 Proposed spatial filter with higher order statistics . . . 61
3.2.1 Experimental conditions . . . 61
3.2.2 Current density estimation under single dipole . . . 62
3.2.3 Current density estimation under multiple dipole . . . 71
3.2.4 Discussion . . . 80
3.3 Spatial filtered reconstruction (SFR) . . . 81
3.3.1 Experimental conditions . . . 81
3.3.2 Examples of the estimations with SFR . . . 81
3.3.3 Influences of noises to SFR . . . 86
3.3.4 Effect of spatial discretization . . . 91
3.3.5 Comparison of SFR, LCMV beamformer and SAM . . . 93
3.3.6 Impact of combination of FA-processed Kalman filter and SFR 98
3.3.7 Discussion . . . 101

4 Real MEG data analysis **102**
4.1 Experimental conditions . . . 102
4.2 SFR in AEF analysis . . . 102

4.3 Combination of FA-processed Kalman filter, ICA and SFR in AEF analysis . . . 110
4.3.1 Simulated AEF data analysis . . . 110
4.3.2 Real AEF data analysis . . . 136
4.4 Discussion . . . 138

5 Conclusion **163**

Chapter 1

Introduction

1.1 Background: functional brain imaging

To precisely and smoothly control muscles in our bodies, to analyze information from the surrounding environment, to handle languages skillfully and to produce art, science and technology etc; those abilities characterize mind of human, namely higher brain function. It fascinates people in history, and understanding the mechanisms of human brain functions is one of the most ambitious and challenging subjects today. At the same time, to overcome mental disorders such as Alzheimer's disease, researchers and medical doctors desire effective diagnosis methods, especially for preventions and early detections of the diseases.

In this context, advances of the functional brain imaging techniques in recent decades, e.g. positron emission tomography (PET) [3], functional magnetic resonance imaging (fMRI) [4], [5] etc., are making it possible to understand how the brain works and to offer diagnoses of neurological disorders. The PET forms images of the spatial distribution of the probes which are radioactively labeled organic molecules, e.g. glucose. They are involved in the metabolism in the brain. The PET measures both regional cerebral blood flow (rCBF) and the metabolic rate of glucose, which relate to the neural activities. The fMRI can detect hemodynamic changes by the MRI technology. The fMRI signal is called blood oxygen level dependent (BOLD) signal, which reflects oxygen level in the blood. It includes complex mul-

tiple factors such as blood flow, blood volume and blood oxygenation that depend on the neural activities. Activations in neurons consume energy thereby increasing the rCBF and the BOLD signal. The knowledge we have partly obtained about the mechanisms of brain now contributes to not only clinical studies and treatments but also several kinds of research fields. It enriches our mind and lives.

On the other hand, and an approach to measure the brain activities via electrophysiology exists, that is to say, electroencephalography (EEG) born in 1924 [2]. The EEG measures the change of the electric potential produced by the neural current flows in the brain. It has made great contributions to neurophysiology and clinical treatment, particularly in the inspection of epilepsy. Recently, it is utilized for Brain-computer interface (BCI) [6]-[10].

Among the modalities for functional brain imaging, magnetoencephalography (MEG) measurement [1], [2], [11], [12], [13], which complements with the EEG, began from the invention of the SQUID (Superconducting QUantum Interference Device) [14] and the first MEG recording conducted by D.S. Cohen at MIT during the term from late 1960s to early 70s. MEG has stimulated the researches of the brain functions since then, and has confronted us with attractive and crucial problems of signal processing and analyses [20]-[23].

1.2 Overview of MEG measurement

MEG (magnetoencephalography) has recently attracted attention as a technique for researching human brain functions. MEG is the method used to measure the magnetic field generated by electrical neural activities. SQUID gradiometers are employed to detect a tiny magnetic flux density outside a skull such as sensory and auditory evoked fields on the order of 10^{-13} T. MEG is a completely non-invasive method and can be safely used for investigations of brain functions and for diagnoses of neurological disorders, e.g. epilepsy [15], Alzheimer's disease [17], Parkinson's disease [16] and dyslexia [18]. The high temporal and spatial resolutions are the main advantages of MEG, compared with other imaging methods, e.g., fMRI, PET and

NIRS. MEG can catch rapid cortical activities [1], [2]. Similarly to EEG (electroencephalography), MEG data directly reflects the activities of neurons; unlike EEG, it is hard to be influenced by the structure of the head such as the conductivities of the tissues [1], [19].

MEG has already been contributing to the neuroscience, providing new knowledge about human brain functions, and is expected to play an increasingly important role in clinical treatments and investigations of human brain. For any applications of the MEG measurement, it is important to extract useful information from the signals and to know which function of the human brain the information reflects and originates from. Besides, handiness and stress-free use are essential to the further contribution of MEG to the demands in neurology. In this point of view, there are mainly two issues in MEG measurement, which must first be addressed to gain the value of MEG, i.e. the issues of the low signal-to-noise ratio (SNR) and of the ill-posed inverse problem.

In this study, for the improvements of MEG measurement, the author proposes solutions comprehensively, a noise reduction method with a combination of some signal processing techniques and an approach to the inverse problem with a utilization of a spatial filter.

1.3 Signal processing in MEG measurement

The signals due to brain activities are very weak, typically on the order of 50-500 fT [1]. Several kinds of noises and artifacts due to eye movements, blinking, heartbeats, an electric power supply, earth magnetism, etc., influence the desired signals, such as event-related responses. Band-pass filtering and stimulus-locked averaging across many trials without contamination from artifact are usually required to reduce the sensor noise and spontaneous brain noises. Though these are powerful ways to improve SNR, the imposition of many trials for averaging turns out not only a considerable burden for patients or experimental subjects but the lost of important temporal information.

It must be also considered that the inverse problem in MEG measurement, which is mentioned later, has a difficulty caused by its ill-posedness and underdetermination. And noises always aggravate the difficulty. Biological artifacts and sensor-specific noise interfere with the estimation of the locations from which desired signals originate, and unwanted brain activities complicate the interpretations of the inverse solutions from MEG data. Noise and artifacts cause trouble through out MEG analyses.

To resolve the issue, independent component analysis (ICA) for MEG and EEG analyses has been studied in recent years [24]-[31]. ICA is one of the blind signal processing methods. It separates linearly mixed signals by the assumption of statistical independence of the signals. Several kinds of algorithms have been proposed. If the artifacts and brain signals are independent of each other, they can be separated by ICA. Although ICA may be able to extract the signals from the data, including noises and artifacts, it does not work correctly under additive independent Gaussian sensor noise, especially in MEG data analysis.

ICA consists of a preprocessing and a main algorithm to estimate independent components. The preprocessing with PCA (principal component analysis) obtains orthogonalized signals before the main algorithm, thereby reducing the calculation cost of the main algorithm.

In the preprocessing step, it is required to prescribe the number of independent components. A large amount of sensor noise makes this decision difficult. Another important issue is that an orthogonalization of signals excluding high level sensor noise and the subsequent estimation of independent components are crucial in practical MEG analysis. It has been proposed that factor analysis be substituted for PCA in the preprocessing [26], [30], [31]. The orthogonalization of signals may be successful with factor analysis. The influence of noise, however, still seems serious factor in MEG measurement, and factor analysis does not reduce the sensor noise sufficiently. Thus, estimated independent components have low SNRs; furthermore, the desired components often cannot be obtained.

ICA algorithms theoretically robust to noise have been proposed [32]. Some

ICA algorithms based on higher order cumulants are theoretically robust to Gaussian noise, and they estimate the inversion matrix which separates independent components regardless of the existence of Gaussian noises. Based on the separating matrix, the Amari-Hopfield neural network estimates independent components, in which the noises are canceled, by minimizing the entropy of the residual. The residual is termed error components, and is assumed to correspond to the noises and to be i.i.d. The algorithm minimizes the magnitude of the error components as well [32]. Eventually, it may appraise the noises as smaller and not remove them sufficiently. An effective noise reduction method for taking advantage of ICA in MEG analysis and of the MEG data itself is thus needed.

1.4 Inverse problem in MEG measurement

Inverse problems appear universally in science and engineering fields from geophysics to biomedical studies. They are exactly ubiquitous [36]. Many researchers in mathematics and engineering appreciate the importance of the inverse problems, and are dedicated to solve them in their research fields. Inverse problems, which attract people working on science and technology, raise an important question: what causes the result we see? To solve the inverse problems is one side of the history of science.

Especially in engineering, we desire to know the physical mechanisms and characteristics which lead to the observed data. In many physical problems, the observation is described with a Fredholm integral equation of first kind [36], [37]:

$$\zeta(x) = \int_{-\infty}^{\infty} k(x - x')\xi(x')dx', \qquad -\infty < x < \infty, \tag{1.1}$$

where $\zeta(x)$ is the observation and $\xi(x)$ is the function of sources generate the observation. $k(x)$ is the kernel function which characterizes the model, and is determined by the equation related to the physical phenomenon. An appropreate discretization makes the equation into a vector-matrix linear equation as follows:

$$K\boldsymbol{\xi} = \boldsymbol{\zeta}, \tag{1.2}$$

where $\boldsymbol{\xi}$ denotes the discretized sources and $\boldsymbol{\zeta}$ represents the observed data. We want to obtain $\boldsymbol{\xi}$ from given $\boldsymbol{\zeta}$ and K. As well as inverse problems in several applications, that in the MEG measurement is formulated similarly (see Section 2.3). Hence, a study on the inverse problem in MEG measurement may make contribution to the other fields and vice versa.

The inverse problem in MEG measurement is to estimate the current density distribution in a brain which produces the magnetic field, and is mathematically ill-posed and underdetermined. The problem is stated as follows:

$$\boldsymbol{m} = L\boldsymbol{Q}, \tag{1.3}$$

where $\boldsymbol{m}$ denotes MEG data, L is the gain matrix called the lead field matrix, and $\boldsymbol{Q}$ represents the current density distribution in a brain [2]-[41].

The solution, namely the current density distribution, obtained by the Moore-Penrose pseudoinverse is the minimum norm least-square solution. It is given by solving the following problem [42]:

$$\min_{\boldsymbol{Q}} \left\{ \|\boldsymbol{Q}\|^2 + (\boldsymbol{m} - L\boldsymbol{Q})^T \boldsymbol{\Lambda} \right\}, \tag{1.4}$$

where $\boldsymbol{\Lambda}$ is the Lagrange multiplier vector, and the solution is:

$$\boldsymbol{Q} = L^T (LL^T)^{-1} \boldsymbol{m}. \tag{1.5}$$

It explains the data with the smallest currents. Consequently, the current distribution is biased toward sensor array. It is difficult to estimate the depths of the brain activities. Another general issue in inverse problems is the redundant expanse of the solution. The estimated current distribution is always ambiguous due to the nature of inverse problems. An adequate localization of a current distribution is required, especially in clinical situations. Some kinds of regularizations are successfully used to improve the estimation.

The least-squares methods with regularizations are generally applied to the in-

verse problem. The Tikhonov regularization method is a typical example of them. The problem is described as follows [36]:

$$\min_{\boldsymbol{Q}} \left\{ \|L\boldsymbol{Q} - \boldsymbol{m}\|^2 + \alpha \|\boldsymbol{Q}\|^2 \right\}, \tag{1.6}$$

where α is the regularization parameter. The solution is obtained as follows:

$$\boldsymbol{Q} = (L^T L + \alpha I)^{-1} L^T \boldsymbol{m}, \tag{1.7}$$

where I is an identity matrix. It is equivalent to the Bayesian estimation with the Gaussian prior. A truncated singular-value decomposition (TSVD) method, which truncates smaller singular value of L, is another kind of regularization. The regularization declines the instability, and gives a smooth solution. Unfortunately, the method with the regularization shows low resolution [2]. Many regularization techniques have been proposed, e.g. the method which utilizes the total variation of the solution and minimizes it [36]. It is possible to refer to the accumulated knowledge about those method [43]-[49]. However, to determine how to regularize the solution is quite difficult. In cases of MEG analyses, it is also available recently to take some information from other modalities, e.g. fMRI, in the regularization terms or prior information [4], [44], [50]. The relationship between MEG and other imaging methods is absorbing. Nonetheless, treating prior information involves some difficulties and is controversial [5].

The moving-dipole method is widespread and commonly used in MEG analyses. It searches an optimum solution minimizing the difference between a measurement and a forward solution given by dipoles in the least-square sense. The locations and orientations of dipoles are optimized by the Nelder-Meade simplex method, etc. The moving-dipole method inadmissibly depends on prior information of the number of dipoles and regions to be searched [1], [2].

MUSIC (multiple signal classification) is another approach; it determines the dipole parameters by requiring the forward solutions of the dipoles to be orthogonal to the noise subspace [51], [52], [53]. MUSIC utilizes the eigenvalue decomposition

of the covariance matrix of the MEG data. It divides the data into the signal subspace spanned by the eigenvectors corresponding to larger eigenvalues and the noise subspace P_n with eigenvectors of smaller eigenvalues. MUSIC identifies the locations and orientations of current dipoles in a brain may generate the observed data basically by minimizing the following function:

$$J(\boldsymbol{r}, \phi) = \frac{\|P_n \boldsymbol{l}(\boldsymbol{r}, \phi)\|^2}{\|\boldsymbol{l}(\boldsymbol{r}, \phi)\|^2}, \tag{1.8}$$

where $\boldsymbol{l}(\boldsymbol{r}, \phi)$ is a forward solution shows the contribution of the current dipole with the specific location $\boldsymbol{r}$ and orientation ϕ to the observation. $\boldsymbol{l}(\boldsymbol{r}, \phi)$ in the signal subspace must be orthogonal to P_n, and yield $J(\boldsymbol{r}, \phi) = 0$. This method needs to assume that the number of the sources is less than that of the sensors, and that the sources are uncorrelated. It is effective for localization of current distribution without prior information. However, it highly relies on temporal information. It is hard to resolve the correlate sources, and the spatial resolution declines in such a case.

Meanwhile, beamformer approaches [54]-[63], e.g., LCMV (linearly constrained minimum variance) beamformer [55] and SAM (synthetic aperture magnetometry) [56] can be operated without prior information. They are basically adaptive spatial filters to pass signals from specific locations and orientations while attenuating interferences by minimizing a covariance matrix of filtered observation with linear constraints. These spatial filters depend on prior or temporal information less than the others. These adaptive beamformers are problematic when the current sources in a brain have correlation; the spatial resolution declines due to the use of temporal information.

Consequently, it can be said that an effective method with less reliance on prior and temporal information is required for the inverse problem to take advantage of the high temporal resolution of MEG and to improve MEG applications.

1.5 Proposals for solutions

In this paper, the author proposes methods for both parts of the MEG analysis, the signal processing and the inverse analysis.

To alleviate the above-described problems in MEG measurement and analysis with ICA, the author proposes a signal processing technique that reduces the sensor noise from MEG data. This method consists of a combination of factor analysis and Kalman filtering [66]-[74]. A state-space model for the Kalman filter of the method is constructed via the forward problem in MEG measurement. Factor analysis is employed to estimate the system and observation noise covariance matrices. Then, the Kalman filter is used to reduce sensor noise before the ICA procedure. The proposed noise reduction method with factor analysis and Kalman filtering (FA-processed Kalman filter) eliminates sensor noise effectively and supports ICA as a preprocessing technique. Kalman filter is practically employed in several applications, and shows high performances to estimate or to predict the state of the system and to smooth signals. The proposed noise reduction does not limit the choice of ICA algorithm. Hence, it can be expected that the proposed combination increases the effects of and reliance on any ICA algorithm for MEG analyses.

The reliabilities of the solutions of some estimation problems, e.g. the inverse problems in MEG measurement, generally depend on prior information and assumptions. In cases where we cannot utilize reliable prior information, such as the cases of neurophysiological researches in progress, that should be minimized and simplified to obtain fair solutions. The proposed method is constructed by simple and minimum assumptions which preserve its reliability and usability: the forward solution of MEG is a linear system formula and suits a Kalman filtering problem. Thus the state-space equations are naturally described with mild assumptions. The Kalman filter does not need to identify specific probability distribution of noises. Though estimation of noise covariances required by the Kalman filter is always controversial, the proposed method provides them by well-known factor analysis, and the result of the factor analysis is utilized while avoiding the difficulty related to the inverse

problem in MEG, namely the direct estimation of the system noise which we assume that current densities in a brain are driven by.

Additionally, for the inverse analysis, a current density estimation with a combination of spatial filtering and a reconstruction utilizing multiple linear regression (spatial filtered reconstruction: SFR) is proposed in this paper.

A spatial filter requiring no temporal information is focused on, and attempts, with a single snapshot, a temporal slice of MEG data, to estimate a current density distribution, i.e. current dipoles in a conductor [64]. The spatial filter in this study is derived from a cost function that is different from that of the SAM and LCMV beamformers. It complies with the requirements that ordinary spatial filters should obey and is optimized with the second and fourth order cumulants [75], [76] of the estimated current dipole, which statistically characterize the current density distribution represented by the dipoles. The cost function suggests how to improve the localization of the current distribution and the depths of the estimated dipoles.

Though non-adaptive spatial filter in MEG analysis is not paid attention, it can be expected that the implementation of an improved non-adaptive spatial filter extends the applications of MEG. Studying a time-invariant spatial filter provides a new approach to inverse problems and helps guide the future progress in MEG analysis.

Moreover, the current distribution estimated with spatial filtering will be reconstructed in this study to increase the localization and obtain feasible distribution of the dipoles. The reconstruction method utilizes a multiple linear regression technique: the regression model is constructed with the dipoles obtained by the spatial filter. The Mallows C_p statistic [77], [78] localizes the current distribution. It is commonly used for selections of variables in multiple linear regression.

A solution of an inverse problem is generally ambiguous due to its ill-posedness, and in the interpretation of the solution, some kind of criterion such as a threshold value is required, even if it is subjective. In this study, the ambiguity appears as the redundant expansion of the current density distribution estimated by spatial filtering. Decision of the range of the brain activity is always controversial in the

inverse problem in MEG measurement. Based on multiple linear regression analysis that is well-studied theory, the proposed method provides an objective criterion for the decision of the activated region of the brain.

The SFR depends on the simple spatial filtering, and the reconstruction is equivalent to the hypothesis tests for the estimated current dipoles. It can be regarded as validation with a criterion. In this point of view, the proposed method follows ordinary approach that is usually taken in inverse problems, especially in MEG analysis. Nevertheless, while it takes advantages of spatial filtering, the SFR effectively clarifies the interpretation of the solution and makes it fair with the objective criterion and less dependence on prior information.

The proposals for the signal processing and the inverse analysis pursue the common ideals, that is to say, less dependence on prior information, maximization of the advantage of high temporal resolution and usability in the practical MEG analysis. In this study, the author proposes combining the FA-processed Kalman filter and SFR.

In the latter chapters, the forward problem of the MEG measurement on which the proposed methods are based is described in Section 2.3. Then the FA-processed Kalman filter is detailed in Section 2.4. The spatial filters in MEG analysis, i.e. the LCMV beamformer, SAM and the novel spatial filter, and the SFR are introduced in Section 2.5. In Chapter 3, the numerical studies are shown to verify the effectiveness of those methods. The proposals, in use for real MEG analysis, including the combination of the FA-processed Kalman filter, ICA and the SFR are also discussed in Chapter 4. Finally, the paper is concluded in Chapter 5.

Chapter 2

Methods

2.1 Electrophysiology in MEG measurement

A brain consists of neurons and glial cells. The glia supports the structure of the brain, maintains proper concentrations of ions and transports nutrients from blood vessels to brain tissues. Neurons process the information. They are constructed with the three components mainly: the soma which contains the nucleus and most of the metabolic mechanism, the dendrites receive signals from other cells, and the axon which transfers signals with action potentials from the soma to other cells. The dendrites and the soma have typically thousands of connections with other neurons, which are called synapses. The neurons pass the signals with the transmitter molecules in the synapses. When the pulse of the action potential arrives the presynaptic cells, the transmitter molecules are released and reach the postsynaptic cells. Then the ion channels open, and as the result the potential in the membrane changes at the dendrites (excitatory postsynaptic potentials: EPSPs) [1], [2].

The currents associated with the EPSPs are the main sources of most of the signals detected by MEG and EEG. The action potentials have the duration of about 1 ms, and it may be too short to measure in MEG. It is empirically known that we observe the signal generated by the sources on the order of 10 nAm, which is obtained by millions of synaptic junctions. According to the nominal calculation of the density of the neurons and cortical thickness, the cortex approximately has a

current density on the order of 100 nA/mm^2. The cerebral cortex has the thickness of 2-4 mm, therefore the area of the surface on the cortex with 5mm $\times$ 5mm is involved at least to yield the current dipole of 10 nAm [2].

2.2 Instrumentation in MEG measurement

The key technology to implement the MEG measurement is the SQUID (Superconducting QUantum Interference Device), which is highly sensitive detector of magnetic flux and is the only device with sufficient sensitivity for biomagnetic measurement [14]. A microscopic state of a superconductor is described by a wave function that is well defined with a phase. This causes flux quantization: a superconducting loop encloses the magnetic flux quantized in units of $\Phi_0 \equiv h/2e$ [Tm^2] where h is Planck's constant and e is the electron charge. The dc-SQUID which is mainly employed nowadays is a loop of two superconductors weakly connected with two Josephson junctions (Fig.2.1). The dc-SQUID is biased with a constant current I_d which is larger than the supercurrent. In this case, the voltage V is developed across the junctions. The $V - I$ characteristics are explained by the resistively and capacitively shunted junction model, in which the Josephson junction is parallel with a resistance and a capacitance. It is known that the external magnetic flux Φ_e changes the voltage V across the SQUID with the period of Φ_0 (Fig.2.2). We can detect the magnetic flux as the change of the voltage V [1], [14].

Meanwhile, the magnetic flux on the observation point is transferred by a gradiometer. Gradiometers measure the spatial gradient of the magnetic induction. For instance, a first-order axial gradiometer has oppositely wounded coaxial pickup and compensation coils. The distance between the coils, the baseline, is usually 4-5 cm. This arrangement is effective to measure the weak magnetic flux produced by sources near the gradiometer, because the large homogeneous magnetic flux in the background is canceled [1].

The electric current due to the change of the magnetic flux in the gradiometer is transformed into Φ_e by the inductance and is transferred to the SQUID. The

dc-SQUID is involved in the feedback circuit called flux locked loop (FLL) consists of an amplifier, a lock-in detector and an oscillator (Fig.2.3). The output voltage V_f of the FLL is fed back to the dc-SQUID as the magnetic flux modulated with the amplitude of $\Phi_0/2$. By the feedback, the voltage V across the dc-SQUID due to Φ_e eventually modulated, and it enable to reduce noises by the lock-in detector. The feedback keeps the flux in the SQUID a constant at an optimum working point on the $V - \Phi_e$ characteristic, and linearizes the SQUID response. The output of the FLL V_f is proportional to the observed magnetic flux Φ_e. MEG measures the magnetic flux by the principle basically, and we can obtain the readout of it.

In actual MEG measurement, sensing devices are cooled with liquid helium in a Dewar to reduce thermal noises. Experiments and measurements are usually conducted in a magnetically shielded room to attenuate environmental noises [1], [14].

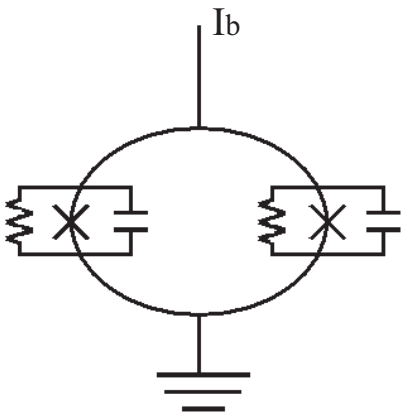

Figure 2.1: Schema of dc-SQUID: × represents the Josephson junction, and it is parallel with a resistance and a capacitance in the shunted junction model. I_b represents a bias current.

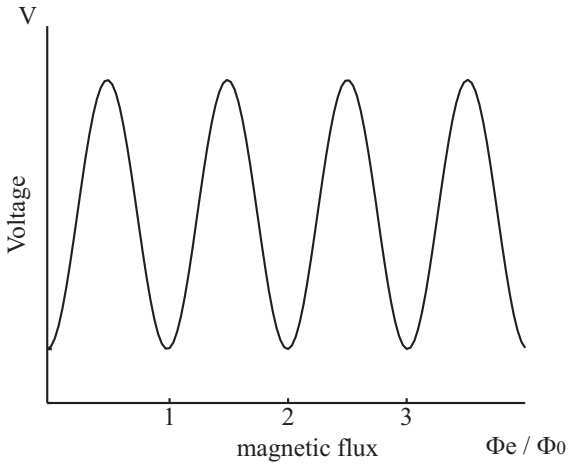

Figure 2.2: $V - \Phi_e$ characteristic. The external magnetic flux Φ_e changes the voltage V across the SQUID with the period of Φ_0.

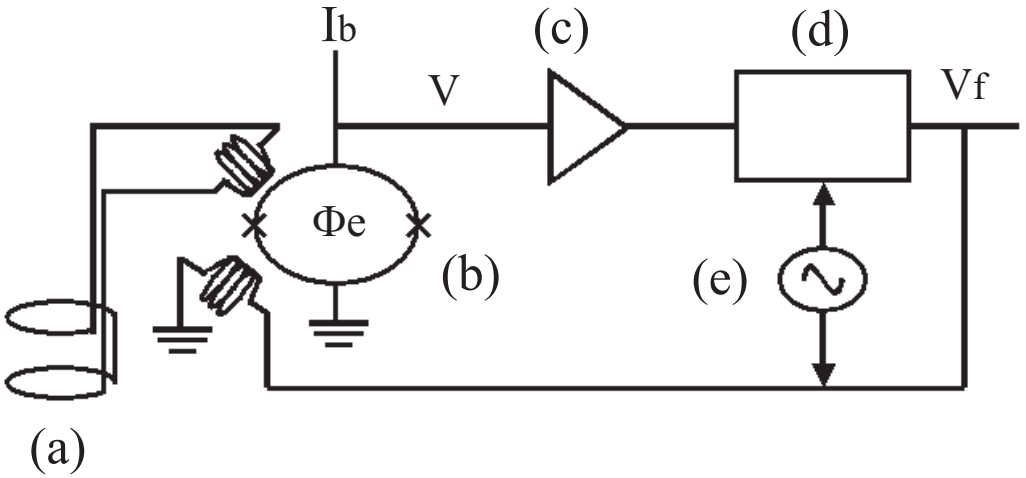

Figure 2.3: Schema of the Flux Locked Loop (FLL): (a) the first-order axial gradiometer, (b) the dc-SQUID, (c) amplifier, (d) lock-in detector and (e) oscillator

2.3 Forward problem in MEG measurement

Electrophysiological phenomena caused by neural electrical activities and observed with MEG and EEG can be described by the quasistatic approximation of Maxwell's equations, because their frequency spectrum is below 1 kHz and time-derivative terms can be ignored. Therefore, a magnetic flux density $\boldsymbol{B}(\boldsymbol{r})$ generated by a current flow in the brain is given by the Biot-Savart law [1], [2]:

$$\boldsymbol{B}(\boldsymbol{r}) = \frac{\mu_0}{4\pi} \int_\Omega \boldsymbol{J}(\boldsymbol{r}') \times \frac{\boldsymbol{r} - \boldsymbol{r}'}{\|\boldsymbol{r} - \boldsymbol{r}'\|^3} d\boldsymbol{r}', \tag{2.1}$$

where μ_0 is the permeability of free space.

Current density in the brain is composed of two components, the primary and volume currents:

$$\begin{aligned} \boldsymbol{J}(\boldsymbol{r}') &= \boldsymbol{J}_p(\boldsymbol{r}') + \boldsymbol{J}_v(\boldsymbol{r}') \\ &= \boldsymbol{J}_p(\boldsymbol{r}') - \sigma(\boldsymbol{r}')\nabla V(\boldsymbol{r}'). \end{aligned} \tag{2.2}$$

The volume current $\boldsymbol{J}_v(\boldsymbol{r}')$ occurs with the macroscopic electric field on charge carriers in the conducting medium. The primary current $\boldsymbol{J}_p(\boldsymbol{r}')$ is considered to be driven by neural activities. Equation (2.1) is transformed into

$$\begin{aligned} \boldsymbol{B}(\boldsymbol{r}) &= \boldsymbol{B}_p(\boldsymbol{r}) \\ &+ \frac{\mu_0}{4\pi} \sum_{ij} (\sigma_i - \sigma_j) \int_{S_{ij}} V(\boldsymbol{r}') \frac{\boldsymbol{r} - \boldsymbol{r}'}{\|\boldsymbol{r} - \boldsymbol{r}'\|^3} \times \boldsymbol{n}(\boldsymbol{r}') dS_{ij}, \end{aligned} \tag{2.3}$$

where $\boldsymbol{B}_p(\boldsymbol{r})$ is the magnetic flux density generated by the primary current, σ_i is the conductivity of the i-th region, S_{ij} is the boundary surface between the i-th and j-th regions, and $\boldsymbol{n}(\boldsymbol{r}')$ is the outer normal vector of the surface. The volume currents are equivalently replaced by the current densities $-(\sigma_i - \sigma_j)V(\boldsymbol{r}')\boldsymbol{n}(\boldsymbol{r}')$ distributed on the surface S_{ij}. Equation (2.3) implies that the volume current does not contribute to the radial magnetic flux for spherical brain [1].

When the conductor is spherically symmetric, a forward solution is analytically

derived as follows [41]:

$$\boldsymbol{B}(\boldsymbol{r}) = \frac{\mu_0}{4\pi} \frac{F\boldsymbol{q}_i \times \boldsymbol{r}_i - (\boldsymbol{q}_i \times \boldsymbol{r}_i \cdot \boldsymbol{r})\, \nabla F(\boldsymbol{r}, \boldsymbol{r}_i)}{F(\boldsymbol{r}, \boldsymbol{r}_i)^2}, \tag{2.4}$$

where $\boldsymbol{q}_i$ is an equivalent current dipole at $\boldsymbol{r}_i$ which approximates the primary current as a point dipole, i.e. $\boldsymbol{J}_p(\boldsymbol{r}') \simeq \boldsymbol{q}_i \delta(\boldsymbol{r}' - \boldsymbol{r})$; $\delta(\boldsymbol{r})$ is the Dirac delta function,

$$F(\boldsymbol{r}, \boldsymbol{r}_i) = a\left(ra + r^2 - \boldsymbol{r}_i \cdot \boldsymbol{r}\right), \tag{2.5}$$

and

$$\begin{aligned} \nabla F(\boldsymbol{r}, \boldsymbol{r}_i) = {} & (r^{-1}a^2 + a^{-1}\boldsymbol{a} \cdot \boldsymbol{r} + 2a + 2r)\boldsymbol{r} \\ & -(a + 2r + a^{-1}\boldsymbol{a} \cdot \boldsymbol{r})\boldsymbol{r}_i, \end{aligned} \tag{2.6}$$

with $\boldsymbol{a} = (\boldsymbol{r} - \boldsymbol{r}_i)$, $a = \|\boldsymbol{a}\|$ and $r = \|\boldsymbol{r}\|$. From Eq.(2.4), radially oriented dipoles do not produce any magnetic flux. Therefore, only a two-dimensional dipole moment is considered in this case.

The magnetic flux is linearly related to the current dipole. When we assume that gradiometers are arranged radially and are sensitive only to radial magnetic flux, i.e., to primary currents, and that a conductor Ω discretized into N pieces ω_i and current dipoles $\boldsymbol{q}_i$ on the grid points $\boldsymbol{r}_i$ $(i = 1, 2, \cdots, N)$ constitute a current density distribution, a measurement $\boldsymbol{m} \in \Re^{m \times 1}$ of m MEG sensors can be written in a vector-matrix formula as a linear system:

$$\boldsymbol{m} = L\boldsymbol{Q} + \boldsymbol{\varepsilon} = \sum_{i=1}^{N} L_i \boldsymbol{q}_i + \boldsymbol{\varepsilon}, \tag{2.7}$$

where $L = [L_1, L_2, \cdots, L_N] \in \Re^{m \times 3N}$ is a lead field matrix, $\boldsymbol{Q} \in \Re^{3N \times 1}$ has all dipole moments $\boldsymbol{q}_i \in \Re^{3 \times 1}$ $(i = 1, 2, \cdots, N)$ as its components, and $\boldsymbol{\varepsilon} \in \Re^{m \times 1}$ is observation noise.

When the conductor is a piecewise homogeneous, such as a model of real head shape, and the sensors are sensitive to the magnetic flux by the volume currents, the

magnetic flux of the primary current is simulated by the boundary element method (BEM) considering the contribution of the volume current, and the lead field can be calculated [1], [40], [39]. In the case of a spherically symmetric model, the matrices and vectors are adjusted to the dipole moment $\boldsymbol{q}_i \in \Re^{2\times 1}$.

The following proposals to MEG analysis, i.e. the noise reduction method and the method for the estimation of the current density distribution, are based on Eq.(2.7). In the numerical studies in Chapter 3 and the real MEG analyses in Chapter 4, it was assumed that the conductor was a sphere and the sensors were arranged radially. Hence, the conductivities are not required. The permeability μ_o can be adopted regardless of the tissues in a head.

2.4 Reduction of noise from MEG data

2.4.1 Sensor noise reduction with Kalman filter

Kalman filtering is applied to several kinds of problems [72]-[74]. Estimation problems to which a Kalman filter is applied can be classified into three types: prediction, filtering and smoothing problems. In this study a Kalman filter is applied to eliminate the noise, which is specific for each sensor, from MEG signals. This procedure supports successive ICA to reduce artifacts.

Kalman filtering is used to estimate the sequence of states of the dynamical system described as a state-space model [66], [67].

Let us assume that the moments of dipoles $\boldsymbol{Q}(t)$ are driven by system noise $\boldsymbol{v}(t)$:

$$\boldsymbol{Q}(t+1) = \boldsymbol{Q}(t) + \boldsymbol{v}(t), \tag{2.8}$$

where the first and second moments of $\boldsymbol{v}(t)$ are $E\{\boldsymbol{v}(t)\} = \boldsymbol{0}$ and $E\{\boldsymbol{v}(t)\boldsymbol{v}(l)^T\} = V(t)\delta_{tl}$. From the above assumption and the forward equation of MEG measurement, Eq.(2.7), MEG data without observation noise, which may include artifacts, are

described as follows:

$$\begin{aligned} \boldsymbol{x}(t+1) &= L\boldsymbol{Q}(t+1) \\ &= L\boldsymbol{Q}(t) + L\boldsymbol{v}(t) \\ &= \boldsymbol{x}(t) + L\boldsymbol{v}(t). \end{aligned} \tag{2.9}$$

In this study, it is assumed that the observation is constructed by MEG signals $\boldsymbol{x}(t)$ including desired signals and artifacts, e.g. unwanted brain activities, and "sensor (observation) noise" $\boldsymbol{\varepsilon}(t)$ which is independently added to the signal of each sensor.

Then, observed MEG data with sensor noise are given as

$$\boldsymbol{m}(t) = \boldsymbol{x}(t) + \boldsymbol{\varepsilon}(t), \tag{2.10}$$

where $\boldsymbol{\varepsilon}(t)$ is the sensor noise whose first and second moments are $E\{\boldsymbol{\varepsilon}(t)\} = \mathbf{0}$ and $E\{\boldsymbol{\varepsilon}(t)\boldsymbol{\varepsilon}(l)^T\} = W(t)\delta_{tl}$. Therefore, the author sets the state-space model for the Kalman filter to be as follows:

$$\boldsymbol{x}(t+1) = \boldsymbol{x}(t) + L\boldsymbol{v}(t) \tag{2.11}$$

$$\boldsymbol{m}(t) = \boldsymbol{x}(t) + \boldsymbol{\varepsilon}(t), \tag{2.12}$$

where L is the lead field matrix.

Furthermore, it is assumed that an initial state $\boldsymbol{x}_0$ is uncorrelated to the system and observation noises, $E\{\boldsymbol{x}_0\} = \bar{\boldsymbol{x}}_0$ and $V\{\boldsymbol{x}_0\} = X_0$. Under the prescribed assumptions, the estimation of the state sequence, namely the sensor noise-free MEG signals, is obtained by the recursive prediction and correction included in the fol-

lowing algorithm:

$$\tilde{\boldsymbol{x}}(t+1) = \hat{\boldsymbol{x}}(t), \tag{2.13}$$

$$M(t+1) = P(t) + LV(t)L^T, \tag{2.14}$$

$$K(t+1) = M(t+1)\left(M(t+1) + W(t+1)\right)^{-1}, \tag{2.15}$$

$$\hat{\boldsymbol{x}}(t+1) = \tilde{\boldsymbol{x}}(t+1) + K(t+1)\left(\boldsymbol{m}(t+1) - \tilde{\boldsymbol{x}}(t+1)\right), \tag{2.16}$$

$$P(t+1) = M(t+1) - K(t+1)M(t+1), \tag{2.17}$$

where $\hat{\boldsymbol{x}}(0) = \bar{\boldsymbol{x}}_0$ and $P(0) = X_0$.

In particular, when $V(t)$ and $W(t)$ are time-invariant in a state-space model that is observable and controllable, $P(t)$ converges to a constant value. Then, a steady-state Kalman filter is obtained [69]:

$$\hat{\boldsymbol{x}}(t) = (I - K)\hat{\boldsymbol{x}}(t-1) + K\boldsymbol{m}(t) \tag{2.18}$$

$$K = PW^{-1}, \tag{2.19}$$

P satisfies the following equation:

$$P = \left[(P + LVL^T)^{-1} + W^{-1}\right]^{-1}. \tag{2.20}$$

In this study, the system and observation noises are assumed to be stationary during the MEG measurement, thus a steady-state Kalman filter algorithm in Eqs.(2.18) and (2.19) is adopted.

Kalman filtering requires knowledge of the system noise covariance matrix V and observation noise covariance matrix W. Factor analysis is utilized to estimate the noise covariances in the following section.

2.4.2 Estimation of noise covariances with factor analysis prior to Kalman filtering

Factor analysis (FA) is one of the methods for multivariate data analysis, and is utilized in the preprocessing of ICA [26], [30].

In FA, factor loading matrix Λ and sensor noise covariance (covariance of unique factors) matrix W are estimated. The observation $\boldsymbol{m}(t)$ is modeled as follows:

$$\begin{aligned} \boldsymbol{m}(t) &= \Lambda \boldsymbol{f}(t) + \boldsymbol{\varepsilon}(t) \\ & \boldsymbol{f}(t) = [f_1(t), f_2(t), \cdots, f_n(t)]^T, \\ & E\{f_i(t)\} = 0,\ E\{f_i(t) f_j(t)\} = \delta_{ij}, \end{aligned} \tag{2.21}$$

where f_i and ε_i are called the common factor and unique factor. From Eqs.(2.7) and (2.21), we can determine that $\boldsymbol{x}(t) = L\boldsymbol{Q}(t) = \Lambda \boldsymbol{f}(t)$.

There are several methods to conduct FA, e.g., the unweighted least squares method, principal factors method and maximum likelihood method [26], [30]. In this study, I adopt the unweighted least squares method which can be used easily due to its simplicities of the formulation and the algorithm. Besides, it requires less prior conditions or assumptions, e.g. a probability distribution function, than the others. However, any methods for FA can be applied to estimate the noise covariances.

The estimation is achieved by solving the following problem:

$$\min_{\Lambda, W} \ \mathrm{tr}\{(S - \Lambda\Lambda^T) - W\}^2, \tag{2.22}$$

where S is an observed covariance matrix.

To minimize the cost function, the algorithm is derived as

$$\Lambda^{(t+1)} = \Lambda^{(t)} + \eta(S - \Sigma^{(t)})\Lambda^{(t)} \tag{2.23}$$

$$W^{(t+1)} = \mathrm{diag}(S - \Lambda^{(t+1)}\Lambda^{(t+1)T}) \tag{2.24}$$

$$\Sigma^{(t+1)} = \Lambda^{(t+1)}\Lambda^{(t+1)T} + W^{(t+1)}. \tag{2.25}$$

We can use the sensor noise covariance W estimated by FA for the Kalman filter algorithm. On the other hand, it is impossible to estimate V directly, but LVL^T in Eq.(2.20) can be estimated from the result of FA as follows.

$\Lambda\Lambda^T$ is the covariance of $\boldsymbol{x}(t)$. When the sample number of MEG data, τ, is sufficiently large, the following relation holds, since $E\{\boldsymbol{v}(k)\boldsymbol{v}(l)^T\} = 0,\ (k \neq l)$ and state equation (2.11) hold.

$$\begin{aligned}\Lambda\Lambda^T &= \frac{1}{\tau}\Big\{\sum_{t=1}^{\tau}\boldsymbol{x}(t)\boldsymbol{x}(t)^T\Big\} \\ &\simeq \frac{1}{\tau}L\big\{\tau\boldsymbol{v}(1)\boldsymbol{v}(1)^T + (\tau-1)\boldsymbol{v}(2)\boldsymbol{v}(2)^T + (\tau-2)\boldsymbol{v}(3)\boldsymbol{v}(3)^T + \cdots + \boldsymbol{v}(\tau)\boldsymbol{v}(\tau)^T\big\}L^T \\ &= \frac{1}{\tau}L\Big\{\sum_{t=1}^{\tau}(\tau+1-t)\boldsymbol{v}(t)\boldsymbol{v}(t)^T\Big\}L^T \quad (2.26)\end{aligned}$$

Normalizing the factor inside the braces $\{\cdot\}$ in the right-hand side of Eq.(2.26) by $\sum_{t=1}^{N} t = (1+\tau)\tau/2$, we get the weighted average of $\boldsymbol{v}(t)\boldsymbol{v}(t)^T$. Thus, the estimation of LVL^T required for Kalman filtering is obtained by the following normalization of $\Lambda\Lambda^T$ estimated with FA:

$$\frac{2}{\tau+1}\Lambda\Lambda^T \simeq LVL^T. \quad (2.27)$$

With this estimation, we can avoid the difficulty to estimate V directly; it includes some issues related to the inverse problem in MEG measurement.

The combination of the Kalman filtering and factor analysis is mentioned as the FA-processed Kalman filter hereafter.

2.4.3 Independent component analysis following the sensor noise reduction

Independent component analysis (ICA) is a method for extracting independent components based only on observation [33]. The observation data are modeled as a mixture of unknown sources. If artifacts and desired signals are independent, we can separate the artifacts from the signals through ICA [32]-[35].

A preprocessing with principal component analysis (PCA) is usually conducted to reduce the dimension and to make signals uncorrelated. After the noise reduction by the combination of FA and Kalman filtering, it is also possible to apply the following procedure for the PCA:

$$\boldsymbol{y}(t) = \left(\Lambda^T \Lambda\right)^{-1} \Lambda^T \hat{\boldsymbol{x}}(t). \tag{2.28}$$

Then, ICA estimates independent components under the assumption that the signals are described as follows:

$$\boldsymbol{y}(t) = H\boldsymbol{s}(t), \tag{2.29}$$

where $\boldsymbol{y}(t)$ is interpreted as the mixed data which by an unknown matrix H that mixes unknown independent components $\boldsymbol{s}(t)$.

The goal of ICA is to estimate an unmixing matrix U that is a generalized inverse of H, so that the estimated independent components $\hat{\boldsymbol{s}}(t)$ can be obtained as

$$\hat{\boldsymbol{s}}(t) = U\boldsymbol{y}(t). \tag{2.30}$$

Several algorithms have been shown to be effective for estimating U. This study adopts the FastICA algorithm based on a fixed-point method, since it has advantages of fast convergence, lack of a learning rate, etc. This algorithm extracts independent components one by one using the row vector $\boldsymbol{u}^T$ of U calculated by the following algorithm:

$$\tilde{\boldsymbol{u}}^{(t)} = \boldsymbol{u}^{(t)} - \frac{E[yg(\boldsymbol{u}^{(t)T}y)] - \beta\boldsymbol{u}^{(t)}}{E[g'(\boldsymbol{u}^{(t)T}y)] - \beta}, \tag{2.31}$$

$$\boldsymbol{u}^{(t+1)} = \frac{\tilde{\boldsymbol{u}}^{(t)}}{\left\|\tilde{\boldsymbol{u}}^{(t)}\right\|}, \tag{2.32}$$

where $g(z) = z^3$ or $g(z) = \tanh(z)$. Some independent components may not be related to the responses we expect from the stimulus which is given to the experimental subject. They can be artifacts and be reduced here. The independent components

except for the artifacts are projected to the sensor space through the inverse of the above procedures and utilized for further analyses.

2.5 Estimation of current density distribution

2.5.1 Spatial filters in MEG analysis

2.5.1.1 LCMV beamformer

A spatial filter is a signal processing technique that attempts to separate a desired signal from interferences by utilizing the differences of the locations from which they originate. There are several applications that employ spatial filters, e.g., RADAR, SONAR, imaging, etc [54]. A spatial filter employed in this study is a linear projection operator that transforms the MEG signals to an estimation of a specific dipole moment:

$$\hat{\boldsymbol{q}}_k = W_k^T \boldsymbol{m} = W_k^T \sum_{i=1}^{N} L_i \boldsymbol{q}_i + \boldsymbol{\varepsilon}, \tag{2.33}$$

where $W_k \in \Re^{m\times 3}$ or $\Re^{m\times 2}$ is the spatial filtering matrix and $\hat{\boldsymbol{q}}_k$ is the estimated dipole at $\boldsymbol{r}_k$. The sizes of the matrices and vectors depend on the models including the sensor array and the shape of the conductor. They are appropriately adjusted to the model. The current distribution is estimated with N spatial filters for the grid points.

A spatial filter for the location of interest $\boldsymbol{r}_k$ should obey the following constraints:

$$W(\boldsymbol{r}_k)^T L(\boldsymbol{r}) = \begin{cases} I, & \|\boldsymbol{r} - \boldsymbol{r}_k\| \leq \delta \\ 0, & \|\boldsymbol{r} - \boldsymbol{r}_k\| > \delta, \end{cases} \tag{2.34}$$

where δ represents a small distance, and I represents an identity matrix.
The LCMV beamformer, one of the representatives of the methods for MEG analysis, is designed with temporal information. It minimizes the covariance of the

estimated dipole and satisfies the above requirements as much as possible by solving the problem as follows [55]:

$$\begin{aligned} &\min_{W_k} \ \mathrm{tr}\left\{W_k^T C_m W_k\right\}, \\ &\text{subject to } W_k^T L_k = I, \end{aligned} \tag{2.35}$$

where $\mathrm{tr}\{\cdot\}$ denotes trace, and C_m is the covariance matrix of MEG data. The beamformer is obtained as follows:

$$W_k = \left[L_k^T C_m^{-1} L_k\right]^{-1} L_k^T C_m^{-1}, \tag{2.36}$$

The activities of interest are estimated by the LCMV beamformer taking noise into account. The neural activity index defined as follows is adopted as the evaluation of the activities. It is similar to the signal-to-noise ratio of the output of the beamformer:

$$\hat{\mathrm{Var}}\left(\boldsymbol{q_k}\right) = \frac{\mathrm{tr}\left\{\left[L_k^T C_m^{-1} L_k\right]^{-1}\right\}}{\mathrm{tr}\left\{\left[L_k^T C_n^{-1} L_k\right]^{-1}\right\}}, \tag{2.37}$$

where C_n is the covariance matrix of noises. The LCMV beamformer localizes current density distribution effectively. However, the minimization of the covariance ends unsuccessfully when multiple sources are activated with extreme correlations.

2.5.1.2 SAM

SAM (synthetic aperture magnetometry) [56] is an adaptive beamformer and is based on minimum variance principle that is adopted in the LCMV beamformer. The SAM targets the dipole amplitude $q_k(\phi)$ with a specific direction ϕ on a location $\boldsymbol{r}_k$; the SAM searches dipole parameters in a location $\boldsymbol{r}_k$ and the orientation ϕ:

$$q_k(\phi) = \boldsymbol{w}_k(\phi)^T \boldsymbol{m}, \tag{2.38}$$

where $\boldsymbol{w}_k(\phi) \in \Re^{m\times 1}$ is the SAM beamformer. The beamformer is computed by minimizing the variance with the constraint:

$$\min_{\boldsymbol{w}_k(\phi)} \ \boldsymbol{w}_k(\phi)^T C_m \boldsymbol{w}_k(\phi), \ \text{ subject to } \boldsymbol{w}_k(\phi)^T \boldsymbol{l}_k(\phi) = 1, \tag{2.39}$$

where $\boldsymbol{l}_k(\phi) \in \Re^{m\times 1}$ is the lead field for the dipole with the specific location and orientation, and the SAM beamformer is proposed as follows:

$$\boldsymbol{w}_k(\phi) = \frac{[C_m + \lambda C_n]^{-1}\boldsymbol{l}_k(\phi)}{\boldsymbol{l}_k(\phi)^T[C_m + \lambda C_n]^{-1}\boldsymbol{l}_k(\phi)}. \tag{2.40}$$

The formula is similar to the LCMV beamformer, though the SAM is modified to minimize the influence of the noise by introducing the noise covariance C_n. λ is the regularization parameter to adjust the effect of the modification. As well as the neural activity index of the LCMV beamformer, the following ratio $\rho_k(\phi)$ of the source power to the noise (or the square root of it which is called a pseudo-Z) is utilized for the evaluation:

$$\rho_k(\phi) = \frac{S_k^2(\phi)}{\sigma_k^2(\phi)}, \tag{2.41}$$

$$S_k^2(\phi) = \left\{\boldsymbol{l}_k(\phi)^T \left(C_m + \lambda C_n\right)^{-1} \boldsymbol{l}_k(\phi)\right\}^{-1}, \tag{2.42}$$

$$\sigma_k^2(\phi) = \boldsymbol{w}_k(\phi)^T C_n \boldsymbol{w}_k(\phi). \tag{2.43}$$

2.5.2 Proposed spatial filter without temporal information

2.5.2.1 Concept of the proposed spatial filter

This paper proposes a non-adaptive spatial filter which does not require temporal information, unlike the LCMV beamformer and the SAM. For the design of the spatial filter, we consider the probability density function (pdf) of the output of the spatial filter. When the current dipole is regarded as a random variable and has its pdf, the output of the spatial filter should obey the pdf and be optimized to reproduce it. Therefore, if the pdf has its probability density strongly concentrated around zero, the dipole estimated by the spatial filter should inherit the character.

As the result, the amplitude of the current dipoles is suppressed in the total current distribution estimated by the spatial filter. It can be interpreted as the improvement of the localization. This prospect can be introduced to a modification of the spatial filter to reduce the redundant expansion of the current density distribution, though identifying the pdf of the dipole is to depend on a prior information.

In this study, using some small assumptions and the cumulant expansion, the objective function for the optimization of the spatial filter is derived with less dependence on the identification of the pdf of the current dipole; the objective function is constructed with the second and fourth order cumulants.

Let us regard the current dipoles $\boldsymbol{q}_i$ as random variables and introduce the probability density functions (pdfs), $f_i(\tilde{\boldsymbol{q}}_i)$ and $g(\hat{\boldsymbol{q}}_k)$ of:

$$\tilde{\boldsymbol{q}}_i = W_k^T L_i \boldsymbol{q}_i, \tag{2.44}$$

$$\hat{\boldsymbol{q}}_k = W_k^T \sum_{i=1}^{N} L_i \boldsymbol{q}_i = \sum_{i=1}^{N} \tilde{\boldsymbol{q}}_i, \tag{2.45}$$

where $\hat{\boldsymbol{q}}_k$ is the estimated current dipole, i.e. the output of the spatial filter, and $\tilde{\boldsymbol{q}}_i$ is the contribution to $\hat{\boldsymbol{q}}_k$ of the dipoles $\boldsymbol{q}_i$ including the target dipole $\boldsymbol{q}_k$ and non-target dipoles $\boldsymbol{q}_i$ $(i \neq k)$.

We assume the current dipoles are i.i.d. Then the pdf $g(\hat{\boldsymbol{q}}_k)$ can be written as the convolutions of $f_i(\tilde{\boldsymbol{q}}_i)$ since $\hat{\boldsymbol{q}}_k$ is the sum of $\tilde{\boldsymbol{q}}_i$. Utilizing the characteristic functions $G(\boldsymbol{t})$ and $F_i(\boldsymbol{t})$, or the logarithms of them, of $g(\hat{\boldsymbol{q}}_k)$ and $f(\tilde{\boldsymbol{q}}_i)$, we obtain simpler formulas as follows:

$$\begin{aligned} F_i(\boldsymbol{t}) &= E\left\{\exp\left(\sqrt{-1}\ \boldsymbol{t}^T \tilde{\boldsymbol{q}}_i\right)\right\} \\ &= \int_{-\infty}^{\infty} f_i(\tilde{\boldsymbol{q}}_i) \exp\left(\sqrt{-1}\ \boldsymbol{t}^T \tilde{\boldsymbol{q}}_i\right) d\tilde{\boldsymbol{q}}_i, \end{aligned} \tag{2.46}$$

$$G(\boldsymbol{t}) = E\left\{\exp\left(\sqrt{-1}\ \boldsymbol{t}^T \hat{\boldsymbol{q}}_k\right)\right\} = \prod_{i=1}^{N} F_i(\boldsymbol{t}), \tag{2.47}$$

or

$$\log G(\boldsymbol{t}) = \sum_{i=1}^{N} \log F_i(\boldsymbol{t}). \tag{2.48}$$

Since the spatial filter is wanted to minimize the contribution $\tilde{\boldsymbol{q}}_i$ $(i \neq k)$ and extract that of the target dipole $\tilde{\boldsymbol{q}}_k$, the spatial filter coefficients W_k should get rid of the contribution $F_i(\boldsymbol{t})$ $(i \neq k)$ in $G(\boldsymbol{t})$ as much as possible. Therefore, the requirement for the design of the spatial filter is described as follows:

$$\log G(\boldsymbol{t}) \longrightarrow \sum_{i=1}^{N} \delta_{ik} \log F_i(\boldsymbol{t}), \tag{2.49}$$

where δ_{ik} is the Kronecker delta.

To achieve the above requirement, we can utilize the cumulants which are the coefficients in the Taylor expansion of the logarithm of the characteristic function and determine $G(\boldsymbol{t})$ and equivalently $g(\hat{\boldsymbol{q}}_k)$. In this study, we use the second and fourth order cumulants. The second order cumulants correspond to the variance of the estimated dipole, and the fourth order cumulants are called the kurtosis. The cumulants of higher order than the second show non-Gaussianity since the Gaussian pdf has the higher order cumulants equal to zero.

We set the objective function with the cumulants and solve the following minimiazation problem to optimize the spatial filter:

$$\min_{W_k} \ \hat{G}, \tag{2.50}$$

$$\hat{G} = (1-\lambda) \cdot \mathrm{tr}(C_2) + \lambda \cdot \mathrm{tr}(C_4), \tag{2.51}$$

$$\text{subject to } \left\| W_k^T L_k \right\|_{Fro}^2 = \text{const.}, \tag{2.52}$$

where $0 \leq \lambda \leq 1$, and C_2 and C_4 are the matrices and have the second and fourth order cumulants of $\hat{\boldsymbol{q}}_k$ as their elements respectively. $\|A\|_{Fro} = \sqrt{\mathrm{tr}(AA^T)}$, which is called the Frobenius norm. Note that the matrices of the cumulants depend on W_k. λ is the parameter to regulate the effect of the fourth order cumulants in the

optimization.

2.5.2.2 Derivation of the optimization problem of the spatial filter

Here, we assume that the components $q_{i\theta}$ $(\theta = 1, 2, 3)$ of the current dipole $\boldsymbol{q}_i$ are i.i.d. Thus the cumulant of rth order for the cumulant expansion of $\log F_i(\boldsymbol{t})$, the logarithm of the charateristic function of the pdf which the contribution $\tilde{\boldsymbol{q}}_i$ of the i-th dipole to the spatial filter output has, is obtained as follows :

$$\begin{aligned} \mathrm{Cum}(\tilde{q}_{i1}^{r_1}, \tilde{q}_{i2}^{r_2}, \tilde{q}_{i3}^{r_3}) = \sum_{\theta} a_{1\theta}^{r_1} a_{2\theta}^{r_2} a_{3\theta}^{r_3} \mathrm{Cum}(q_{i\theta}^{r}), \\ r = r_1 + r_2 + r_3,\ r_1, r_2, r_3 \in \mathbf{N} \end{aligned} \tag{2.53}$$

where

$$\tilde{\boldsymbol{q}}_i = [\tilde{q}_{i1}, \tilde{q}_{i2}, \tilde{q}_{i3}]^T, \tag{2.54}$$

$$a_{\tilde{\theta}\theta} = \boldsymbol{w}_{k\tilde{\theta}}^T \boldsymbol{l}_{i\theta}, \tag{2.55}$$

$\boldsymbol{w}_{k\tilde{\theta}}$ and $\boldsymbol{l}_{i\theta}$ are the vectors of the columns of W_k and L_i, respectively.

For instance,

$$\begin{aligned} &\mathrm{Cum}(\tilde{q}_{i1}^2, \tilde{q}_{i2}, \tilde{q}_{i3}) \\ &= \mathrm{Cum}(a_{11}q_{i1} + a_{12}q_{i2} + a_{13}q_{i3}, a_{11}q_{i1} + a_{12}q_{i2} + a_{13}q_{i3}, a_{21}q_{i1} + a_{22}q_{i2} + a_{23}q_{i3}, \\ &\qquad a_{31}q_{i1} + a_{32}q_{i2} + a_{33}q_{i3}) \\ &= \mathrm{Cum}(a_{11}q_{i1}, a_{11}q_{i1}, a_{21}q_{i1}, a_{31}q_{i1}) + \mathrm{Cum}(a_{12}q_{i2}, a_{12}q_{i2}, a_{22}q_{i2}, a_{32}q_{i2}) \\ &\qquad + \mathrm{Cum}(a_{13}q_{i3}, a_{13}q_{i3}, a_{23}q_{i3}, a_{33}q_{i3}) \\ &= a_{11}^2 a_{21} a_{31} \mathrm{Cum}(q_{i1}^4) + a_{12}^2 a_{22} a_{32} \mathrm{Cum}(q_{i2}^4) + a_{13}^2 a_{23} a_{33} \mathrm{Cum}(q_{i3}^4) \end{aligned}$$

Here, we use the following identities:

$$\begin{aligned}
&\mathrm{Cum}(x_1 + y_1, x_2 + y_2, \cdots, x_n + y_n) \\
&\qquad = \mathrm{Cum}(x_1, x_2, \cdots, x_n) + \mathrm{Cum}(y_1, y_2, \cdots, y_n), \qquad (2.56) \\
&\mathrm{Cum}(a_1 x_1, a_2 x_2, \cdots, a_n x_n) \\
&\qquad = a_1 a_2 \cdots a_n \mathrm{Cum}(x_1, x_2, \cdots, x_n), \qquad (2.57)
\end{aligned}$$

where $\{x_1, x_2, \cdots, x_n\}$ and $\{y_1, y_2, \cdots, y_n\}$ are independent sets of random variables, and $a_1, \cdots, a_n$ are constants [75], [76].

Under the assumption of i.i.d., we notice $\mathrm{Cum}(q_{i1}^r) = \mathrm{Cum}(q_{i2}^r) = \mathrm{Cum}(q_{i3}^r)$, and it is obvious that they are equally included in the elements among rth order cumulants. Thus, the cumulant tensors for $F_i(\boldsymbol{t})$, which are defined with $\mathrm{Cum}(\tilde{q}_{i1}^{r_1}, \tilde{q}_{i2}^{r_2}, \tilde{q}_{i3}^{r_3})$, are essentially determined with $a_{\tilde{\theta}\theta}$, i.e. W_k and L_i, and the cumulant tensors for the characteristic function $G(\boldsymbol{t})$ of the spatial filter output are represented by the sum of those of $F_i(\boldsymbol{t})$.

We construct the respective cumulant matrices, C_2 and C_4 of the second and the fourth orders for $G(\boldsymbol{t})$, which have the cumulants as their elements. The cumulant matrix of the second order is identical to the second order cumulant tensor, and that of the fourth order is arranged to have identical eigenvalues with the fourth order cumulant tensor [33]. The spatial filter is designed to minimize the sum of the eigenvalues of C_2 and C_4. Finally, we can describe the objective function positively, and the optimization problem of the spatial filter is stated as follows:

$$\min_{W_k} \ \hat{G} \qquad (2.58)$$

$$\hat{G} = (1-\lambda) \cdot \mathrm{tr}(C_2) + \lambda \cdot \mathrm{tr}(C_4) \qquad (2.59)$$

$$= (1-\lambda) \cdot \sum_{i=1}^{N} \sum_{\theta} \sum_{\tilde{\theta}} \left(\boldsymbol{w}_{k\tilde{\theta}}^T \boldsymbol{l}_{i\theta} \right)^2 + \lambda \cdot \sum_{i=1}^{N} \sum_{\theta} \left\{ \sum_{\tilde{\theta}} \left(\boldsymbol{w}_{k\tilde{\theta}}^T \boldsymbol{l}_{i\theta} \right)^2 \right\}^2, \qquad (2.60)$$

subject to $\|W_k^T L_k\|_{Fro}^2 = \text{const.}$,

where $0 \leq \lambda \leq 1$.

The spatial filter which minimizes the interferences of the non-target dipoles in the output, the estimation of the target dipole, is obtained by solving the above problem. It approximately accomplishes the purpose of the design, Eq.(2.49). Ignoring $\mathrm{Cum}(q_{i\theta}^r)$ makes it possible to construct a non-adaptive spatial filter.

2.5.2.3 Effect of the fourth order cumulant

In Eq.(2.60), with λ, we can adjust the weight of the fourth order cumulants in the optimization. The characteristics of the spatial filter and the current density distribution estimated with it vary, depending on λ. The objective function $\hat{G}$ provides the approximation of the characteristic function assuming the symmetric pdf, i.e. $\mathrm{Cum}(q_{i\theta}^r) = 0$ for odd r, and the approximation with the cumulant expansion terminated at the fourth order. λ prescribes the ratio of $\mathrm{Cum}(q_{i\theta}^2)$ to $\mathrm{Cum}(q_{i\theta}^4)$. When we set larger λ, it implies that the pdf of the output of the spatial filter is characterized dominantly with the fourth order cumulants. They are the criteria of non-Gaussianity, $\lambda > 0$ is equivalent to the positive kurtosis, and the respective pdf is supergaussian. It has a sharper peak and longer tails than the Gaussian pdf [33].

In this interpretation, the optimization is to obtain W_k which approximates $F_k(\boldsymbol{t})$ in a parametric model. The larger the λ is, the higher degree of non-Gaussianity the pdf $f(\tilde{\boldsymbol{q}}_k)$ is assumed to possess. The spatial filter attempts to reproduce it as much as possible. Thus it means that the current dipole estimated by the spatial filter with larger λ possesses strong non-Gaussianity and has smaller entropy; it is relatively not random, and its probability densities tend to concentrate and takes larger value in limited intervals around zero. The current density distribution constructed with the dipoles which have such characters should show highly localized activated regions.

Moreover, the spatial filter makes the contribution of $\boldsymbol{q}_i$ $(i \neq k)$ to the pdf of $\hat{\boldsymbol{q}}_k$ smaller as much as possible. It means that $\hat{\boldsymbol{q}}_k$ tends to be independent from $\boldsymbol{q}_i$, and the estimated dipoles $\hat{\boldsymbol{q}}_k$ and $\hat{\boldsymbol{q}}_i$ $(i \neq k)$ consequently attempt to be independent from each other. It indicates that the number of the current dipoles activated at the same time decreases in the current density distribution estimated by the spatial

filter. The central limit theorem tells the sum of the independent random variables each has finite variance approaches a Gaussian distributed random variable. Therefore, non-Gaussianity shows independence. Larger λ, the enhancement of the fourth order cumulants in the objective function, offers the estimated dipole $\hat{\boldsymbol{q}}_k$ a higher degree of independence.

The above considerations indicate that it is expected that the fourth order cumulants increase the localization of the current density distribution estimated by the spatial filter. The second order cumulants should be minimized enough to suppress the interferences especially when the multiple dipoles are activated, though. Independent current dipoles with larger variances may not localize the current distribution in some cases.

2.5.2.4 Normalization of the spatial filter

Finally, to satisfy the equality of the variances of the current dipoles estimated by the spatial filters as well as the assumption, we normalize the optimum spatial filter as follows:

$$W_k = \frac{W_k}{\|W_k^T L\|_{Fro}}. \tag{2.61}$$

This normalization results the correction of the depth of the current density estimated by the spatial filter.

In the optimization of the spatial filter, the contributions $\tilde{\boldsymbol{q}}_i$ $(i \neq k)$ to the variance of the estimated current dipole are minimized. The normalization transforms the filter coefficients to the solution which maximizes the contribution of the variance of $\boldsymbol{q}_k$ to the estimation $\hat{\boldsymbol{q}}_k$ under the constraint $\mathrm{tr}(C_2) = \|W_k^T L\|_{Fro}^2 = 1$, though the term of the fourth order cumulants also works as a constraint. In other words, especially in the case of the optimization only with the second order cumulants, the

optimum spatial filter can be interpreted as the solution of the following problem:

$$\max_{W_k} \left\| W_k^T L_k \right\|_{Fro}^2, \tag{2.62}$$

$$\text{subject to } \left\| W_k^T L \right\|_{Fro}^2 = 1. \tag{2.63}$$

Since all of the spatial filters for the dipoles satisfy the same constraints and are the members of the same set of the matrices, the maximization let the spatial filter W_k output the larger norm with L_k, with the contribution to the observation $\boldsymbol{m}$ of the target dipole, than the other filters W_i $(i \neq k)$. Therefore, the following inequality holds among the spatial filters:

$$\left\| W_k^T L_k \right\|_{Fro} \geq \left\| W_i^T L_k \right\|_{Fro}, \ (i \neq k). \tag{2.64}$$

The above relation illustrates that when L_k contributes significantly to the observation $\boldsymbol{m}$, the spatial filter W_k corresponding to L_k tends to output larger dipole amplitude than the other spatial filters W_i $(i \neq k)$. This indicates that even if the spatial filters cannot sufficiently inhibit undesirable signals from locations that are different from their own targets, the true activated dipoles must exist near the region where maximal current density is estimated by the spatial filters. It is also indicated that the depths of the estimated current densities are improved by the normalization. In the optimization with the fourth order cumulants, it can be expected that the inequality is hold since the same constraints, in which the minimization of the fourth order cumulants is included, are satisfied among the spatial filters.

2.5.2.5 Spatial filter only with the second order cumulants

The optimization of the spatial filter only with the second order cumulants, i.e. λ=0 in Eq.(2.60), is expressed as follows:

$$\min_{W_k} \ \hat{G}, \tag{2.65}$$

$$\hat{G} = \mathrm{tr}(C_2) = \left\| W_k^T L \right\|_{Fro}^2, \tag{2.66}$$

$$\text{subject to } \left\| W_k^T L_k \right\|_{Fro}^2 = \text{const.} \tag{2.67}$$

The solution may be obtained using the method of Laglange mutipliers. Let c_1 and c_2 be Lagrange multipliers, and we add one more subject which maintains the rank of the spatial filter W_k full. Assume that the conductor is spherically symmetric, that is $\boldsymbol{q}_i \in \Re^{2\times 1}$ and $W_k,\ L_k \in \Re^{m\times 2}$, and note the following equation:

$$\left\| W_k^T L \right\|_{Fro}^2 \quad = \quad \mathrm{tr}\left(W_k^T L L^T W_k \right) \quad = \quad \boldsymbol{w}_{k1} L L^T \boldsymbol{w}_{k1} \ + \ \boldsymbol{w}_{k2} L L^T \boldsymbol{w}_{k2}, \tag{2.68}$$

where $W_k = [\boldsymbol{w}_{k1}, \boldsymbol{w}_{k2}]$, and $\left\| W_k^T L_k \right\|_{Fro}^2$ can be expressed similarly. Then, the optimization problem of the spatial filter can be rewritten as follows:

$$\min_{\boldsymbol{w}_{k1}, \boldsymbol{w}_{k2}} \ \tilde{G} \tag{2.69}$$

$$\begin{aligned} \tilde{G} = {} & \boldsymbol{w}_{k1} L L^T \boldsymbol{w}_{k1} + \boldsymbol{w}_{k2} L L^T \boldsymbol{w}_{k2} \\ & + c_1 \left(\text{const.} - \boldsymbol{w}_{k1} L_k L_k^T \boldsymbol{w}_{k1} \right) + c_2 \left(\text{const.} - \boldsymbol{w}_{k2} L_k L_k^T \boldsymbol{w}_{k2} \right), \end{aligned} \tag{2.70}$$

$$\text{subject to } \boldsymbol{w}_{k1} \neq c_3 \boldsymbol{w}_{k2}, \ \forall c_3 \in \Re. \tag{2.71}$$

The optimal spatial filter coefficients satisfy the following equations:

$$\frac{\partial \tilde{G}}{\partial \boldsymbol{w}_{k1}} = L L^T \boldsymbol{w}_{k1} - c_1 L_k L_k^T \boldsymbol{w}_{k1} = \boldsymbol{0}, \tag{2.72}$$

$$\frac{\partial \tilde{G}}{\partial \boldsymbol{w}_{k2}} = L L^T \boldsymbol{w}_{k2} - c_2 L_k L_k^T \boldsymbol{w}_{k2} = \boldsymbol{0}. \tag{2.73}$$

We should find vectors which minimize Eq.(2.71) and satisfy the above equations. Therefore the optimization of the spatial filter is transformed into the following eigenvalue problems:

$$c_1' \boldsymbol{w}_{k1} = \left(LL^T\right)^{-1} L_k L_k^T \boldsymbol{w}_{k1}, \tag{2.74}$$

$$c_2' \boldsymbol{w}_{k2} = \left(LL^T\right)^{-1} L_k L_k^T \boldsymbol{w}_{k2}, \tag{2.75}$$

where $c_1' = 1/c_1$ and $c_2' = 1/c_2$. The optimal solution of Eqs.(2.67)-(2.71) can be obtained, taking the eigenvectors corresponding to the largest and the second-largest eigenvalues c_1' and c_2', as the spatial filter coefficients $\boldsymbol{w}_{k1}$ and $\boldsymbol{w}_{k2}$.

It is obvious that the eigenvector corresponding to the maximum eigenvalue minimizes the cost function $\hat{G}$ if there is not the constraint (2.71), and the spatial filter W_k has the column vectors $\boldsymbol{w}_{k1} = \boldsymbol{w}_{k2}$. As a result, the current dipole estimated by the spatial filter loses the information of its orientation and it can not be recovered, since $\mathrm{rank}\,(W_k) = 1$.

In the spatial-filter optimizations with the fourth order cumulants, $\lambda \neq 0$, the spatial filter optimized only with the second order cumulants is adopted as the initial value for the iterative algorithms in the latter numerical studies. The optimization is regarded as a modification.

2.5.3 Reconstruction of current distribution estimated by the spatial filters

A general concern with a current distribution estimated by spatial filters is its redundant expansion. It appears not only when the proposed spatial filter estimates current distribution but also when the LCMV and SAM beamformers estimate multiple correlated activities in a brain. The poor resolving power of spatial filtering is due to the strong ill-posedness of the inverse problem in MEG measurement. A reconstruction of current density distribution for localization and elimination of the redundant expansion is described in this section.

The orientation of each dipole estimated by the proposed spatial filter is cor-

rected first. Since the spatial filter W_k is designed to attenuate the contributions of L_i $(i \neq k)$ to the observation as much as possible, multiplying $\left(W_k^T L_k\right)^{-1}$ by Eq.(2.33) gives an estimation of the dipole orientation. To conserve the amplitude of the dipole appraised by the spatial filter, the dipole moment is corrected as follows:

$$\tilde{\boldsymbol{q}}_k = \alpha_k \left(W_k^T L_k\right)^{-1} \hat{\boldsymbol{q}}_k, \tag{2.76}$$

$$\alpha_k = \|\hat{\boldsymbol{q}}_k\| \Big/ \left\| \left(W_k^T L_k\right)^{-1} \hat{\boldsymbol{q}}_k \right\|. \tag{2.77}$$

Because of Eq.(2.64), we can assume that actual activated regions in a brain are included in the regions with larger current densities estimated by the proposed spatial filter. Hence, the observation is composed of the following components calculated with the estimated dipoles:

$$\boldsymbol{g}_i = L_i \tilde{\boldsymbol{q}}_i, \tag{2.78}$$

$$\|\tilde{\boldsymbol{q}}_1\| \geq \|\tilde{\boldsymbol{q}}_2\| \geq \cdots \geq \|\tilde{\boldsymbol{q}}_p\|, \ p < m. \tag{2.79}$$

where the subscripts of $\tilde{\boldsymbol{q}}_i$ are renumbered in decreasing-norm order. With the above prospect, a multiple linear regression model is constructed as follows:

$$\boldsymbol{m} = G_p \boldsymbol{s} + \hat{\boldsymbol{\varepsilon}}, \tag{2.80}$$

$$G_p = \left[\boldsymbol{g}_1, \boldsymbol{g}_2, \cdots, \boldsymbol{g}_p\right], \tag{2.81}$$

where it is assumed that there are no current densities at the locations corresponding to $\tilde{\boldsymbol{q}}_i$ $(i > p)$ or that their contributions to the observation can be ignored.

Localization of the current density distribution is accomplished by removing unnecessary components in G_p with the Mallows C_p criterion [77], [78].

The C_p statistic selects the optimal model in a linear regression problem, i.e., that fits data well with the fewest variables in a way similar to AIC (Akaike's information criterion). The C_p statistic is defined as Eq.(2.82), and the model which gives the

minimum C_p is the best one:

$$
\begin{aligned}
C_p &= \frac{\|\boldsymbol{e}_p\|^2}{\hat{\sigma}^2} + 2p - m, && (2.82)\\
\boldsymbol{e}_p &= \boldsymbol{m} - G_p\hat{\boldsymbol{s}}, && (2.83)\\
\hat{\boldsymbol{s}} &= \left(G_p^T G_p\right)^{-1} G_p^T \boldsymbol{m} && (2.84)\\
&= [\hat{s}_1, \hat{s}_2, \cdots, \hat{s}_p]^T, && (2.85)
\end{aligned}
$$

where $\hat{\sigma}$ is the estimated variance of the error $\hat{\boldsymbol{\varepsilon}}$. When the model with G_{p-1} requires fewer dipoles to compose the observation and gives smaller a C_p than the model with G_p, and $\hat{\sigma}^2 = \|\boldsymbol{e}_p\|^2/(m-p)$, the following relation holds:

$$
\omega = \frac{\|\boldsymbol{e}_{p-1}\|^2 - \|\boldsymbol{e}_p\|^2}{\|\boldsymbol{e}_p\|^2/(m-p)} \leq 2 \tag{2.86}
$$

where $\boldsymbol{e}_{p-1}$ is the error of the model with G_{p-1}. The model with G_{p-1} is constructed by setting $\boldsymbol{g}_i = \boldsymbol{0}$ for every $i = p, p-1, \cdots, 2, 1$. Each component $\boldsymbol{g}_i$ will be deleted when G_{p-1} satisfies Eq.(2.86). It is determined that there is no current dipole in the position $\boldsymbol{r}_i$ corresponding to the deleted $\boldsymbol{g}_i$, and G_p is updated to G_{p-1}. The localization of the current density distribution estimated by the spatial filters is completed when the redundant current dipoles have been eliminated as much as possible in the sense of the minimization of the C_p statistic. Finally, the current density distribution is reconstructed with $\hat{\boldsymbol{s}}$ given by Eq.(2.84) with the optimal G_p,

$$
\bar{\boldsymbol{q}}_i = \begin{cases} \hat{s}_i \tilde{\boldsymbol{q}}_i & (i = 1, 2, \cdots, p) \\ \boldsymbol{0} & (i = p+1, \cdots, N). \end{cases} \tag{2.87}
$$

The method including the proposed spatial filtering and the reconstruction with multiple linear regression is proposed as the spatial-filtered reconstruction (SFR).

In Chapter 3, the proposals for the phases of the signal processing and inverse analysis of the MEG measurement, i.e. the FA-processed Kalman filter, the spatial filter with the higher order cumulants and the SFR, are numerically studied to verify the effectiveness and to be shown with their features in practical uses.

Chapter 3

Numerical studies

3.1 Reduction of noise from MEG data

3.1.1 Experimental conditions

Numerical experiments were done to investigate the performance of the proposed method. Results of the noise reduction with the FA and Kalman filter combination (FA-processed Kalman filter) and of ICA following the noise reduction were compared to those with band-pass filtering, which is the usual noise reduction method used in MEG data processing.

In each experiment, MEG data were simulated by the forward equation of MEG measurement. Gaussian noises were added to the simulated MEG data as sensor noises. It was assumed that the conductor was a homogeneous spherical object with a radius of 8 cm, and data were obtained with the whole head type MEG system with 64 sensors. The locations of the conductor and sensors are illustrated in Fig.3.1. The sensor numbers are shown in Fig.3.2.

3.1.2 FA-processed Kalman filter

In the first experiment, a single dipole on $(x,\ y,\ z) = (0, 4, 0)$ was placed in the conductor to simulate brain activity in a lateral lobe, e.g., an auditory evoked response. The maximum strength of the dipole in temporal series was set as 100 nAm. The

SNRs of the sensors are shown in Fig.3.3. We examine and discuss the effectiveness of the proposed method and the robustness to errors in the number of common factors by the simulation. The sampling rate was 1024Hz. The noise reduction by an ideal low-pass filter whose cutoff was at 40Hz (40Hz LPF) was implemented as a reference.

The proposed method reduced the sensor noise significantly. Figure 3.4 shows the superimposed 64 original noise-free signals which are normalized by the maximum value of the original signals. The examples of the observed signals are shown in Fig.3.5, and MEG signals obtained by the FA-processed Kalman filter is illustrated in Fig.3.6. They are normalized by the maximum of the original signals as well as Fig.3.4 for comparison. An approximately 0.01 s time delay and attenuation of the amplitude occurred by the proposed method. The amplitude of the estimated signals at their peak latency are about 50-80% of the original ones, e.g. in 20th and 25th sensors (Fig.3.7). However, the FA-processed Kalman filter was able to extract the features of the original noise-free MEG data despite this noisy situation. On the other hand, a considerable amount of noise still remained in the MEG data processed with 40Hz LPF. They are normalized and shown in Fig.3.8.

The proposed method succeeded in the noise reduction even when the number of common factors was incorrect. Figure 3.9 shows the eigenvalues of the covariance matrix of the MEG data after the noise reduction by the FA-processed Kalman filter with one common factor, that is, with the correct number of common factors. The largest eigenvalue contributes to a 98.8 % of the total value. Figure 3.10 shows the eigenvalues of the covariance matrix of the data processed by the method with five common factors. Even though the number of common factors was set wrongly as five, the maximum eigenvalue contributed 85.4 % of the total value. This indicated that the sensor noises and the redundant factors were eliminated effectively.

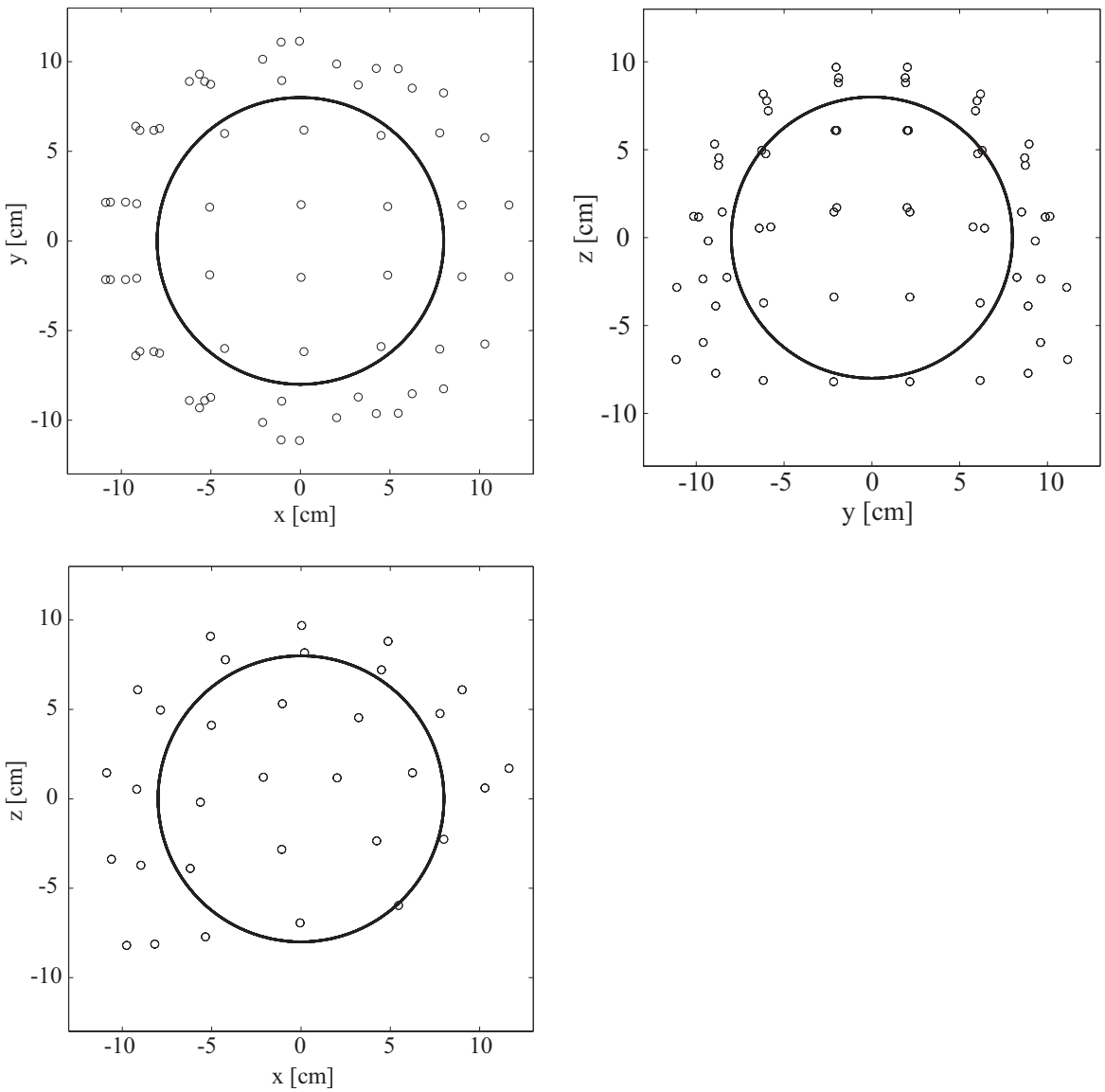

Figure 3.1: 64 sensors and a conductor for the numerical experiments for the FA-processed Kalman filter: the small circles represent the sensor locations. The conductor has the radius of 8 cm.

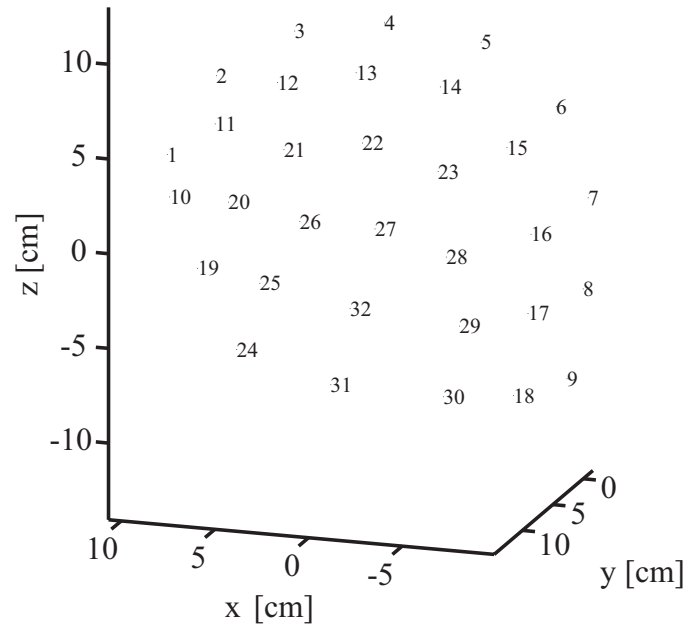

(a)

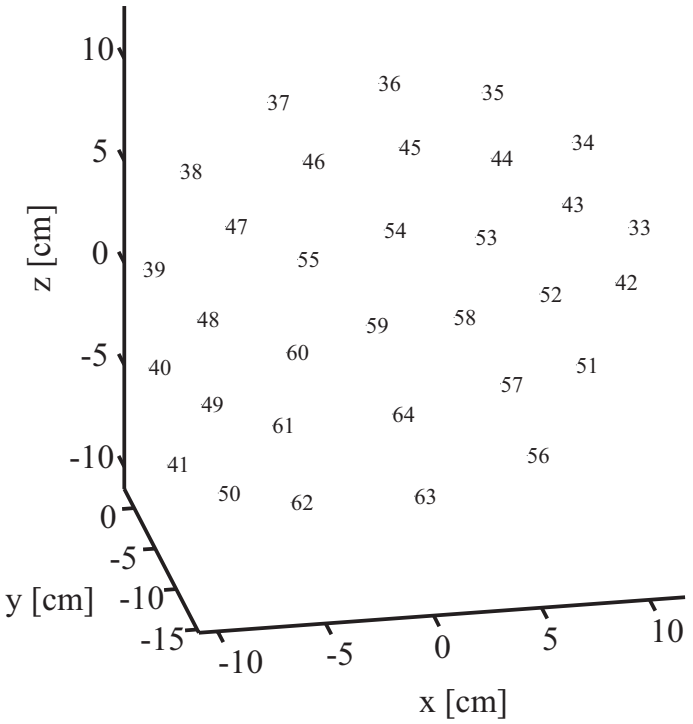

(b)

Figure 3.2: Locations and numbers for 230 sensors: the sensor numbers are shown in the regions with (a) $y \geq 0$ and (b) $y \leq 0$.

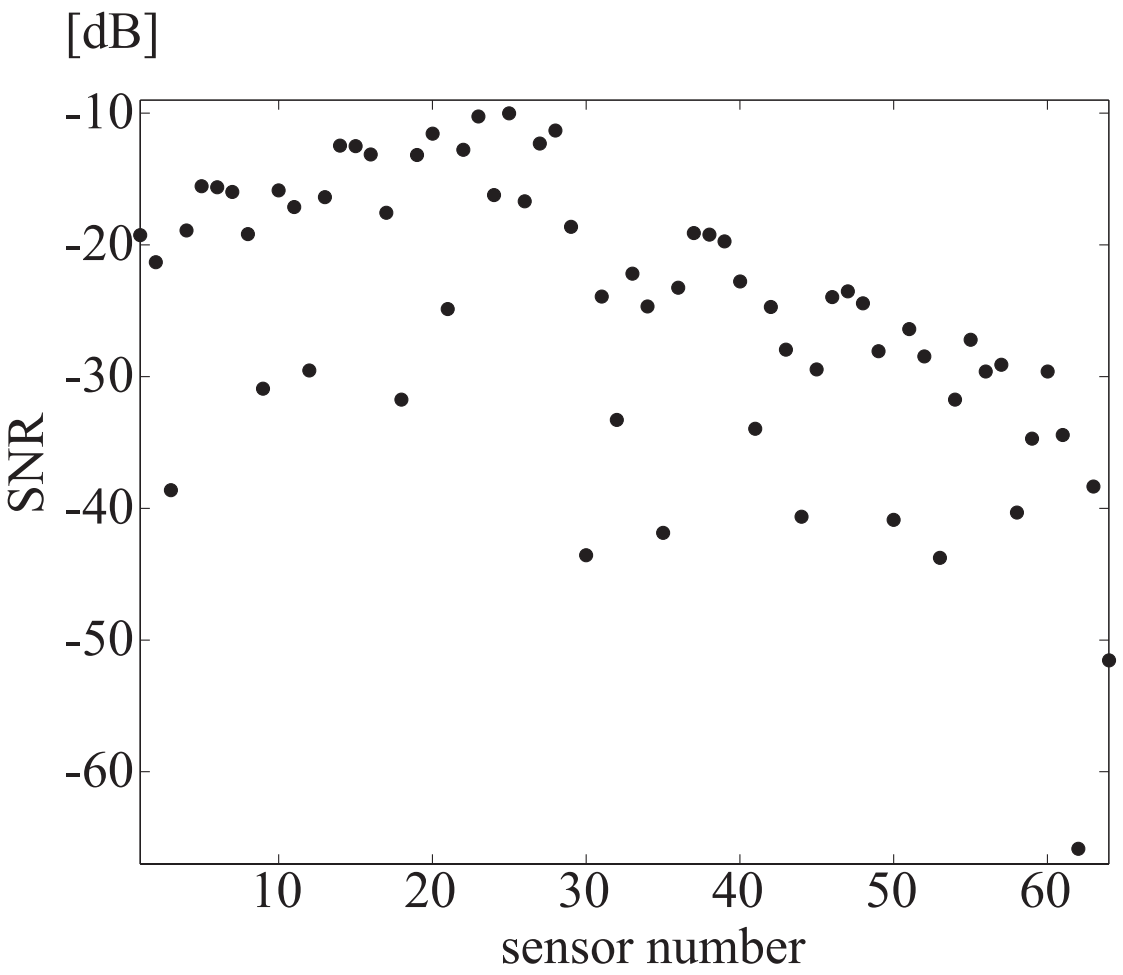

Figure 3.3: SNR of each sensor in the single dipole case

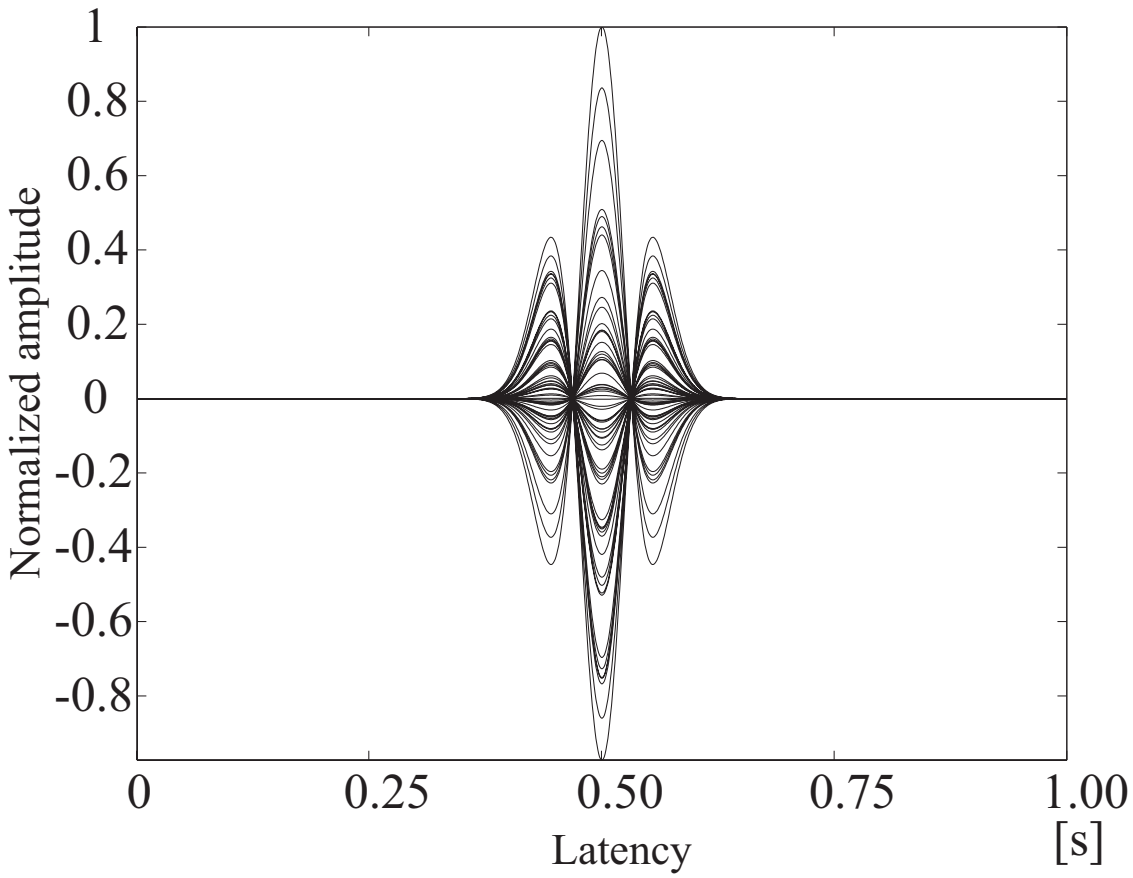

Figure 3.4: 64 noise-free MEG signals in the first numerical experiment

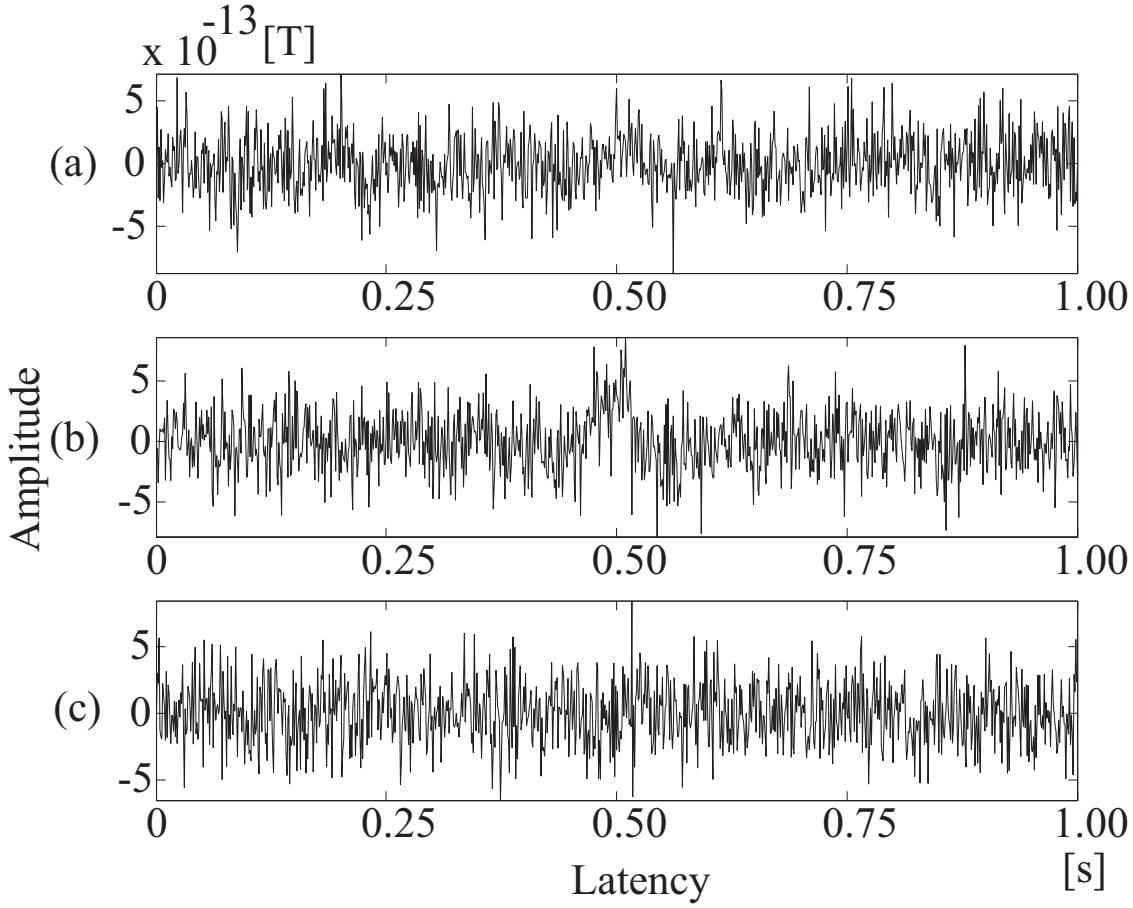

Figure 3.5: Examples of the observed MEG signals in the first numerical experiment: the signals observed with 21th, 25th and 62th sensors are shown.

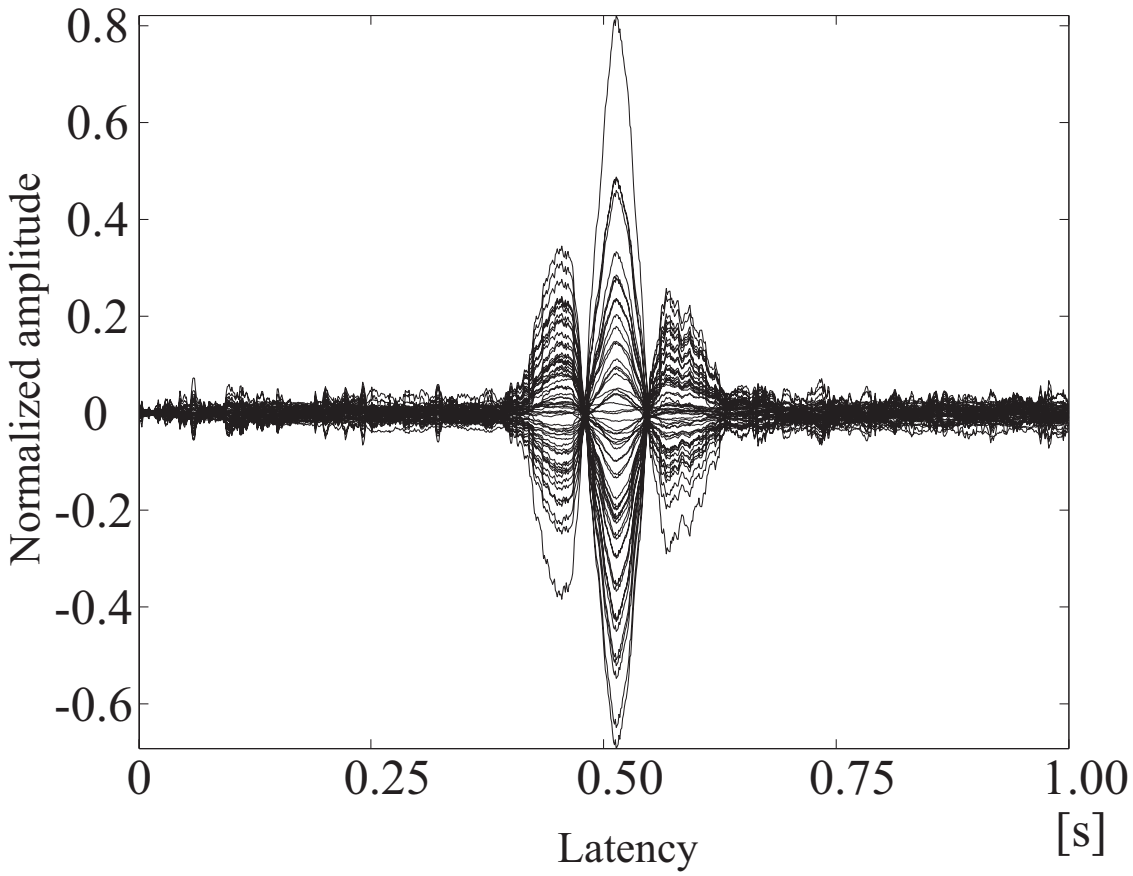

Figure 3.6: 64 FA-processed Kalman filtered signals in the first numerical experiment

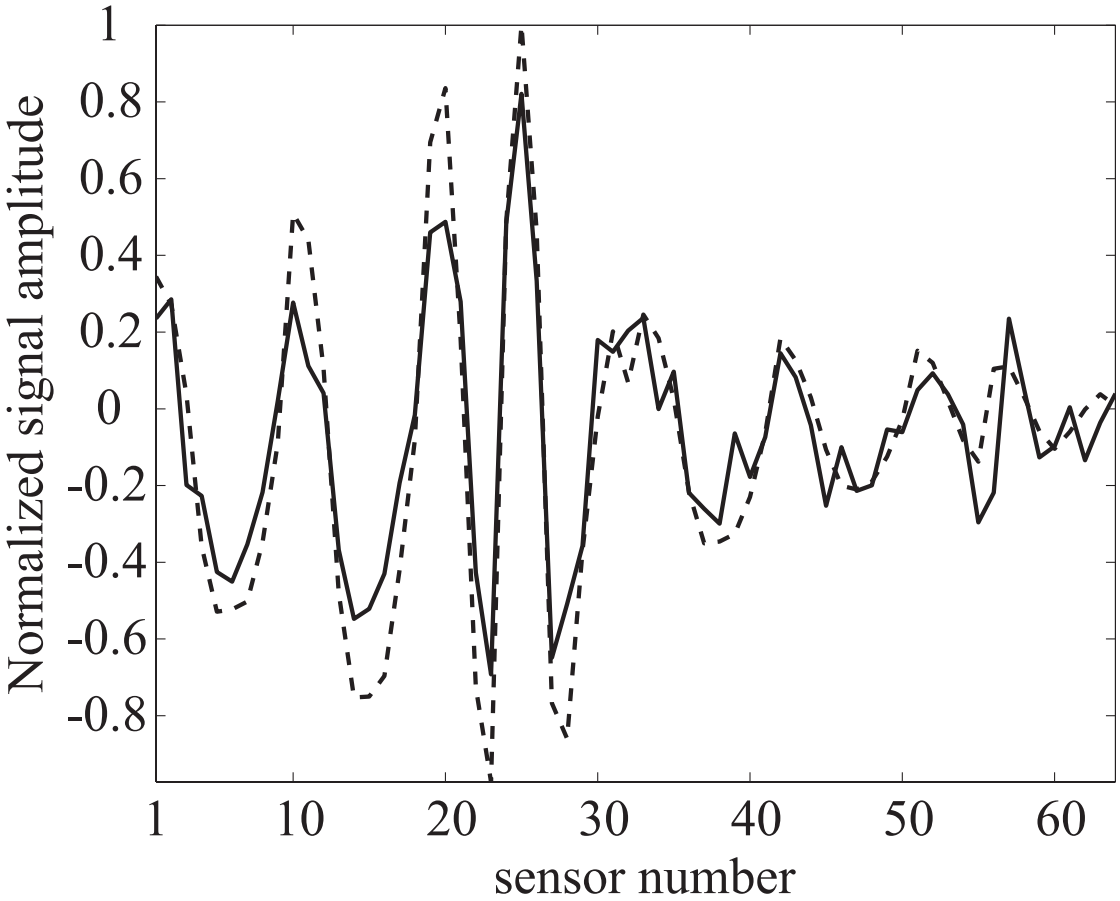

Figure 3.7: signal amplitude of the original and FA-processed Kalman filtered signal at the latency with the maximum norm of the data: the dashed and solid lines illustrate the original and Kalman filtered signals, respectively

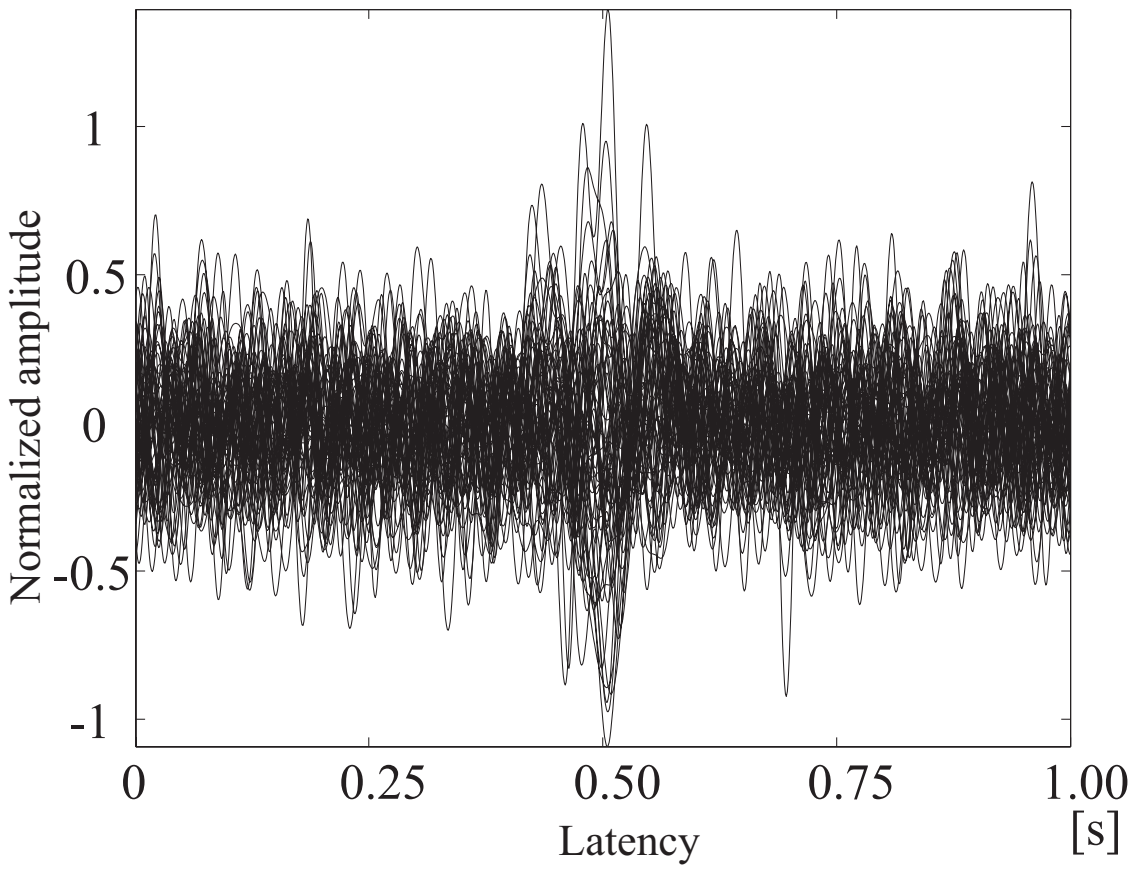

Figure 3.8: MEG signals processed with a 40Hz low-pass filter in the first numerical experiment

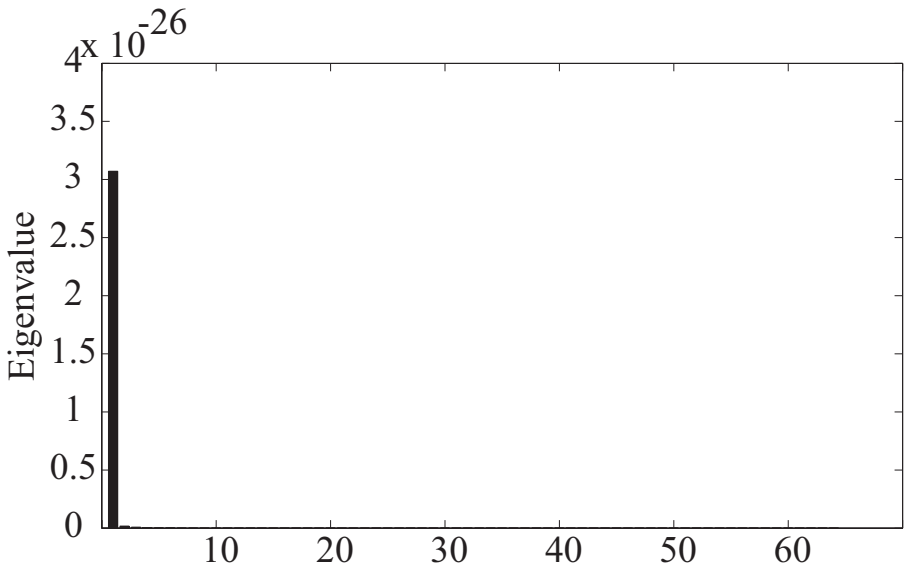

Figure 3.9: Eigenvalues of the covariance matrix of the FA and Kalman-filtered MEG data with one common factor in the first numerical experiment

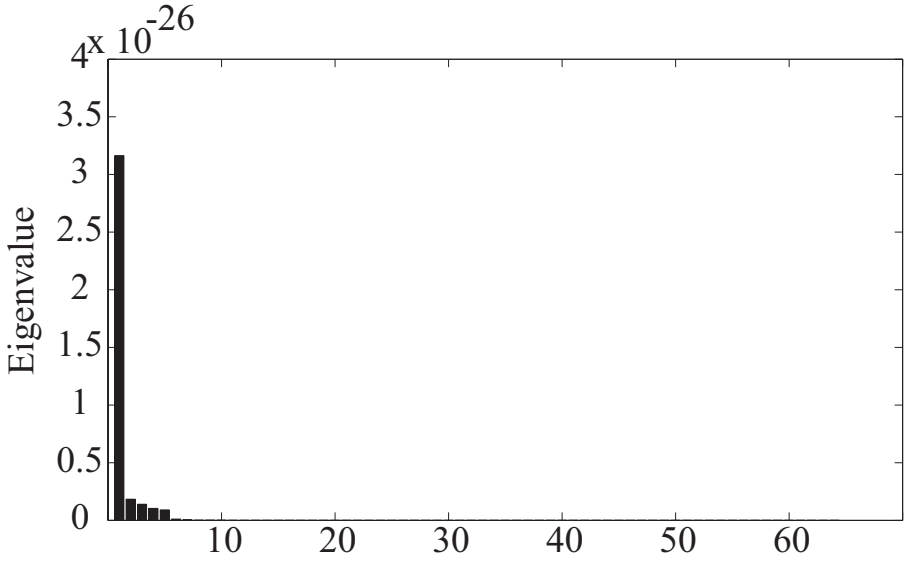

Figure 3.10: Eigenvalues of the covariance matrix of FA and Kalman-filtered MEG data with five common factors in the first numerical experiment

3.1.3 ICA followiong FA-processed Kalman filtering

The author also demonstrated the noise reduction in a case of multiple independent components (ICs) in a second numerical experiment to investigate the influence of the FA-processed Kalman filtering as a method for preprocessing ICA. Dipoles were located at $(x,\ y,\ z) = (0, 4, 0),\ (0, -3, 0),\ (0, 0, 5)$, and $(-7, 0, 3)$. Figure 3.11 shows the time series of each dipole activity. The SNR of each sensor is shown in Fig.3.12. The examples of the observed signals are illustrated in Fig.3.13

The sampling rate was 512Hz. Two kinds of filters, i.e., 40Hz LPF and an ideal band-pass filter whose passband was from 1 to 100Hz (1-100Hz BPF) were compared to the filter used in the proposed method. Both of these filters are conventionally used in MEG measurement. The number of the common factors was given as four. The issue of the number of common factors was excluded to investigate the effect of the connection between Kalman filter and ICA. After each noise reduction, four independent components (ICs) were estimated by the FastICA algorithm.

Four ICs that agreed with the original signals were able to be obtained by ICA after each noise reduction. Figures 3.14, 3.15 and 3.16 show the ICs estimated by the proposed method, the 40Hz LPF method and the 1-100Hz BPF method, respectively. The estimated ICs in Fig.3.14 coincided well with the original signals. It is confirmed that the state-space model constructed with the forward equation of MEG measurement and the estimation of the system noise covariance are reasonable.

There were high correlations between the ICs estimated by the proposed noise reduction and ICA and the corresponding original signals. Figure 3.17 shows the autocorrelation function of (s1) and the cross-correlation functions between (s1) and corresponding ICs(a1), (b1) and (c1). They were normalized by the maximum of the autocorrelation function. In addition, the maximum absolute values of the cross-correlation functions between the original signals and the corresponding estimated ICs are shown in Table 1.

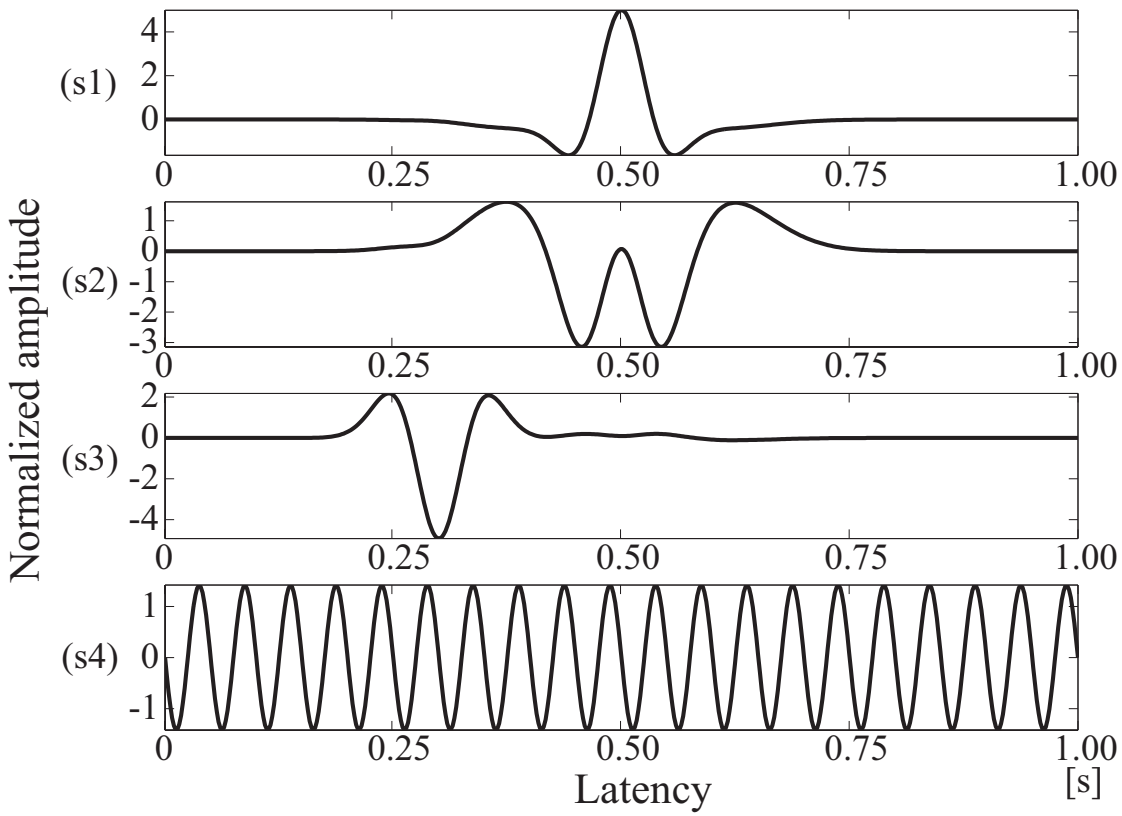

Figure 3.11: Original signals. The signals (s1)-(s4) are located at $(x,\ y,\ z) = (0, 4, 0),\ (0, -3, 0),\ (0, 0, 5)$, and $(-7, 0, 3)$, respectively.

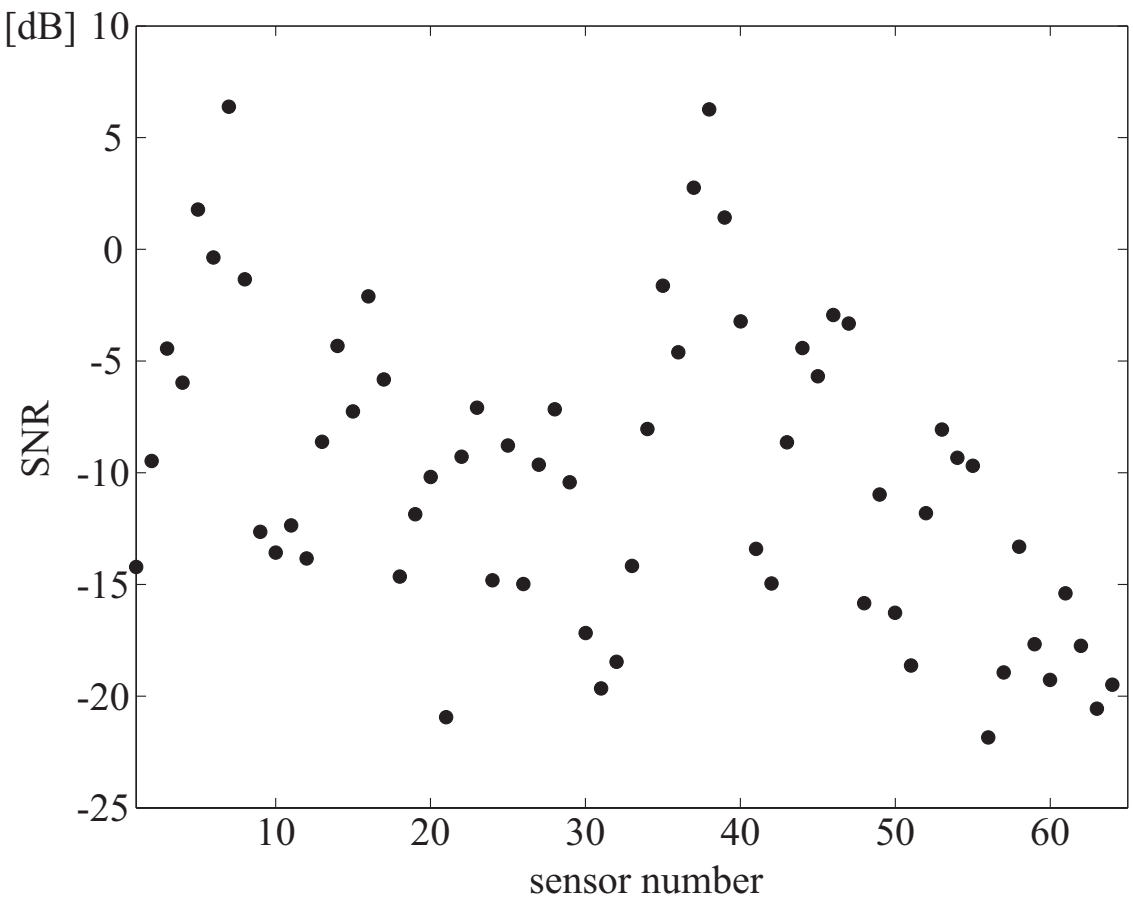

Figure 3.12: SNR of each sensor in the case of multiple ICs

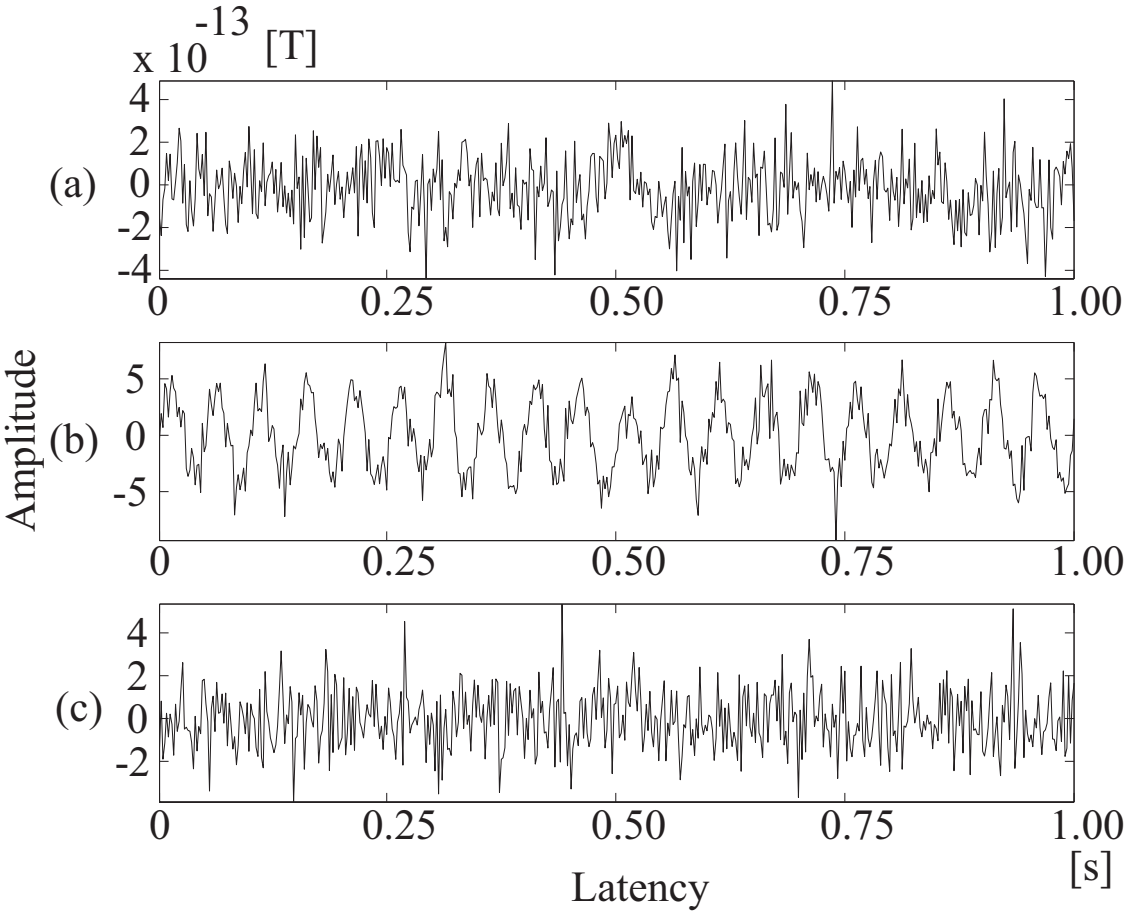

Figure 3.13: Examples of the observed signals in the multiple IC case: the signals observed with 20th, 7th and 56th sensors are illustrated.

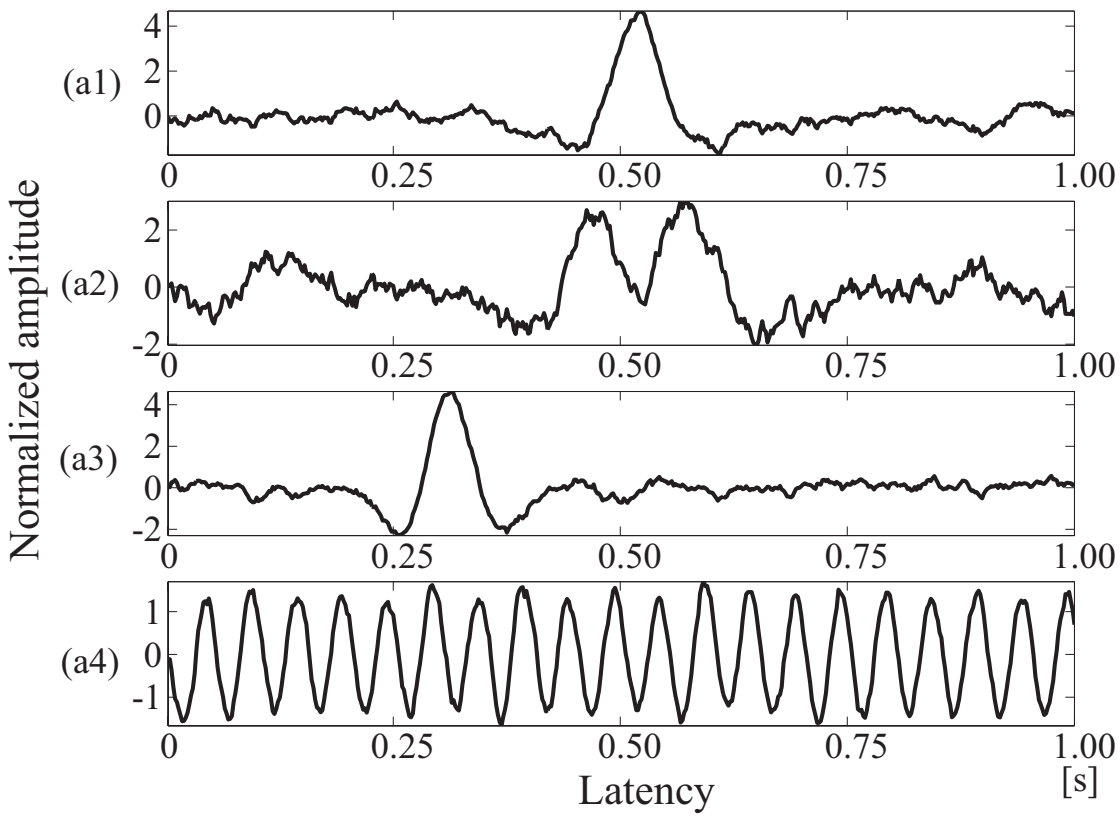

Figure 3.14: Independent components estimated from FA-processed, Kalman-filtered MEG data

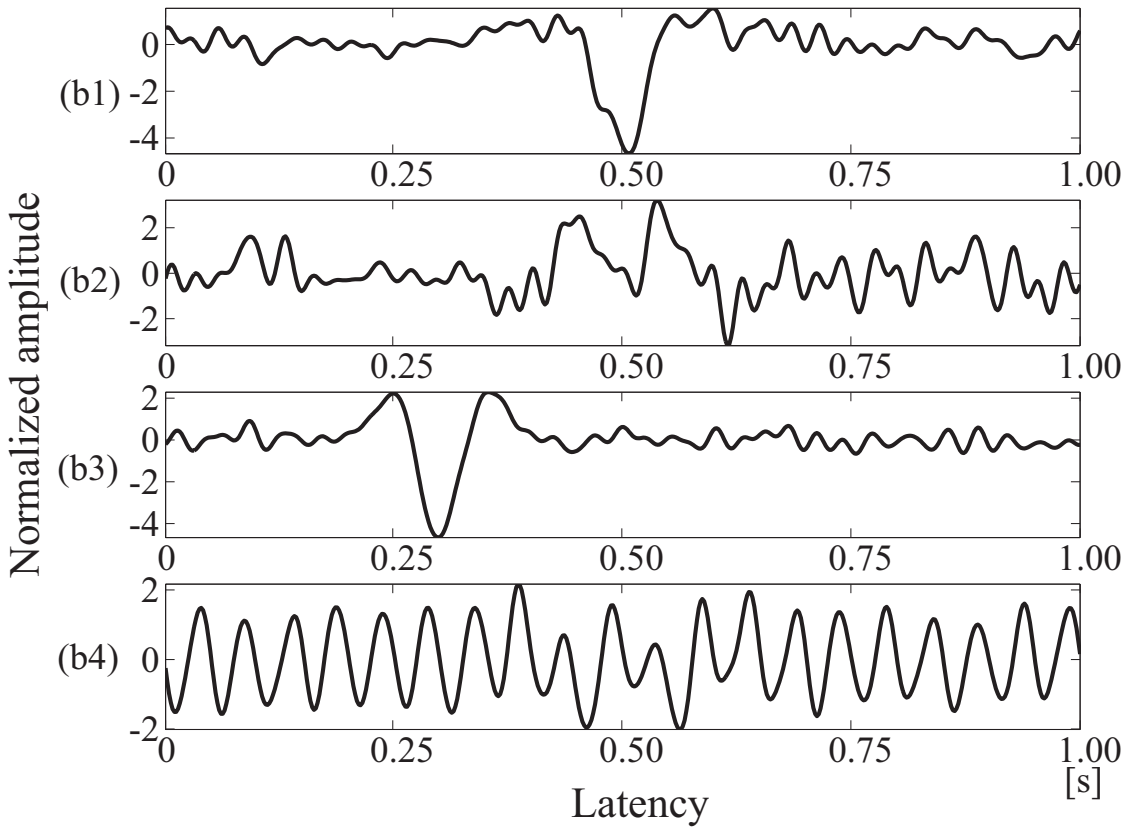

Figure 3.15: Independent components estimated from 40Hz low-pass filtered MEG data

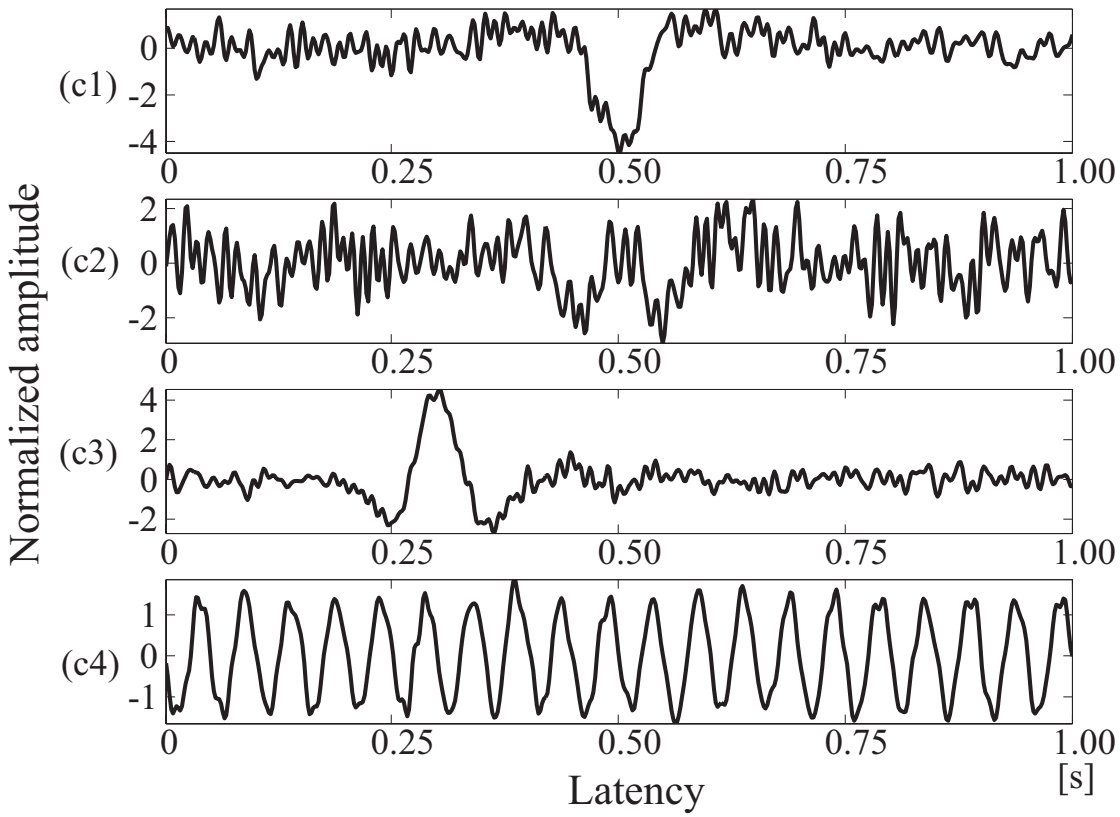

Figure 3.16: Independent components estimated from 1-100Hz band-pass filtered MEG data

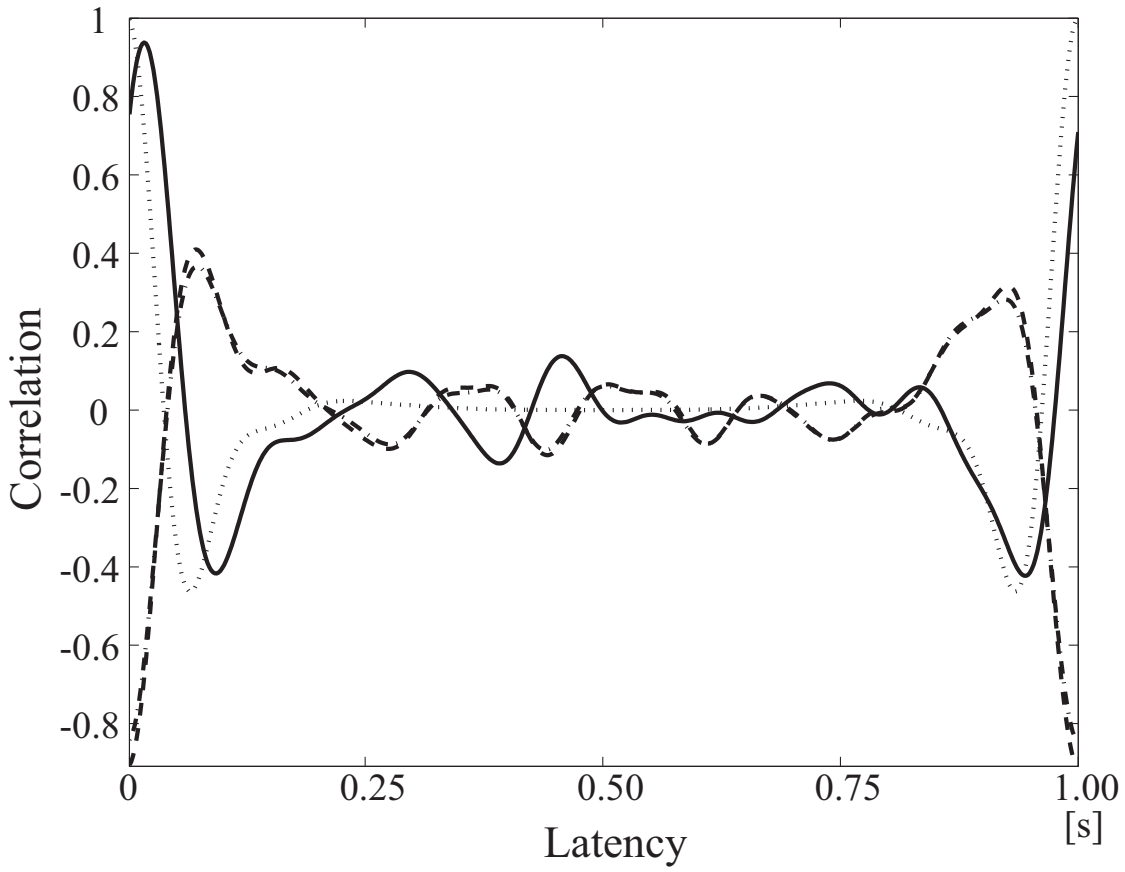

Figure 3.17: Cross-correlation functions between (s1) and (a1) (solid line), (s1) and (b1) (heavy broken line) and (s1) and (c1) (light broken line). The dashed line represents autocorrelation of (s1).

Table 1 Maximum absolute values of cross-correlation functions

		ai (proposed)	bi (40Hz LPF)	ci (1-100Hz BPF)
	i=1	0.938	0.909	0.844
si	2	0.879	0.692	0.526
	3	0.968	0.954	0.919
	4	0.989	0.939	0.985

3.1.4 Discussion

The proposed method was shown to eliminate sensor noise significantly. In the first numerical experiment, the maximal SNR of the simulated MEG data was -10dB and agree with that of typical evoked fields on the order of 10^2fT, such as auditory and sensory evoked fields. This can be estimated from the fact that in the case of the typical evoked field, we attain a 90 % GOF (goodness-of-fit) in dipole fitting after averaging on the order of 10^2 trials. This estimation suggests that the FA-processed Kalman filter method can at least significantly reduce the number of trials required for averaging; in addition, the method may extract desired signals from unaveraged MEG data.

The FA-processed Kalman filter is robust to the error in the number of common factors to some extent. This constitutes an advantage of the proposed method for the preprocessing of ICA.

The number of ICs must be decided before a preprocessing, however, high level noise makes this decision difficult. The number of ICs is usually determined by referring to the contribution ratios of PCs. In Section 3.1.3., although the true number of ICs was four, we needed nine PCs to achieve an 80 % contribution in 40Hz LPF data. 25 PCs were needed in 1-100Hz BPF data. Some criteria, such as MDL (minimum description length) or AIC (Akaike's information criteria) [79], have been shown to be useful to refine the number of ICs [26]. However, to determine the actual number of ICs is impossible, especially in practical MEG analysis. The proposed method is also able to utilize those criteria in the FA step to estimate

the number of common factors. Moreover, it does not tend to be influenced by an incorrect number of common factors, as shown in Section 3.1.2.

The proposed method overcomes the issue of the orthogonalization of signals under independent additive noises, and obtains high SNR ICs through sensor noise reduction with Kalman filtering. Sensor noise causes unsuccessful orthogonalization of signals, with the eventual result that the desired ICs cannot be obtained. With its powerful noise reduction, the proposed method allows extractions of ICs from low SNR data. In Section 3.1.3, the dipole generated the original signal (s2) in Fig.3.11 was located at the position $(x, y, z) = (0, -3, 0)$, which was further from the sensor array than the other dipoles. Therefore, it was weaker and had lower SNR than the other signals. We were able to obtain IC (a2), the estimation of (s2), which showed high correlation with the original signal (s2). In addition, the FA-processed Kalman filter eliminated the sensor noise without any difficulty of choosing a frequency band.

3.2 Proposed spatial filter with higher order statistics

3.2.1 Experimental conditions

The features of the proposed spatial filtering with higher order cumulants, especially the second and fourth order cumulants were investigated in the numerical experiments, which were conducted for the single and multiple dipole cases. Four kinds of the spatial filters optimized with $\lambda = 0, 1/3, 1/2, 1$ were prepared for the following numerical studies. MEG data were simulated with Eq.(2.7). A 160ch whole-head type MEG system was adopted in these numerical experiments. The conductor was a homogeneous sphere with a radius of 8 cm, which is discretized, and the dipoles estimated by the spatial filters were on the grid points positioned at intervals of 1cm. The locations of the sensors and the grid points are shown in Fig.3.18.

3.2.2 Current density estimation under single dipole

Some examples of the estimation results are shown in Figs.3.19-3.21. In these experiments, the true single dipoles were assumed at $(x, y, z) = (0, 0, 6)$, $(0, 0, -1)$ and $(0, 0, -4)$, respectively. The orientation of the dipole was $(x, y, z) = (1, 0, 0)$ for each case. No observation noises were added to the simulated MEG data. Figures show the dipole amplitude $\|\hat{\boldsymbol{q}}_i\|^2$ in decreasing order. The amplitude is normalized by the maximum value. The dipole estimated at the true dipole position was represented by the marks $+, \Box, \bigcirc$ and $\triangle$ corresponding to the spatial filtering with $\lambda = 0, 1/3, 1/2$ and 1 respectively.

In each case, the maximum dipole was estimated at the position of the true dipole. The figure shows that the spatial filters with $\lambda > 0$ appraised the dipoles as smaller at the locations except for the correct one. This indicates that the fourth order cumulants are effective to improve the locations of localization of the current density distribution. However, the effect depends on the cases. Figures 3.22 and 3.23 show the normalized dipole amplitude in decreasing order averaged over 1000 single dipole cases. Figure 3.23 is the enlargement of Fig.3.22. The locations and the orientations were randomly selected, and the averaged position of the single dipoles was $(x, y, z) = (0.096, -0.15, -0.001)$. These figures show that the degree of the localization was increased by larger λ on average. More weight on the fourth order cumulants we put, more localized the estimated current density distribution is in single dipole case.

Robustness of the spatial filtering to noises in single dipole case was investigated. This can serve as a reference in multiple dipole case. We estimated current distribution by the spatial filtering for 100 single dipole cases which were chosen randomly. The average dipole position was $(x, y, z) = (-0.62, 0.45, 0.35)$. For each signle dipole case, the signal-to-noise ratio (SNR) was varied, and 100 tirals with Gaussian noise $\boldsymbol{\varepsilon}$ were conducted in every SNR. The SNR is defined as $\|L\boldsymbol{Q}\|^2/\|\varepsilon\|^2$ here. Figure 3.24 shows, for various SNRs, the frequencies of the successful estimation in which the maximum current dipole was estimated at the location of the true dipole. The frequencies were averaged over 100 single dipole cases.

This result indicates that the spatial filter minimized the second order cumulants possesses the robustness to the noises. The frequency of the successful estimation with the spatial filter only with the second order cumulants exceeded the others by about 5-10% in the SNR less than 10^1. In the practical uses, the observation noise can be assumed as Gaussian. When the noises are Gaussian, for the robust estimation, it seems important to minimize the second order cumulants similarly in this numerical experiment. It was shown that the other spatial filters with the fourth order cumulants function well while the noises were sufficiently removed. Though the robustness to noises is inferior to that of the spatial filter only with the second order cumulants, they are still robust to noises to some extent.

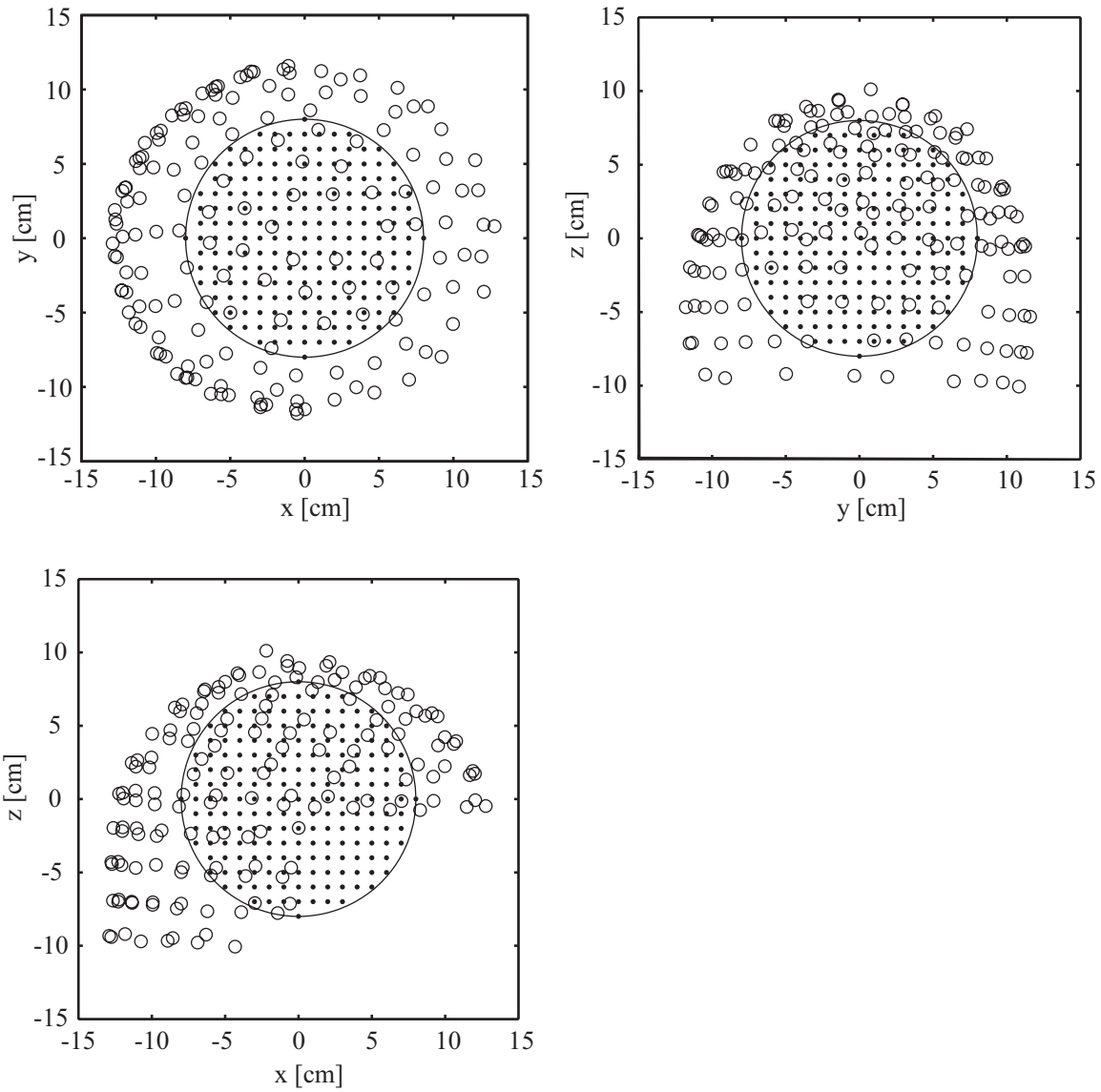

Figure 3.18: Locations of the sensors and grid points: ◯ and · represent the locations of the sensors and the grid points. The dipoles were estimated on the grid positions.

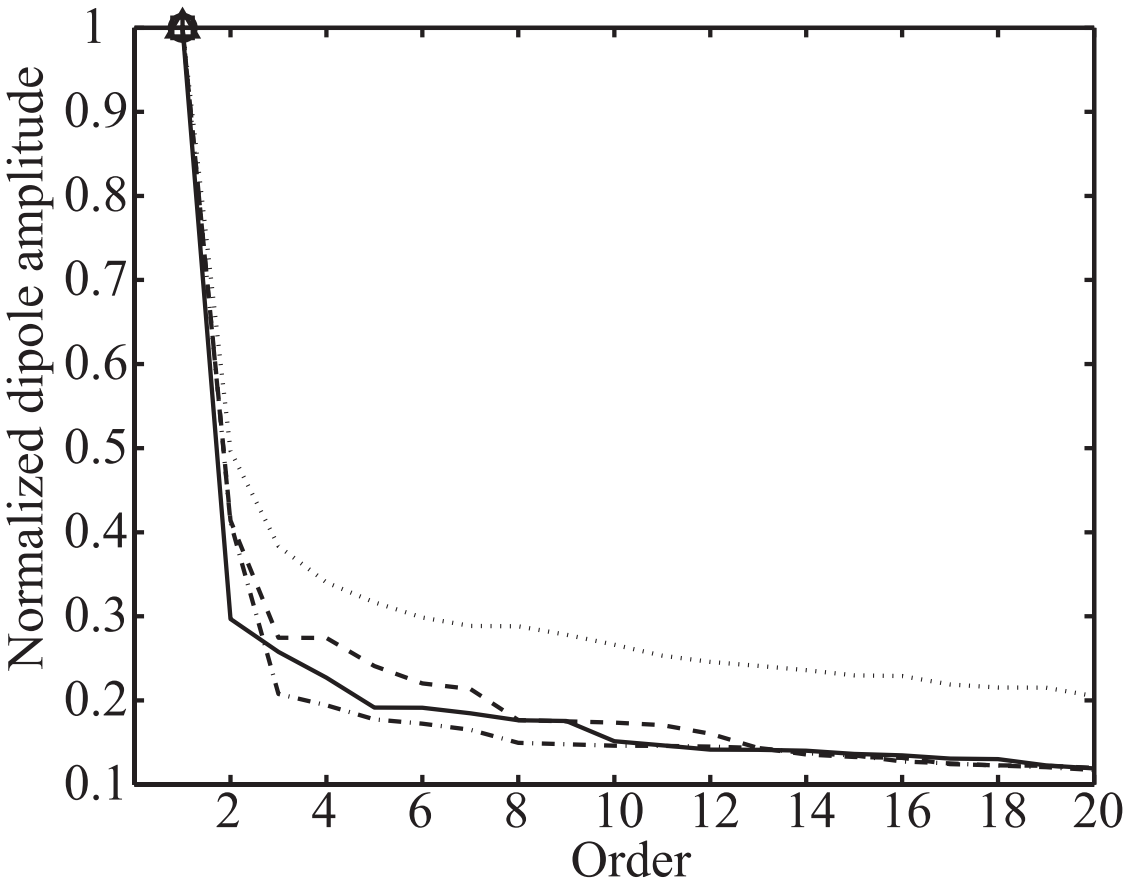

Figure 3.19: Example of single dipole estimation with the proposed spatial filter: the true dipole was at $(x, y, z) = (0, 0, 6)$ and its orientation was $(x, y, z) = (1, 0, 0)$. The strengths of the current dipoles estimated by the spatial filtering are plotted in decreasing order. They are shown with the respective lines and symbols, i.e. the results of spatial filtering with $\lambda = 0$ (dashed line with $+$), $\lambda = 1/3$ (heavy broken line with $\square$), $\lambda = 1/2$ (solid line with $\bigcirc$) and $\lambda = 1$ (light broken line with $\triangle$). The symbols indicate the dipole estimated at the location of the true dipole.

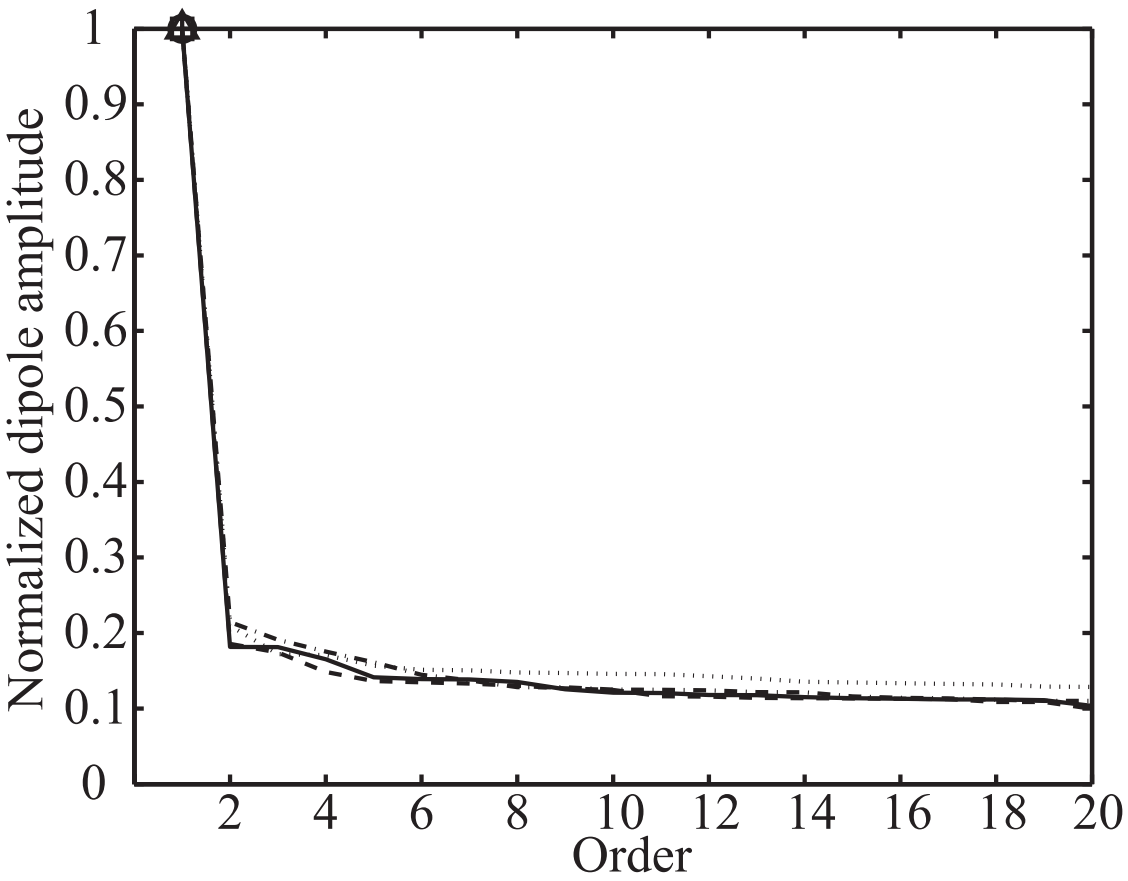

Figure 3.20: Example of single dipole estimation with the proposed spatial filter: the true dipole was at $(x, y, z) = (0, 0, -1)$ and its orientation was $(x, y, z) = (1, 0, 0)$. The strengths of the current dipoles estimated by the spatial filtering are plotted in decreasing order. They are shown with the respective lines and symbols, i.e. the results of spatial filtering with $\lambda = 0$ (dashed line with +), $\lambda = 1/3$ (heavy broken line with $\square$), $\lambda = 1/2$ (solid line with $\bigcirc$) and $\lambda = 1$ (light broken line with $\triangle$). The symbols indicate the dipole estimated at the location of the true dipole.

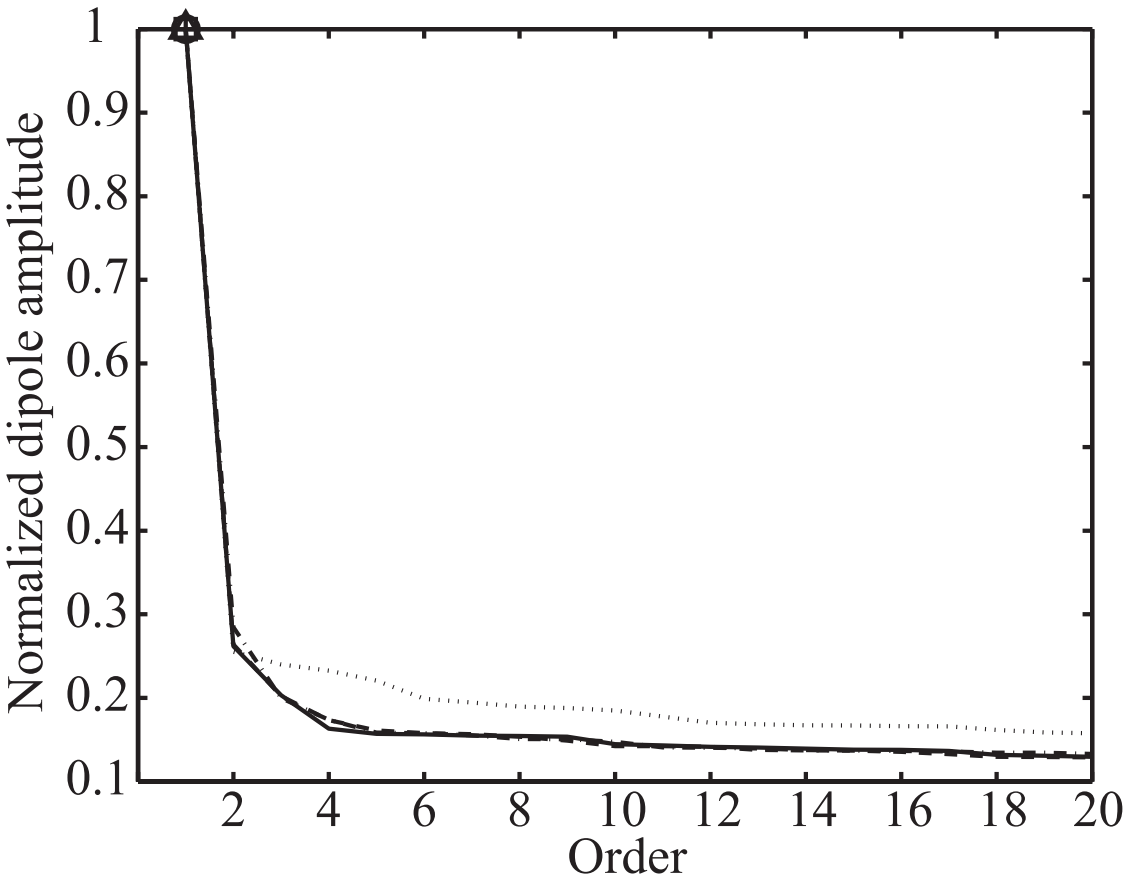

Figure 3.21: Example of single dipole estimation with the proposed spatial filter: the true dipole was at $(x, y, z) = (0, 0, -4)$ and its orientation was $(x, y, z) = (1, 0, 0)$. The strengths of the current dipoles estimated by the spatial filtering are plotted in decreasing order. They are shown with the respective lines and symbols, i.e. the results of spatial filtering with $\lambda = 0$ (dashed line with $+$), $\lambda = 1/3$ (heavy broken line with $\square$), $\lambda = 1/2$ (solid line with $\bigcirc$) and $\lambda = 1$ (light broken line with $\triangle$). The symbols indicate the dipole estimated at the location of the true dipole.

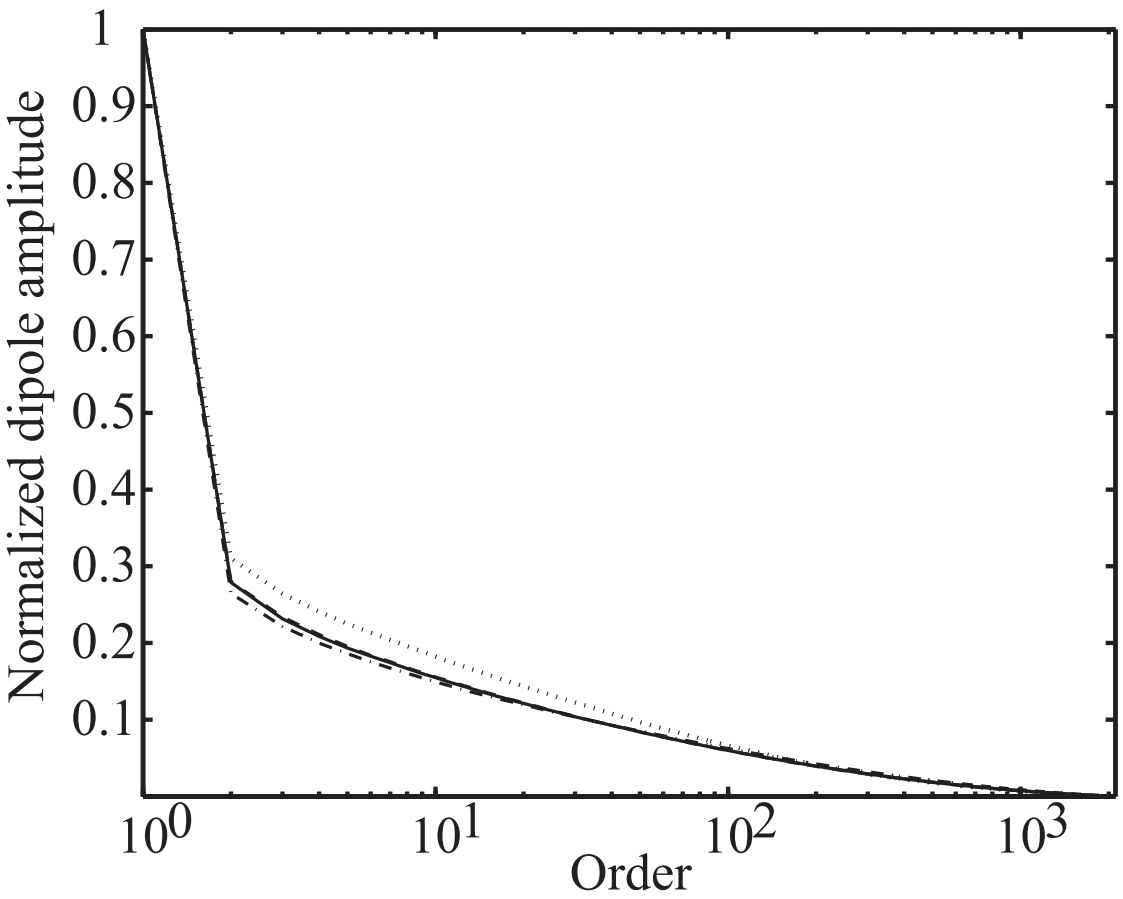

Figure 3.22: Normalized dipole amplitude estimated with the proposed spatial filter: the normalized dipole amplitude in decreasing order was averaged over 1000 single dipole cases. The average true dipole was at $(x, y, z) = (0.10, -0.15, 0)$. The strengths of the current dipoles in the decreasing order are plotted with the respective lines, i.e. the results of spatial filtering with $\lambda = 0$ (dashed line), $\lambda = 1/3$ (heavy broken line), $\lambda = 1/2$ (solid line) and $\lambda = 1$ (light broken line).

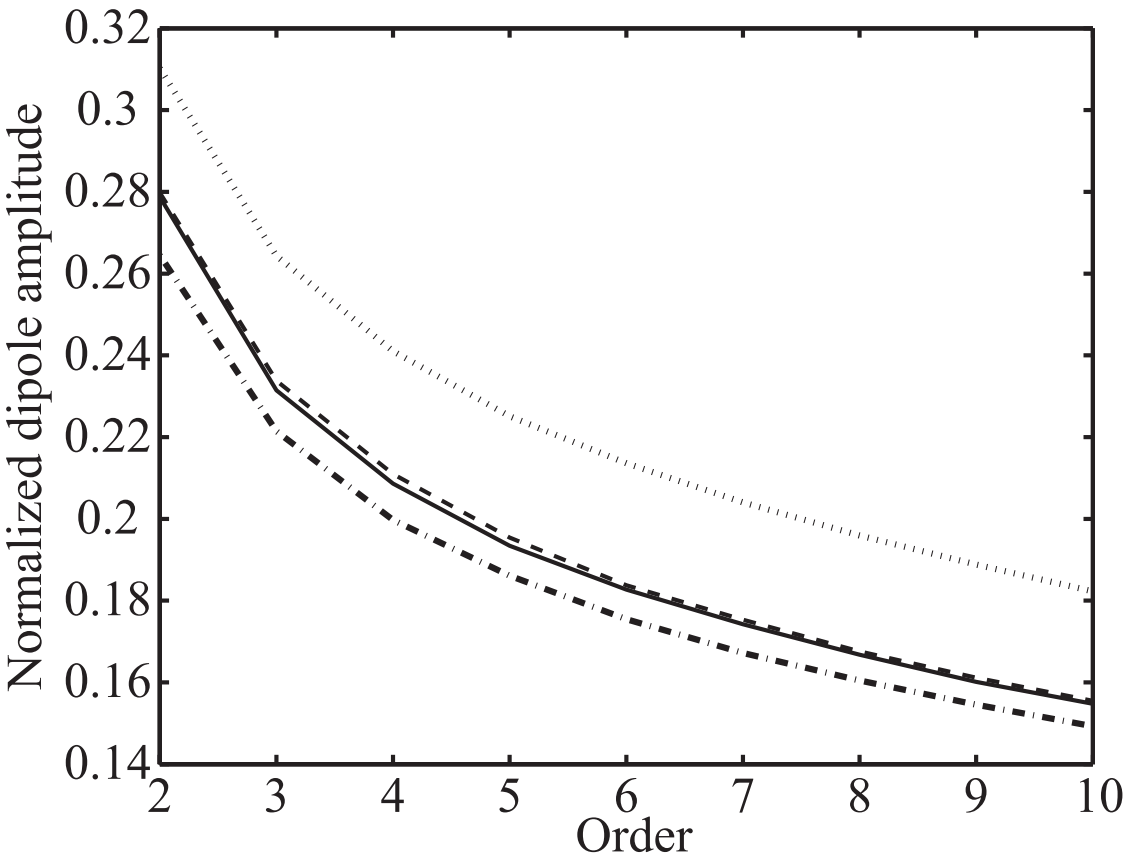

Figure 3.23: Normalized dipole amplitude estimated with the proposed spatial filter: The normalized dipole amplitude in decreasing order was averaged over 1000 single dipole cases. The average true dipole was at $(x, y, z) = (0.10, -0.15, 0)$. The amplitude from the second to tenth in the order is shown. The strengths of the current dipoles in the decreasing order are plotted with the respective lines, i.e. the results of spatial filtering with $\lambda = 0$ (dashed line), $\lambda = 1/3$ (heavy broken line), $\lambda = 1/2$ (solid line) and $\lambda = 1$ (light broken line).

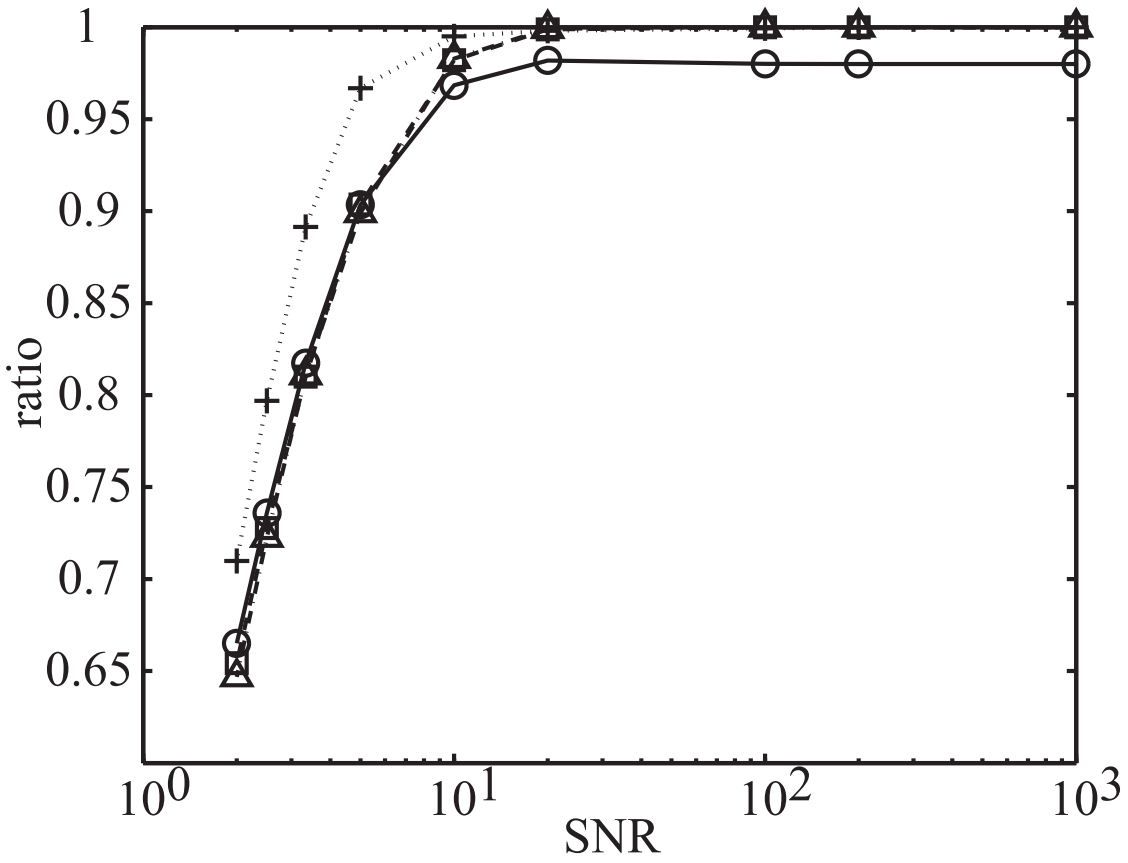

Figure 3.24: Frequencies of the successful estimation in single dipole cases for various SNRs: the frequency of the successful estimation, in which the largest dipole was estimated at the true dipole location, is shown. For each single-dipole estimation, 100 trials were conducted. The frequency is averaged over 100 single dipole cases selected randomly. The frequencies are show for the respective spatial filters with $\lambda = 0$ (dashed line, +), $\lambda = 1/3$ (heavy broken line, $\square$), $\lambda = 1/2$ (solid line, $\bigcirc$) and $\lambda = 1$ (light broken line, $\triangle$)

3.2.3 Current density estimation under multiple dipole

As well as in the single dipole cases, Figures.3.25-3.30 show some examples of the estimation results with the spatial filters. Figures 3.25-3.27 show the dipole strengths in the decreasing order in the two-dipole cases where the true dipoles were the pairs of the locations $(x, y, z) = (0, \pm 6, 0)$, $(0, \pm 3, 0)$ and $(0, \pm 1, 0)$, and Figures 3.28-3.30 illustrate the four-dipole cases, where the four true dipoles were at the locations $(x, y, z) = (0, 6, 0)$, $(0, -6, 0)$, $(-6, 0, 0)$ and $(0, 0, 6)$ (Fig.3.28), $(x, y, z) = (0, 3, 0)$, $(0, -3, 0)$, $(-3, 0, 0)$ and $(0, 0, 3)$ (Fig.3.29) and $(x, y, z) = (0, 1, 0)$, $(0, -1, 0)$, $(-1, 0, 0)$ and $(0, 0, 1)$ (Fig.3.30). Following the manner in the single dipoe cases, the symbols in the figures correspond to the dipole estimated at the location of the true dipoles. In every estimation, larger dipoles were appraised at the true-dipole positions.

It is recognized that the fourth order cumulants improve the localization of the estimated current distribution. Through the results shown in Figs.3.19-3.21 and 3.25-3.30, the improvements of the localization with the fourth order cumulants were more remarkable in the cases where the dipoles were farther from the center of the spherical conductor.

To investigate the effectiveness of the fourth order cumulants in multiple dipole cases, the estimation of the current density distribution was conducted, in which the dipoles at all of the locations in the discrete conductor were activated randomly: the activities of the dipoles were Gaussian. Therefore, we can not specify the number of the dipoles, and there were no specified location on average where the current density distribution was localized. However, the strengths of the dipoles in the decreasing order should decline steeplier if the spatial filter has more localization power.

Figures 3.31 and 3.32 show the strengths of the dipoles in the decreasing order of the above-described estimation. The strengths were normalized and averaged over ten thousands of trials. Figure 3.32 focused on a part of Fig.3.31. The result shows that the spatial filter which minimized both of the second and fourth order cumulants localizes the current distribution more effectively in multiple dipole cases.

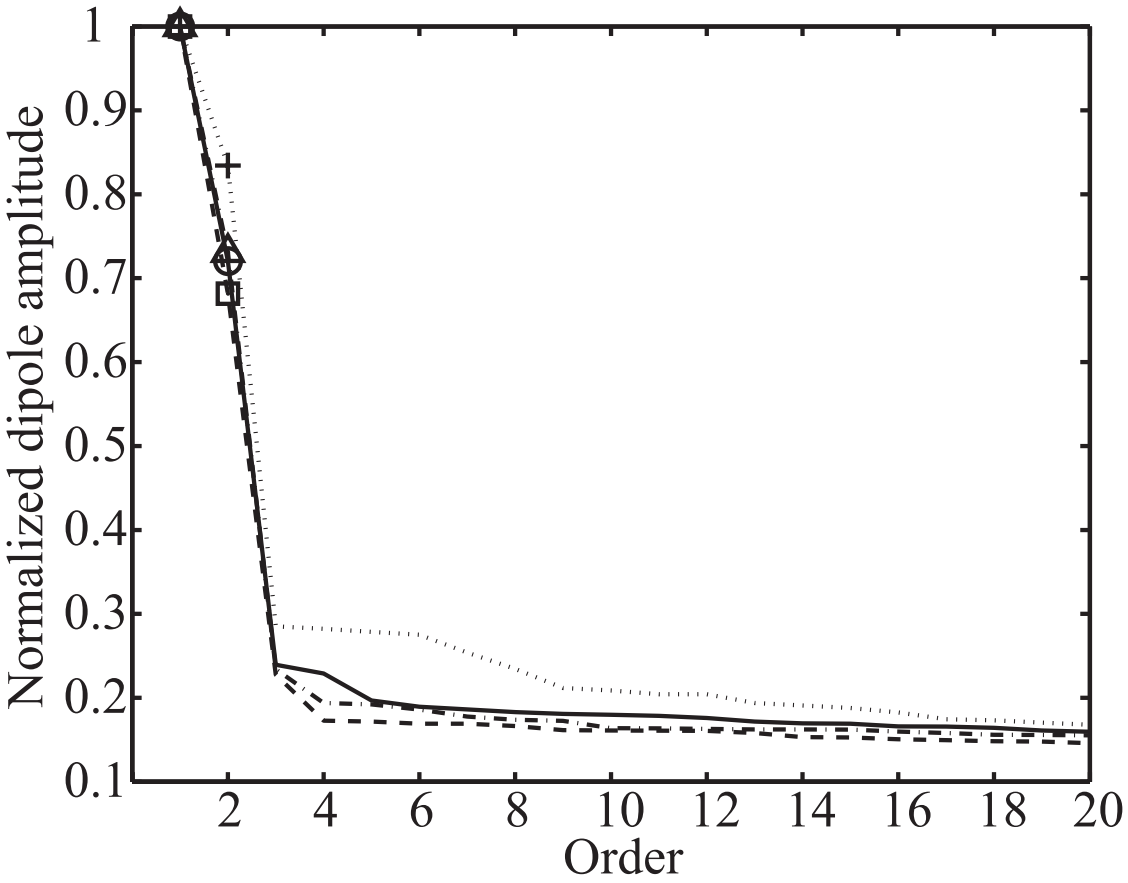

Figure 3.25: Example of multiple dipole estimation with the proposed spatial filter: the true dipoles were at $(x, y, z) = (0, -6, 0), (0, 6, 0)$. The strengths of the current dipoles estimated by the spatial filtering are plotted in decreasing order. They are shown with the respective lines and symbols, i.e. the results of spatial filtering with $\lambda = 0$ (dashed line with $+$), $\lambda = 1/3$ (heavy broken line with $\square$), $\lambda = 1/2$ (solid line with $\bigcirc$) and $\lambda = 1$ (light broken line with $\triangle$). The symbols indicate the dipole estimated at the location of the true dipole.

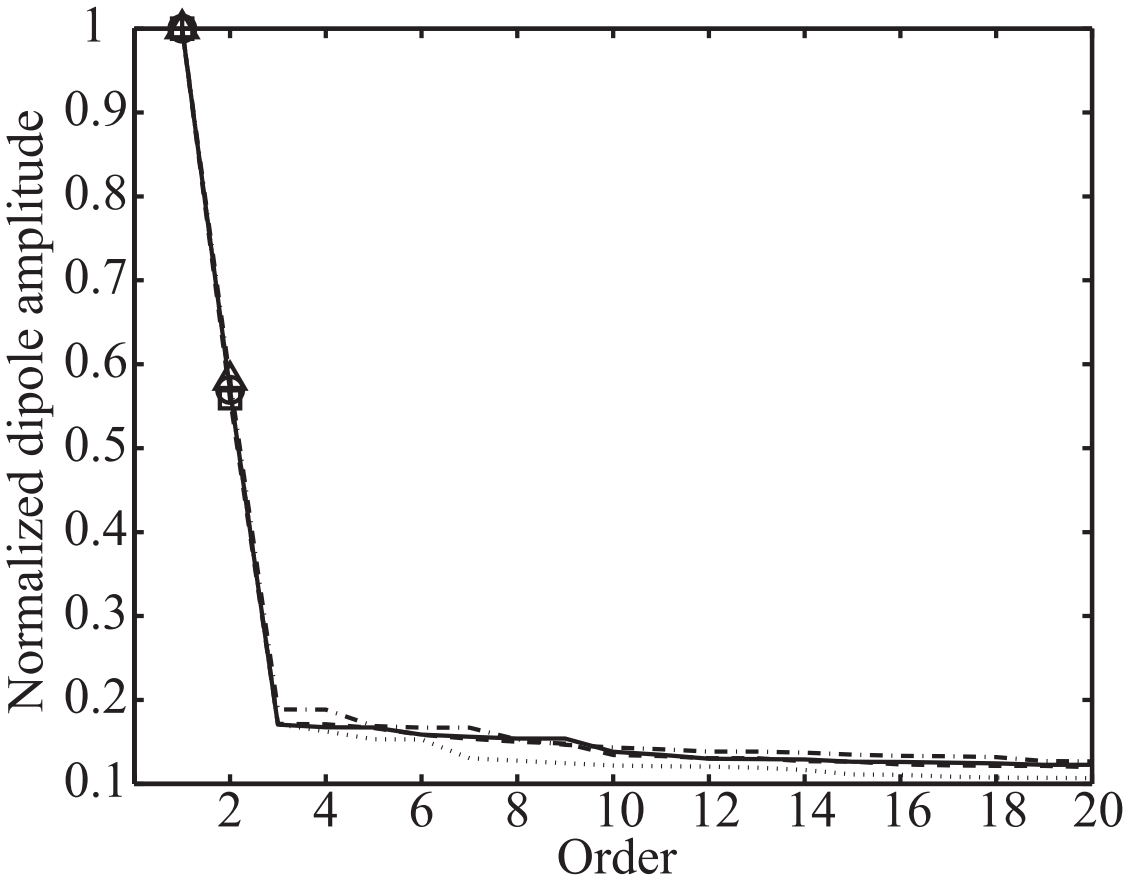

Figure 3.26: Example of multiple dipole estimation with the proposed spatial filter: the true dipoles were at $(x, y, z) = (0, -3, 0), (0, 3, 0)$. The strengths of the current dipoles estimated by the spatial filtering are plotted in decreasing order. They are shown with the respective lines and symbols, i.e. the results of spatial filtering with $\lambda = 0$ (dashed line with $+$), $\lambda = 1/3$ (heavy broken line with $\square$), $\lambda = 1/2$ (solid line with $\bigcirc$) and $\lambda = 1$ (light broken line with $\triangle$). The symbols indicate the dipole estimated at the location of the true dipole.

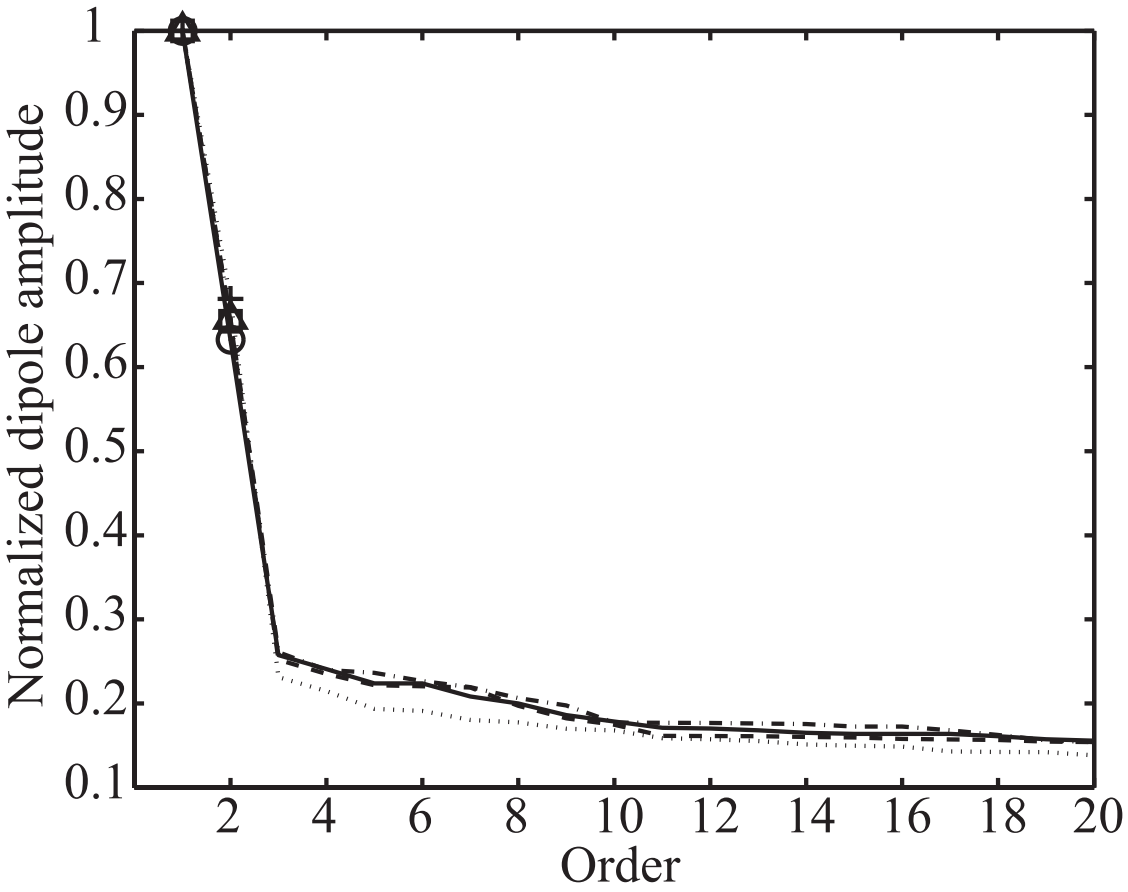

Figure 3.27: Example of multiple dipole estimation with the proposed spatial filter: the true dipoles were at $(x, y, z) = (0, -1, 0)$, $(0, 1, 0)$. The strengths of the current dipoles estimated by the spatial filtering are plotted in decreasing order. They are shown with the respective lines and symbols, i.e. the results of spatial filtering with $\lambda = 0$ (dashed line with $+$), $\lambda = 1/3$ (heavy broken line with $\square$), $\lambda = 1/2$ (solid line with $\bigcirc$) and $\lambda = 1$ (light broken line with $\triangle$). The symbols indicate the dipole estimated at the location of the true dipole.

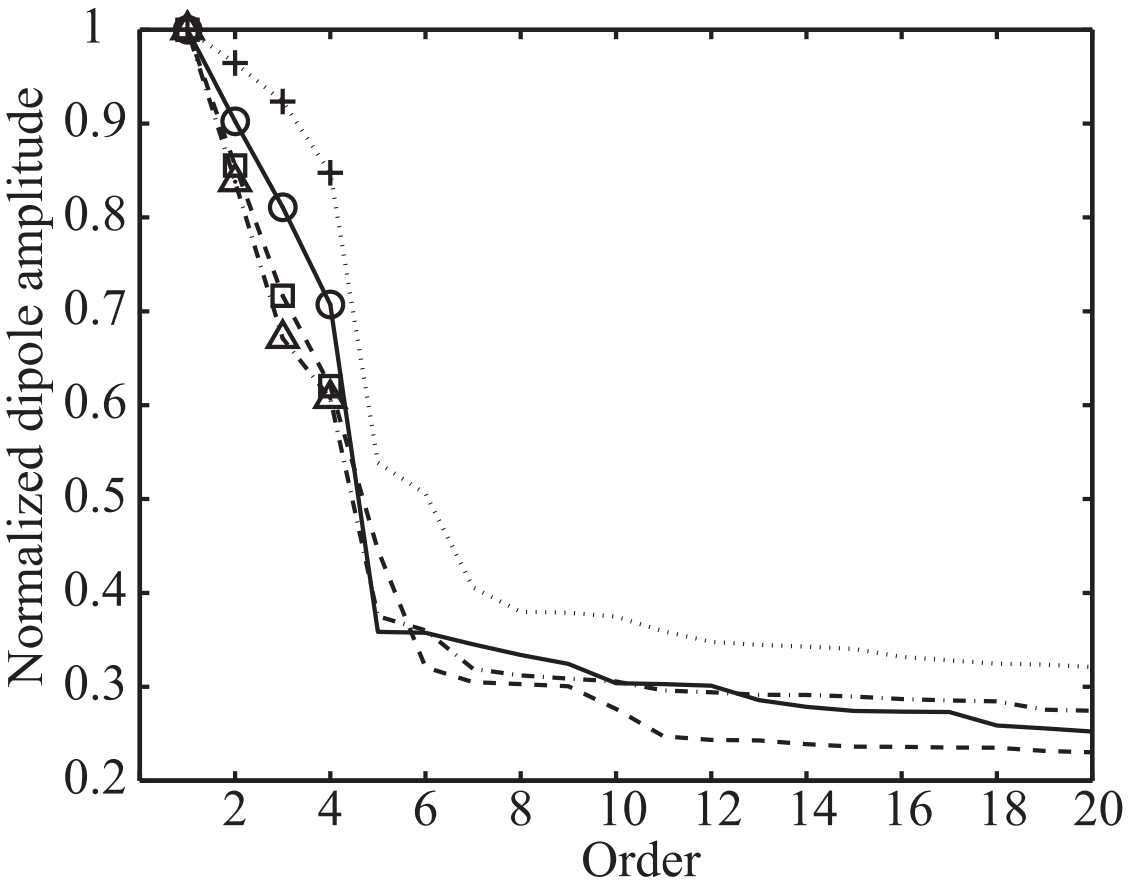

Figure 3.28: Example of multiple dipole estimation with the proposed spatial filter: the true dipoles were at $(x, y, z) = (0, -6, 0)$, $(0, 6, 0)$, $(-6, 0, 0)$ and $(0, 0, 6)$. The strengths of the current dipoles estimated by the spatial filtering are plotted in decreasing order. They are shown with the respective lines and symbols, i.e. the results of spatial filtering with $\lambda = 0$ (dashed line with +), $\lambda = 1/3$ (heavy broken line with $\square$), $\lambda = 1/2$ (solid line with $\bigcirc$) and $\lambda = 1$ (light broken line with $\triangle$). The symbols indicate the dipole estimated at the location of the true dipole.

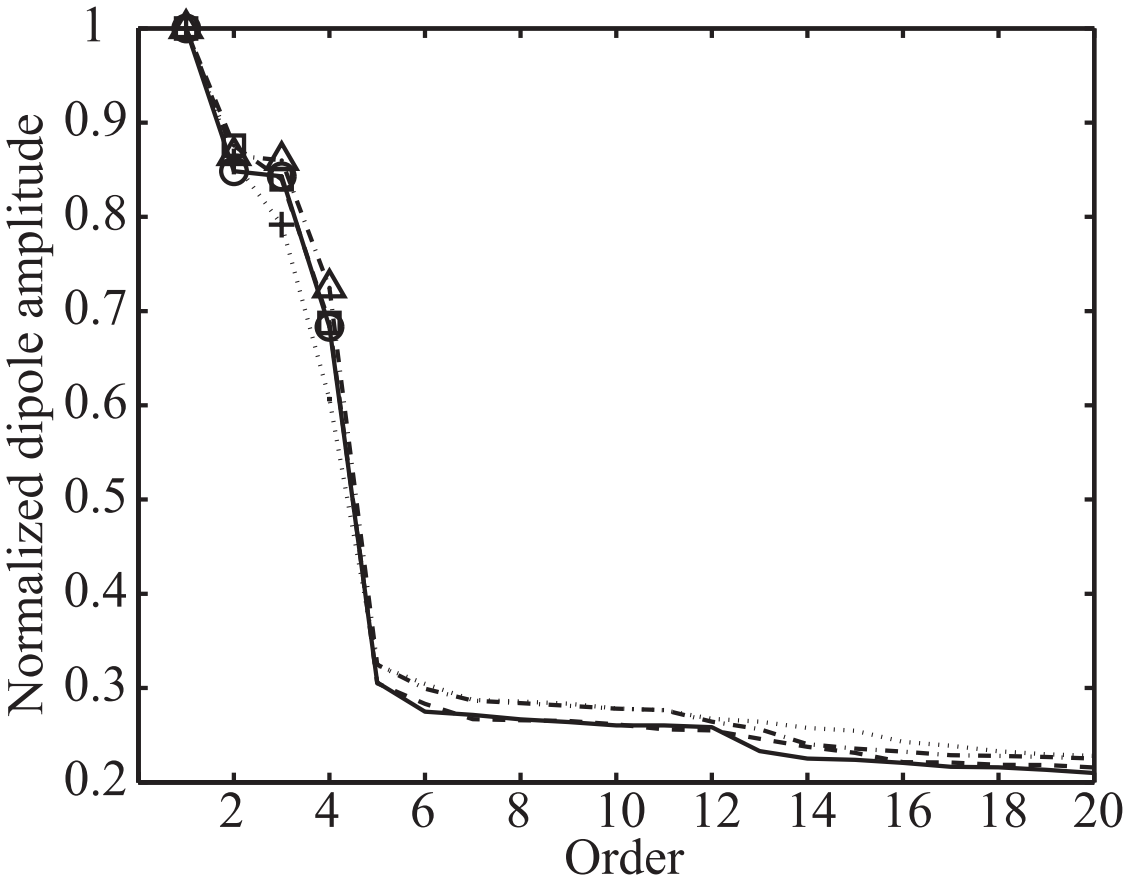

Figure 3.29: Example of multiple dipole estimation with the proposed spatial filter: the true dipoles were at $(x, y, z) = (0, -3, 0)$, $(0, 3, 0)$, $(-3, 0, 0)$ and $(0, 0, 3)$. The strengths of the current dipoles estimated by the spatial filtering are plotted in decreasing order. They are shown with the respective lines and symbols, i.e. the results of spatial filtering with $\lambda = 0$ (dashed line with $+$), $\lambda = 1/3$ (heavy broken line with $\square$), $\lambda = 1/2$ (solid line with $\bigcirc$) and $\lambda = 1$ (light broken line with $\triangle$). The symbols indicate the dipole estimated at the location of the true dipole.

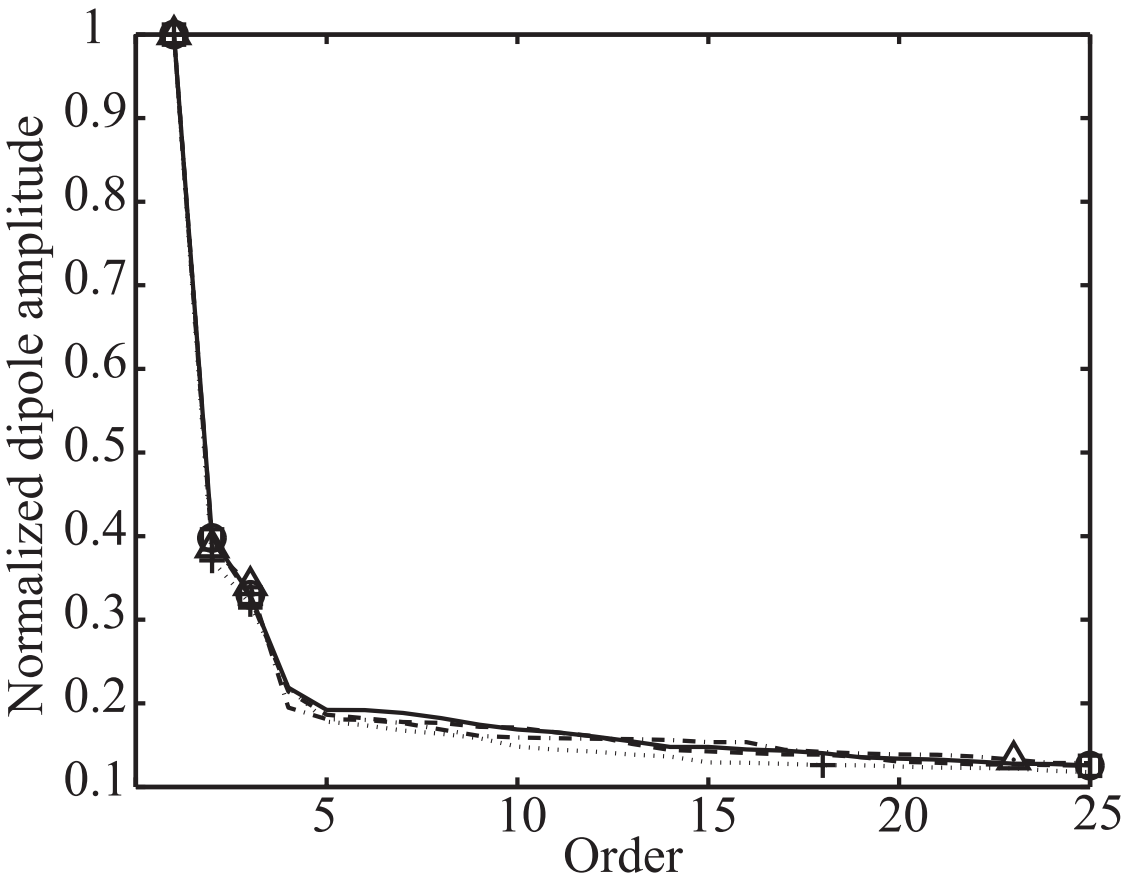

Figure 3.30: Example of multiple dipole estimation with the proposed spatial filter: the true dipoles were at $(x, y, z) = (0, -1, 0)$, $(0, 1, 0)$, $(-1, 0, 0)$ and $(0, 0, 1)$. The strengths of the current dipoles estimated by the spatial filtering are plotted in decreasing order. They are shown with the respective lines and symbols, i.e. the results of spatial filtering with $\lambda = 0$ (dashed line with +), $\lambda = 1/3$ (heavy broken line with $\square$), $\lambda = 1/2$ (solid line with $\bigcirc$) and $\lambda = 1$ (light broken line with $\triangle$). The symbols indicate the dipole estimated at the location of the true dipole.

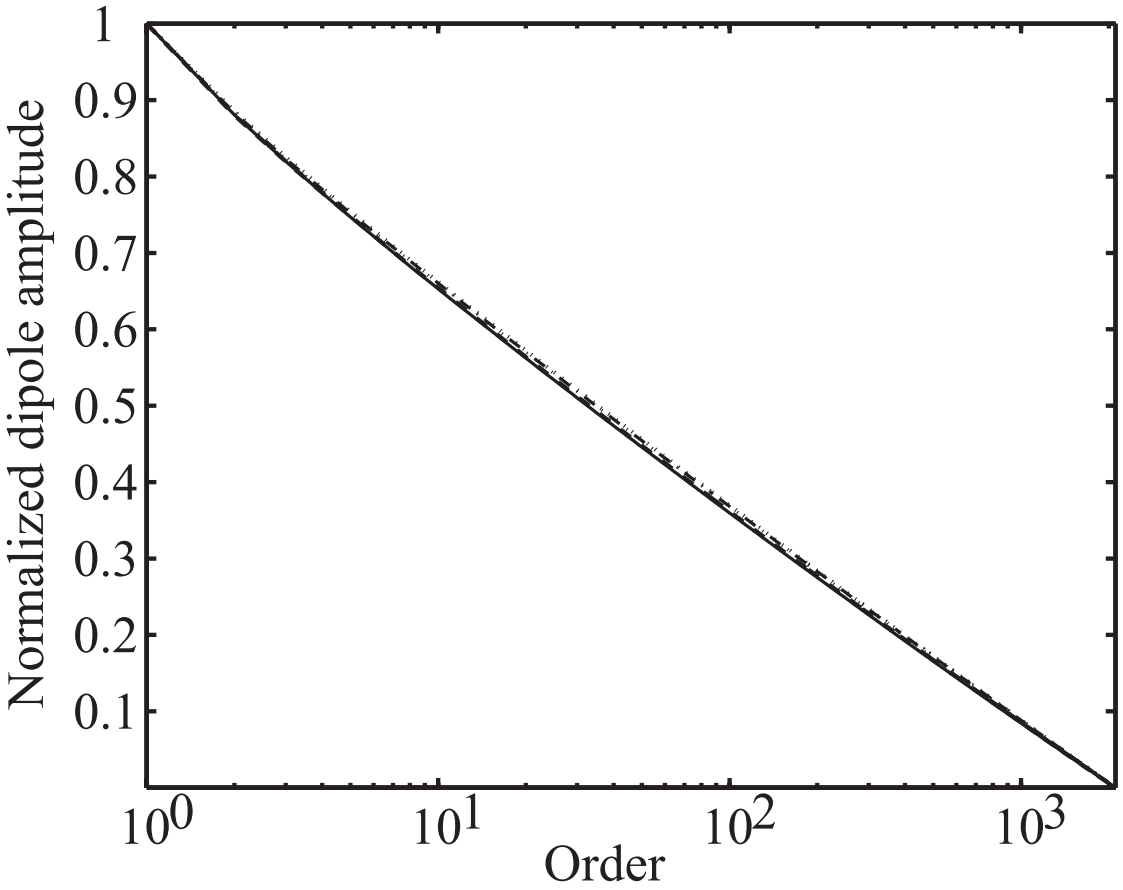

Figure 3.31: Normalized dipole amplitude estimated with the proposed spatial filter in multiple dipole case: the normalized dipole amplitude in decreasing order was averaged over 10000 cases where all of the dipoles were activated randomly. The dipole activities were Gaussian. The strengths of the current dipoles in the decreasing order are plotted with the respective lines, i.e. the results of spatial filtering with $\lambda = 0$ (dashed line), $\lambda = 1/3$ (heavy broken line), $\lambda = 1/2$ (solid line) and $\lambda = 1$ (light broken line).

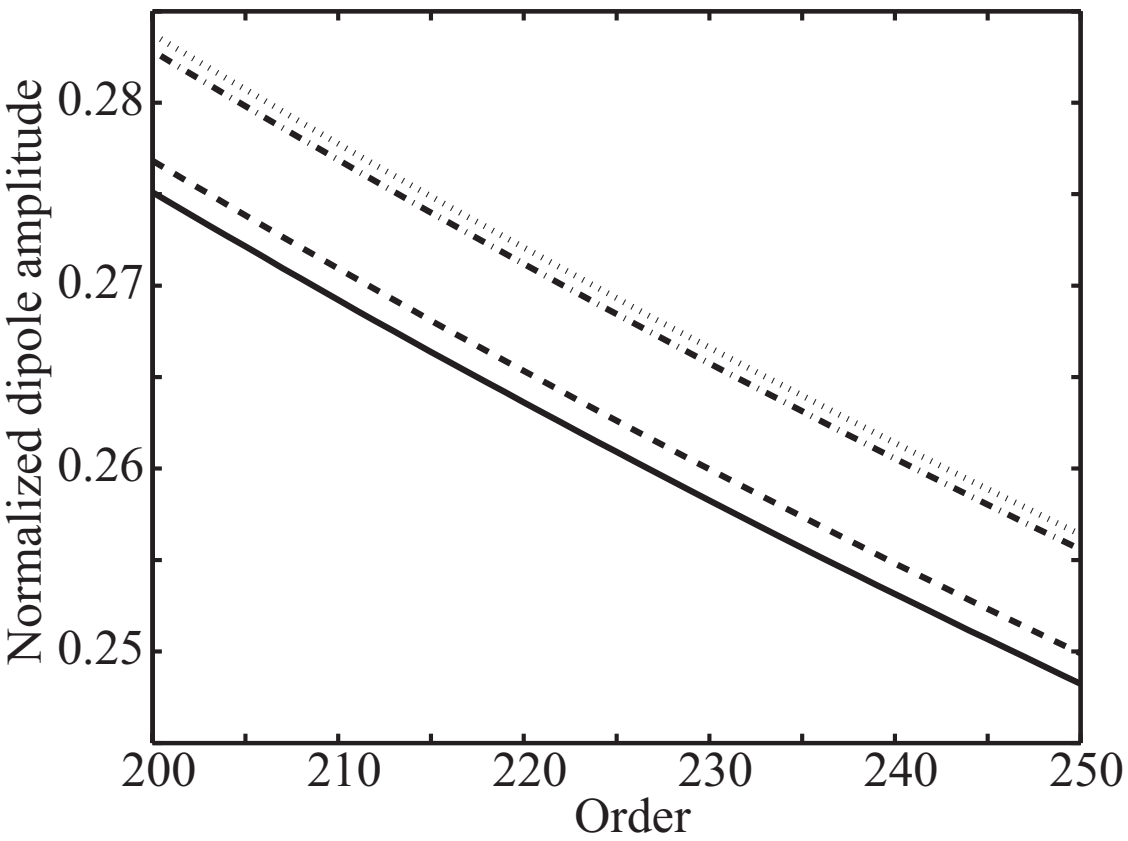

Figure 3.32: Normalized dipole amplitude estimated with the proposed spatial filter in multiple dipole case: the normalized dipole amplitude in decreasing order was averaged over 10000 cases where all of the dipoles were activated randomly. The dipole activities were Gaussian. The amplitude from the 200th to 250th in the order is shown. The strengths of the current dipoles in the decreasing order are plotted with the respective lines, i.e. the results of spatial filtering with $\lambda = 0$ (dashed line), $\lambda = 1/3$ (heavy broken line), $\lambda = 1/2$ (solid line) and $\lambda = 1$ (light broken line).

3.2.4 Discussion

In this section, the current density estimation with the proposed spatial filter is numerically illustrated. The numerical experiments show that the fourth order cumulants in the optimization of the spatial filter improve the localization. The current distribution estimated with the spatial filter enhanced the fourth order cumulants was localized well. As mentioned in Section 2.5.2, the output of the spatial filter inherits the statistical character of the prescribed pdf, i.e. the smaller entropy and the higher degree of independence, and the amplitude of the current densities is suppressed. It is indicated that the minimization of the second order cumulants is crucial to increase the localization in multiple dipole cases. The spatial filter should inhibit the interference in the variance to get rid of the influences of the non-target dipoles from the estimation $\hat{\boldsymbol{q}}_k$.

Through the numerical experiments, it is verified that the depths of the current dipoles are correctly estimated with the proposed spatial filter. The normalization of the spatial filter enables the estimation of the depths. Especially in the single dipole cases, as shown in Fig.3.24, the current dipole was estimated on the correct location regardless of its depth with the robustness to the noises. Larger current dipoles were successfully located on the positions of the true dipoles in the multiple dipole cases, though the estimation may be not successful when the dipole does not contribute sufficiently to the MEG data among the other dipoles which simultaneously exist. The investigation of the robustness to the noise will be a reference.

The current density distribution estimated by the spatial filter is increasingly complex against the number of the true dipoles and loses the localization. The nature of the underdetermined problem aggravates the estimation in multiple dipole case. Though we need to contrive the techniques in the experiment with MEG, the reconstruction of the current dipoles estimated by the proposed spatial filtering, the SFR, alleviates the issue.

3.3 Spatial filtered reconstruction (SFR)

3.3.1 Experimental conditions

Here, the performances of the SFR, i.e. the spatial filtering and successive reconstruction with multiple linear regression, were investigated through numerical experiments. The reconstruction of the current distribution estimated with the spatial filter only with the second order cumulants is evaluated in this section. For the spatial filter with the fourth order cumulants, similar discussion can be applied.

The conductor was a homogeneous sphere with a radius of 8 cm, which is discretized, and dipoles were assumed on the grid points positioned at intervals of 1 cm. A 160ch whole-head type MEG system was adopted in these numerical studies. The positions of the sensors and the grid points are shown in Fig.3.18. MEG data were obtained from Eq.(2.7). The additive sensor noises $\boldsymbol{\varepsilon}$ are Gaussian.

3.3.2 Examples of the estimations with SFR

Figures 3.33-3.35 are the examples of the estimation of the current density distribution with the SFR. In these estimations, the initial number of the dipoles p was prescribed as 10, and redundant dipoles were removed in the sense of minimization of the Mallows C_p. The signal-to-noise ratio (SNR) was defined as $\|L\boldsymbol{Q}\|^2 \Big/ \|\boldsymbol{\varepsilon}\|^2$ in the following simulations.

The result when the true dipoles were at $(x, y, z) = (0, 6, 0)$ and $(0, 7, 0)$ with an SNR of 10 is shown in Fig.3.33. The orientations of the true dipoles were $(x, y, z) = (1, 0, 0)$. The true dipoles had same strengths. Though some small redundant dipoles appeared except for in the true dipole positions, the current density distribution was well localized. This result also shows that the spatial resolution is 1 cm and worse in the conditions of the simulation. It depends on several conditions, e.g. the number of sensors, locations of sensors, number of dipoles, orientations of dipoles, and methods for discretizing the conductor and SNR, etc. Mallows C_p selects the model that fits the data with the fewest dipoles; therefore, dipoles that do not make much differences to the data will be removed from the estimated current

distribution.

Figure 3.34 shows the current distribution estimated by the SFR when the true current dipoles were at $(x, y, z) = (0, -4, 0)$ and $(0, 4, 0)$ with SNR of 10. The true dipole orientations were $(x, y, z) = (1, 0, 0)$. The true dipoles had same strengths. Even if the dipoles existed apart from each other, the SFR could pick up the dipoles in the true positions. If there is a dipole that is further from the sensor array than the others and does not contribute sufficiently to the data, estimating the dipole is difficult.

The estimation result in the case of four true dipoles at $(x, y, z) = (-6, 0, 0)$, $(0, -6, 0)$, $(0, 6, 0)$ and $(0, 0, 6)$ with an SNR of 100 is shown in Fig.3.35. The orientations of the true dipoles were $(x, y, z) = (0, 1, 0)$, $(-1, 0, 0)$, $(1, 0, 0)$ and $(0, -1, 0)$, respectively. The true dipoles had same strengths. Prior information is less of a concern in the SFR than in the other methods such as the Moving-dipole method. Thus, we can appraise more complex current distributions such as those it is possible to confront in actual neurological studies.

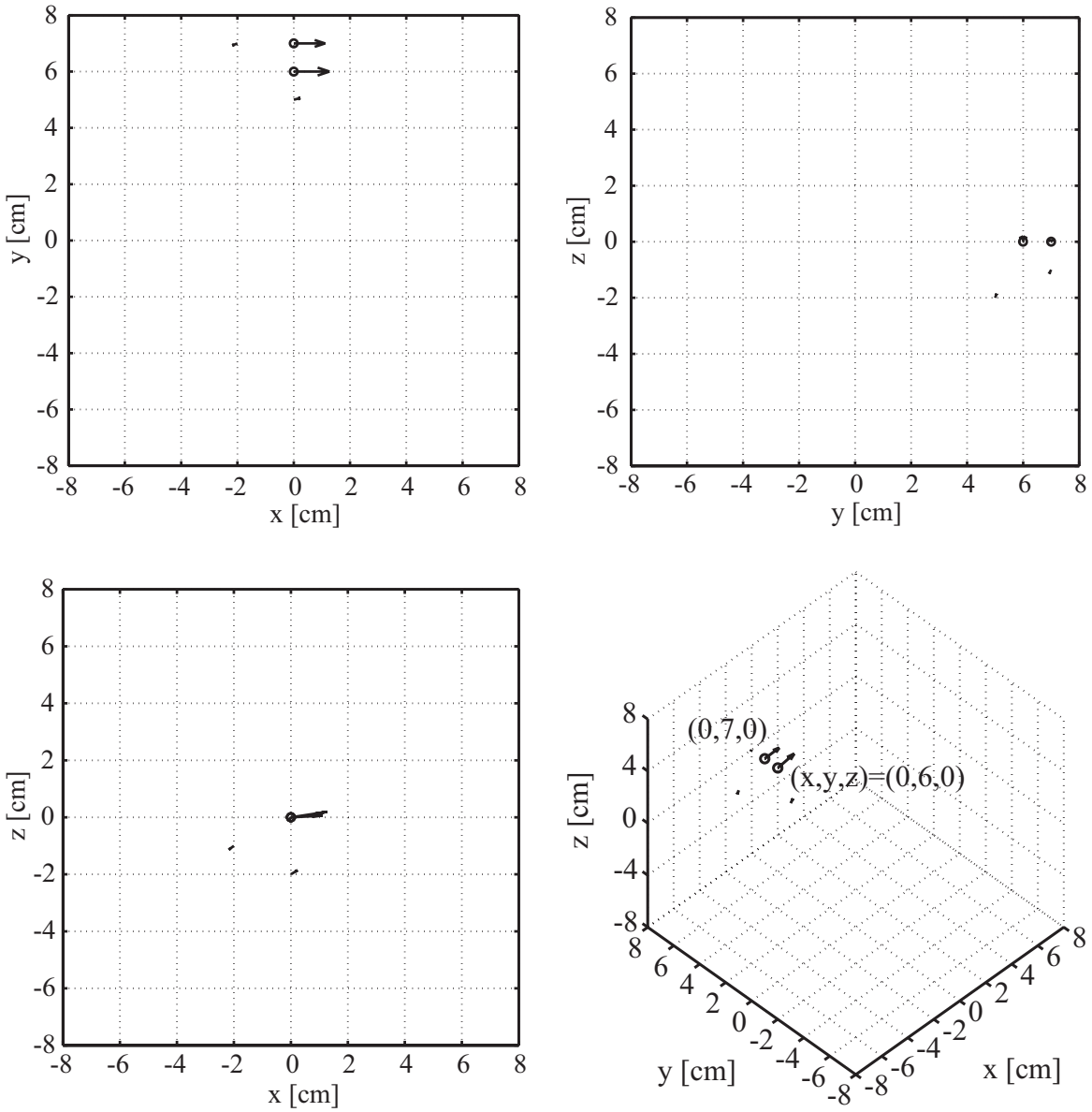

Figure 3.33: Example of dipole estimation with the SFR: the case of two adjacent dipoles with a SNR of 10. The locations of the true dipoles were at $(x, y, z) = (0, 6, 0)$ and $(0, 7, 0)$. The true dipole orientations were $(x, y, z) = (1, 0, 0)$.

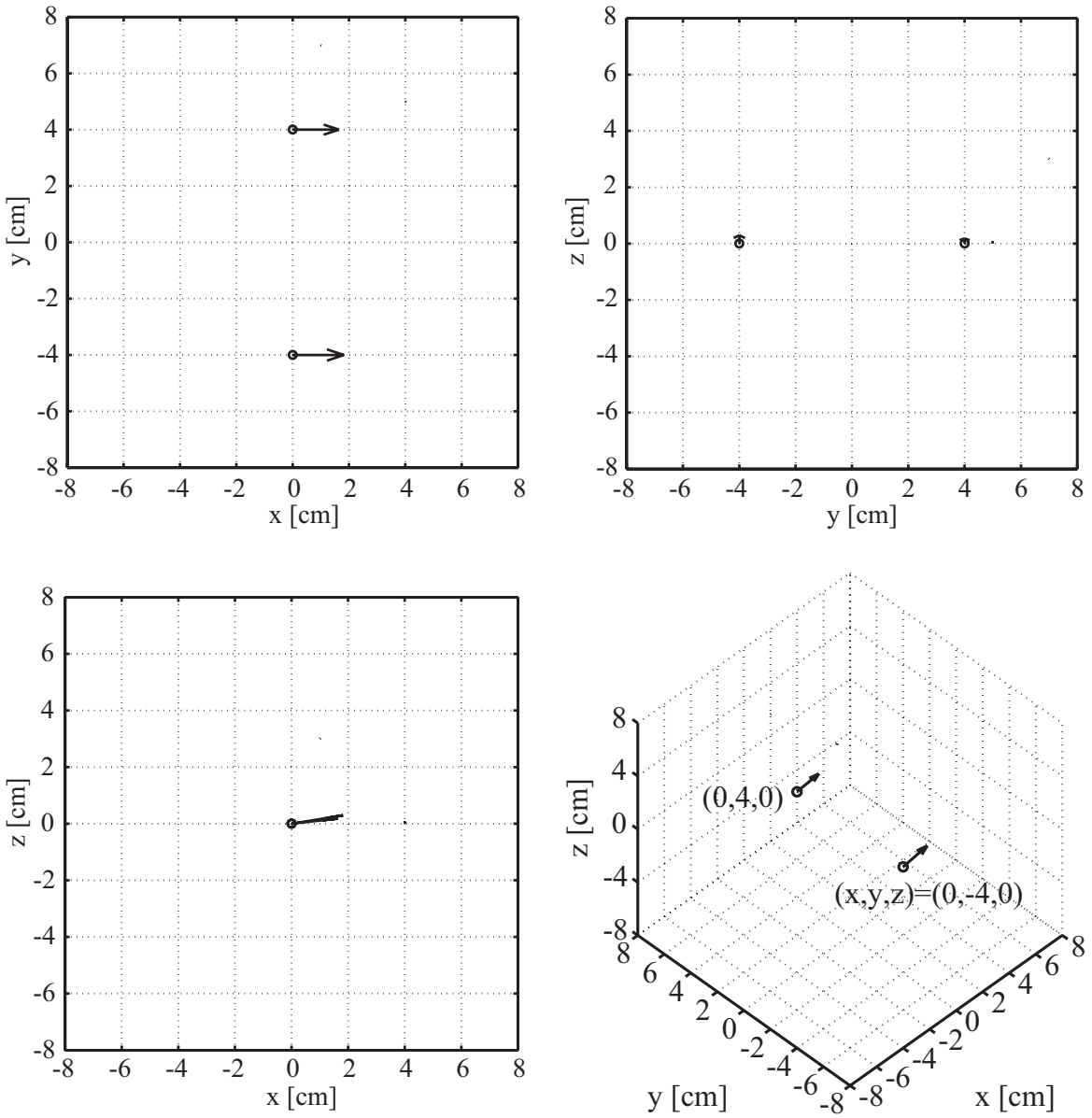

Figure 3.34: Example of dipole estimation with the SFR: the case of two distant dipoles with a SNR of 10. The locations of the true dipoles were at $(x, y, z) = (0, -4, 0)$ and $(0, 4, 0)$. The true dipole orientations were $(x, y, z) = (1, 0, 0)$.

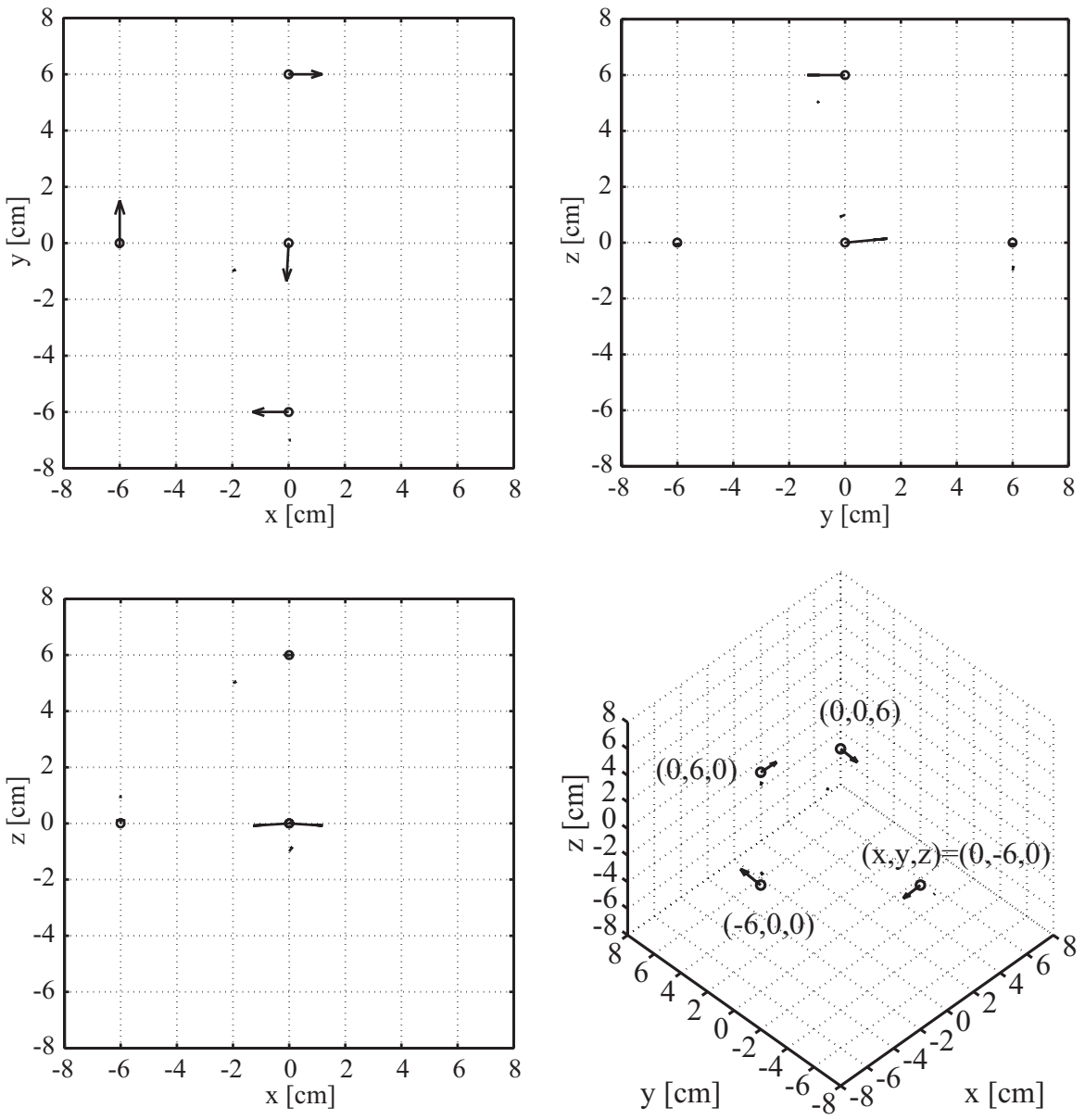

Figure 3.35: Example of dipole estimation with the SFR: the case of two distant dipoles with a SNR of 100. The locations of the true dipoles were at $(x, y, z) = (0, 6, 0),\ (0, 0, 6),\ (0, -6, 0)$ and $(-6, 0, 0)$. The true dipole orientations were $(x, y, z) = (1, 0, 0),\ (0, -1, 0),\ (-1, 0, 0)$ and $(0, 1, 0)$, respectively.

3.3.3 Influences of noises to SFR

The performances of the SFR in single-dipole cases with noise were investigated. The influence of noise in the case of multiple dipoles must be more complicated due to several factors to be considered. However, the following numerical studies illustrate the performances of the SFR we can expect generally, even in multiple-dipole cases.

A hundred trials of estimations with the SFR were implemented for each SNR, and the results were averaged over a hundred single-dipole cases with different locations and orientations of dipoles. The locations and orientations were selected randomly. The average of the locations was $(x, y, z) = (0.36, -0.15, -0.52)$.

The frequencies of the occurrence of three cases in the current density estimation with the SFR for various SNRs are shown in Fig.3.36. The three cases are; the case (i) where the maximum current density was estimated at the correct location by the proposed spatial filter, the case (ii) where the maximum dipole was estimated at the correct location by the SFR and the case (iii) where the dipole located at the position of the true dipole was included in the current dipoles reconstructed by the SFR. Additionally, the contribution rate of the dipole on the correct position, $\bar{\boldsymbol{q}}_{true}$, to the total dipoles in the estimated current distribution, that is, $\|\bar{\boldsymbol{q}}_{true}\|^2 \Big/ \sum_{i=1}^{p} \|\bar{\boldsymbol{q}}_i\|^2$, is plotted for each SNR in Fig.3.37. It was averaged over cases (ii). For each SNRs, the average number of the current dipoles reconstructed by the SFR is appended in Fig.3.37.

With the SNR at 10^1 and above, we obtained steady performance of the SFR (Fig.3.36). The proposed spatial filter identified the true dipole locations correctly, and the SFR localized the current distribution. Figures 3.36 and 3.37 indicate that there were no redundant dipoles in the estimation results. This implies that the SFR estimation is conducted stably with usual noise reduction, e.g. averaging over about 10^2 trials which gives 90 % GOF (goodness-of-fit) in ordinary MEG analysis such as AEF (auditory evoked field) and SEF (somatosensory evoked field). In cases with SNRs smaller than 10^1, the effect of the proposed reconstruction was remarkable. While the proposed spatial filter estimated the maximum current on the right

position for about 70 % of the estimation trials, the reconstruction with multiple linear regression improved the ratio of successful reconstruction, the case (ii), by nearly 10%, and almost 20 % for the case (iii). The SFR often captures the true dipole position even when the proposed spatial filter misses it. The reconstruction also strengthens the robustness of the estimation to noises.

Furthermore, the SFR gets the current distribution sufficiently localized toward the correct location, as shown in Fig.3.37. The dipole on the correct position contributed to more than 75 % of the total dipoles even when the SNR was 10^1 and below. Localization is improved with higher SNRs.

Figure 3.38 shows the average errors in positions of the maximum current dipoles estimated by the SFR. The positions of the marks show the mean values of the errors for the axes. The larger the SNR is, the smaller the standard deviation of the error is. The mean error for each axis and standard deviations were less than 2 cm. The difference between the true and the estimated maximum dipole location was within 1 or 2 grid points on average. When the SNR was more than 10^1, the noise did not cause error in position.

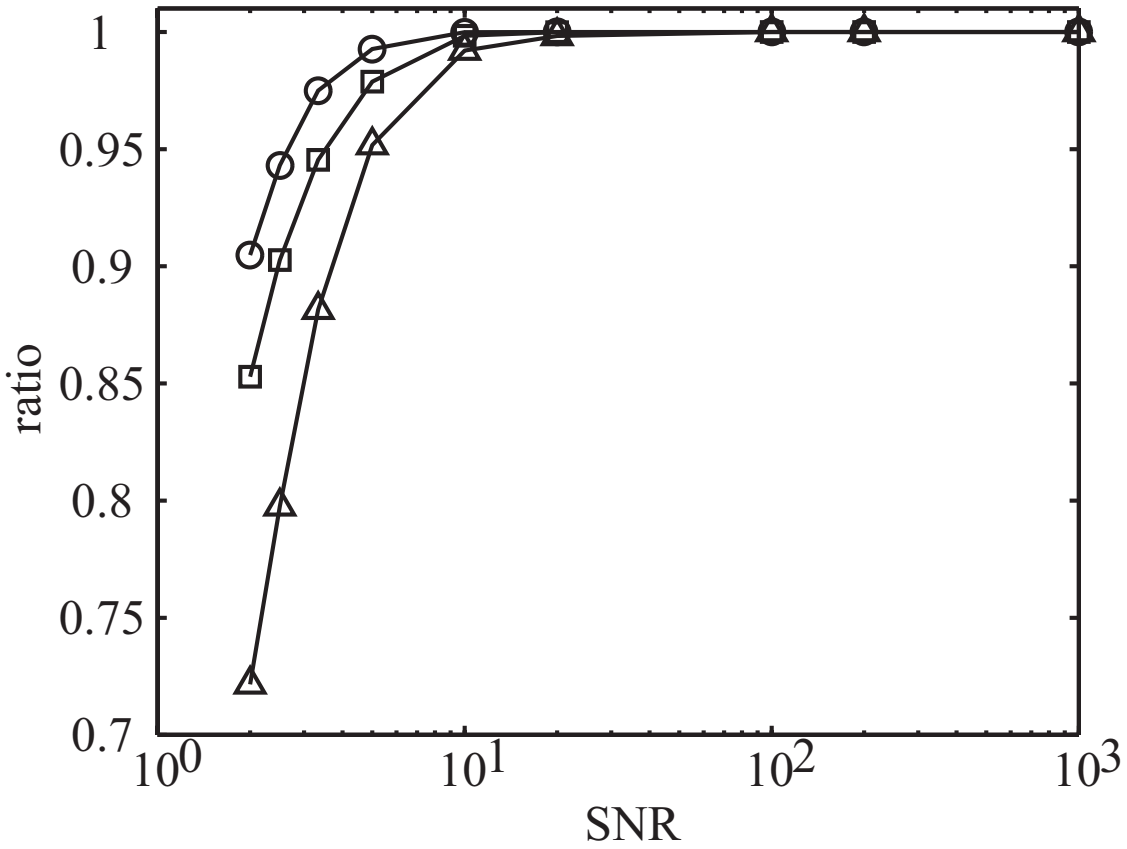

Figure 3.36: Frequencies of the cases for SNRs: case (i) where the maximum current density was estimated at the correct location by the proposed spatial filter (△), case (ii) where the maximum dipole was estimated at the correct location by the SFR (□), and case (iii) where the dipole on the correct location was reconstructed by the SFR (◯). 100 trials were conducted for each SNR in the single-dipole estimation, and the frequencies are averaged across the 100 single-dipole cases.

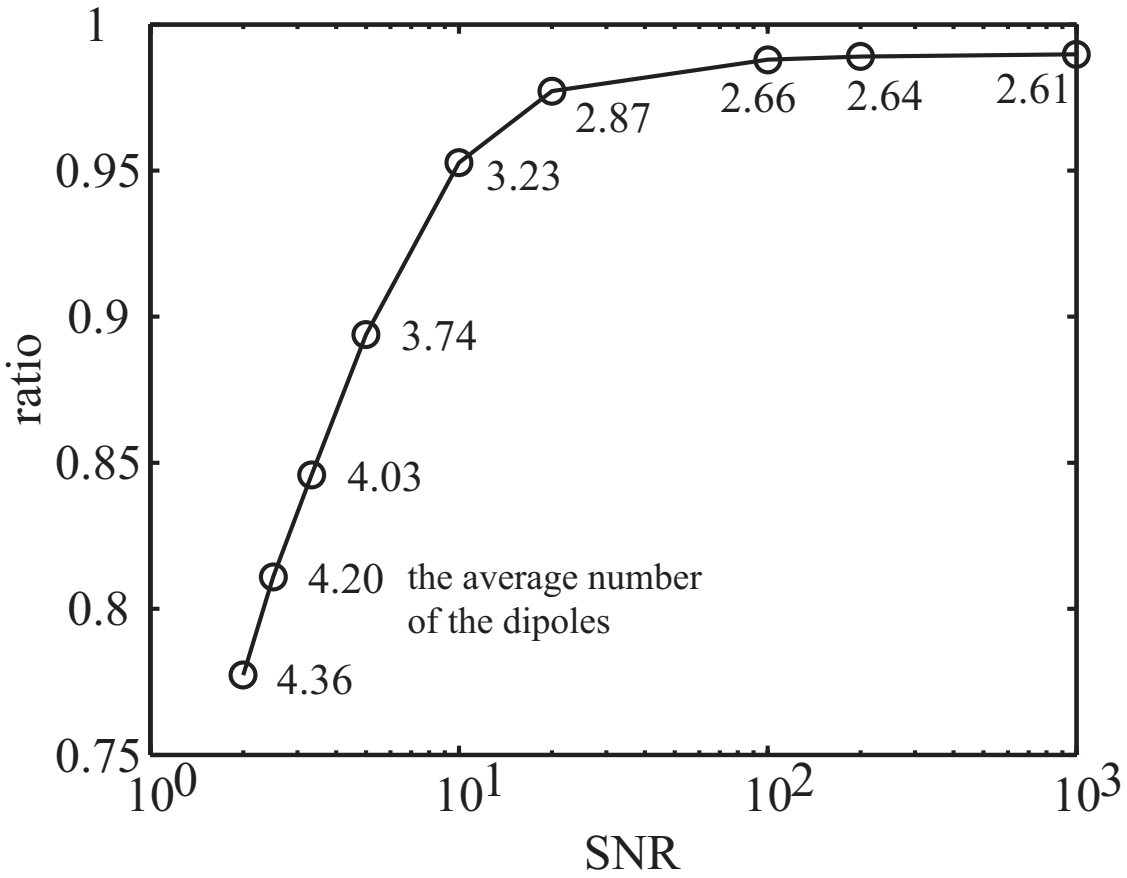

Figure 3.37: The contribution rate of the dipole estimated on the correct position for each SNR ($\|\bar{\boldsymbol{q}}_{true}\|^2 / \sum_{i=1}^{p} \|\bar{\boldsymbol{q}}_i\|^2$). It is averaged over cases (ii).

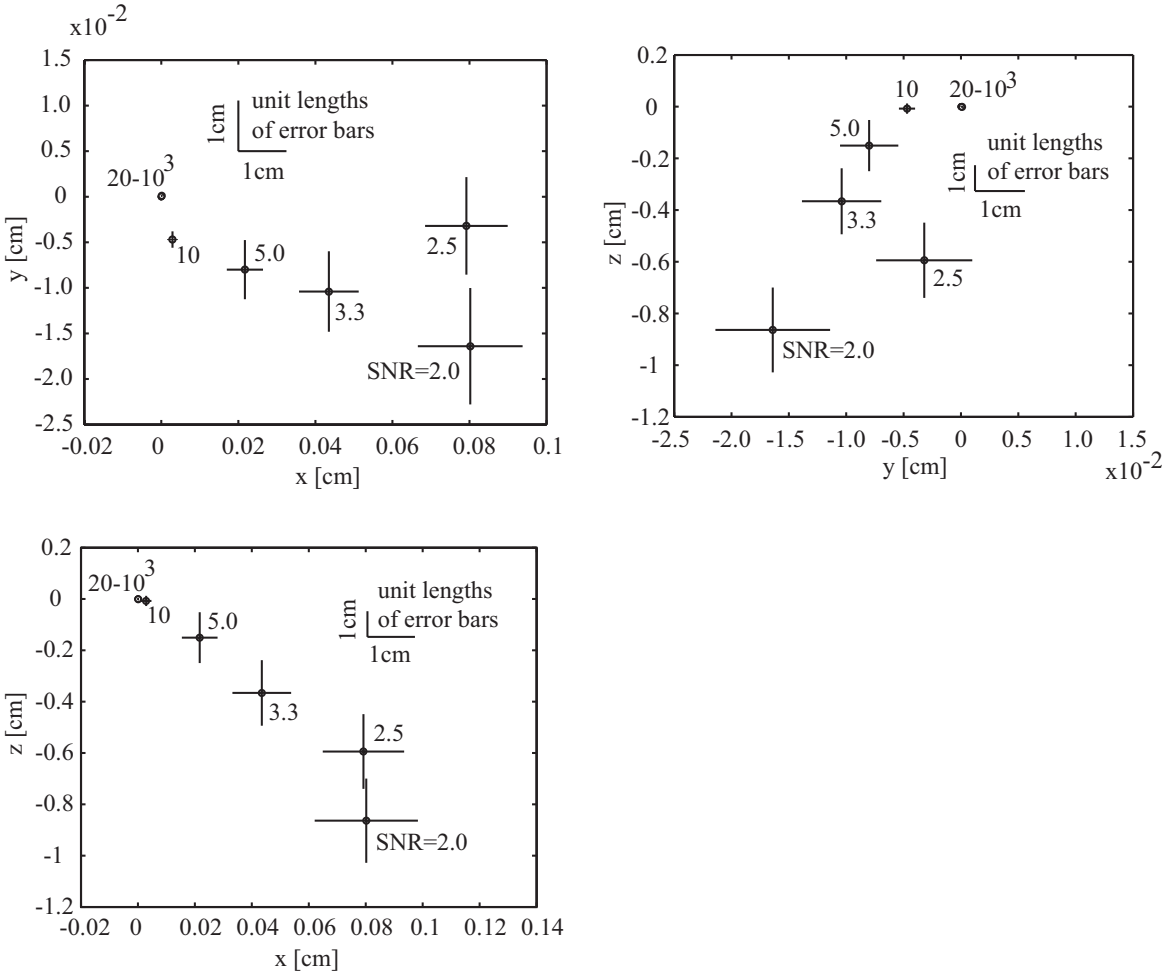

Figure 3.38: Average error in position of the maximum dipole estimated by the SFR: the error and the standard deviation are average over 100 single dipole cases. The origin indicates the correct location.

3.3.4 Effect of spatial discretization

In actual MEG analysis, current dipoles are hardly located on the discrete grid points. We need to estimate the dipoles out of the grid points. In this section, we researched the influence of the out-of-grid dipoles to the SFR.

The location and the orientation of the dipole were chosen randomly without concerning whether the dipole was on the grid point or not. A thousand trials of the current dipole estimation with the SFR were conducted. The average dipole location was $(x, y, z) = (0.02, 0.03, 0, 06)$. Figure 3.39 shows that the average difference between the positions of the true dipole and of the reconstructed dipoles. $\bar{\boldsymbol{r}}_{max}$ represents the average difference of the locations of the maximum dipole reconstructed by the SFR, and $\bar{\boldsymbol{r}}_2$, $\bar{\boldsymbol{r}}_3$ and $\bar{\boldsymbol{r}}_4$ correspond to the scond, third and fourth largest dipoles respectively. $\bar{\boldsymbol{r}}_{true}$ shows the origin. Note that the dipoles were estimated on the grid points by the SFR, actually.

The reconstructed dipoles tended to appear the locations farther from the sensor array. The density of the sensors was low in the region with $x > 0$ and $z < 0$ in which the current dipoles were reconstructed on average. The current distribution was reconstructed with the current dipoles on deeper position. The distances between the true and estimated dipoles (Table 2) approximately concurred with halves of the length of the diagonals or the edges, e.g. $\sqrt{3}/2$, $\sqrt{2}/2$ and $1/2$, in the cube composed of the grid points with the intervals of 1cm. The maximum dipole was estimated on the farthest grid points, on average, in the cube which the true dipole was enclosed. The contribution of the dipole located deeply is weak. Therefore, the amplitude has no choice but becomes larger to make significant contribution. The result in Table 2 shows that the redundant expanse of the current distribution appears with the estimation of the dipoles which are not on the grid points. It will be relieved, increasing the number of the grid points.

Table 2 Average distance between the true and reconstructed dipole, and ratio of the dipole amplitude of the reconstructed dipole

	$\bar{\boldsymbol{r}}_{max}$	$\bar{\boldsymbol{r}}_2$	$\bar{\boldsymbol{r}}_3$	$\bar{\boldsymbol{r}}_4$
$\|\bar{\boldsymbol{r}}\|$ [cm]	0.87	0.70	0.48	0.26
$\|\bar{\boldsymbol{q}}_k\|^2 / \sum_{i=1}^{p} \|\bar{\boldsymbol{q}}_i\|^2$	0.45	0.22	0.14	0.09

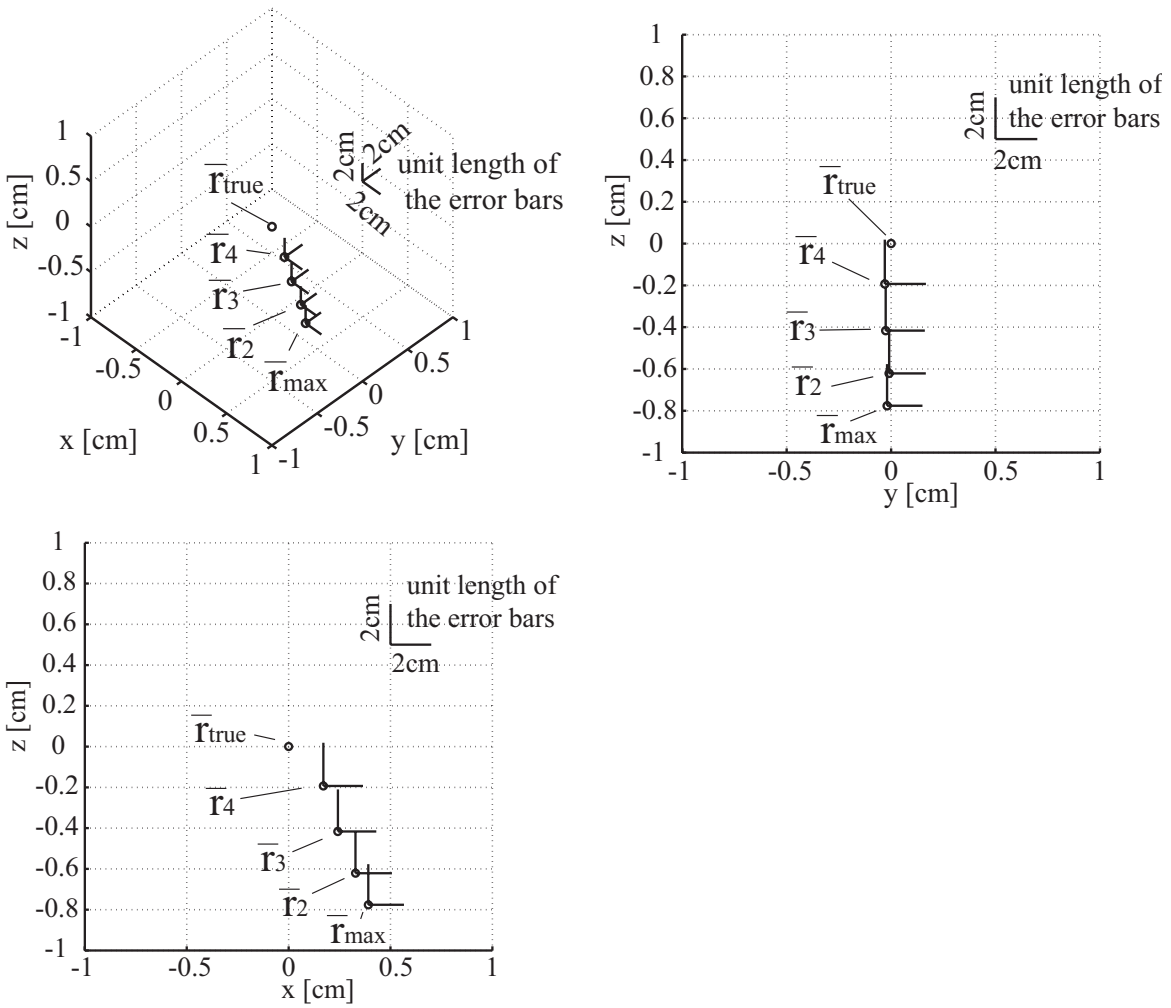

Figure 3.39: Differences between the true position and the reconstructed dipoles averaged over 1000 trials.

3.3.5 Comparison of SFR, LCMV beamformer and SAM

The main difference among the spatial filters, i.e, the LCMV beamformer, the SAM and the spatial filter proposed in this paper, is the usage of temporal information. The LCMV beamformer and the SAM utilize the covariance matrix of MEG data as described in Section 2.3.1. They localize current distribution effectively, and reflect actual neural activities due to the use of observed covariances. However, the temporal correlation of the source activities depresses the spatial resolution of the estimation with the LCMV beamformer, the SAM and MUSIC.

We conducted numerical experiments, in which the two true dipoles were located at $(x, y, z) = (0, -4, 0)$ and $(0, 4, 0)$, and MEG data were simulated by Eq.(2.7). The SNR at the peak latency of the MEG signals $\boldsymbol{LQ}$ was 10^1 , and the noise strength $\|\boldsymbol{\varepsilon}\|^2$ was constant for each temporal sample.

Estimation with the LCMV beamformer and the SAM were implemented in two cases: when the dipole activities were perfectly correlated (case (a)) and when they were partially correlated (case (b)). The covariance matrices of the simulated data and noise were utilized for the LCMV beamformer and the SAM. Besides, the SFR was applied for the case (a). The estimation with the SFR used only the snapshot of simulated MEG data at the peak latency.

Figure 3.40 shows the estimation results with the LCMV beamformer. The neural activity indexes, Eq.(2.37), on the plane with $z = 0$ of the estimation in the case (a) are shown in Fig.3.40 (a). The estimated activities were expanded in the whole of the conductor, while the neural activity indexes in the case (b) were localized better.

The results in the cases (a) and (b) with the SAM are shown in Fig.3.41. They are similar to the results with the LCMV beamformer. However, the spatial resolution with the LCMV beamformer is slightly better than with the SAM, and it seems not to consist with [58]. In [58], the spatial resolution is compared based on the pseudo-Z of the SAM, that is, $Z^2_{LCMV} = \mathrm{tr}\left(W_k^T C_m W_k\right) / \mathrm{tr}\left(W_k^T C_n W_k\right)$ substitutes for the neural activity index in Eq.(2.37). Following this manner, the SAM showed better spatial resolution than the LCMV beamformer in the simulations. Here, we

obeyed the original methods of the LCMV and SAM beamformers described in [55] and [56].

On the other hand, as shown in Fig.3.42, the SFR successfully localized the current densities in the case (a). Although the LCMV beamformer and the SAM are superior to the SFR in their robustness to noise, the SFR can offer better spatial resolution since it does not rely on temporal information to localize current distribution. This suggests that avoiding dependence on temporal information is a choice to improve the localization and spatial resolution in MEG analysis. The SFR, or a spatial filter that does not use any prior and temporal information but incorporates other methods, can be one of the options. Furthermore, reconstruction with multiple linear regression technique can cooperate with other spatial filters to obtain localized current distribution and convincing estimations in MEG analysis.

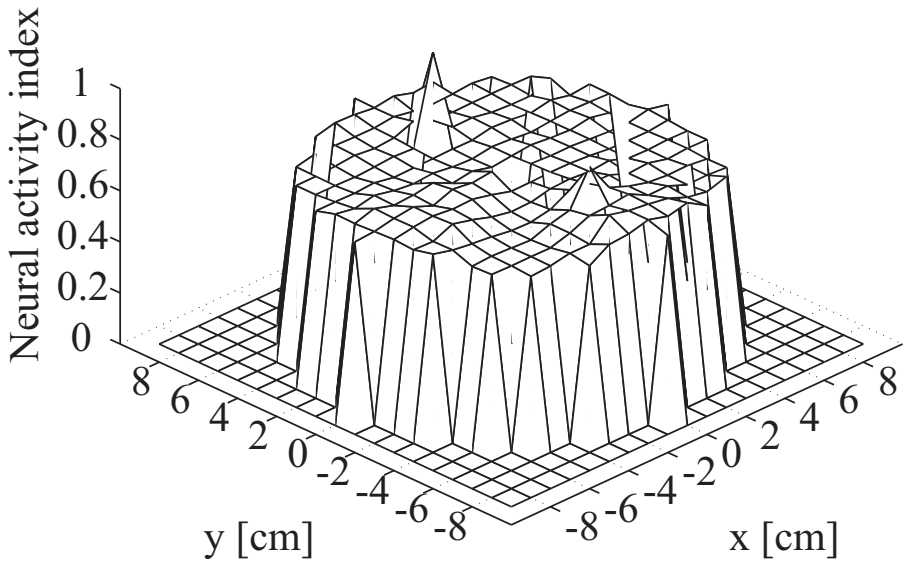

(a)

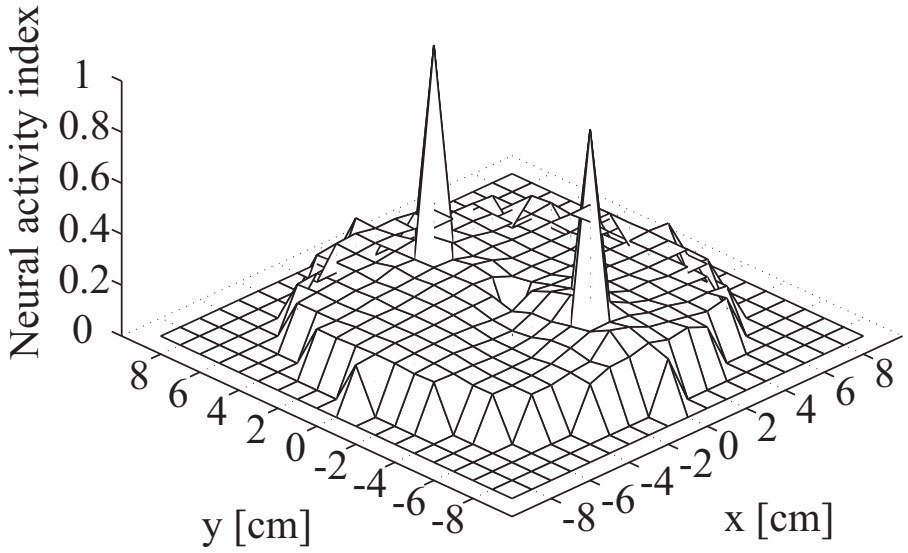

(b)

Figure 3.40: Estimation results with the LCMV beamformer: the neural activity indexes on plane $z = 0$ are shown for two cases where the activities of two dipoles at $(x, y, z) = (0, -4, 0)$ and $(0, 4, 0)$ are correlated (a) perfectly and (b) partially.

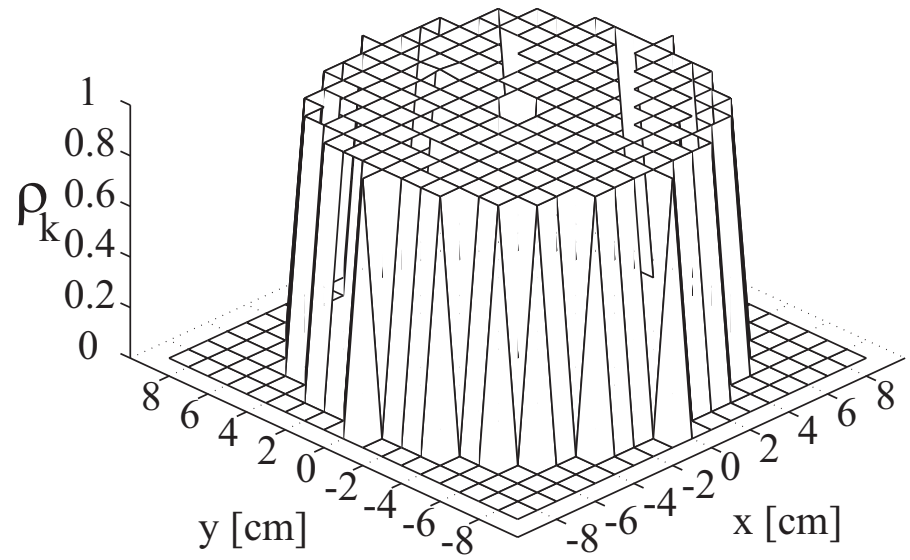

(a)

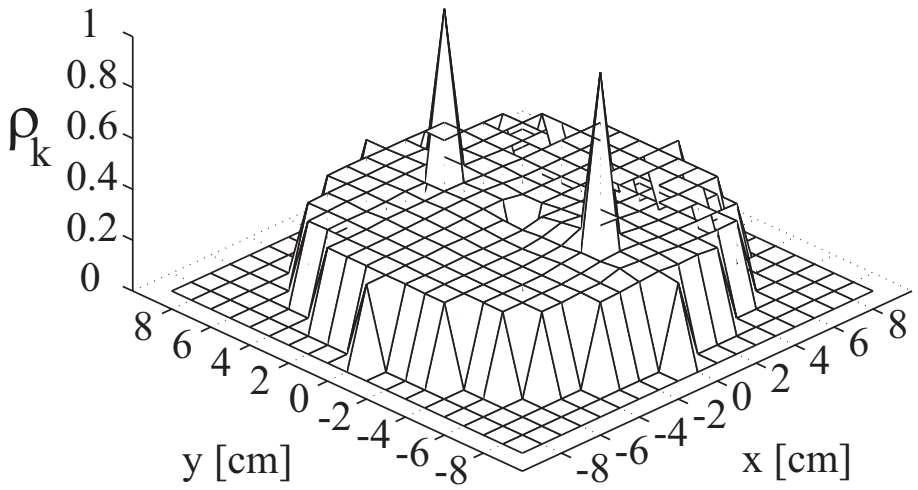

(b)

Figure 3.41: Estimation results with the SAM beamformer: $\rho_k = \text{argmax}_\phi \; S_k^2(\phi)/\sigma_k^2(\phi)$ on plane $z = 0$ are shown for two cases where the activities of two dipoles at $(x, y, z) = (0, -4, 0)$ and $(0, 4, 0)$ are correlated (a) perfectly and (b) partially.

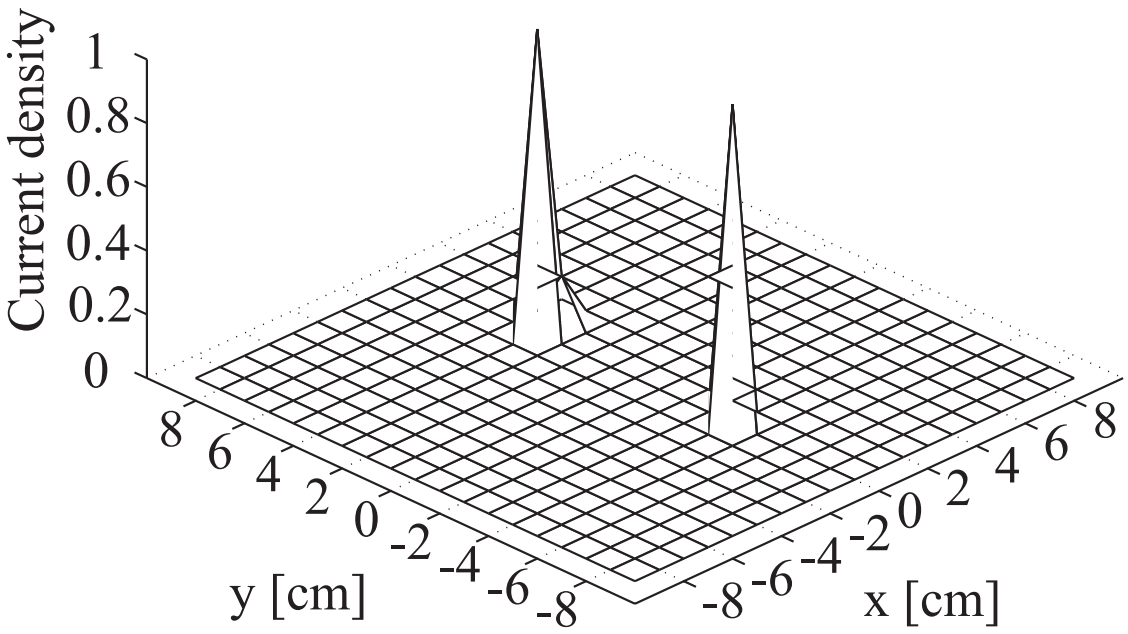

Figure 3.42: Current density distribution estimated in case (a) by the proposed SFR

3.3.6 Impact of combination of FA-processed Kalman filter and SFR

The SFR after the FA-processed Kalman filtering is considered through the following numerical experiment.

The dipole was assumed at the location $(x, y, z) = (0, 0, 1)$ and the orientation was $(x, y, z) = (1, 0, 0)$. The location and the orientation did not make much difference in the result of the following numerical experiment. The time series of the dipole activity was given similarly to the numerical experiment in Section 3.1.1. The SNR of the pre- and post-Kalman filtering were investigated. The SNR of pre-Kalman filtering was defined as $\|L\boldsymbol{Q}\|^2/\|\boldsymbol{\varepsilon}\|^2$ at the latency t_{max} with the maximum of the MEG signals, and noises with same level at t_{max} were added to each temporal slice of the MEG signals. The noise $\hat{\boldsymbol{\varepsilon}}$ included in the estimated MEG signals $\hat{\boldsymbol{m}}$ at t_{max} was calculated as $\hat{\boldsymbol{\varepsilon}} = \hat{\boldsymbol{m}} - (\hat{\boldsymbol{m}}^T\bar{\boldsymbol{m}}_{true})\bar{\boldsymbol{m}}_{true}$ where $\bar{\boldsymbol{m}}_{true} = L\boldsymbol{Q}/\|L\boldsymbol{Q}\|$ at t_{max}, that is to say, the component orthogonal to the noiseless MEG signals which affects the estimation with the SFR. The SNR of post-Kalman filter was defined as $\|\hat{\boldsymbol{m}} - \hat{\boldsymbol{\varepsilon}}\|^2/\|\hat{\boldsymbol{\varepsilon}}\|^2$. A hundred trials of the FA-processed Kalman filtering were conducted for each SNR, and Figure 3.43 shows the average SNRs obtained after the Kalman filtering.

The result indicates that the SNR was improved and became ten times larger than the SNR of the post-Kalman filter. As referred in the discussion in Section 3.1.5., the SNR of typical raw MEG data can be estimated as approximately 10^{-1}, assuming that averaging over about 10^2 trials offers a 90 % GOF in a conventional estimation. Therefore, after FA-processed Kalman filtering, it is expected that the SNR of the MEG data increase to the order of 10^0. The result shown in Fig.3.36 indicates that the SFR may estimate the true dipole location with the probability around 85 %.

The possibility that the combination of the FA-processed Kalman filter and the SFR estimates the current dipole on the correct location from raw MEG data was indicated through the numerical experiment in this section. At least, it is verified

that the robust estimation is available by the combination in MEG analysis with low SNR.

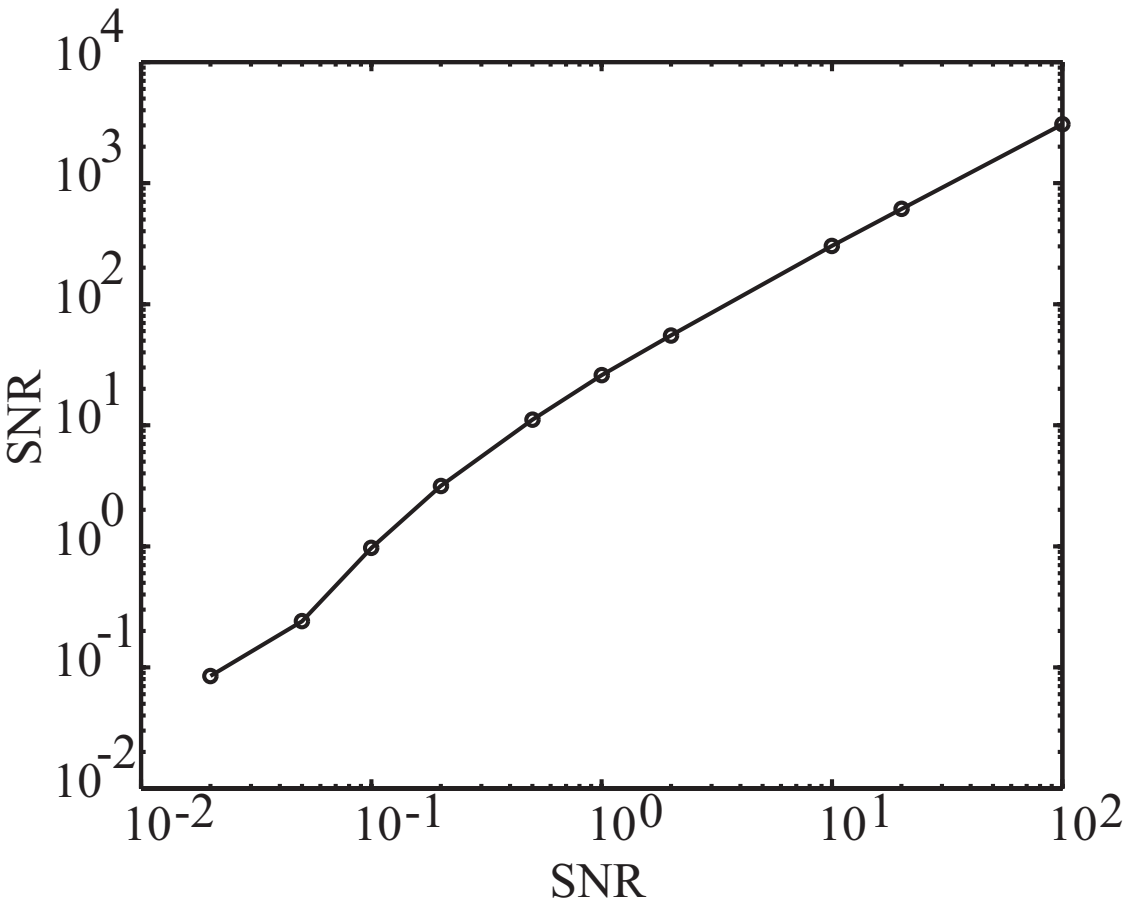

Figure 3.43: SNRs of pre- and post FA-processed Kalman filter: the SNRs are averaged across 100 trials. The location of the single dipole was $(x, y, z) = (1, 0, 0)$.

3.3.7 Discussion

The main advantage of the spatial filtered reconstruction (SFR) is the powerful localization with the objective criterion, the C_p statistic. In the numerical experiments in this section, the current density distribution was well reconstructed by the SFR. The spatial filter improves the localization with the fourth order cumulants. In cases where the true dipole distribution is not so complex, the estimation only with the proposed spatial filter identifies the locations of the dipoles clearly. Besides, the spatial filtering easy-to-use, and it can be prepared in advance of the analysis.

However, the redundant dipole activities are not able to be ignored in the estimation of the complex current distribution. The effect of the modification is not standardized for each spatial filter: the localization of the current distribution depends on the cases. To resolve the issue, the C_p statistic can be a reliable criterion for localization of the current distribution. The reconstruction with the multiple linear regression effectively supports the spatial filter, especially in noisy MEG analyses. It modifies the error in position of the dipole estimated by the spatial filter, and offers higher possibility of the successful estimation of the brain activity from raw data, combined with the FA-processed Kalman filter. It will be discussed in the next section.

The SFR implemented without temporal information shows the effect which is different from that of the conventional spatial filters such as the SAM and the LCMV beamformer using temporal information as shown in Section 3.3.5. It is another important advantage of the SFR.

Chapter 4

Real MEG data analysis

4.1 Experimental conditions

Analyses with the FA-processed Kalman filter, ICA and the SFR were applied to real MEG data. The current distribution was estimated from averaged AEF data in which the noises were reduced sufficiently. The combination of the FA-processed Kalman filter, ICA and the SFR processed the simulated raw AEF data consisted of real MEG noises and simulated AEF. The proposed combination was employed for real AEF data analyses, such as unaveraged single trial AEF data.

AEF data were acquired with using 230 gradiometers of whole-head MEG system (Yokogawa, Japan). A subject was 27-year-old male. 1000Hz tone bursts with the duration of 100 ms were presented to both ears simultaneously. The sampling rate was 1000 Hz, and a data set of the trial had its length of 1000 ms, 500ms for pre- and post-stimulus terms each. The data were filtered online to a bandwidth of 0.03 to 200Hz.

4.2 SFR in AEF analysis

The current density distribution was estimated with the SFR for the averaged AEF data. The AEF data were averaged over 169 trials, and processed with the off-line low pass filter whose cut-off frequency was 40 Hz (Fig.4.1). The MEG signals have

the peak at the latency of 100 ms, which is called N1m and characterizes typical AEF [80], [81].

In this analysis, the conductor was assumed as a homogeneous sphere with a radius of 8.1 cm, and the dipoles were estimated on $N = 2204$ discrete points with the intervals of 1 cm as in Section 3.2.1. The location of the sensors and the conductor are shown in Fig.4.2. The sensor index numbers are described in Fig.4.8. The estimation by the SFR was conducted for the MEG data at the latency of 85 ms. The initial number of the dipoles in the reconstruction was prescribed as 10.

As a result, the four dipole were estimated as shown in Fig.4.3. Figures 4.4, 4.5 and 4.6 show the dipole locations superimposed to the MR image. The estimation with the SFR successfully indicated the bilateral activities in the brain, around the auditory cortexes.

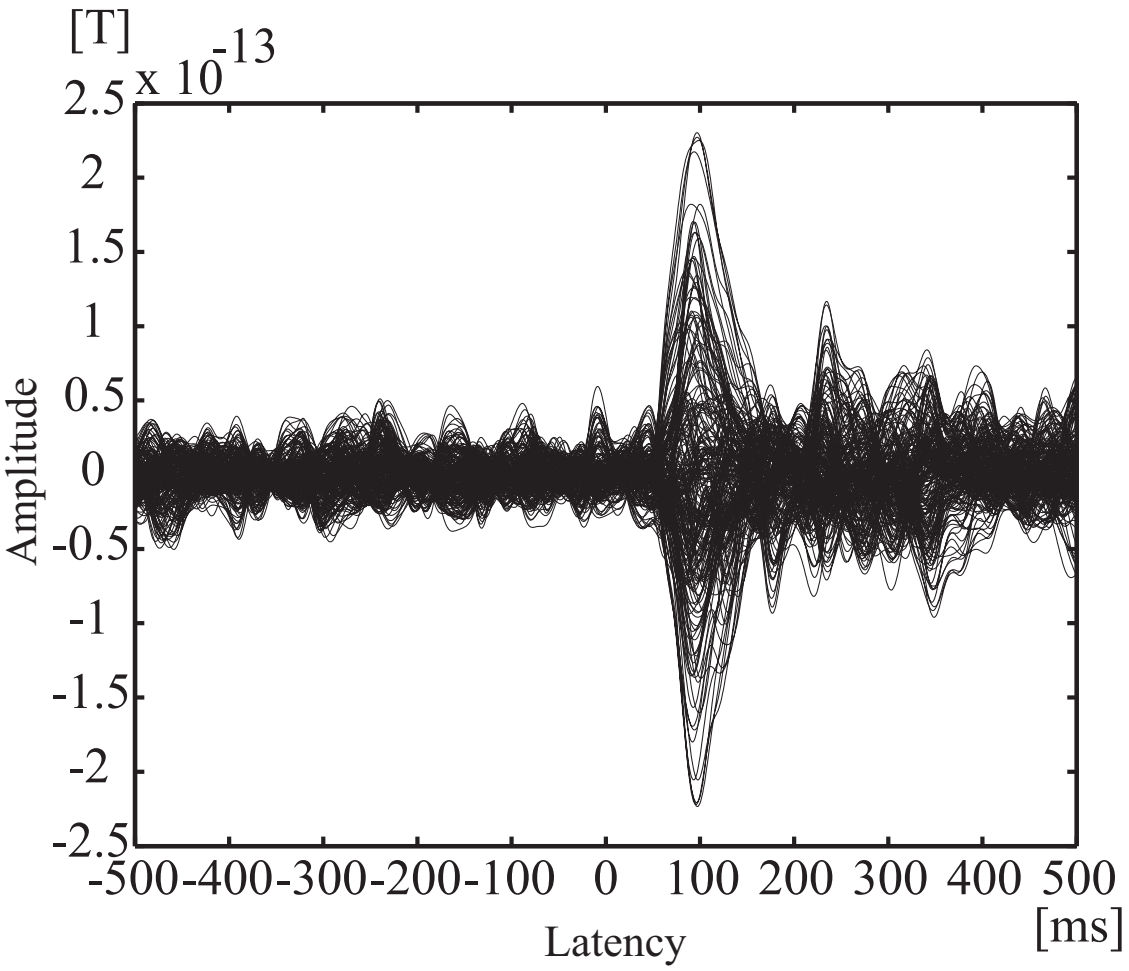

Figure 4.1: AEF signals averaged across 169 trials

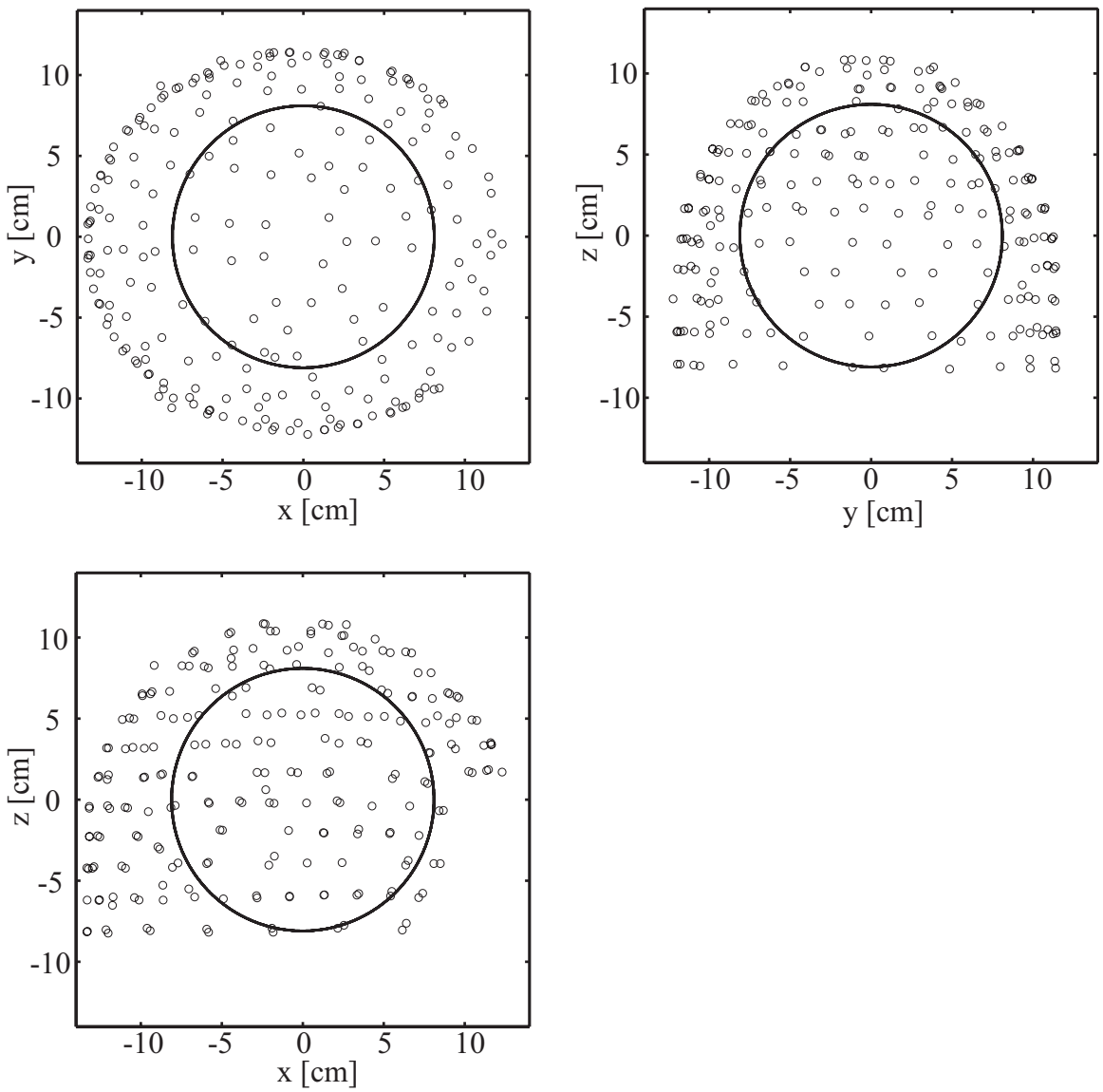

Figure 4.2: Locations of the sensors and the conductor: ◯ show 230 sensor positions

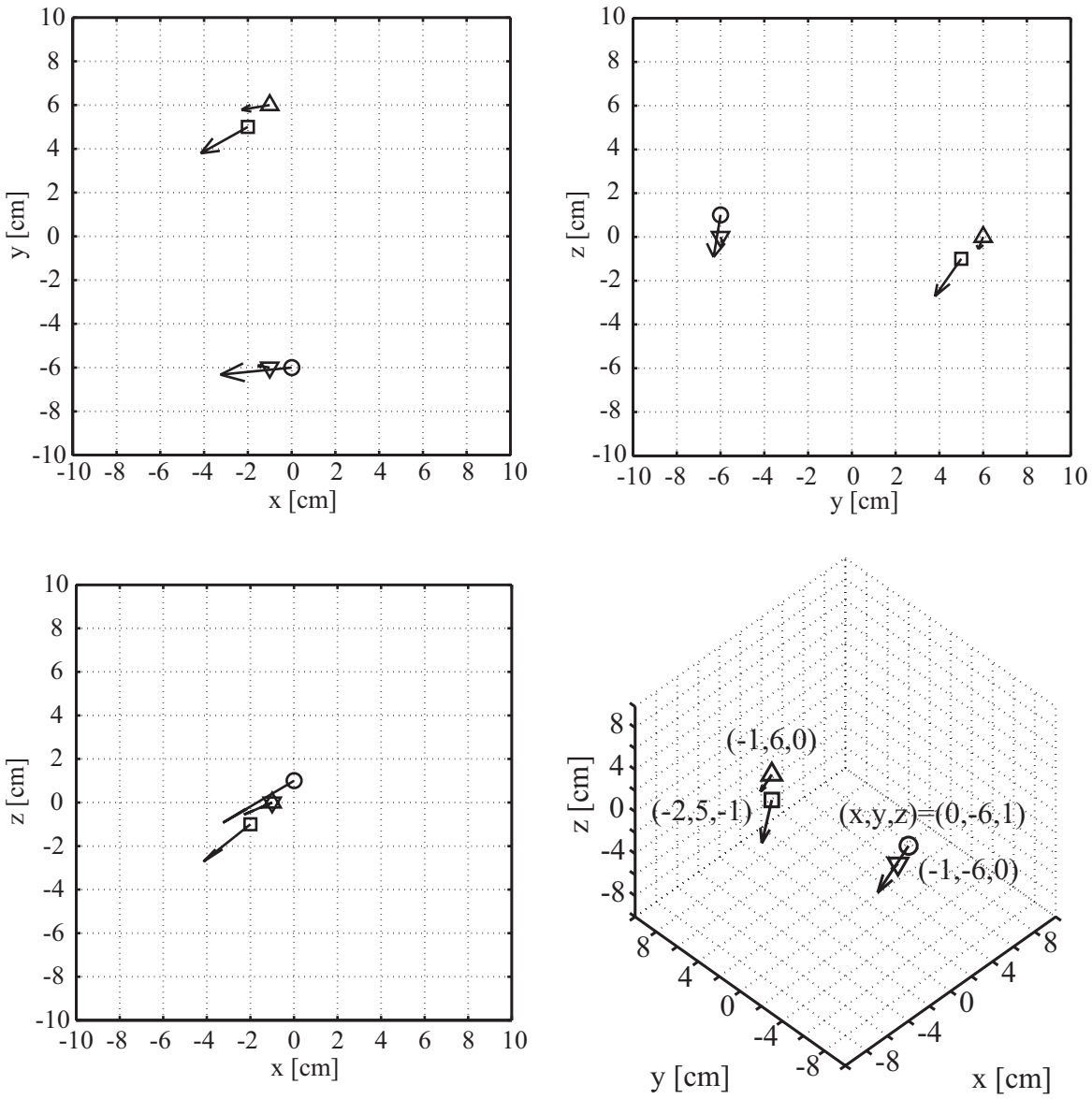

Figure 4.3: Current dipoles reconstructed from the averaged AEF data by the SFR

Figure 4.4: Locations of the dipoles in the MR image estimated from the averaged AEF data by the SFR (axial)

Figure 4.5: Locations of the dipoles in the MR image estimated from the averaged AEF data by the SFR (cornal)

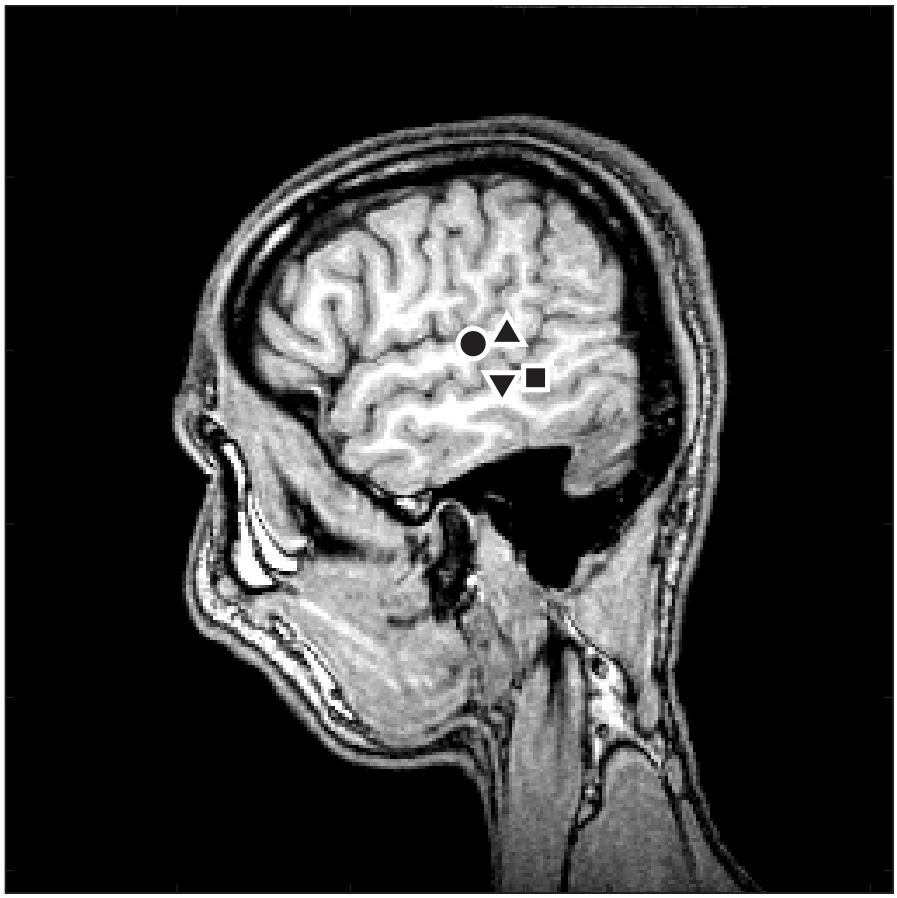

Figure 4.6: Locations of the dipoles in the MR image estimated from the averaged AEF data by the SFR (sagittal)

4.3 Combination of FA-processed Kalman filter, ICA and SFR in AEF analysis

With the combination of the FA-processed Kalman filter, ICA and the SFR, the author attempted to appraise the activities in the brain from the AEF data averaged across the lower number of the trials than usual, and single-trial unaveraged AEF data. The result of processing the simulated AEF data in the following Section 4.3.1 will support the latter real AEF data analyses.

In the estimation introduces in the following sections, the SFR was conducted with the assumptions that the conductor was a homogeneous sphere with a radius of 8.1 cm and discretized with the same manner as in Section 4.3. The region for the estimation of the current dipole distribution was restricted with in $\Omega = \{\boldsymbol{r} = (x, y, z) \mid 4 < \|\boldsymbol{r}\| \leq 8.1, z > -4\}$. The locations of the sensors and the region for the estimation are shown in Fig.4.7. The sensors are numbered as shown in Fig.4.8.

4.3.1 Simulated AEF data analysis

Unaveraged AEF data were simulated with the phantom dipoles located at $(x, y, z) = (-2, 5, -1)$ and $(0, -6, 1)$ in which the larger dipoles were estimated in the averaged AEF analysis in the previous section. The dipole orientations were set as $(x, y, z) = (-0.87, -0.33, 0.067)$ and $(-1.00, 0, 0)$, and the amplitude was adjusted to produce the simulated AEF data with the maximum amplitude of 250 fT, similarly to the dipoles reconstructed by the SFR in Section 4.2. The simulated noise-free AEF data are shown in Fig.4.9. The real MEG noises were added to the simulated AEF data. The data in the pre-stimulus terms in the experiment (see Section 4.1) were utilized for the noises which consisted of the real sensor noises and may include artifacts. The data includes the simulated AEF and the real MEG noises are termed as the simulated raw AEF data (Fig.4.10). The SNR for each sensor is shown in Fig.4.11. The maximum SNR was -6.1 dB.

The factor analysis was conducted to estimate the covariance matrices for the

Kalman filter. In the FA step, the number of the common factors was determined from referring to the variation of the error between the estimated and observed covariances, Eq(2.22) namely. While the number of the common factors was 10 or more, the estimation errors were adequately minimized less than 1 % in Fig.4.12. This indicates that the model with 10 common factors explained the observation covariance sufficiently. With more than 30 common factors, the variation of the error converged. And hence the noise covariances estimated with 40 common factors were adopted. The FA-processed Kalman filtering was implemented with the estimated noise covariances. The sensor noises were effectively eliminated by the FA-processed Kalman filter as shown in Fig.4.13.

In the ICA step, 30 PCs contributed a 99.8 % to the total value in the Kalman filtered data covariance. The result of the noise reduction with the FA-processed Kalman filter was successful. The number of the PCs was able to be significantly reduced. The ICA step needed fewer ICs after the proposed noise reduction. 30 ICs were estimated with the FastICA. One of the estimated ICs shown in Fig.4.14 has its peak around 100 ms, and it can be interpreted as a component originated from the simulated AEF data, the simulated typical N1m. The current dipole estimation was conducted for the extracted IC.

The current dipoles reconstructed by the SFR are shown in Fig.4.15. The initial number of the dipoles was prescribed as 10, and 6 dipoles were estimated. Although there exsit some redundant dipoles that may be caused by the artifacts ICA could not separate, we can find the dipoles estimated at the true locations. In this case, the estimation error rate, i.e. $\|\boldsymbol{m}_{est} - \boldsymbol{m}_{obs}\|^2/\|\boldsymbol{m}_{obs}\|^2$ with the MEG data $\boldsymbol{m}_{est}$ caluculated with the estimated dipoles and observation $\boldsymbol{m}_{obs}$, was 0.1727. When the initial number of the dipoles was prescribed as 3, 3 dipoles were survived the elimination. As shown in Fig.4.16, the redundant dipoles were removed. The error rate remained small. The orientations of the dipoles were well reconstructed. This simulation shows that the FA-processed Kalman filter reduces noises in real MEG data, ICA can extract the signal components due to the dipoles of interest, and the SFR can reconstruct the dipoles.

The estimation only with the SFR and the combinations of the SFR and each of the noise reductions, an ideal band-pass filter with a bandwidth of 1-40 Hz (1-40Hz BPF), the FastICA, the 1-40Hz BPF and FastICA, and the FA-processed Kalman filter without ICA, were investigated. The processed signals and the estimated current distribution are shown in Figs.4.17-4.21. In those cases, the current dipole at the location of $(x, y, z) = (-2, 5, -1)$, which had been set deeply in the spherical conductor and farther from the sensor array, was not estimated by the SFR, even though the independent components with the peak at the latency of 100 ms were extracted in the reconstructions accompanying ICA. The error rates were quite large. In this numerical experiment, the combination of the FA-processed Kalman filter supported well the successive ICA. The importance of the sensor noise reduction was confirmed. The SFR was able to pick up the dipole with the lower SNR component after the proposed noise reduction. The proposed combination was the most robust method in this case.

The estimation with the combination of the SFR, the FA-processed Kalman filter and ICA was applied for the analysis of the simulated AEF data averaged over 10 trials. The conditions of the analysis were set similarly in the previous experiment. The averaged data and the SNRs are shown in Fig.4.23. The maximum SNR was 2.56 dB. The FA-processed Kalman filtered data and the IC extracted after Kalman filtering are illustrated in Fig.4.23. The proposed combination succeeded in the localization of the dipoles as shown in Fig.4.24. Without any noise reduction, the SFR estimated the dipoles in the true positions (Fig.4.25). This result shows the robustness of the SFR to the noise. The combinations of the SFR and the other noise reductions reconstructed the dipoles in the locations of the true dipoles. The processed signals and the reconstructed dipole distribution with each combination are shown in Figs.4.26-4.29.

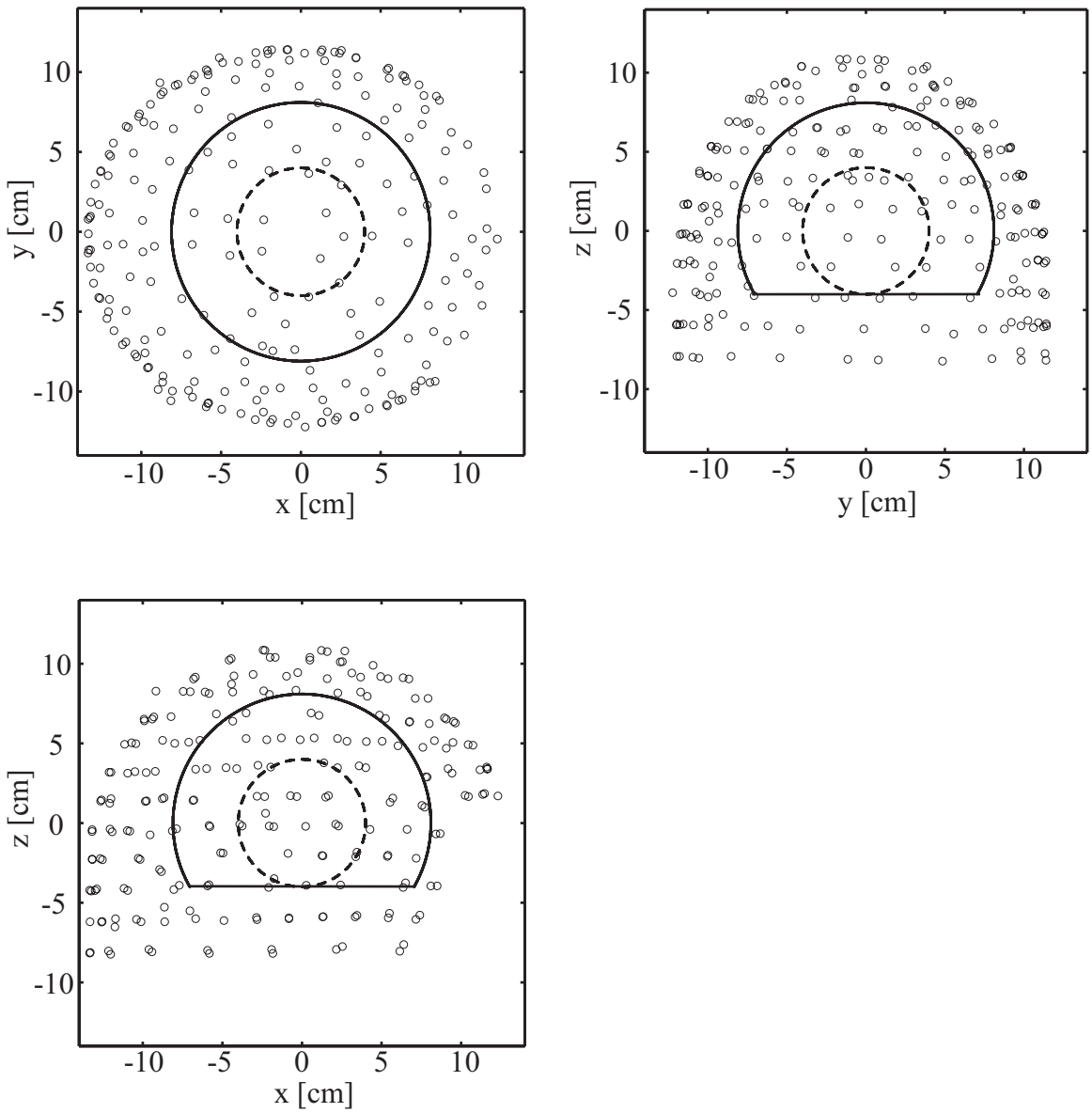

Figure 4.7: Locations of the sensors and the conductor. The region where the current distribution was estimated was bounded by the solid and broken lines.

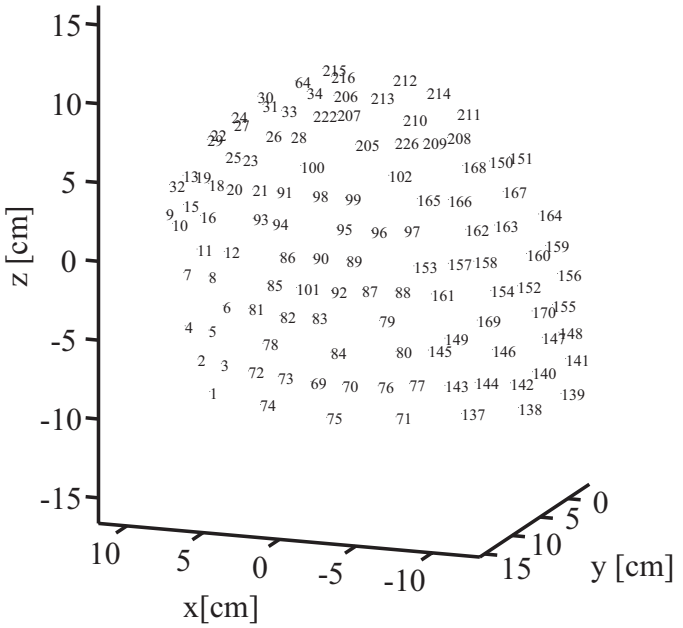

(a)

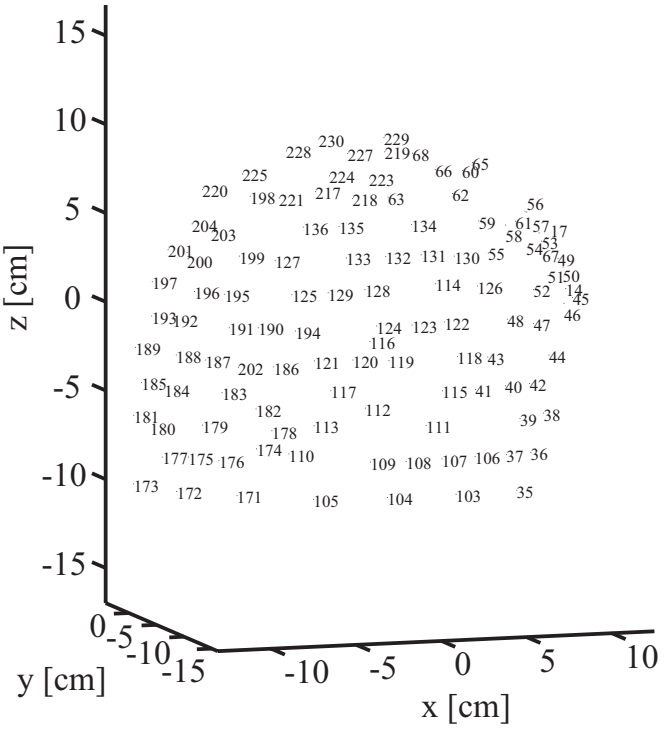

(b)

Figure 4.8: Locations and numbers for 230 sensors: the sensor numbers are shown in the regions with (a) $y \geq 0$ and (b) $y \leq 0$.

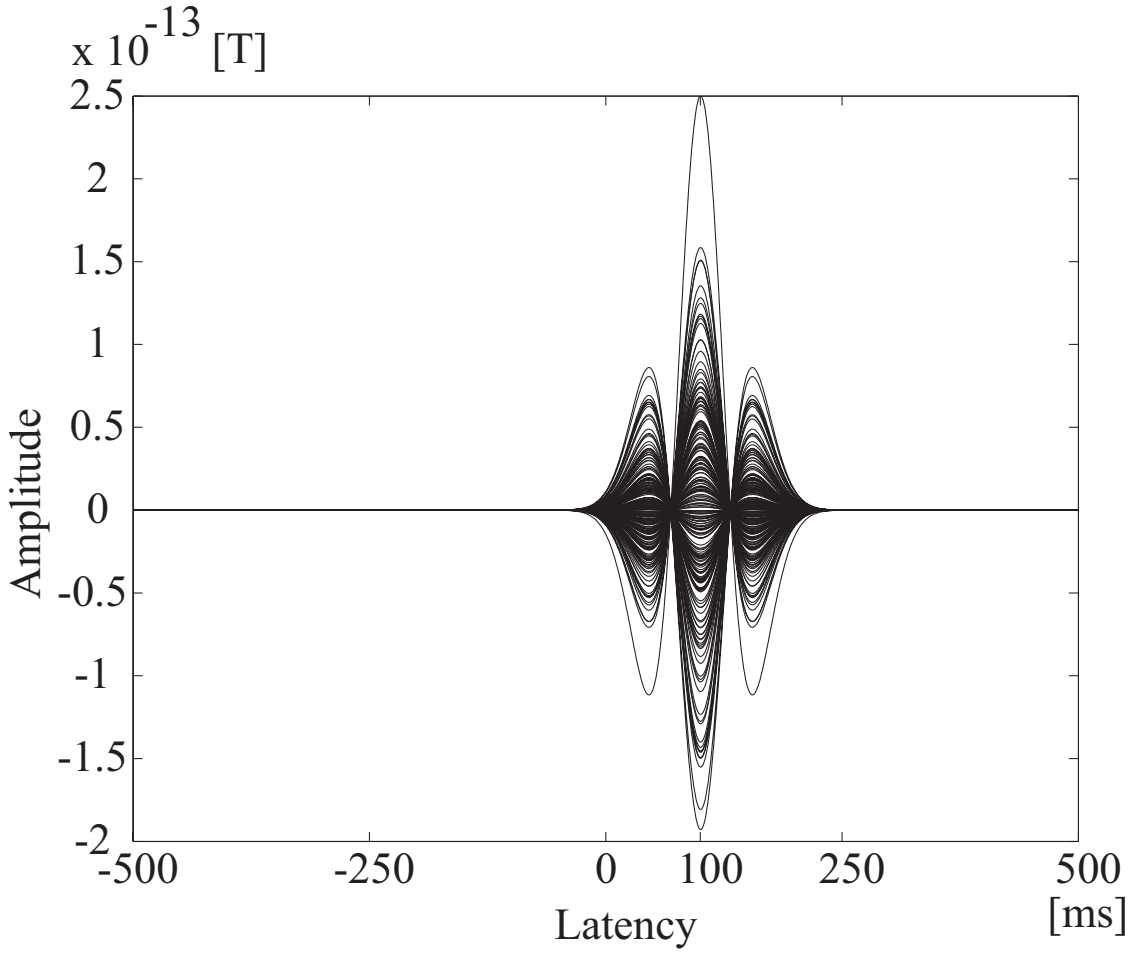

Figure 4.9: Simulated noise-free AEF data. The signals were originated from the dipoles on $(x, y, z) = (-2, 5, -1)$ and $(-1, -6, 0)$

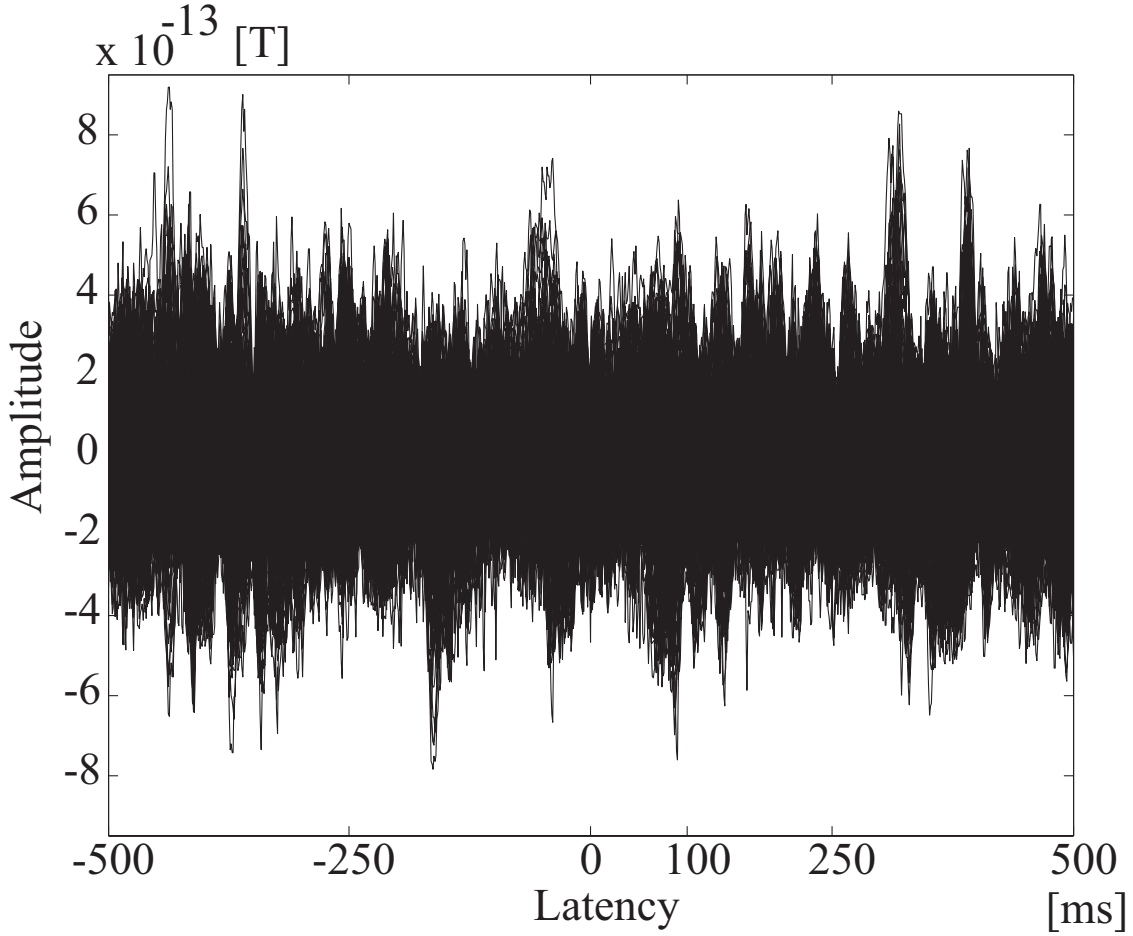

Figure 4.10: The simulated raw AEF data including real MEG noises and the simulated AEF data

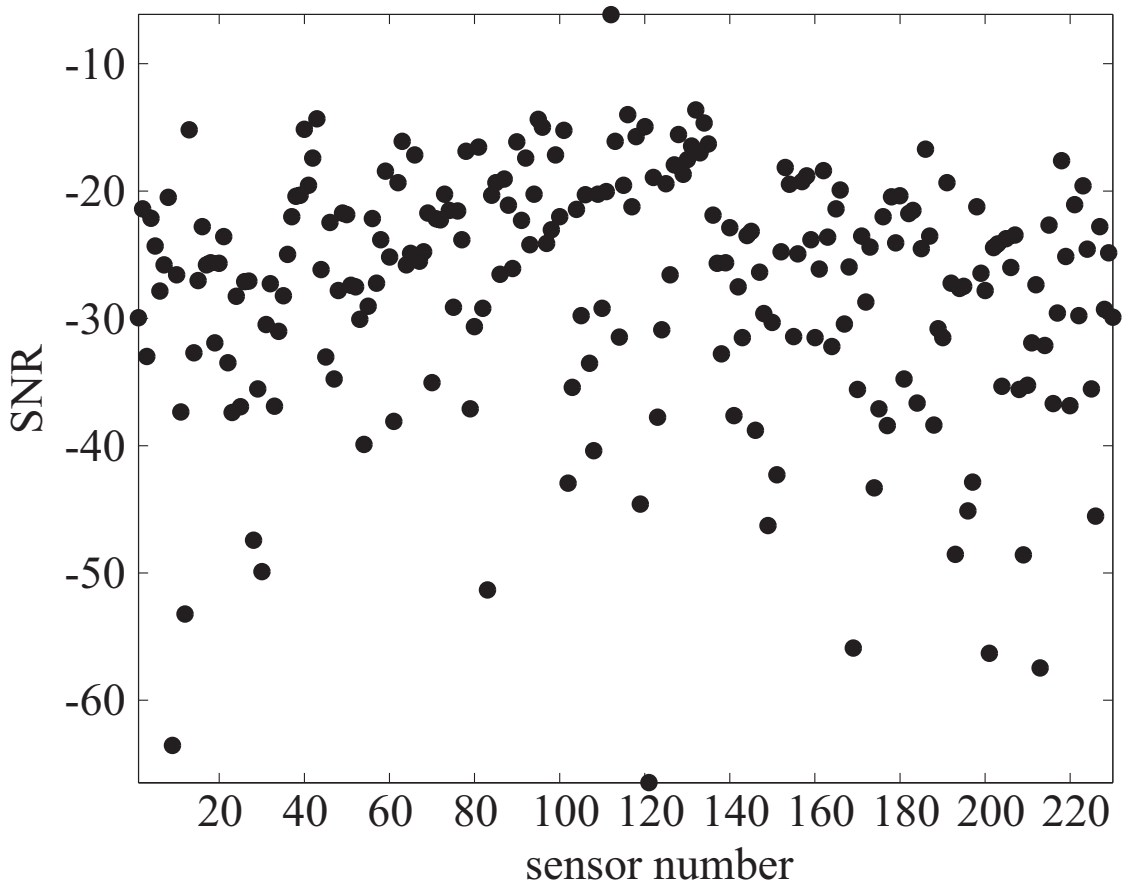

Figure 4.11: SNR of each sensor for the simulated raw AEF analysis (see Fig.4.8)

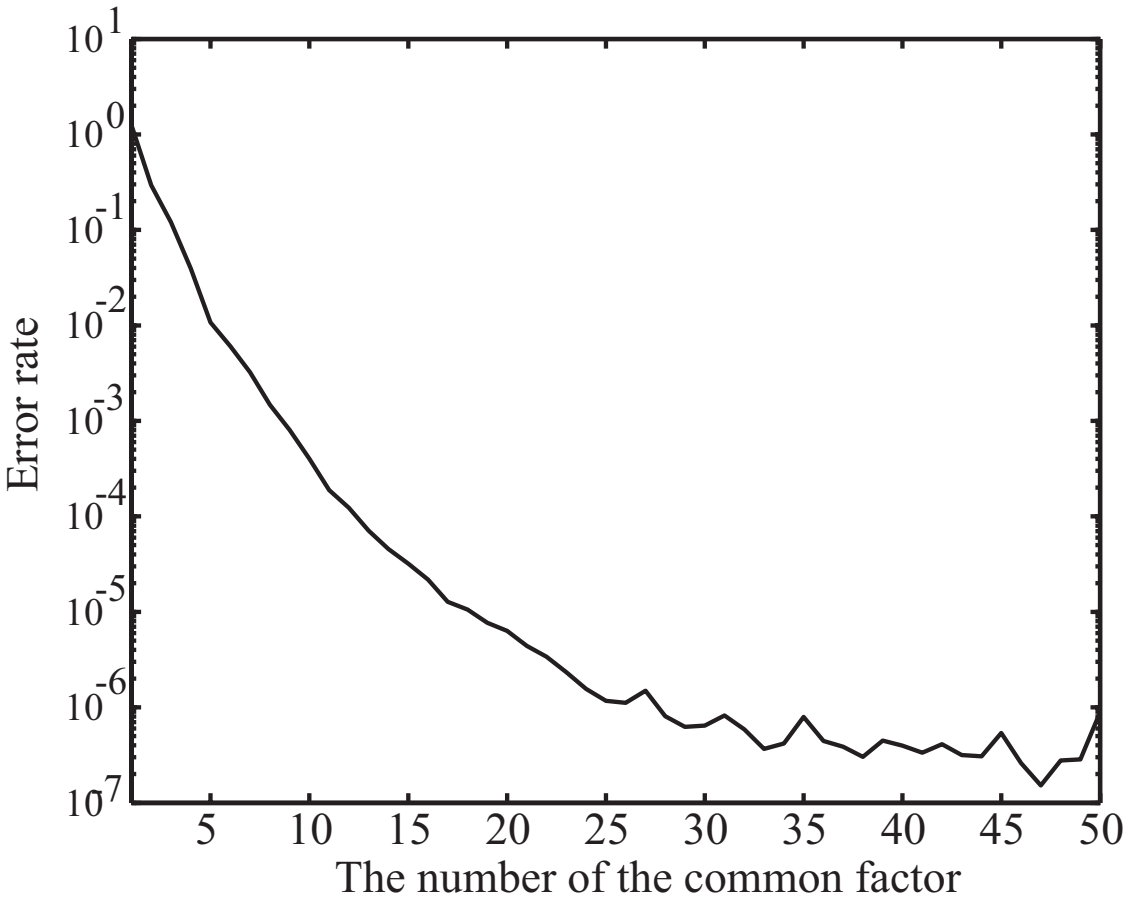

Figure 4.12: Error ratio of the covariance estimated by factor analysis. The error ratio is defined as $\|\Sigma - S\|^2/\|S\|^2$ where $\Sigma = \Lambda\Lambda^T + W$

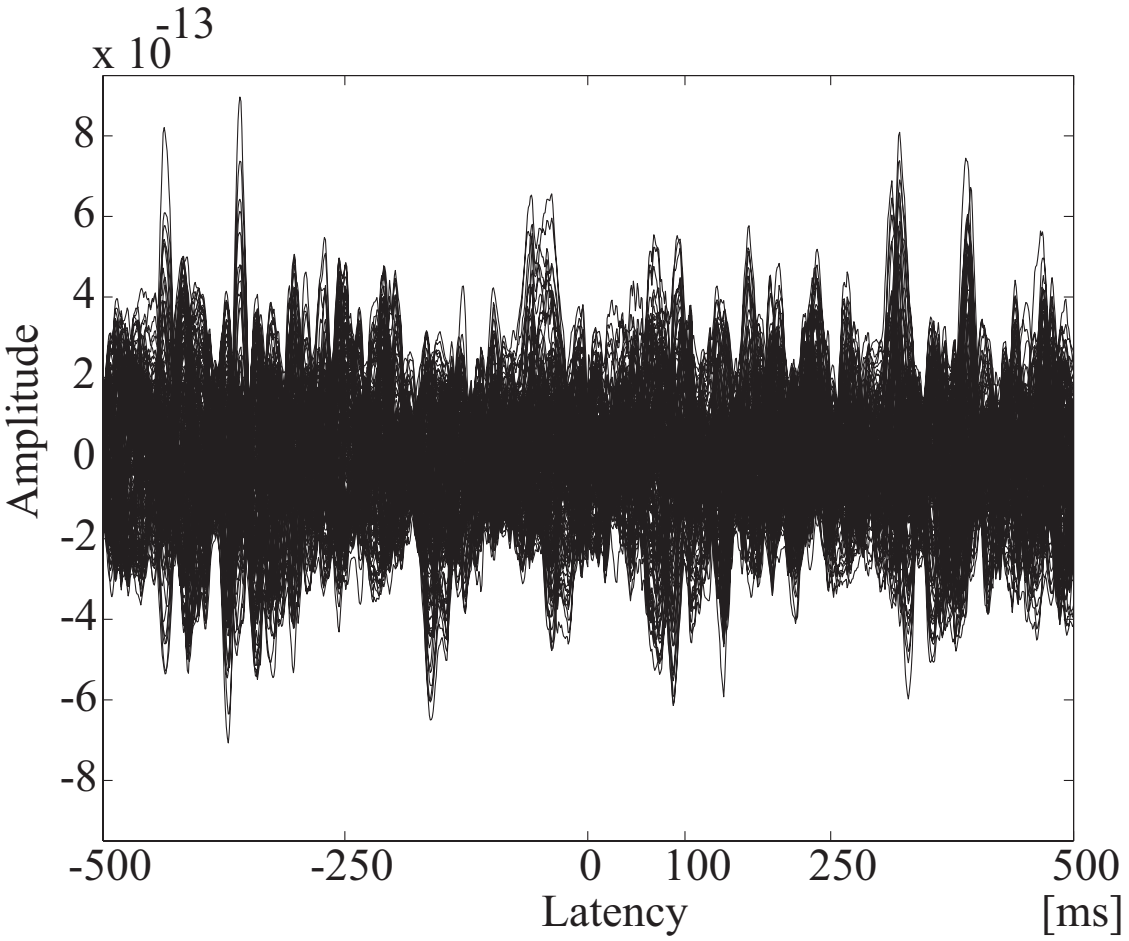

Figure 4.13: FA-processed Kalman filtered 230 signals in the simulated raw AEF data analysis

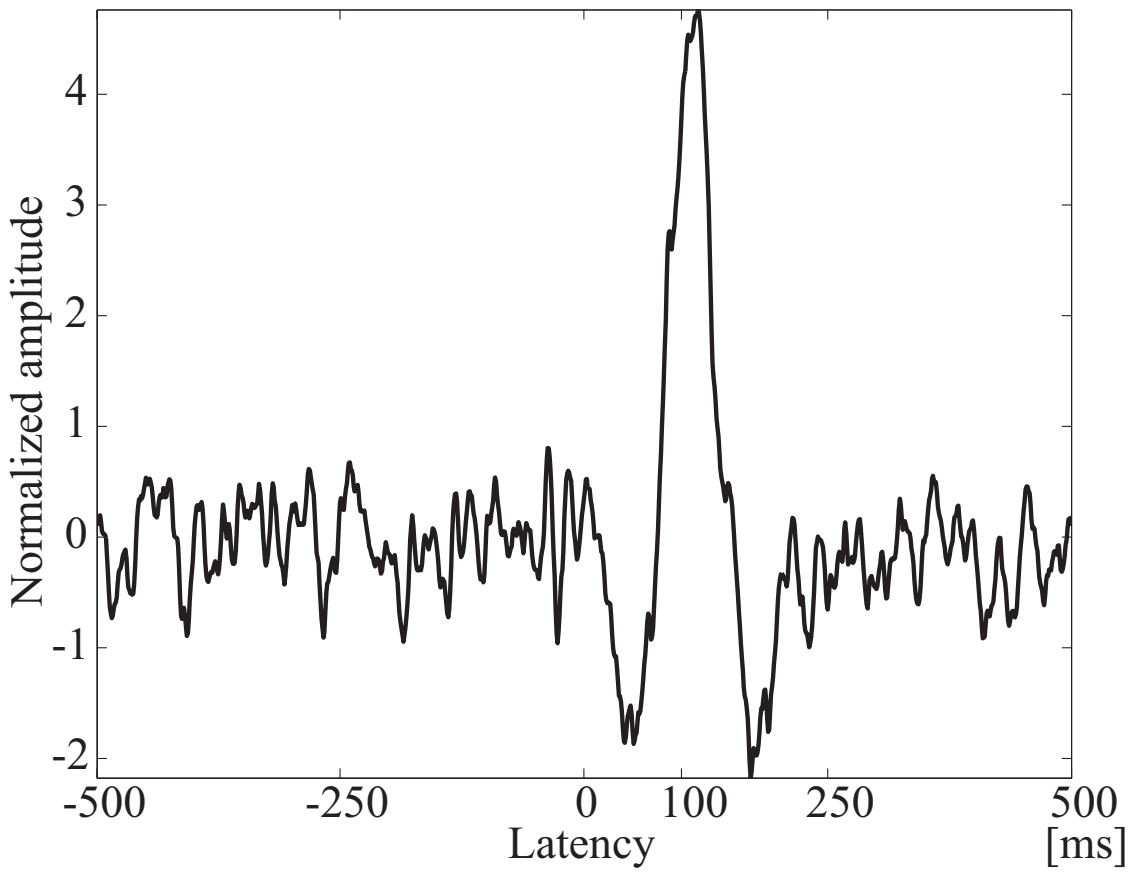

Figure 4.14: One of the independent components estimated by the FastICA following the FA-processed Kalman filter

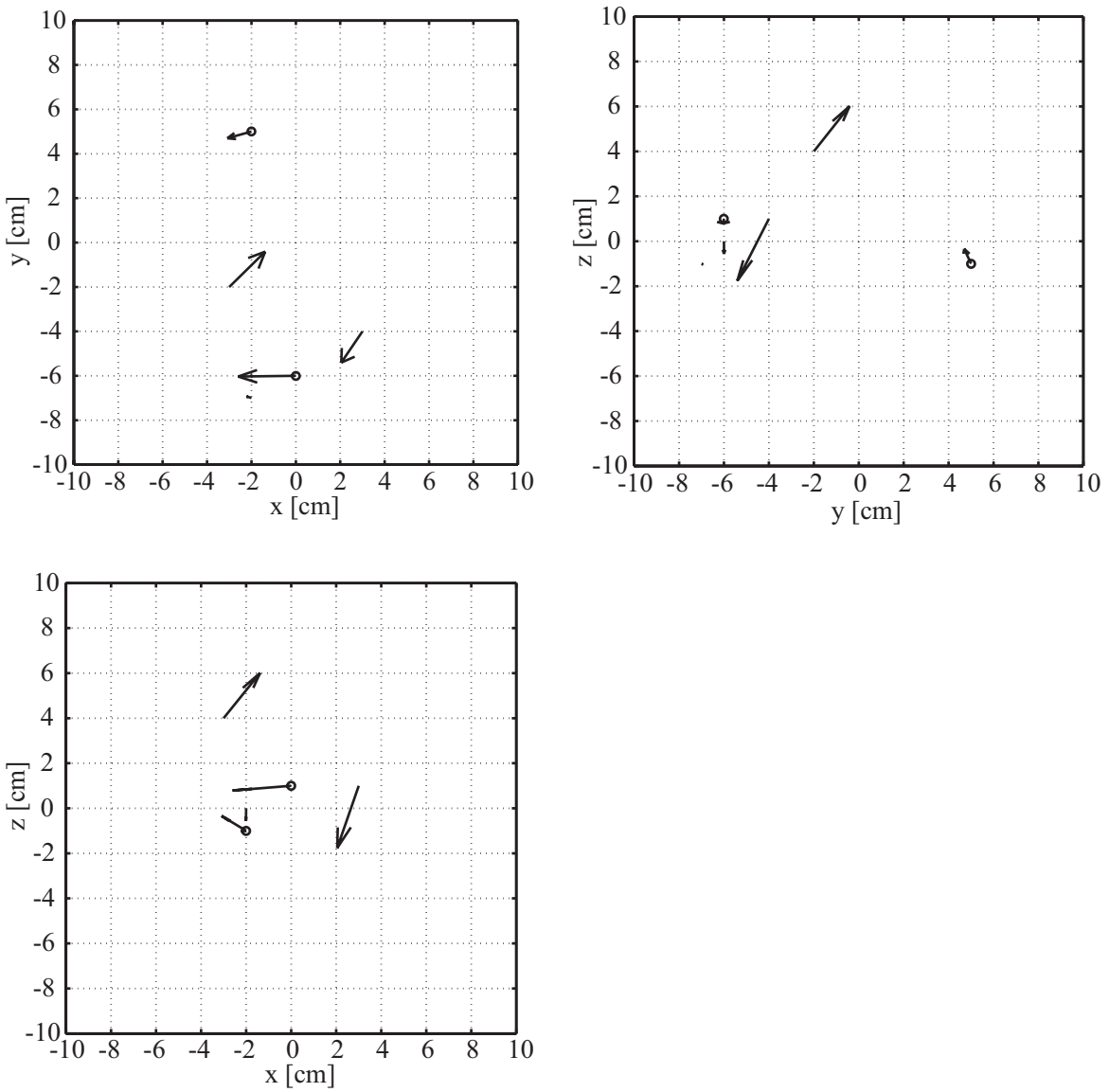

Figure 4.15: Dipoles reconstructed by the combination of the FA-processed Kalman filter, the FastICA and the SFR in the simulated raw AEF data analysis: ∘ represents the true dipole locations. The initial number of the dipoles was prescribed as 10 in the proposed reconstruction, and the 6 dipoles were estimated. The error rate was 0.173.

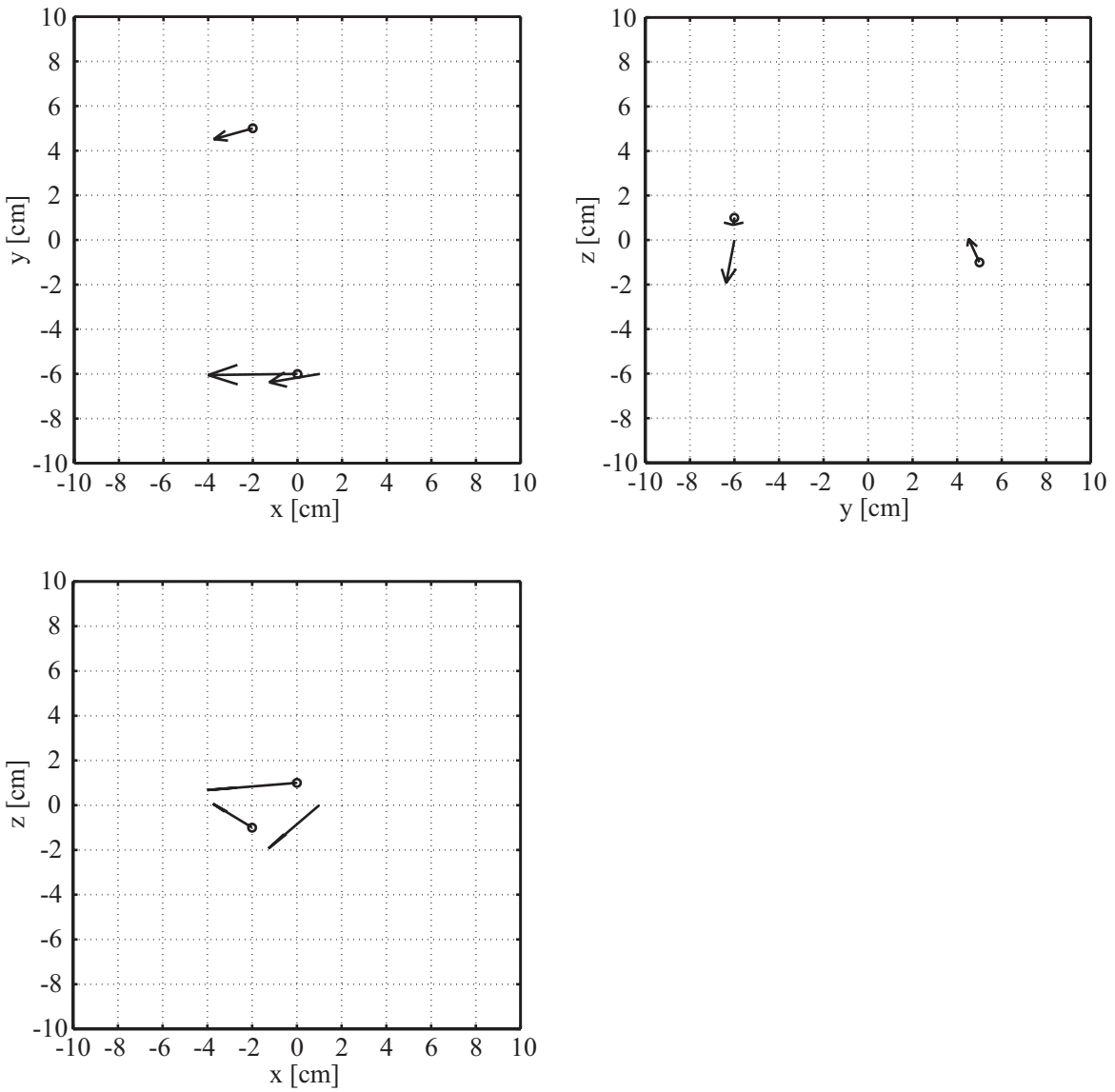

Figure 4.16: Dipoles reconstructed by the combination of the FA-processed Kalman filter, the FastICA and the SFR in the simulated raw AEF data analysis: ∘ represents the true dipole locations. The initial number of the dipoles was prescribed as 3 in the proposed reconstruction, and the 3 dipoles were estimated. The error rate was 0.332.

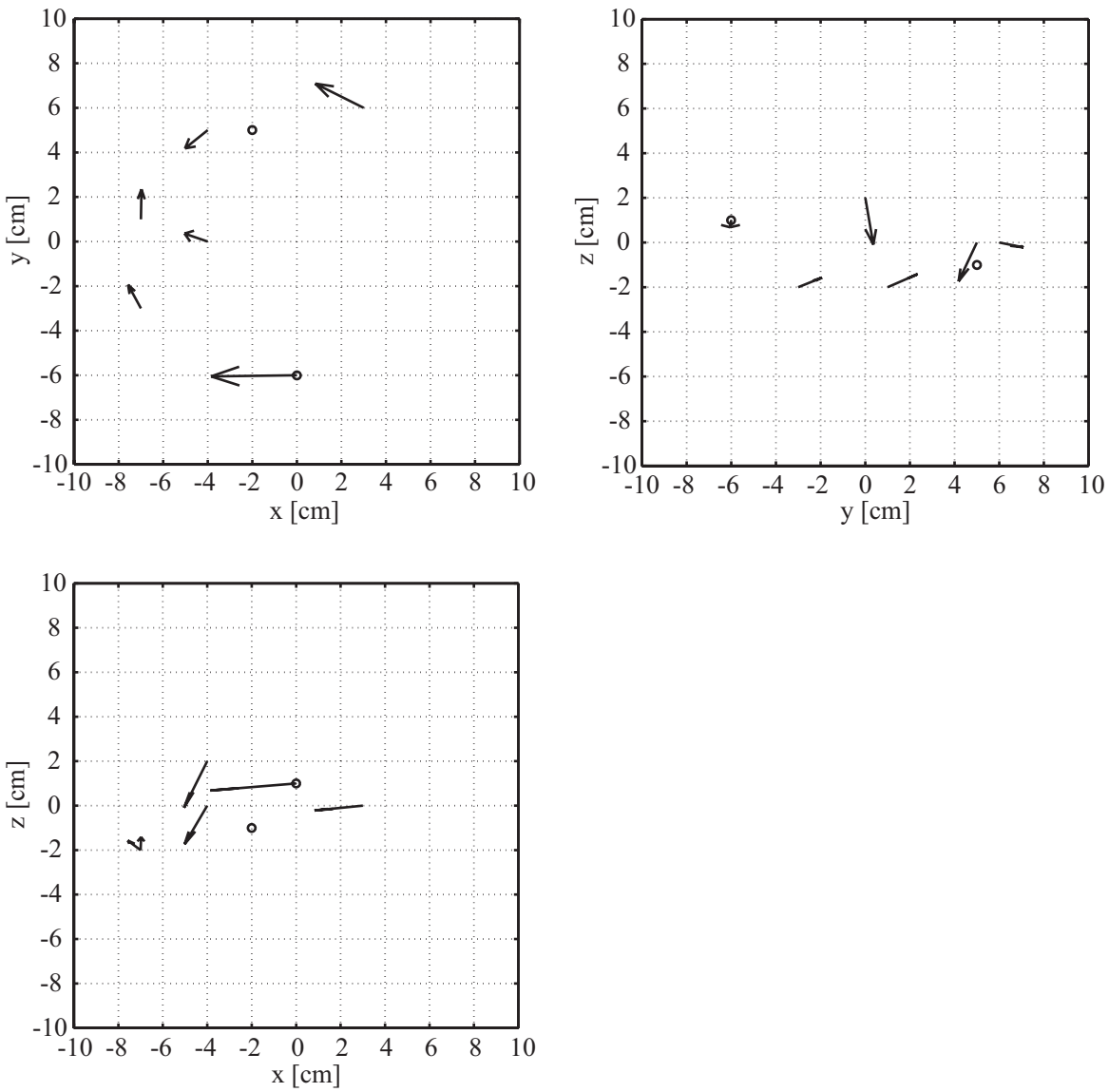

Figure 4.17: Dipoles reconstructed only by the SFR in the simulated raw AEF data analysis: ∘ represents the true dipole locations. The initial number of the dipoles was prescribed as 10 in the proposed reconstruction, and the 6 dipoles were estimated. The error rate was 0.702.

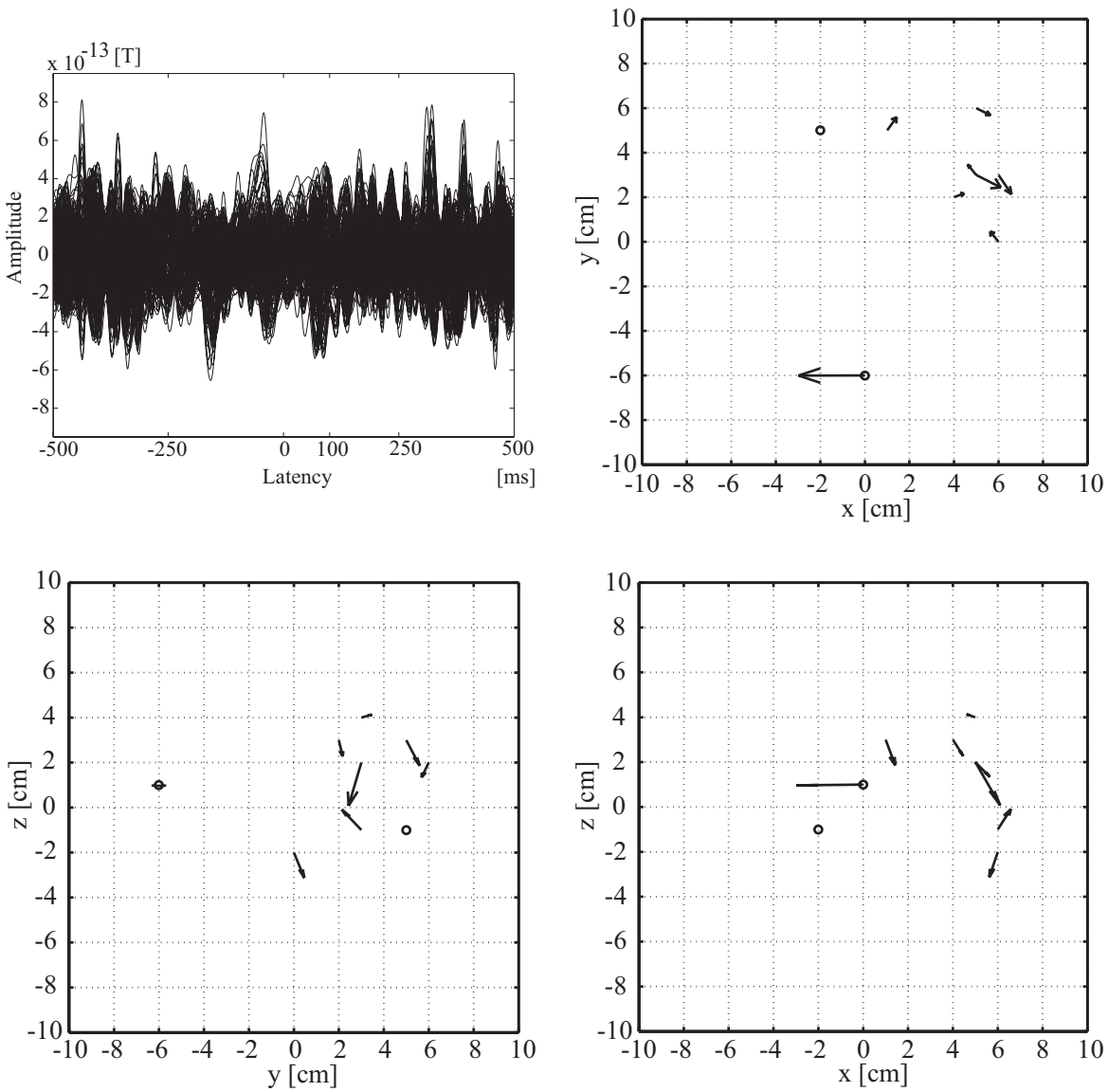

Figure 4.18: Band-pass filtered signals (upper left) and dipoles reconstructed by the combination of the 1-40Hz BPF and the SFR in the simulated raw AEF data analysis: ∘ represents the true dipole locations. The initial number of the dipoles was prescribed as 10 in the proposed reconstruction, and the 8 dipoles were estimated. The error rate was 0.607.

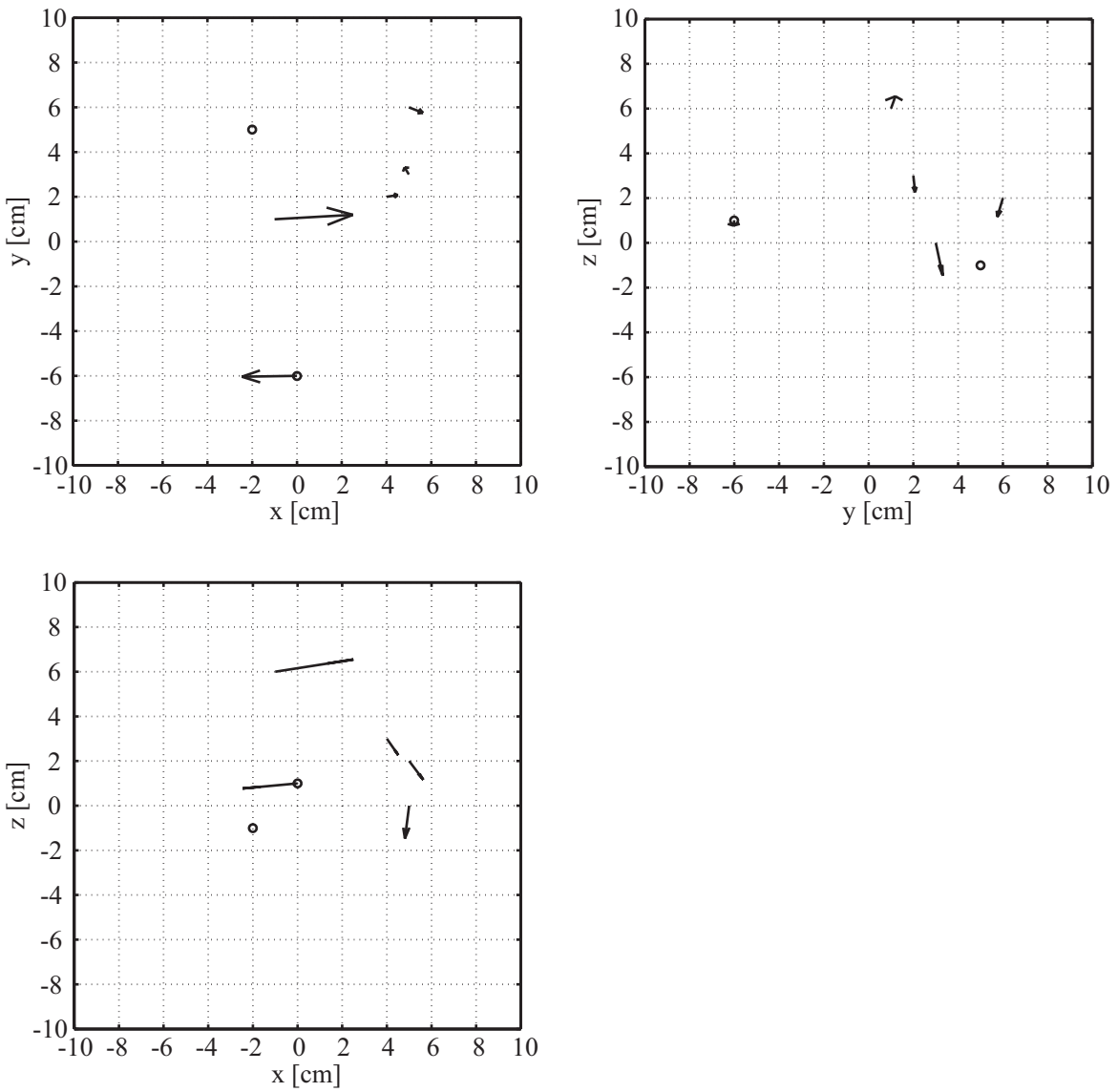

Figure 4.19: Dipoles reconstructed by the combination of the FA-processed Kalman filter without ICA and the SFR in the simulated raw AEF data analysis: ∘ represents the true dipole locations. The initial number of the dipoles was prescribed as 10 in the proposed reconstruction, and the 5 dipoles were estimated. The error rate was 0.480. The FA-processed Kalman filtered data are shown in Fig.4.13.

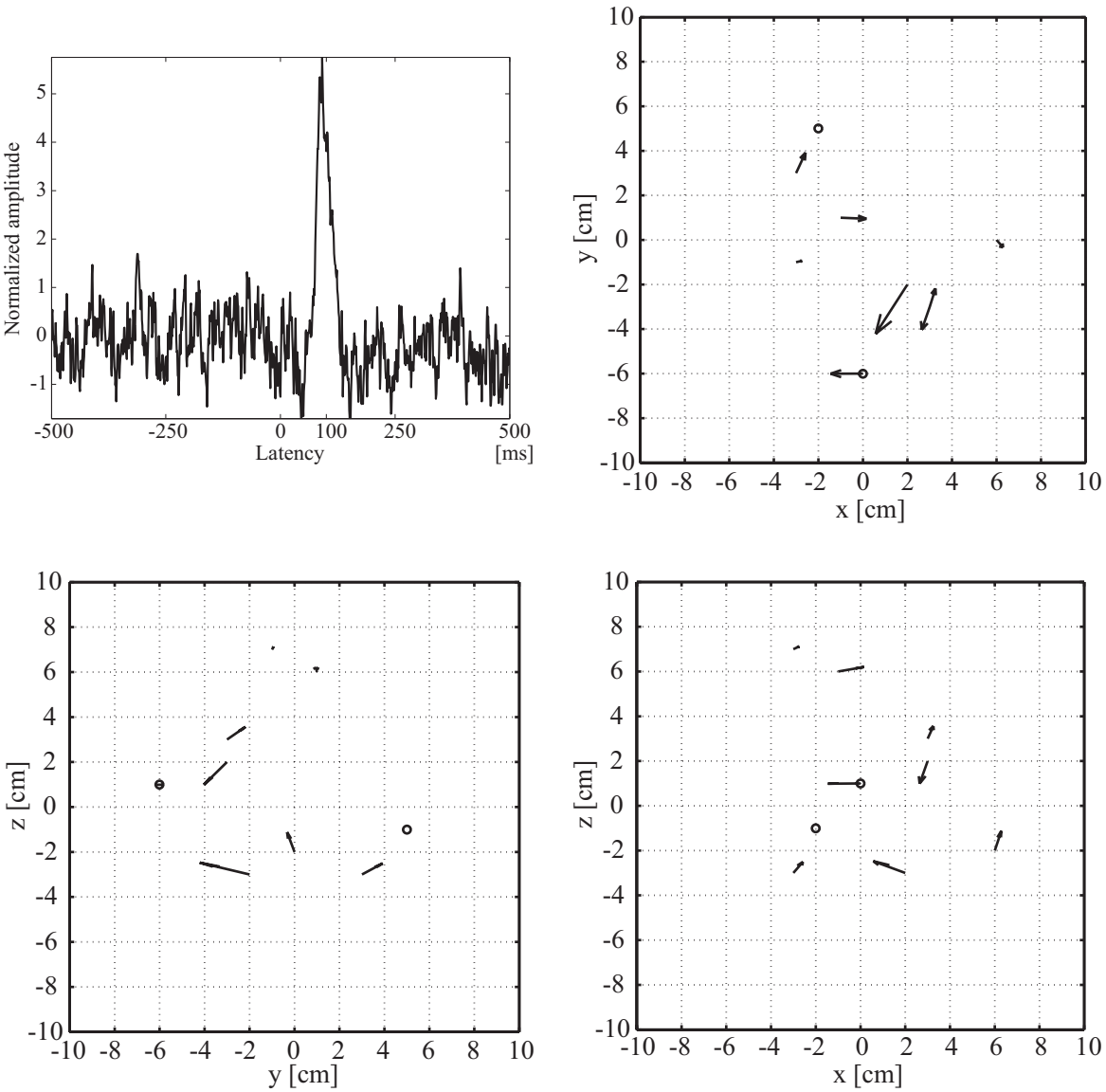

Figure 4.20: Extracted independent component (upper left) and dipoles reconstructed by the combination of the FastICA and the SFR in the simulated raw AEF data analysis: ∘ represents the true dipole locations. The 30 PCs with a 90.4 % contribution were utilized in ICA. The initial number of the dipoles was prescribed as 10 in the proposed reconstruction, and the 8 dipoles were estimated. The error rate was 0.433.

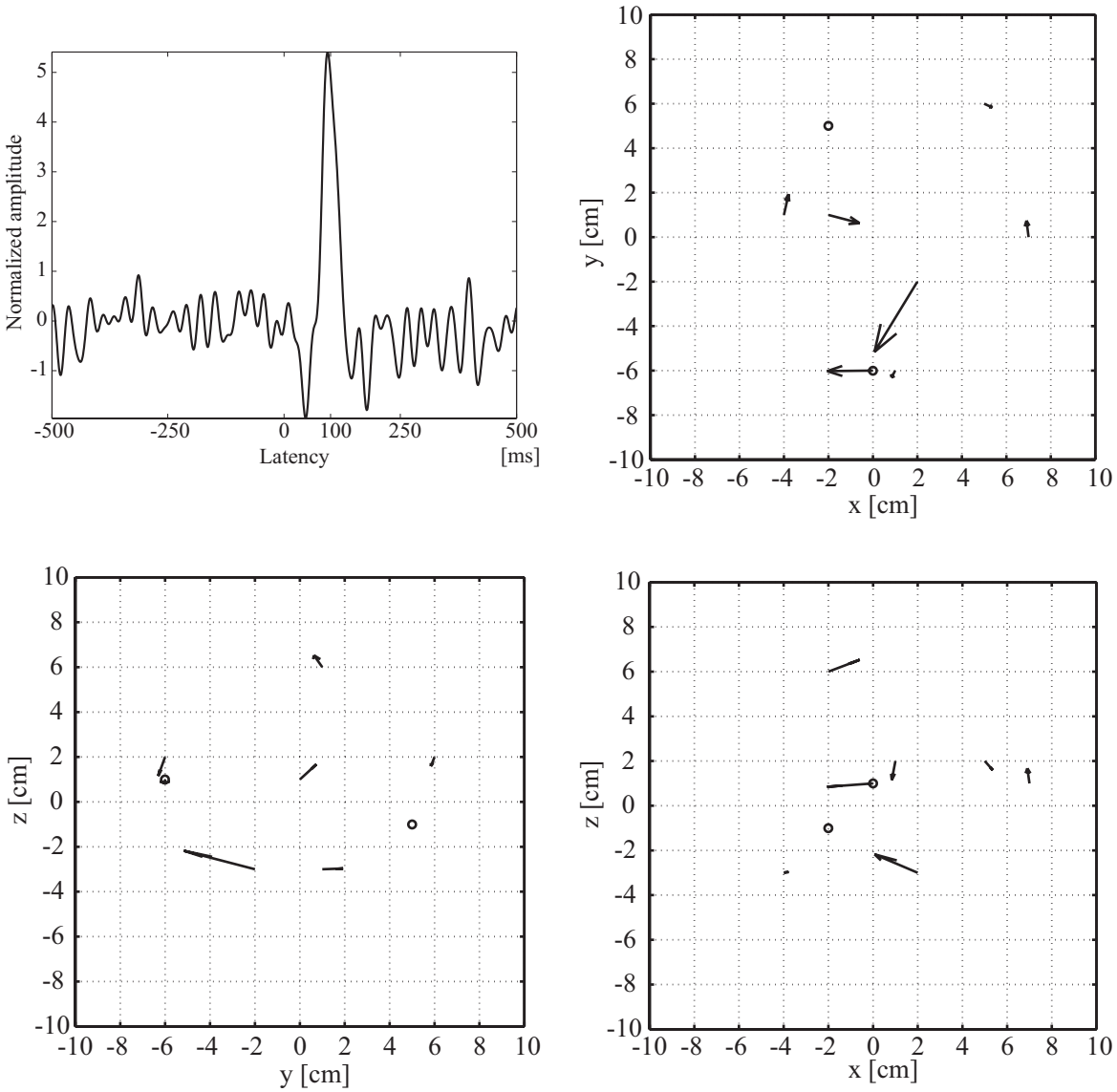

Figure 4.21: Extracted independent component (upper left) and dipoles reconstructed by the combination of the 1-40Hz BPF, the FastICA and the SFR in the simulated raw AEF data analysis: ∘ represents the true dipole locations. The band-pass filtered data are shown in Fig.4.18. The 30 PCs with a 97.7 % contribution were utilized in ICA. The initial number of the dipoles was prescribed as 10 in the proposed reconstruction, and the 7 dipoles were estimated. The error rate was 0.356.

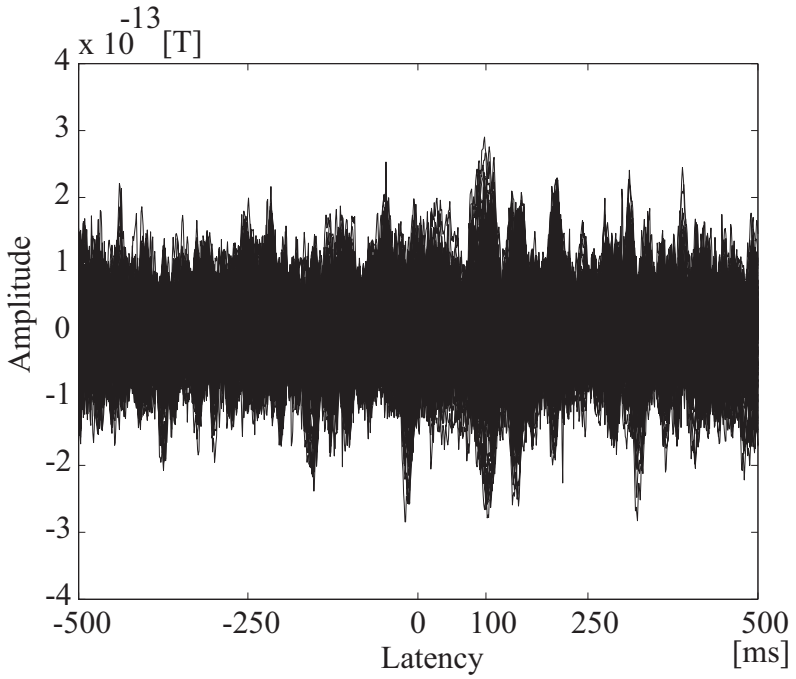

(a)

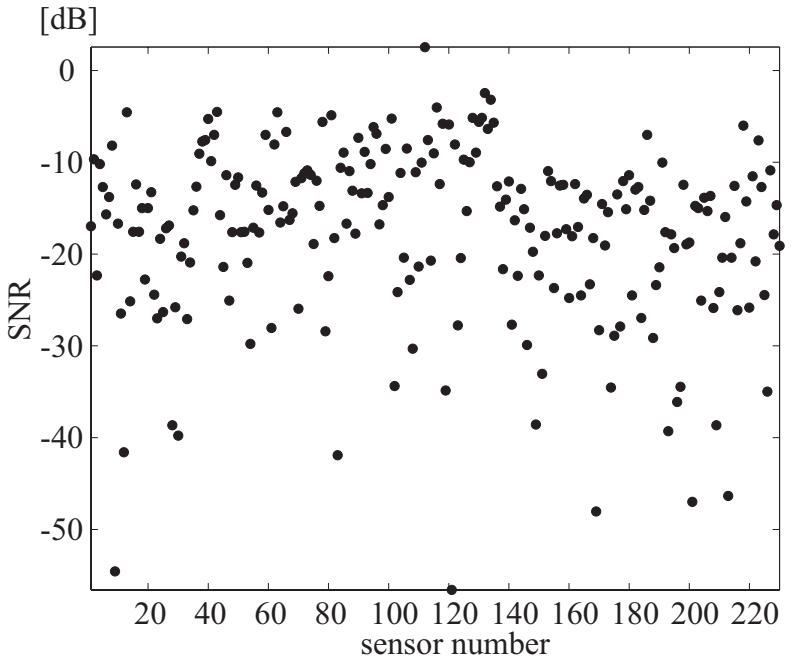

(b)

Figure 4.22: (a) Simulated AEF data averaged across 10 trials and (b) SNR of each sensor

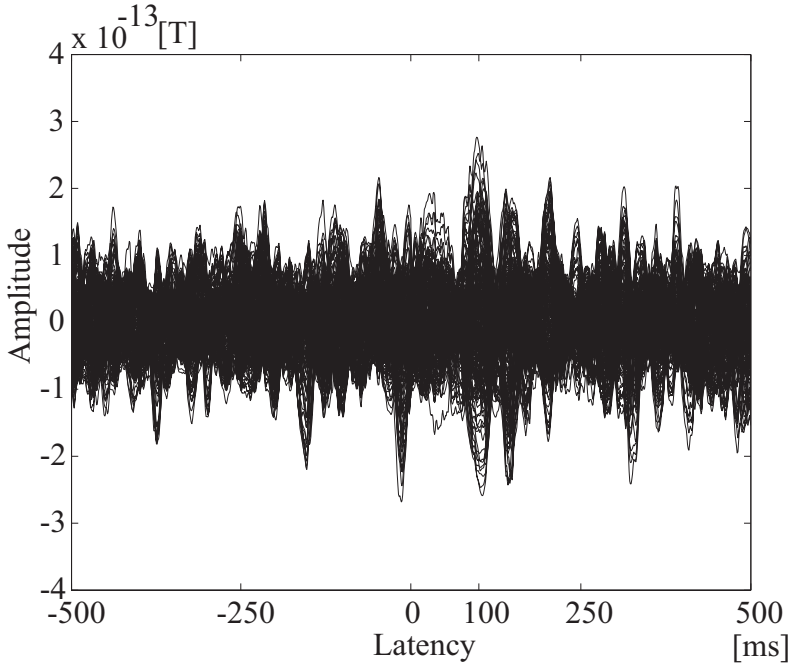

(a)

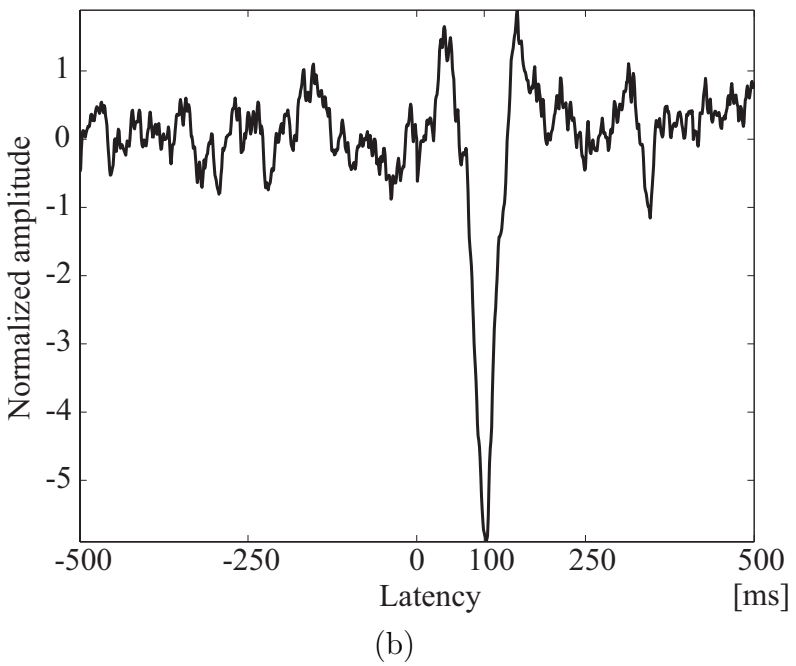

(b)

Figure 4.23: (a) Simulated AEF data after averaging across 10 trials and the FA-processed Kalman filtering and (b) Extracted independent component. The covariance matrices were estimated with 40 common factors. 30 PCs with a 99.82 % contribution were utilized in ICA. The IC has a sharp peak at the latency of 100 ms.

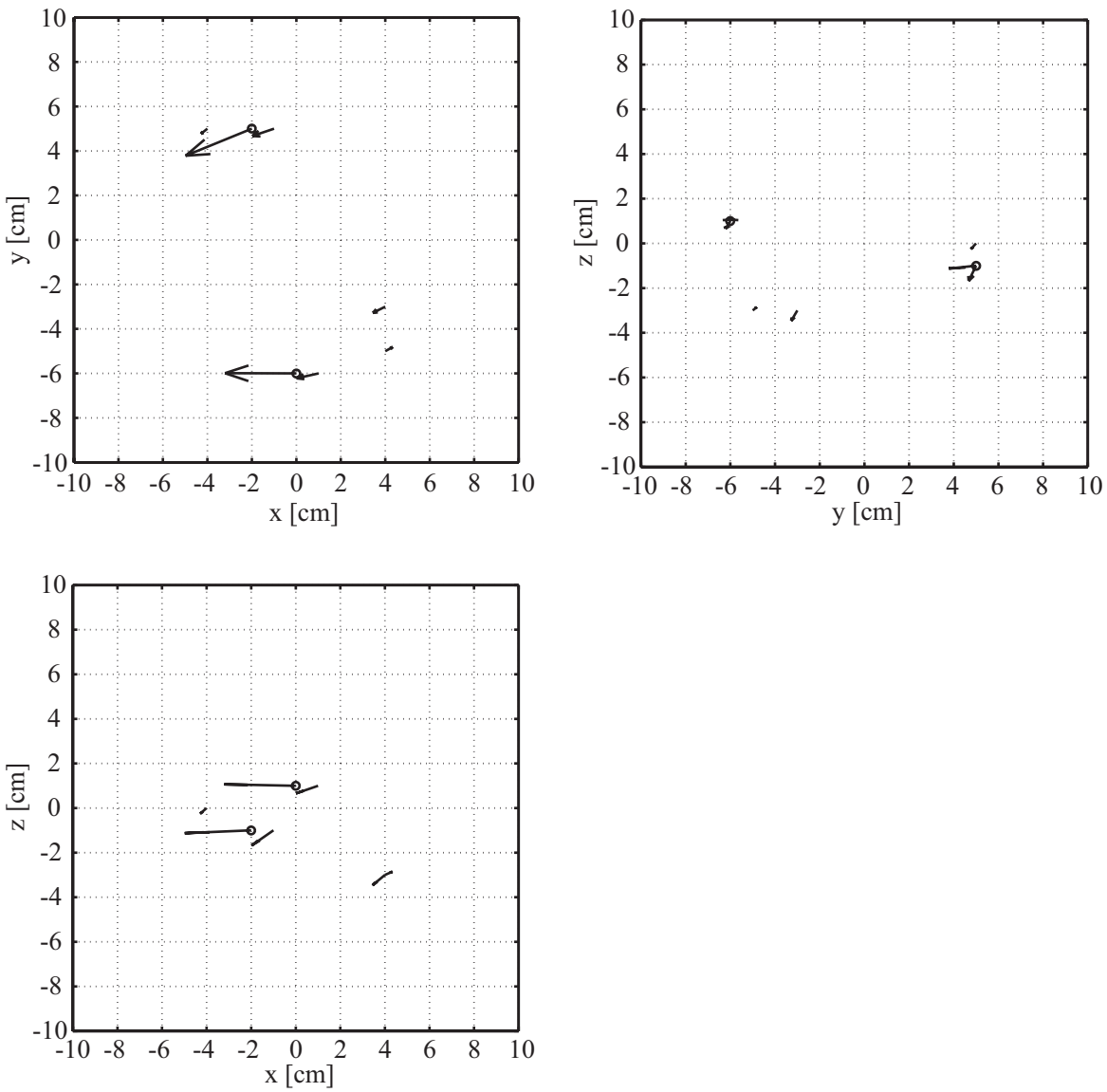

Figure 4.24: Dipoles reconstructed by the combination of the FA-processed Kalman filter, ICA and the SFR in the analysis of the simulated AEF data averaged across 10 trials: ∘ represents the true dipole locations. The initial number of the dipoles was prescribed as 10 in the proposed reconstruction, and the 7 dipoles were estimated. The error rate was 0.096.

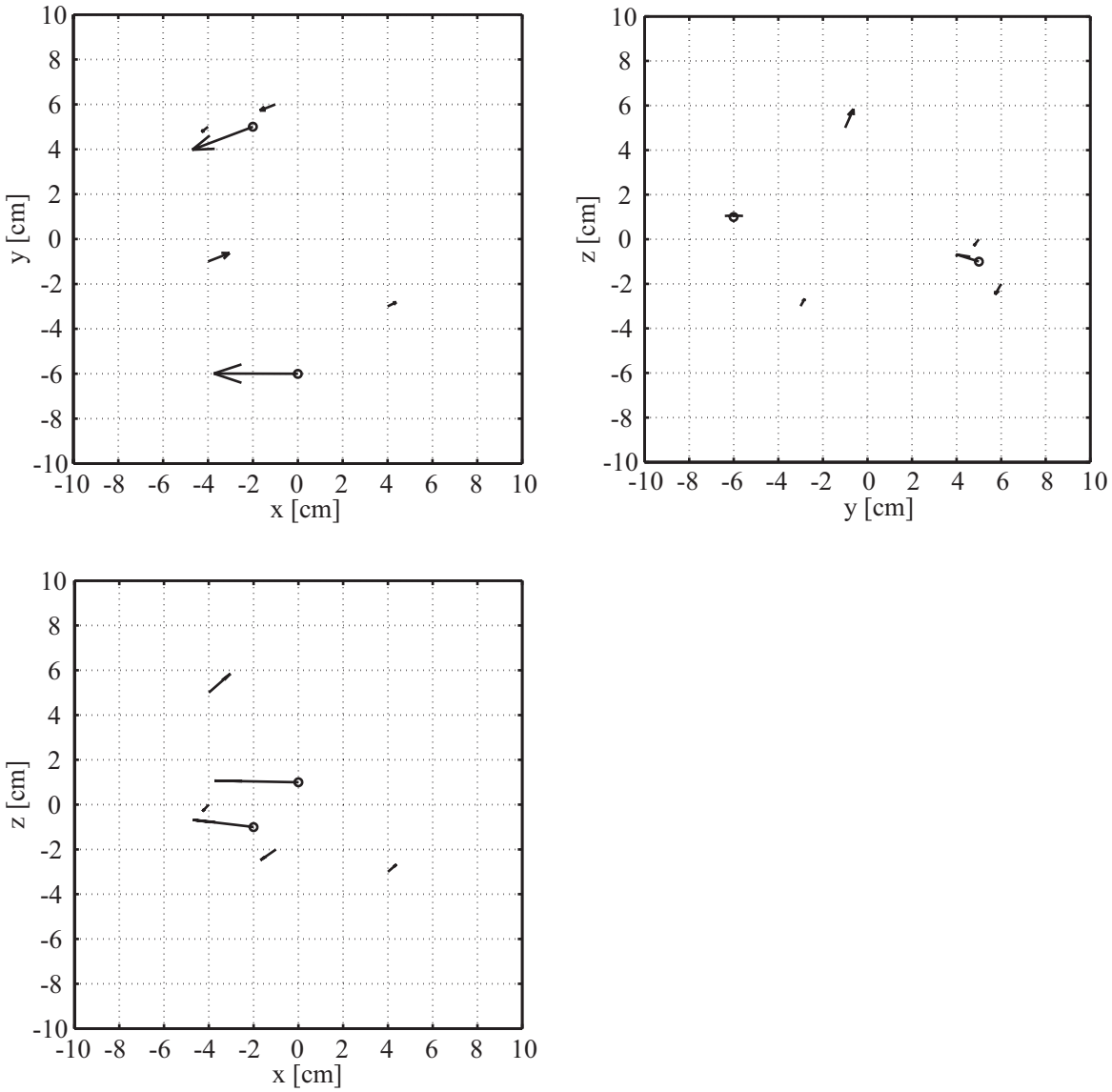

Figure 4.25: Dipoles reconstructed only by the SFR in the analysis of the simulated AEF data averaged across 10 trials: ∘ represents the true dipole locations. The initial number of the dipoles was prescribed as 10 in the proposed reconstruction, and the 6 dipoles were estimated. The error rate was 0.109.

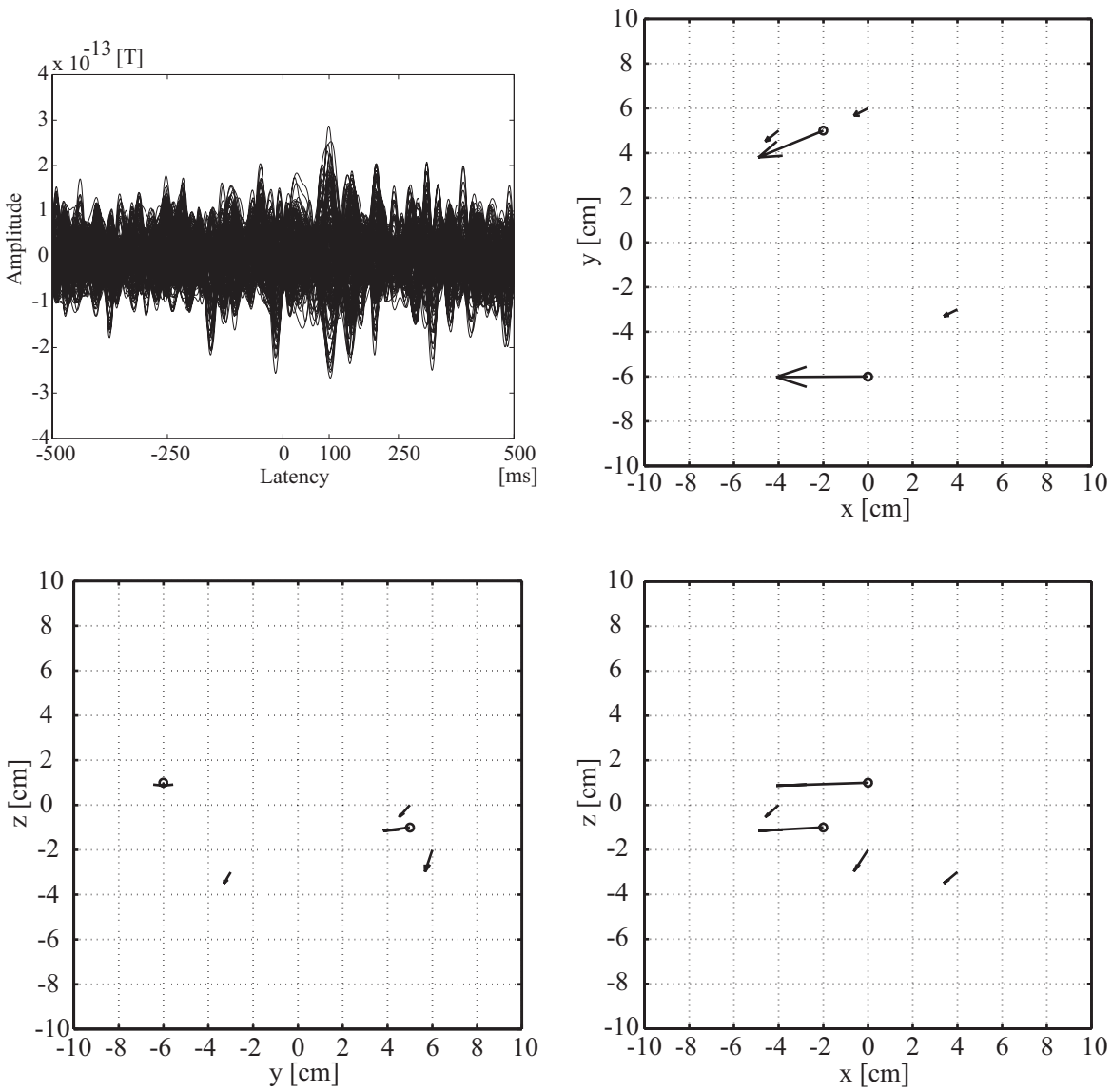

Figure 4.26: Band-pass filtered signals (upper left) and dipoles reconstructed by the combination of the 1-40Hz BPF and the SFR in the analysis of the simulated AEF data average across 10 trials: ∘ represents the true dipole locations. The initial number of the dipoles was prescribed as 10 in the proposed reconstruction, and the 5 dipoles were estimated. The error rate was 0.119.

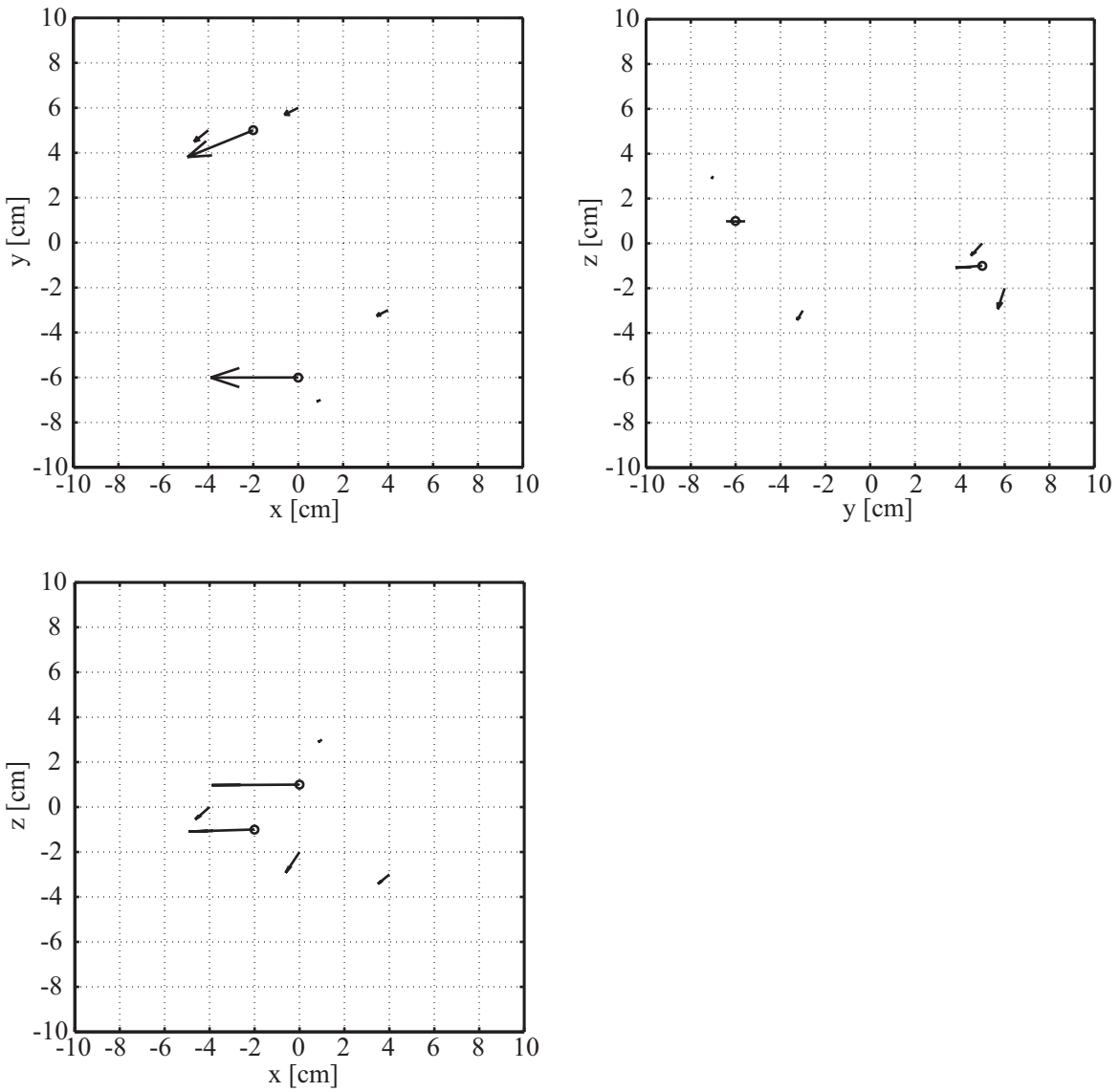

Figure 4.27: Dipoles reconstructed by the combination of the FA-processed Kalman filter without ICA and the SFR in the simulated AEF data analysis: ∘ represents the true dipole locations. The initial number of the dipoles was prescribed as 10 in the proposed reconstruction, and the 6 dipoles were estimated. The error rate was 0.0944. The FA-processed Kalman filtered data are shown in Fig.4.23.

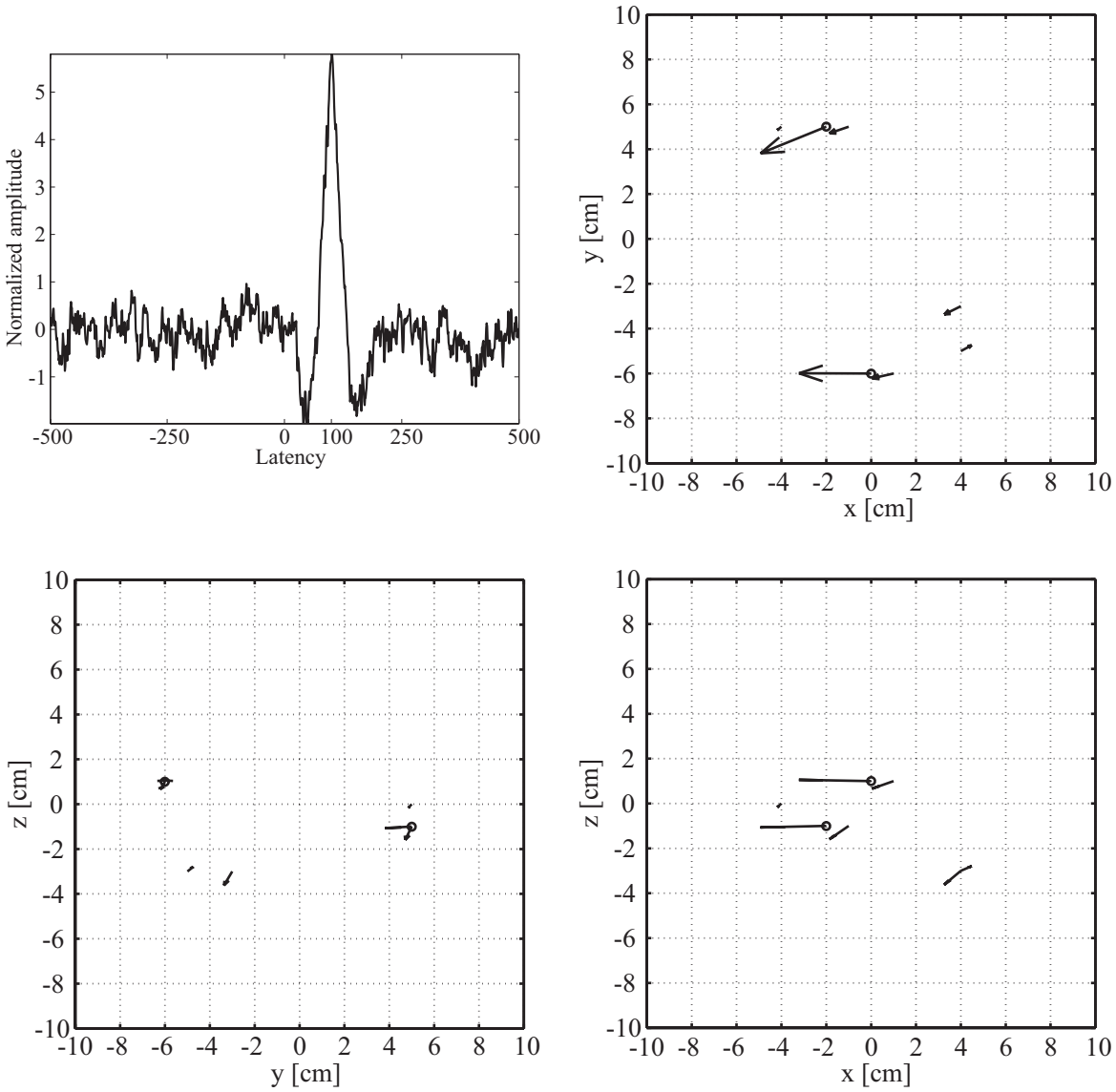

Figure 4.28: Extracted independent component (upper left) and dipoles reconstructed by the combination of the FastICA and the SFR in the analysis of the simulated AEF data averaged across 10 trials: ∘ represents the true dipole locations. The 30 PCs with a 91.32 % contribution were utilized in ICA. The initial number of the dipoles was prescribed as 10 in the proposed reconstruction, and the 7 dipoles were estimated. The error rate was 0.063.

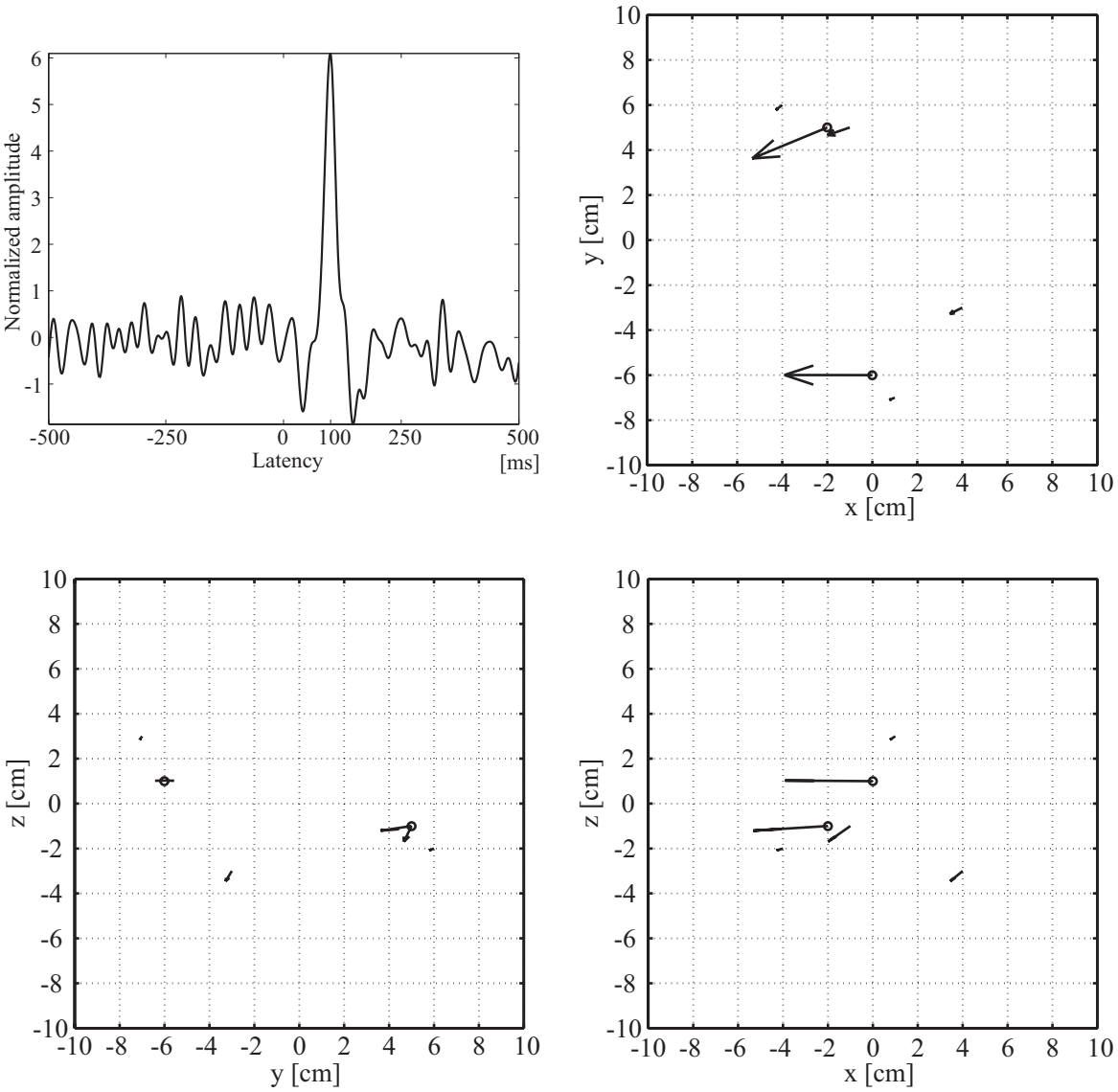

Figure 4.29: Extracted independent component (upper left) and dipoles reconstructed by the combination of the 1-40Hz BPF, the FastICA and the SFR in the analysis of the simulated AEF data averaged across 10 trials: ∘ represents the true dipole locations. The band-pass filtered data are shown in Fig.4.26. The 30 PCs with a 97.88 % contribution were utilized in ICA. The initial number of the dipoles was prescribed as 10 in the proposed reconstruction, and the 6 dipoles were estimated. The error rate was 0.1123.

4.3.2 Real AEF data analysis

The signal processing and the current dipole estimation for real MEG data were conducted with the FA-processed Kalman filter, ICA and the SFR. The estimation with the proposed combination was employed for 5 kinds of AEF data, namely a single-trial unaveraged AEF data and the AEF data averaged across 10, 20, 40 and 80 trials. In the FA step, the number of the common factors was set as 40, and the number of the components was reduced to 20 in the ICA step in the each estimation.

The single-trial AEF data were illustrated in Fig.4.30. The 230 signals were superimposed. After the FA-processed Kalman filtering, the noises were reduced (Fig.4.31). In the ICA step, 20 PCs contributed a 98.4 % to the total value in the Kalman filtered data covariance, while 130 PCs were needed to achieve a 98.2 % contribution in the raw data covariance. 20 ICs were estimated with ICA. The IC with the peak around the latency of 100 ms, which must be originated from the N1m in AEF, was extracted (Fig.4.32). For the IC in the single-trial raw AEF data analysis, the isofield contour map of the magnetic field pattern of the IC is shown in Fig.4.33, which suggests that the existence of the bilateral brain activities in the neighborhood of the auditory cortexes. The current dipole distribution was reconstructed for the IC. The initial number of the dipoles for the reconstruction was prescribed as 25, and 10 dipoles survived the elimination to minimize the C_p statistic. Figure 4.34 shows the current dipole distribution estimated by the SFR. In the result of the estimation with the proposed combination, the current dipoles were localized similarly to the result in the analysis for the AEF data averaged across 169 trials shown in the previous section. Some dipoles were not related to the activities in the auditory cortexes were estimated, though. They seem to be caused by the artifacts correlated to the AEF component.

The combinations of the other noise reductions and the SFR, and the estimation only with the SFR were studied as well as the simulated AEF analyses. Figures 4.35-4.39 show the processed data and the reconstructed dipoles. In this unaveraged AEF data analysis, the SNR seems worse than that in the simulated data.

The SFR after the noise reduction with each of the 1-40Hz BPF, the FastICA and the FA-processed Kalman filter, hardly reconstructed the current dipole distribution (Figs.4.36-4.38). The activities in the right hemisphere was barely estimated in the reconstruction with the combination of the 1-40Hz BPF and the FastICA as shown in Fig.4.39. These results indicate that the noise reduction with the FA-processed Kalman filter and ICA is more effective than the conventional noise reductions. The combination of the proposed noise reduction and the SFR shows high performance in real MEG analyses.

The results of the dipole reconstructions, for the real AEF data averaged across 10 trials, with the SFR and the noise reductions, the proposed method and the others are shown in Figs.4.40-4.46. Figures 4.40 and 4.41 show that the combination of the FA-processed Kalman filter and ICA extracted the signals with N1m, and the SFR was able to estimate the dipoles. The dipole on the left hemisphere was not reconstructed only with the SFR in the case as shown in Fig.4.42. The other combinations worked well. The noise reduction with the FA-processed Kalman filter and the proposed combination enable to estimate the current dipoles with the SFR in real MEG analysis. The SFR is robust in real MEG analyses with the adequate noise reduction.

The estimation results are illustrated for the AEF data averaged over 20, 40 and 80 trials in Figs.4.47-4.52. For each result, the AEF data before the proposed processing, the FA-processed Kalman filtered data, the estimated IC with the peak around 100 ms and the current dipole distribution reconstructed by the SFR are shown. In the each estimation, the FA-processed Kalman filter reduced noises effectively, and succeeded in refining the number of the ICs. The contributions of the 20 PCs to pre- and post-Kalman filtered data in the each estimation are described in Table 3. In the pre-Kalman filtering, more than 120 components were needed to obtain the contribution of about 99 % which is the same level of the contribution of 20 PCs in the post-Kalman filtered data. The current dipole distribution was clearly reconstructed in the estimation for the AEF data averaged over 10 trials as well as for the AEF data with more averaging. This indicates that the steady performance

of the proposed noise reduction and SFR can be obtained in lower SNRs cases in real MEG analyses. It is apparent that the dipoles were estimated around the locations where the dipoles were reconstructed in the high SNR data analysis shown in Section 4.1. The estimation with the proposed combination of the FA-processed Kalman filter, ICA and the SRF captured the activities in the auditory cortexes in the real MEG analyses with low SNRs.

Table 3 Contributions of 20 eigenvalues of the covariance matrix to the total value in pre and post FA-processed Kalman filter

averaging [trials]	1	10	20	40	80
pre-Kalman filter [%]	86.4	89.4	91.4	93.1	94.5
post-Kalman filter [%]	98.4	98.9	99.4	99.5	99.6

4.4 Discussion

In these numerical studies in which the real MEG data were employed, the FA-processed Kalman filter and ICA extracted the desired signals such as the AEF signal from the real MEG data. The results show that the proposed method is robust to sensor noises in real MEG measurement and certify the practical utility of the proposed method. The robustness to the error of the number of common factors was also confirmed. By the Kalman filtering, the redundant factors were reduced sufficiently enough to ignore as with the case of the incorrect number of common factors in the numerical experiment in Section 3.1.2., and we succeeded to refine the number of components in the ICA step. Those results not only show the effectiveness of the FA-processed Kalman filter but also support the validities of the numerical studies. We assumed the sensor noise was Gaussian in the previous numerical experiments. However, even if sensor noises in real MEG data do not satisfy the assumption of Gaussianity, the proposed method still retains its effectivity since

Kalman filter is the optimal linear minimum variance filter regardless of Gaussianity of noises. The effect of the FA-processed Kalman filter is more significant in analyses with lower SNRs as shown in the previous sections.

The SFR localized the current densities around the auditory cortexes for the averaged AEF data. Accompanying the sufficient noise reduction, the SFR estimated the current dipoles reasonably in the real MEG analysis. The robustness of the SFR to real MEG noises was indicated in Sections 4.3.1. and 4.3.2. In the AEF analysis, the SFR succeeded in localizing the bilateral current dipoles from the data averaged across 10 trials. The current density estimation for the raw AEF data with the combination of the FA-processed Kalman filter and the SFR was also successful. There were the redundant expansions of the current distribution estimated by the combination. It was due to the noise, errors due to the dipoles out of the grids, and the artifacts. However, the combination of the FA-processed Kalman filter, ICA and the SFR successfully located the current dipoles. Though some pieces of prior information, i.e. the region for the estimation and the initial number of the dipoles for the reconstruction with multiple linear regression, were needed, they can be deemed acceptable. Compared with the conventional estimation such as the moving-dipole method, the dependence on the prior information declines by the proposed method. The proposed combination of the FA-processed Kalman filter, ICA and the SFR solves the issues, such as the patients' burden for the noise reduction with averaging and the dependence on prior and temporal information in the estimation of the dipoles. The usability and reliability will be gained in practical MEG analyses.

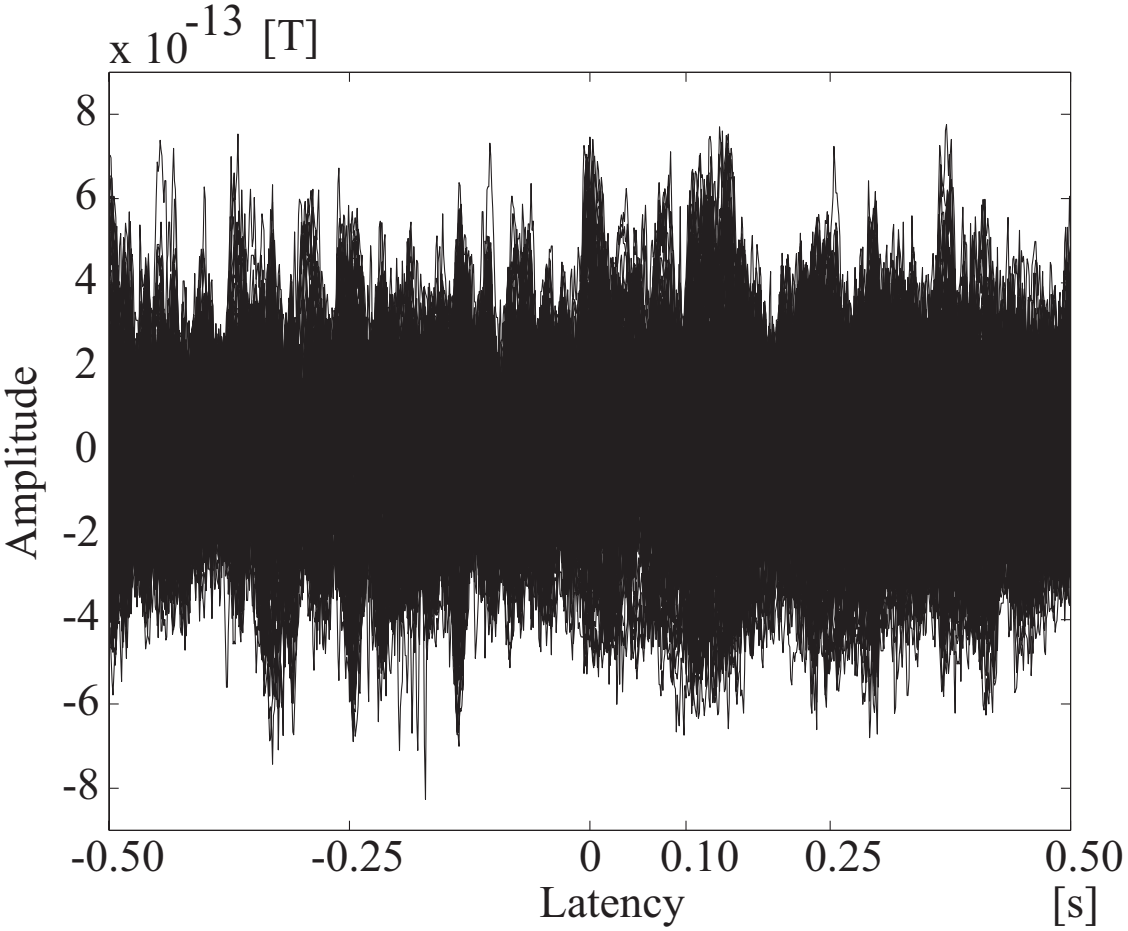

Figure 4.30: Single-trial unaveraged MEG data: 230 signals are superimposed.

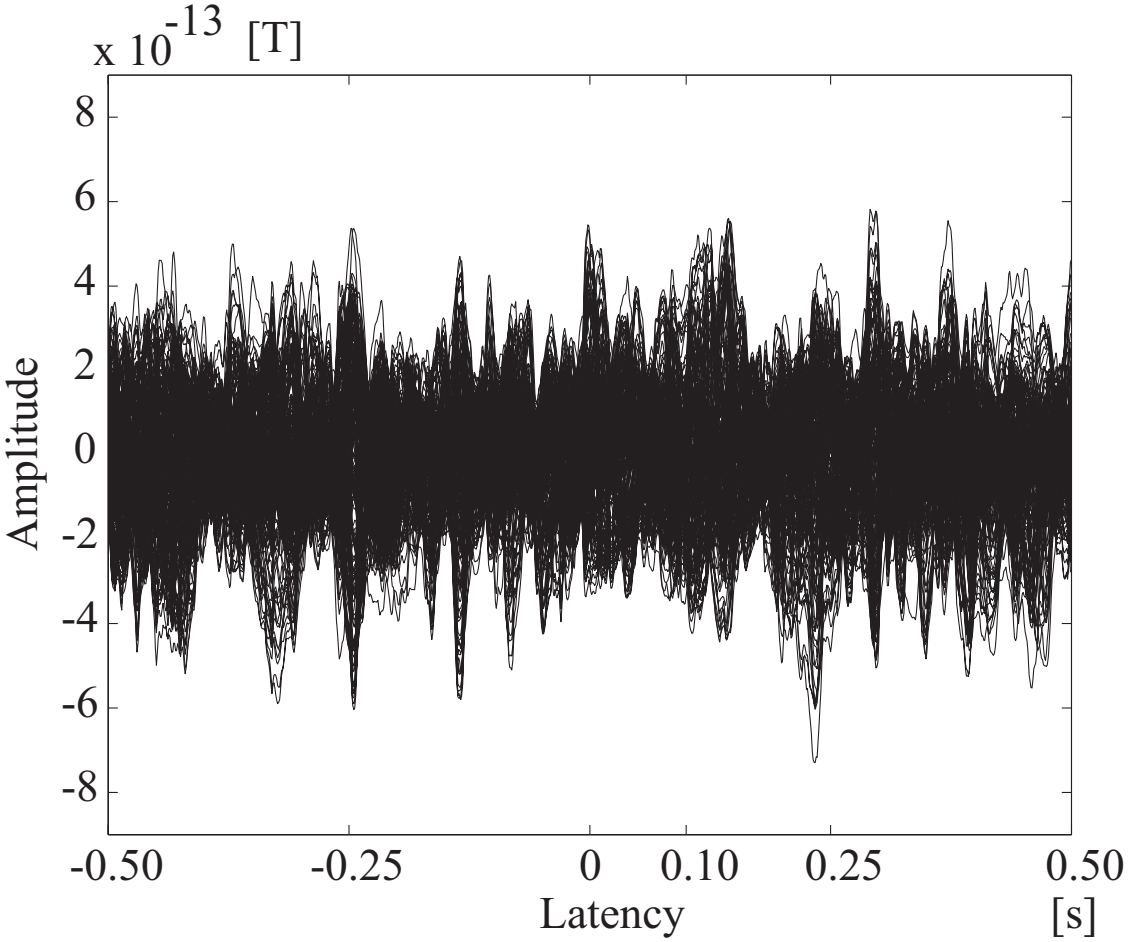

Figure 4.31: FA-processed Kalman filtered MEG data in the raw AEF data analysis: 230 signals are superimposed.

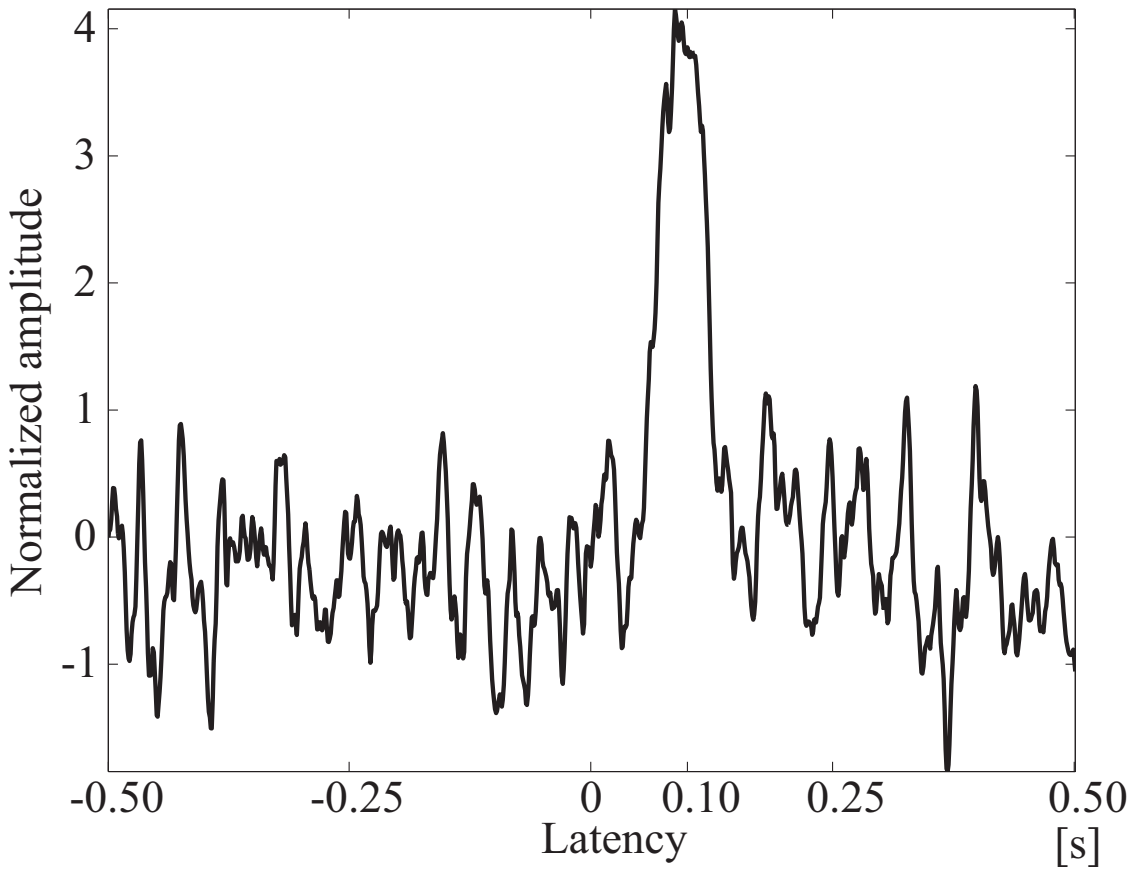

Figure 4.32: Extracted independent components after the FA-processed Kalman filter in the raw AEF data analysis. The current dipoles were reconstructed for this component.

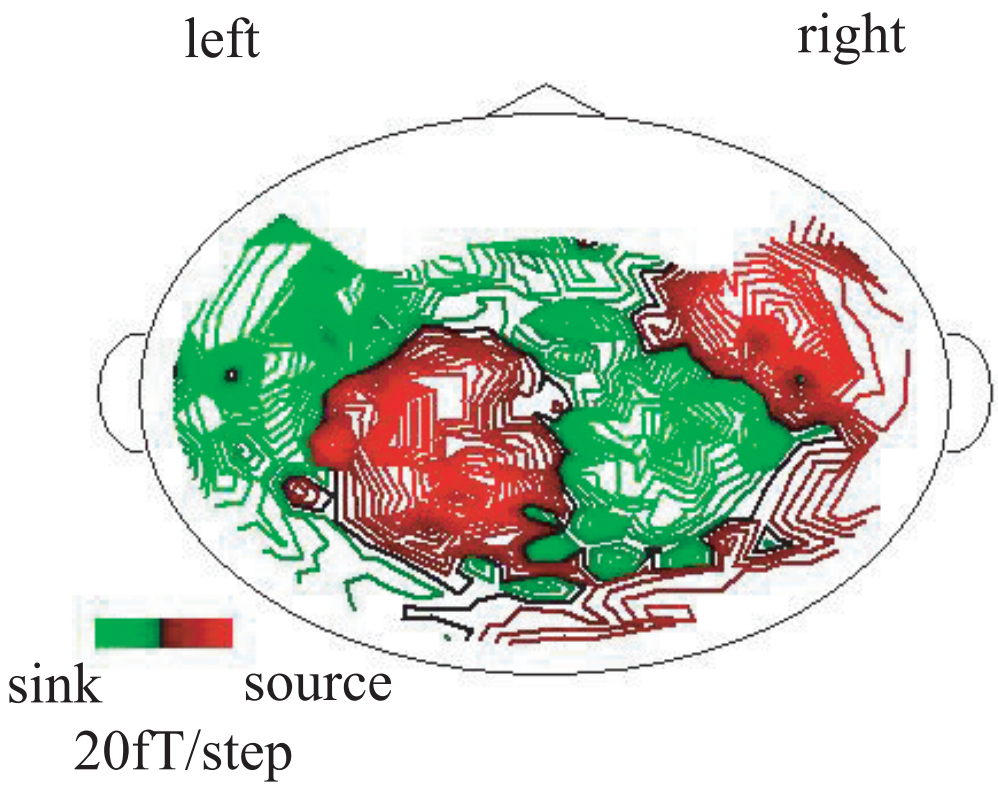

Figure 4.33: Isofield contour map of the magnetic field pattern of the extracted independent component; red and green regions show positive and negative magnetic fields, respectively.

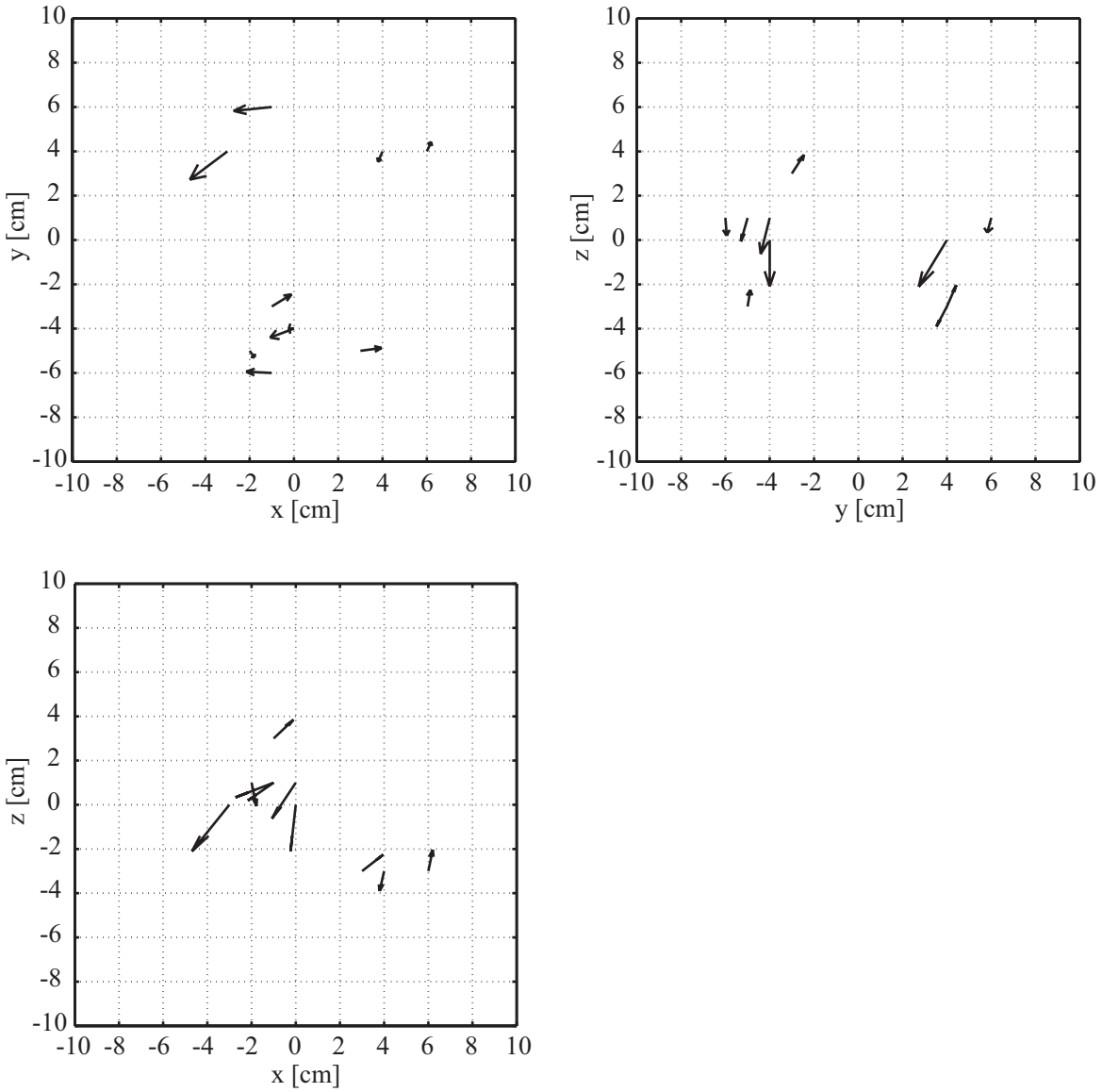

Figure 4.34: Dipole reconstructed by the combination of the FA-processed Kalman filter, ICA and the SFR in the raw AEF data analysis. The initial number of the dipoles were 25 and 10 dipoles remained. The error rate was 0.237.

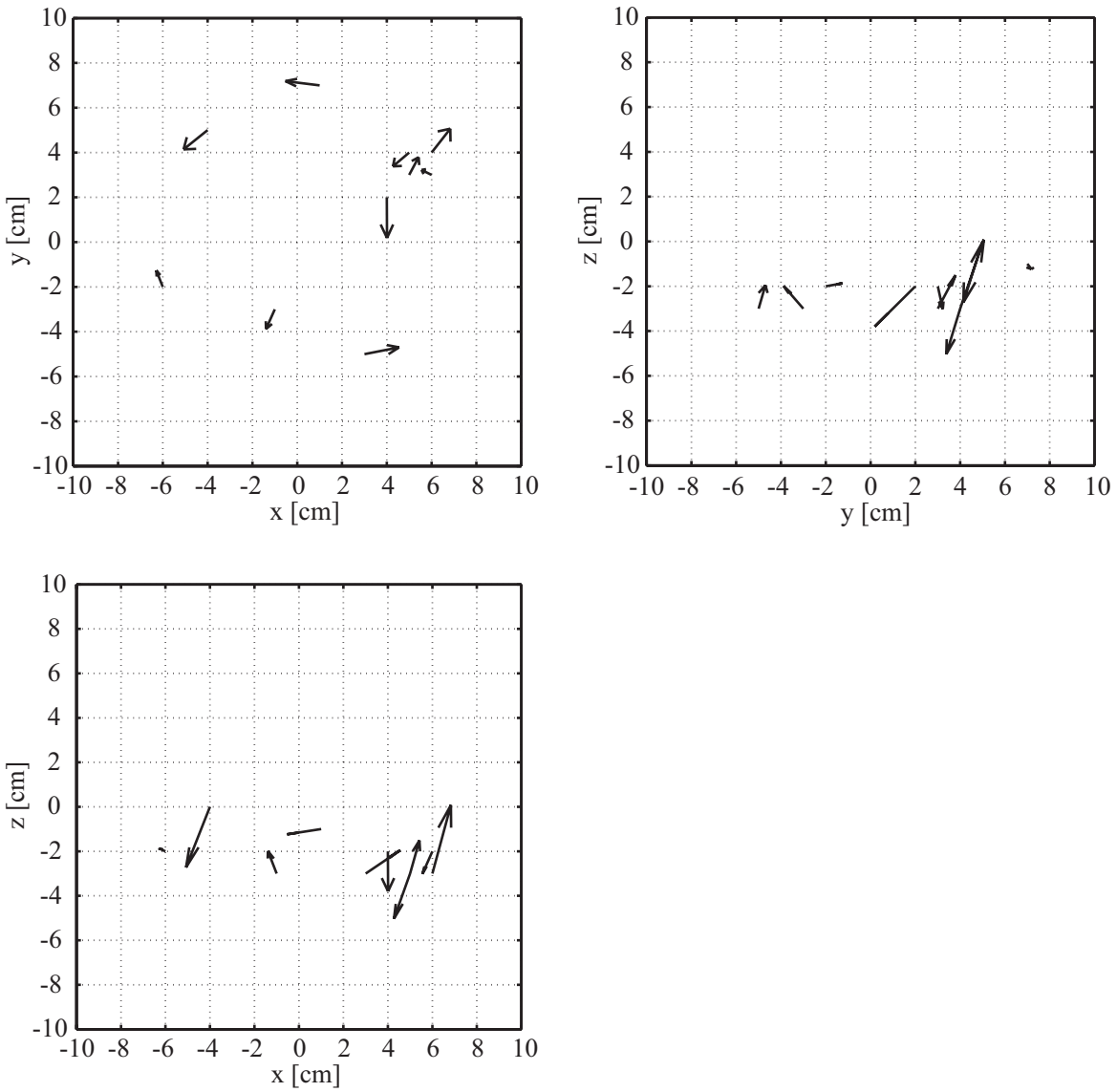

Figure 4.35: Dipoles reconstructed only by the SFR in the analysis of the real raw AEF data. The initial number of the dipoles was prescribed as 25 in the proposed reconstruction, and the 10 dipoles were estimated. The error rate was 0.571.

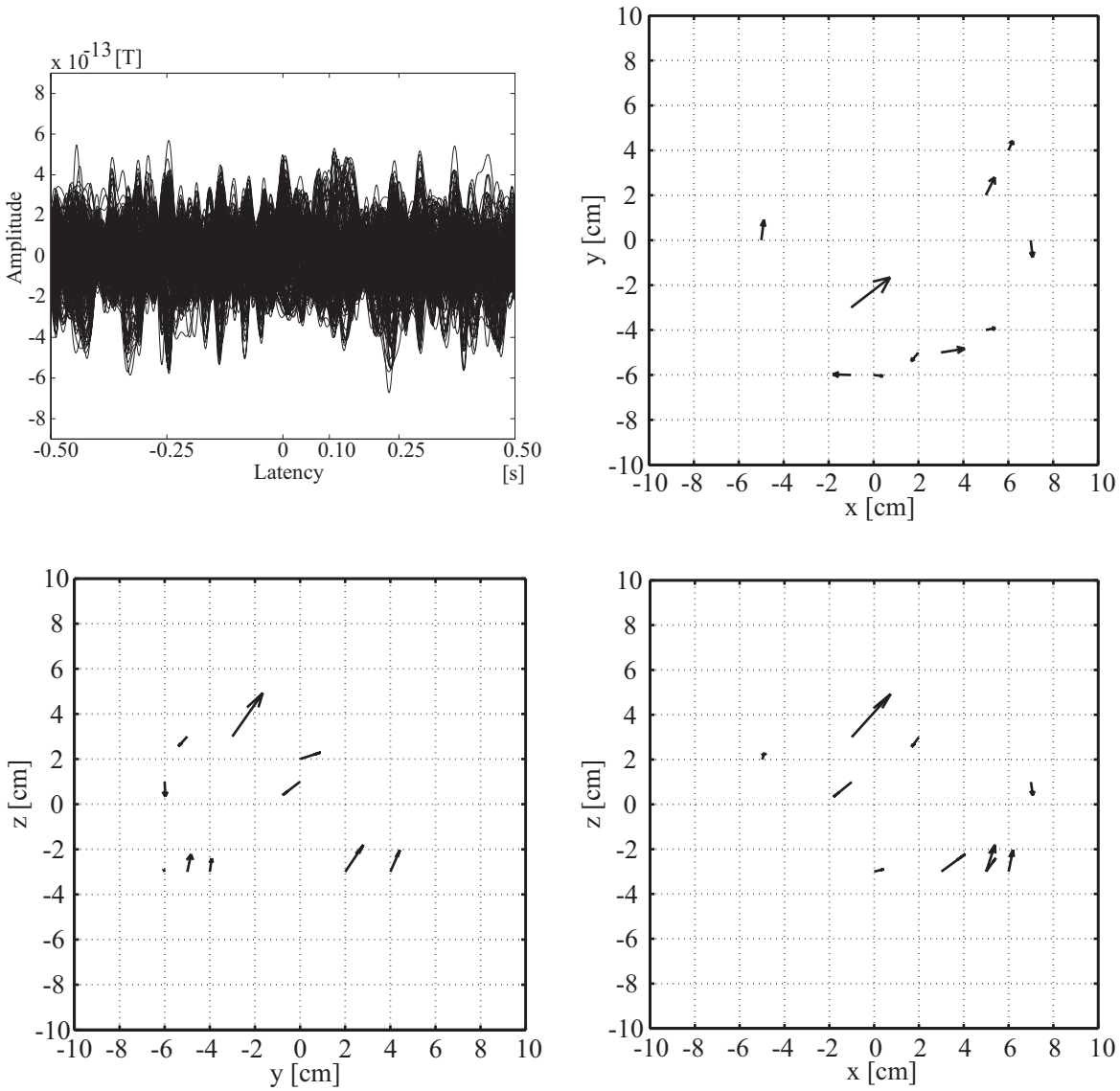

Figure 4.36: Band-pass filtered signals (upper left) and dipoles reconstructed by the combination of the 1-40Hz BPF and the SFR in the analysis of the real raw AEF data. The initial number of the dipoles was prescribed as 25 in the proposed reconstruction, and the 10 dipoles were estimated. The error rate was 0.42.

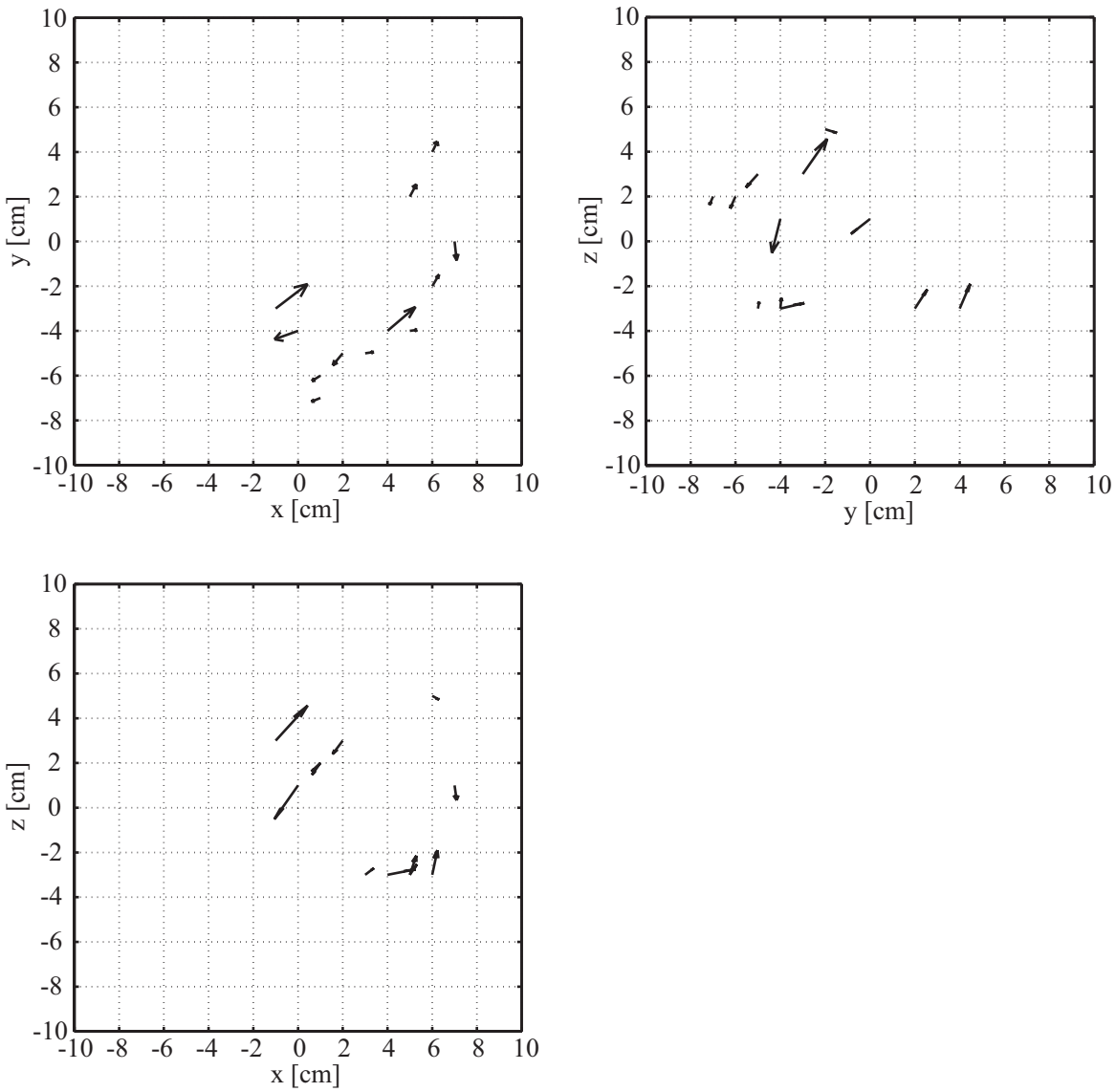

Figure 4.37: Dipoles reconstructed by the combination of the FA-processed Kalman filter without ICA and the SFR in the real raw AEF data analysis. The initial number of the dipoles was prescribed as 25 in the proposed reconstruction, and the 12 dipoles were estimated. The error rate was 0.34. The FA-processed Kalman filtered data are shown in Fig.4.31.

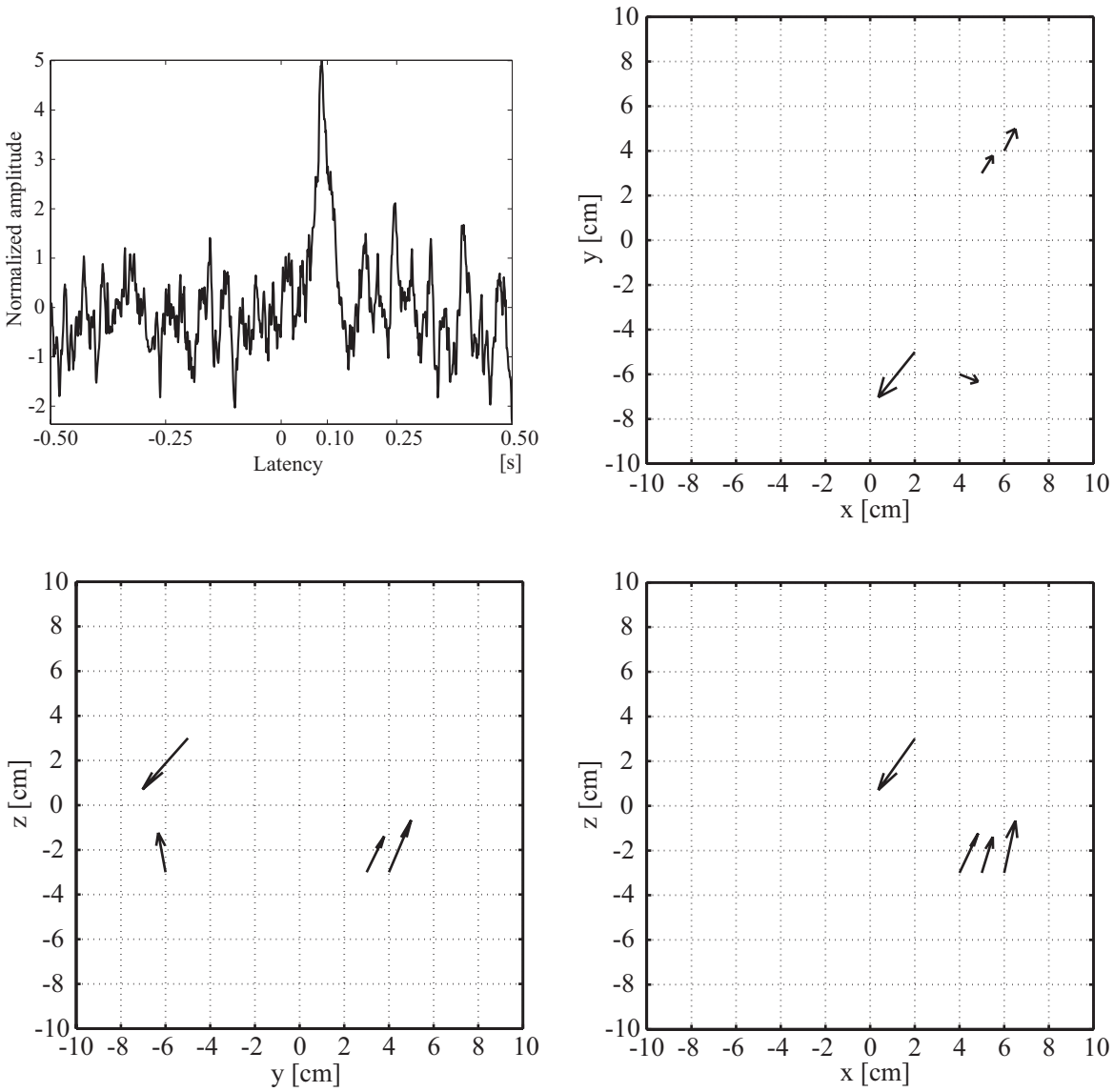

Figure 4.38: Extracted independent component (upper left) and dipoles reconstructed by the combination of the FastICA and the SFR in the analysis of the real raw AEF data. The 20 PCs with a 86.41 % contribution were utilized in ICA. The initial number of the dipoles was prescribed as 25 in the proposed reconstruction, and the 4 dipoles were estimated. The error rate was 0.426.

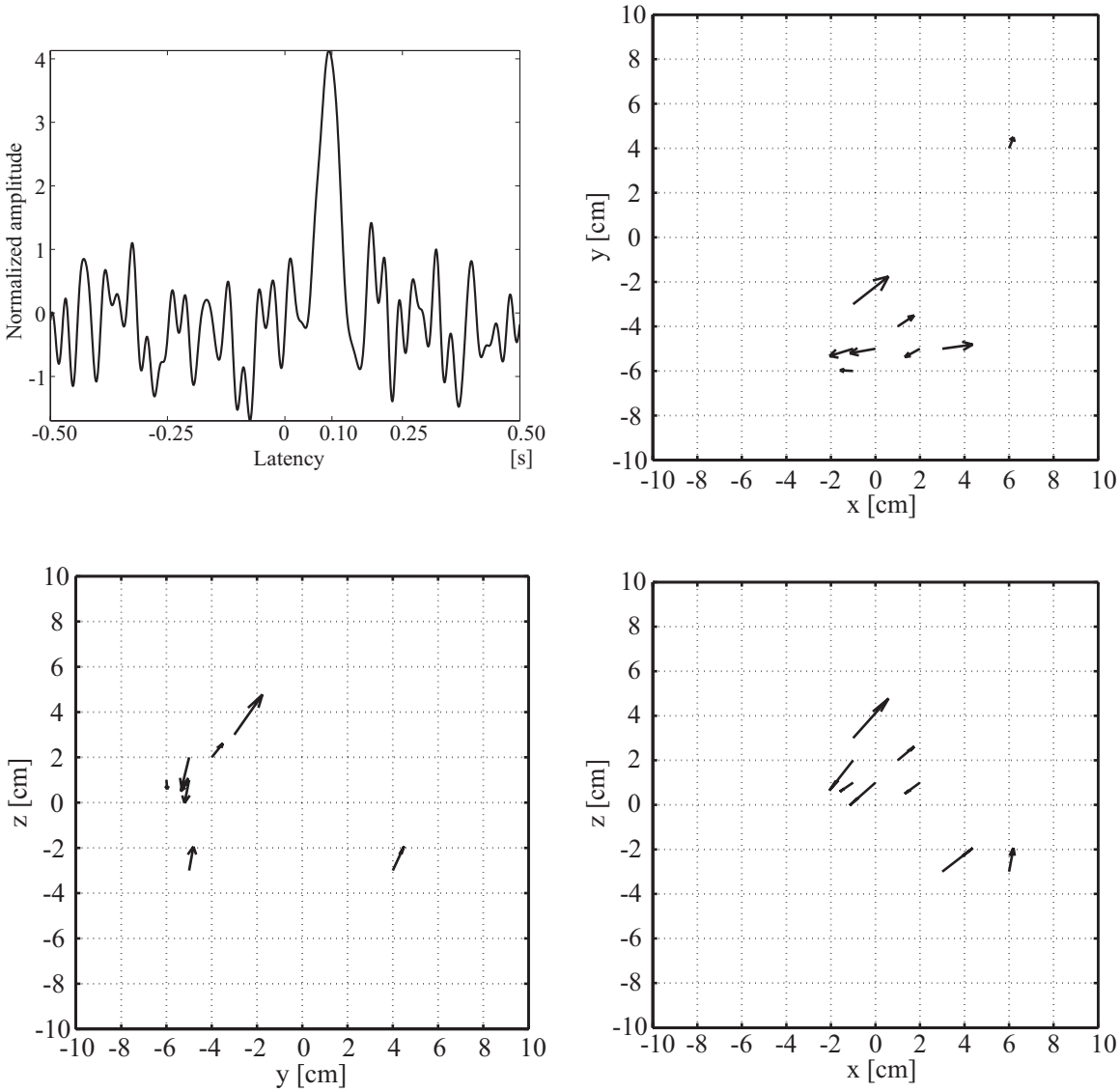

Figure 4.39: Extracted independent component (upper left) and dipoles reconstructed by the combination of the 1-40Hz BPF, the FastICA and the SFR in the analysis of the real raw AEF data. The band-pass filtered data are shown in Fig.4.36. The 20 PCs with a 95.1 % contribution were utilized in ICA. The initial number of the dipoles was prescribed as 25 in the proposed reconstruction, and the 8 dipoles were estimated. The error rate was 0.39.

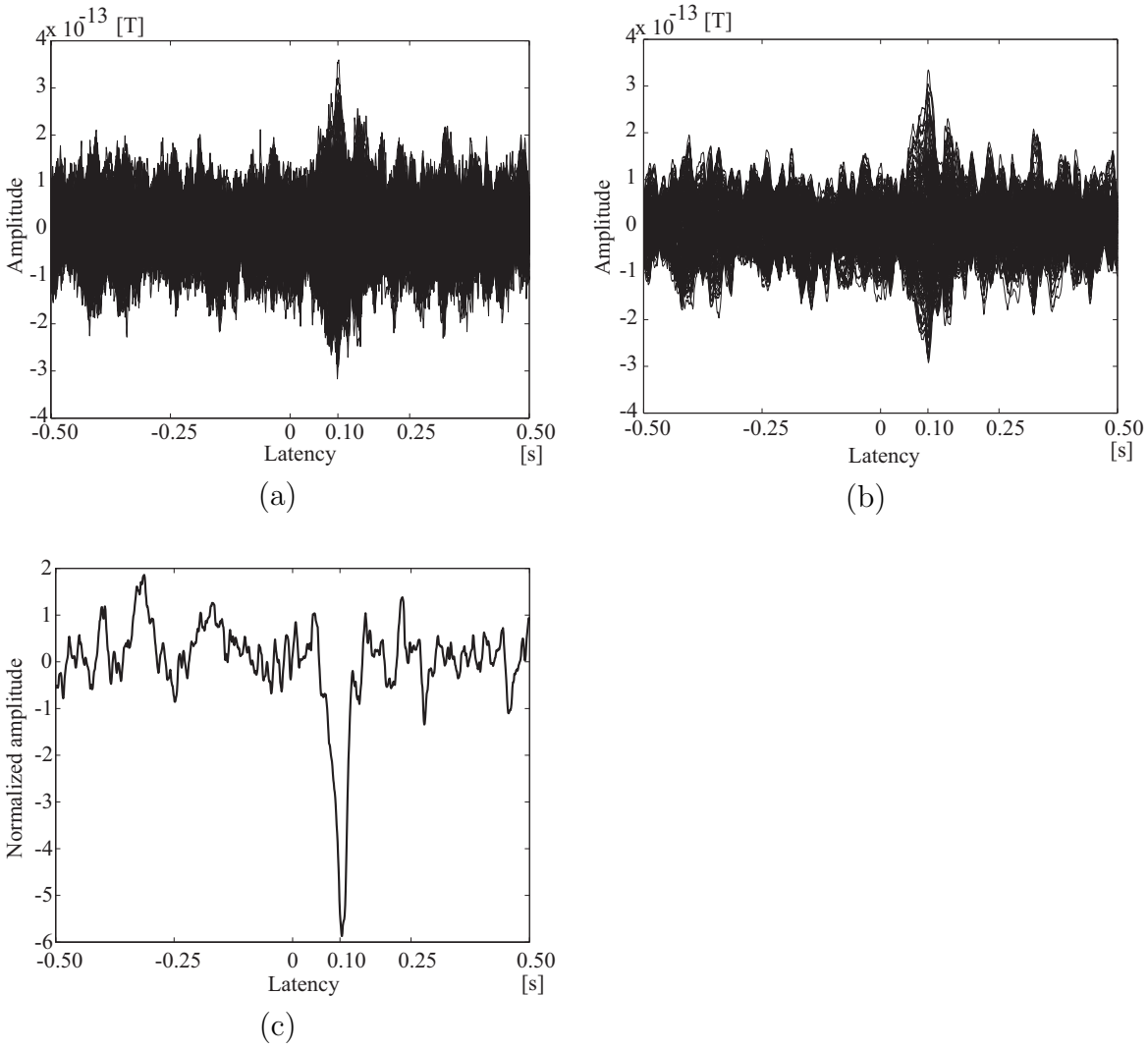

Figure 4.40: MEG data in the analysis of the real AEF averaged over 10 trials: (a) the AEF signals averaged across 10 trials, (b) the FA-processed Kalman filtered signals with 40 common factors and (c) the extracted IC with the peak due to N1m.

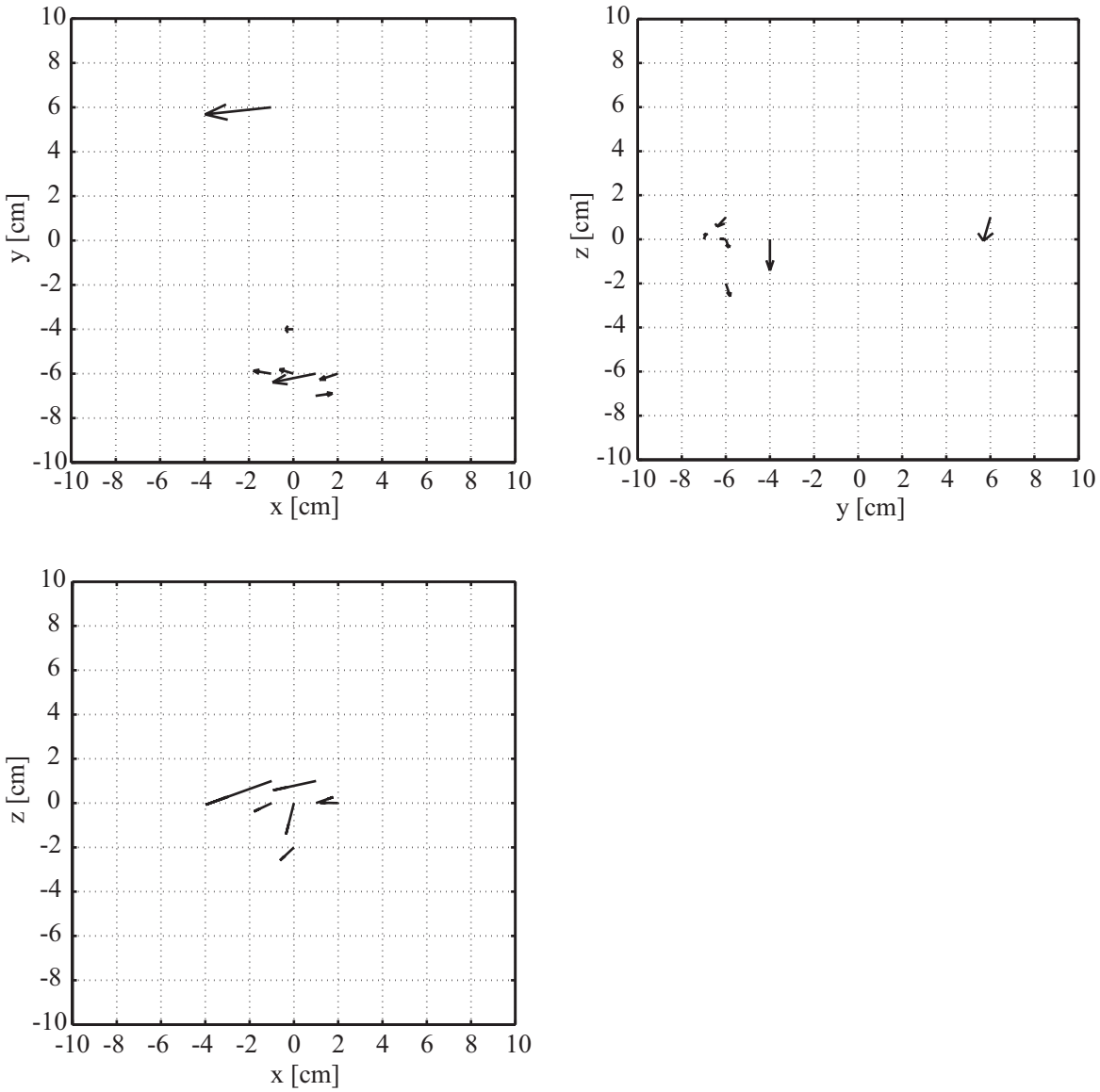

Figure 4.41: Dipoles reconstructed by the combination of the FA-processed Kalman filter, ICA and the SFR in the analysis of the real AEF data averaged 10 trials. The initial number of the dipoles were 20 and 7 dipoles remained. The error rate was 0.247.

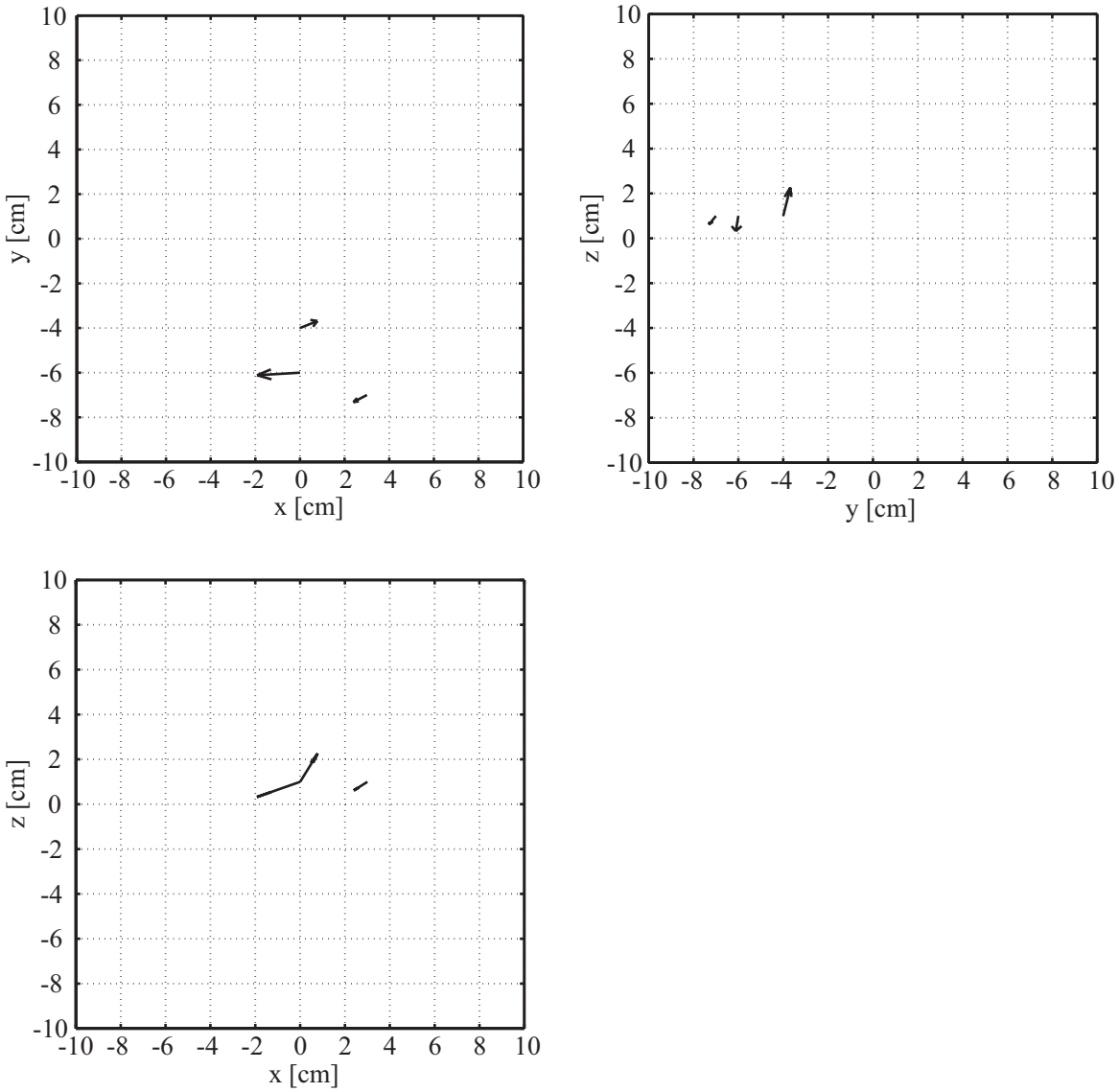

Figure 4.42: Dipoles reconstructed only by the SFR in the analysis of the real AEF data averaged across 10 trials. The initial number of the dipoles was prescribed as 20 in the proposed reconstruction, and the 3 dipoles were estimated. The error rate was 0.615.

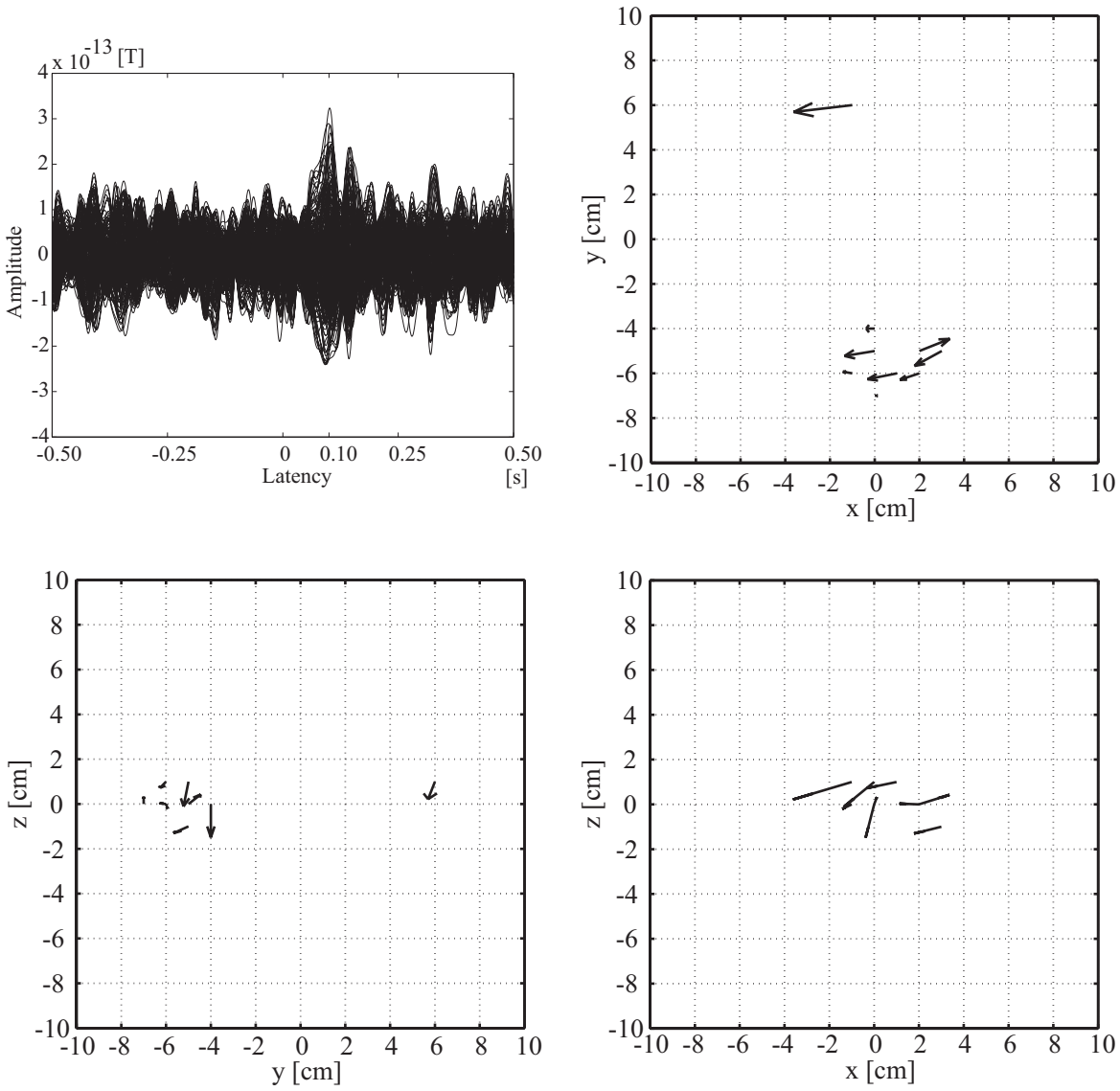

Figure 4.43: Band-pass filtered signals (upper left) and dipoles reconstructed by the combination of the 1-40Hz BPF and the SFR in the analysis of the real AEF data average across 10 trials. The initial number of the dipoles was prescribed as 20 in the proposed reconstruction, and the 9 dipoles were estimated. The error rate was 0.299.

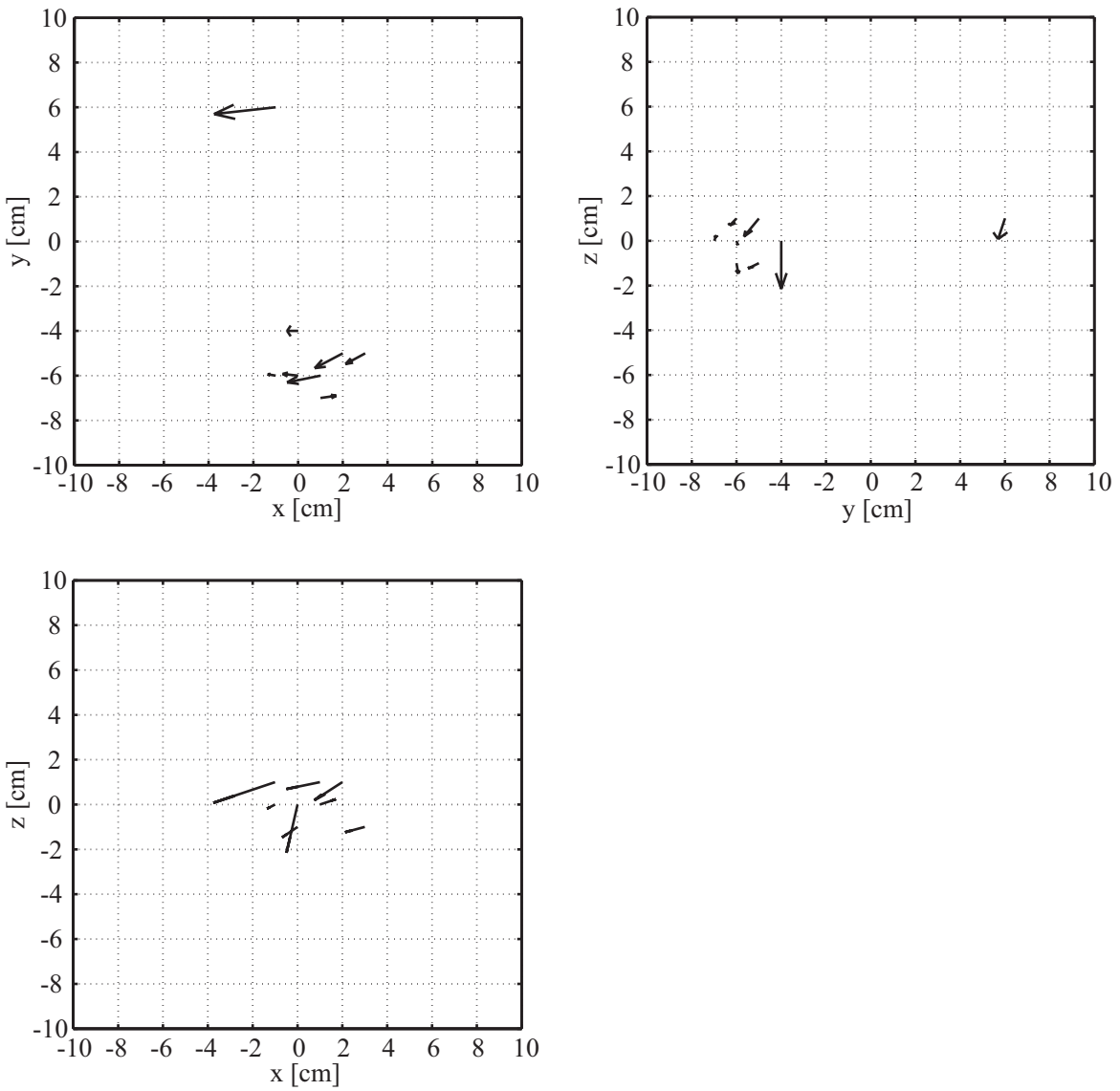

Figure 4.44: Dipoles reconstructed by the combination of the FA-processed Kalman filter without ICA and the SFR in the real AEF data analysis. The initial number of the dipoles was prescribed as 20 in the proposed reconstruction, and the 8 dipoles were estimated. The error rate was 0.289. The FA-processed Kalman filtered data are shown in Fig.4.40.

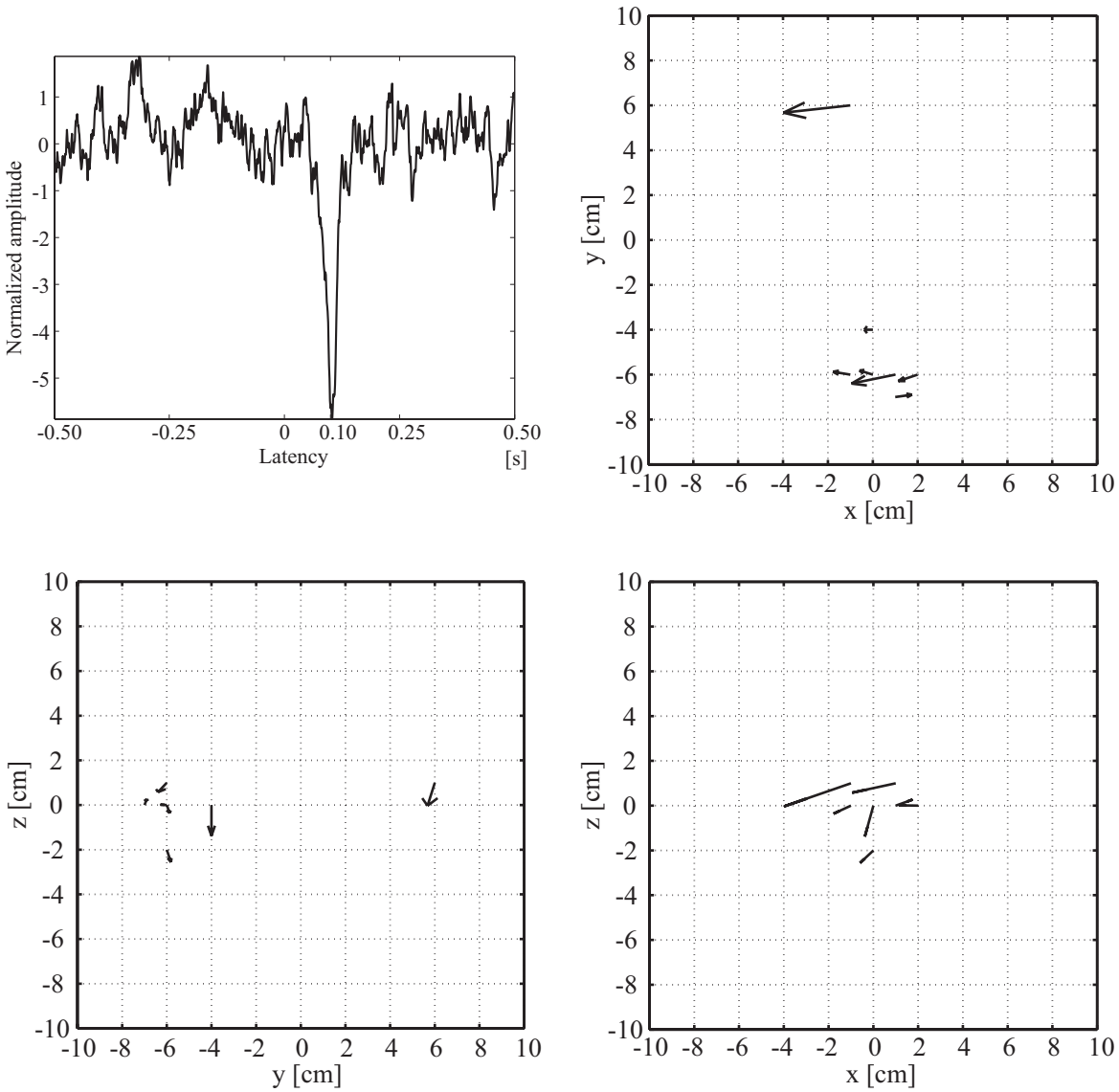

Figure 4.45: Extracted independent component (upper left) and dipoles reconstructed by the combination of the FastICA and the SFR in the analysis of the real AEF data averaged across 10 trials. The 20 PCs with a 89.41 % contribution were utilized in ICA. The initial number of the dipoles was prescribed as 20 in the proposed reconstruction, and the 7 dipoles were estimated. The error rate was 0.252.

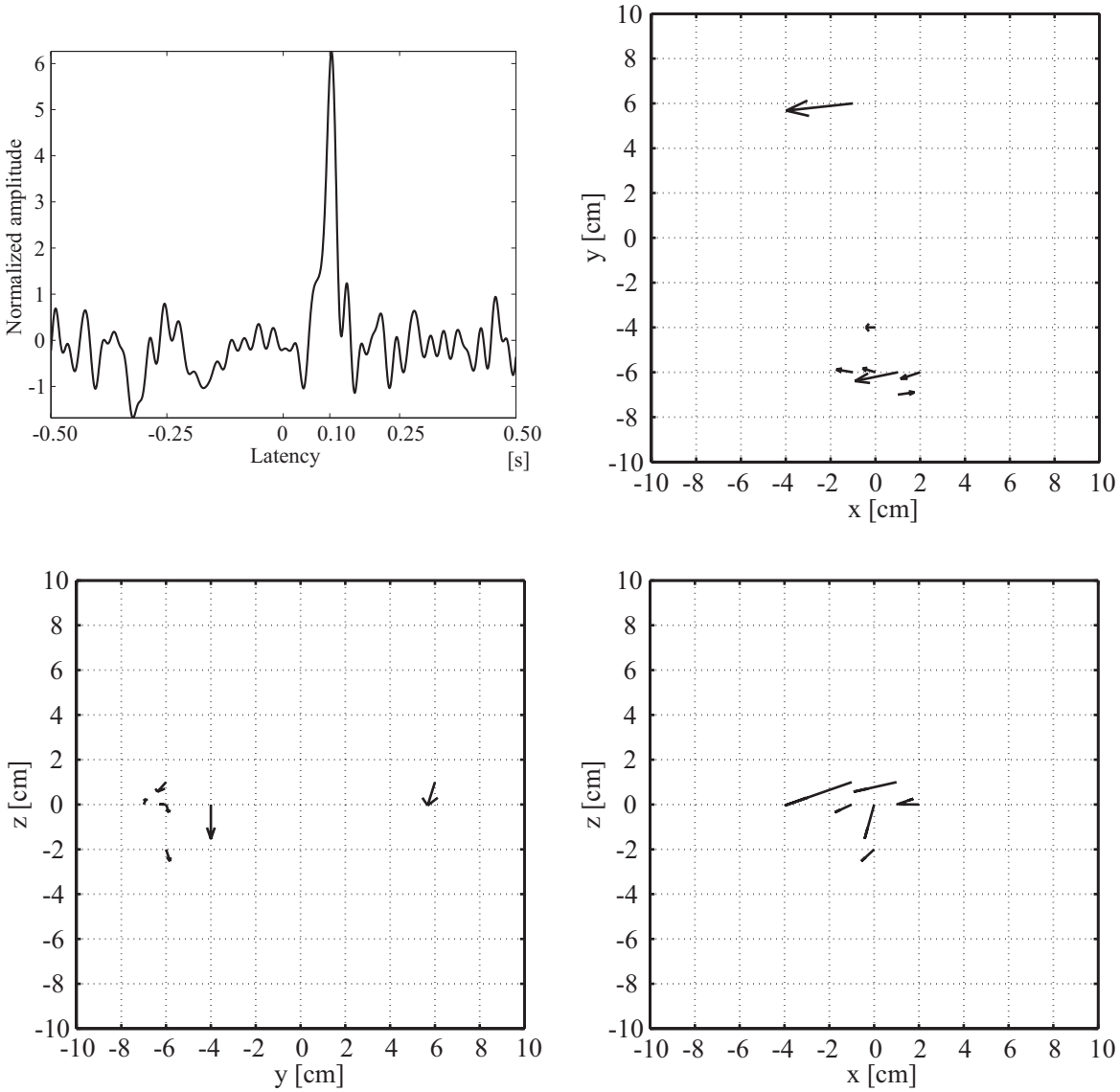

Figure 4.46: Extracted independent component (upper left) and dipoles reconstructed by the combination of the 1-40Hz BPF, the FastICA and the SFR in the analysis of the real AEF data averaged across 10 trials. The band-pass filtered data are shown in Fig.4.26. The 20 PCs with a 96.27 % contribution were utilized in ICA. The initial number of the dipoles was prescribed as 20 in the proposed reconstruction, and the 7 dipoles were estimated. The error rate was 0.26.

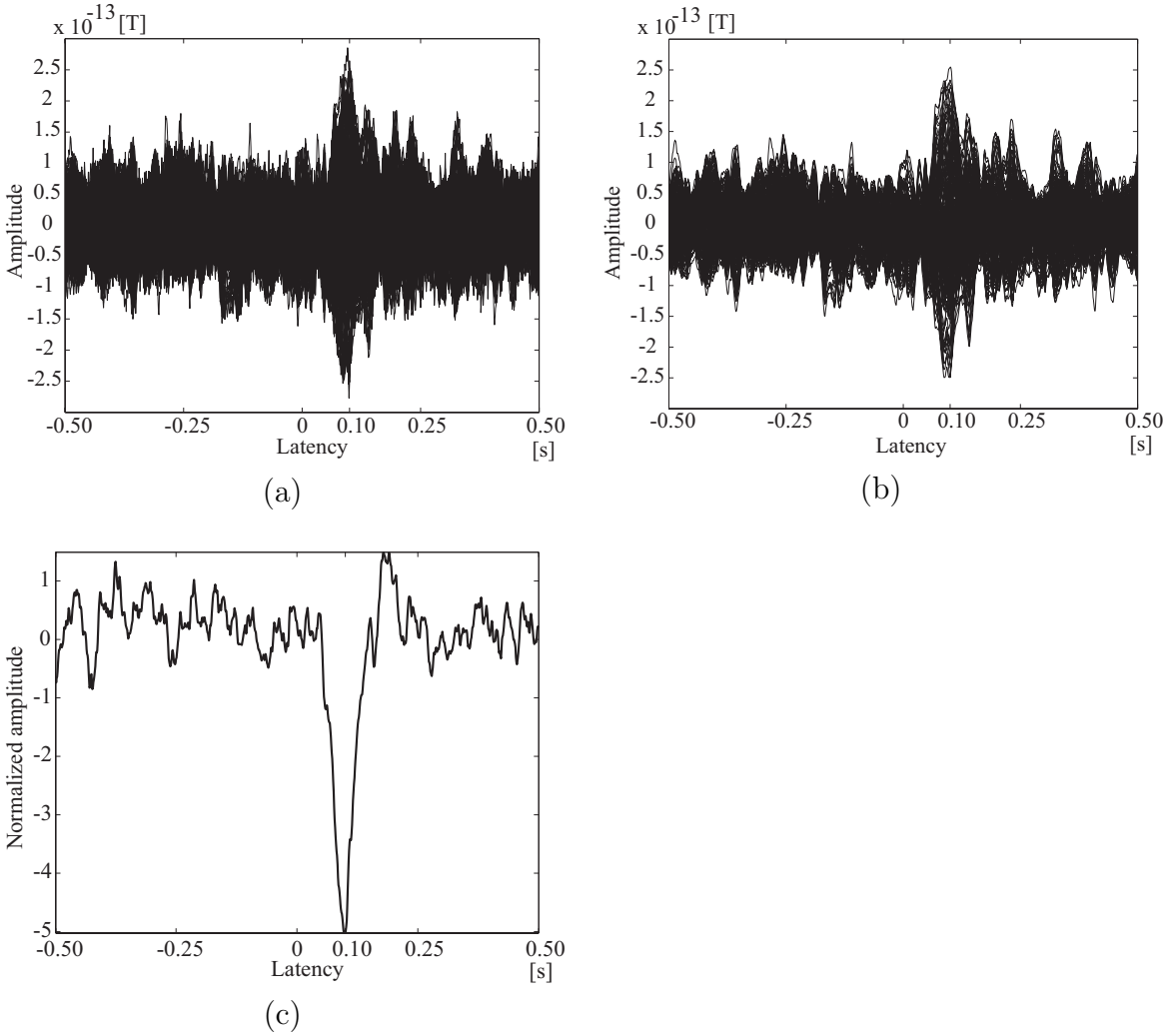

Figure 4.47: MEG data in the analysis of the real AEF averaged over 20 trials: (a) the AEF signals averaged across 20 trials, (b) the FA-processed Kalman filtered signals with 40 common factors and (c) the extracted IC with the peak due to N1m.

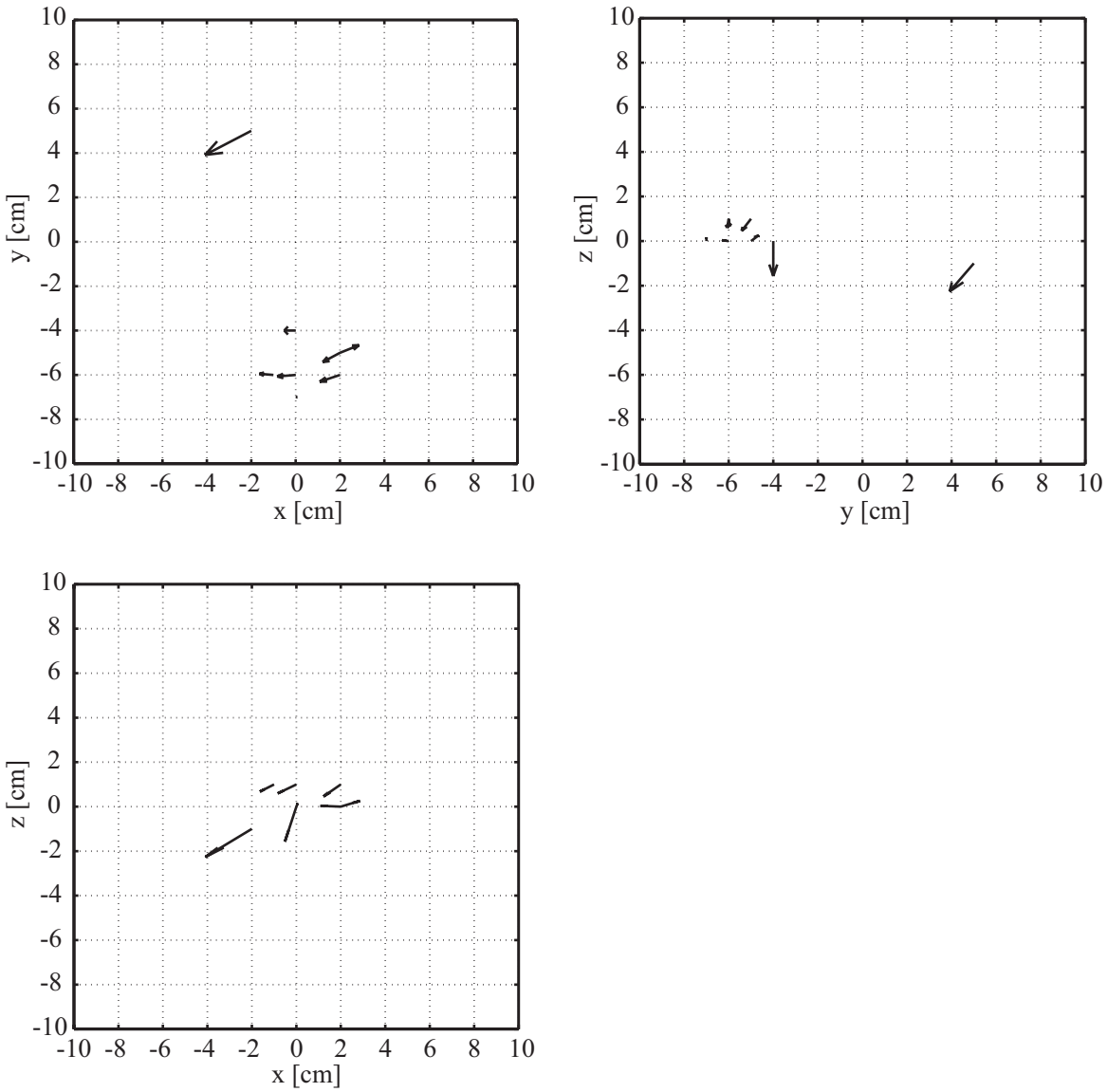

Figure 4.48: Dipoles reconstructed by the combination of the FA-processed Kalman filter, ICA and the SFR in the analysis of the real AEF data averaged 20 trials. The initial number of the dipoles were 20 and 8 dipoles remained. The error rate was 0.183.

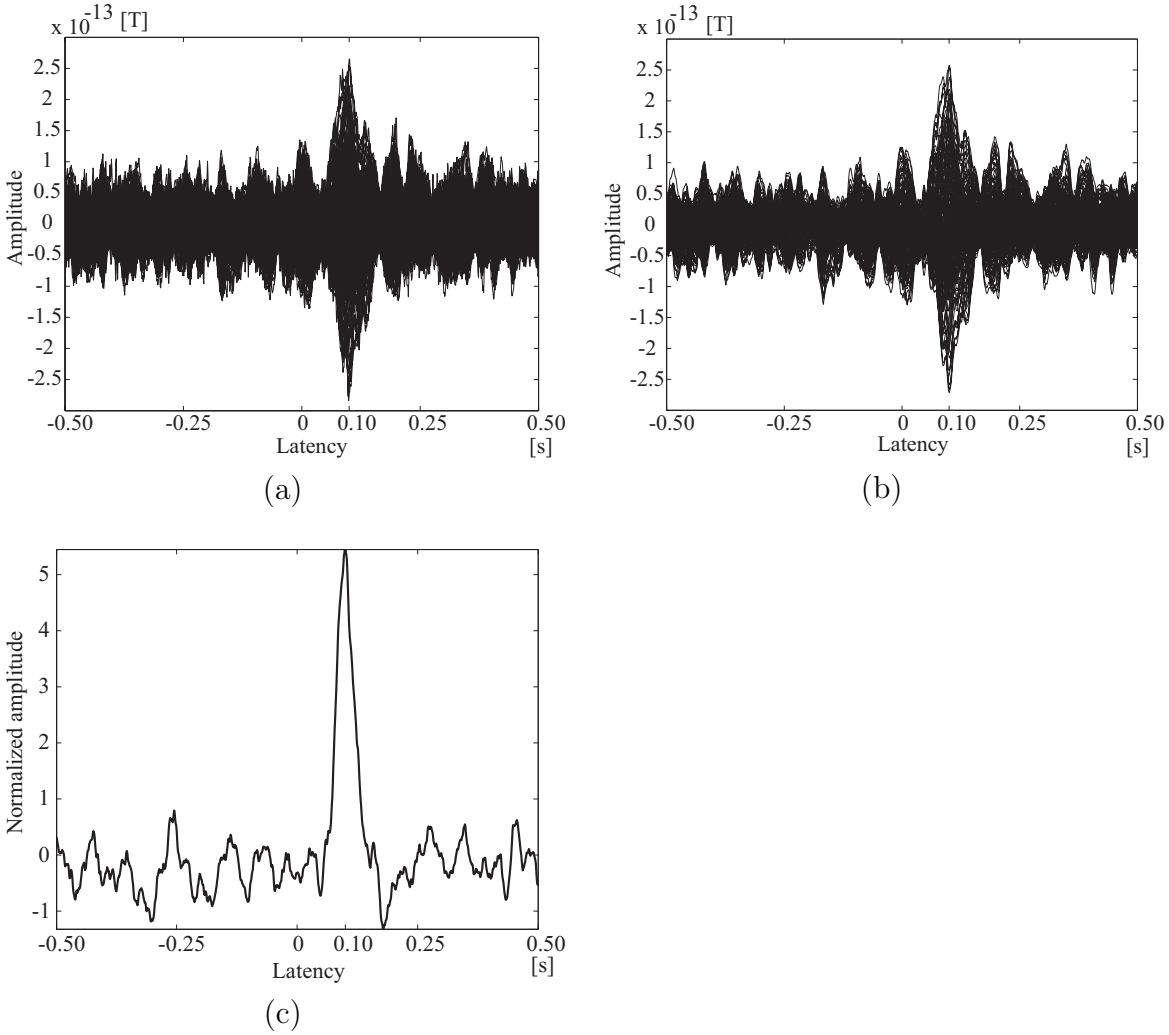

Figure 4.49: MEG data in the analysis of the real AEF averaged over 40 trials: (a) the AEF signals averaged across 40 trials, (b) the FA-processed Kalman filtered signals with 40 common factors and (c) the extracted IC with the peak due to N1m.

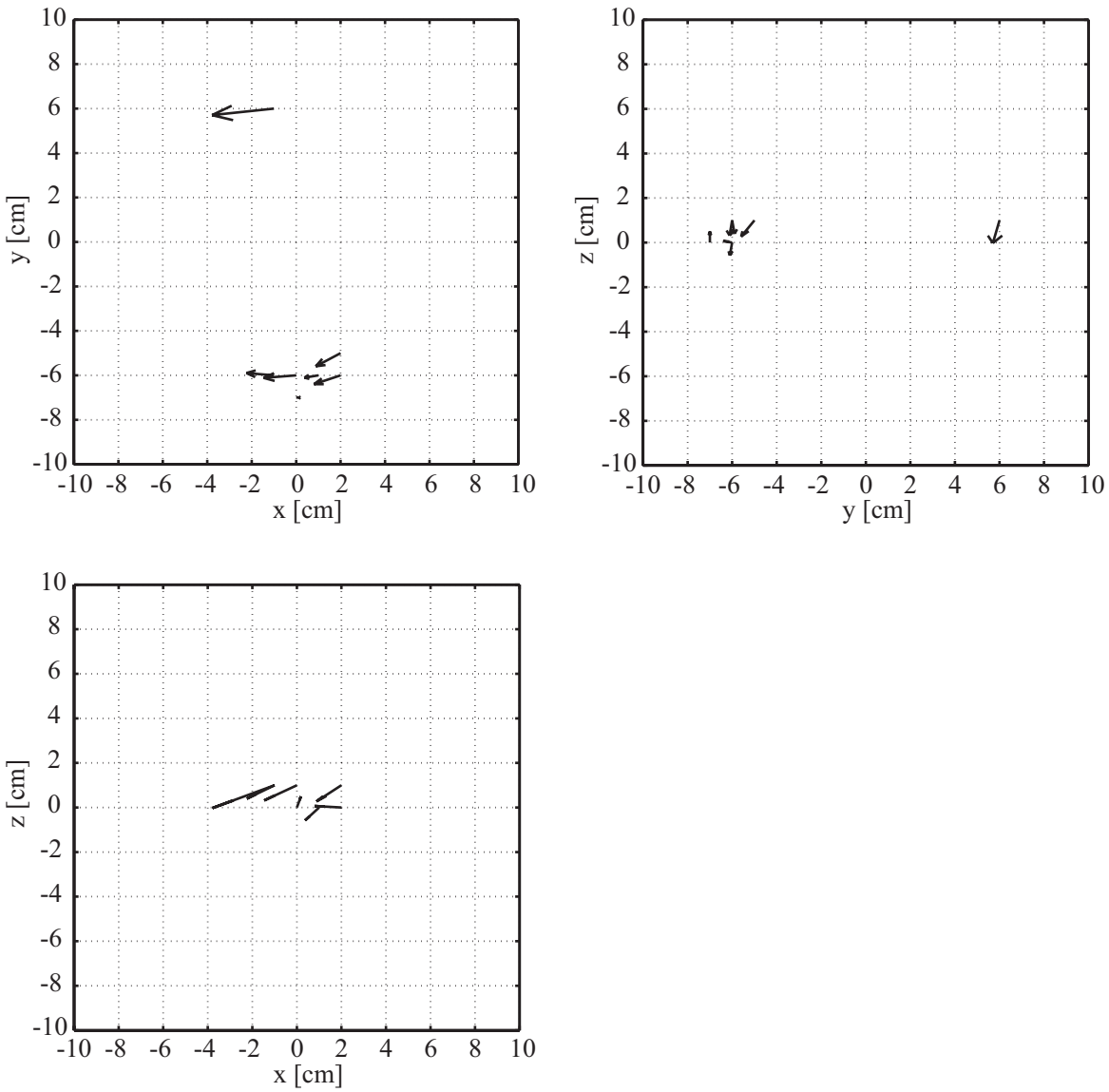

Figure 4.50: Dipoles reconstructed by the combination of the FA-processed Kalman filter, ICA and the SFR in the analysis of the real AEF data averaged 40 trials. The initial number of the dipoles were 23 and 8 dipoles remained. The error rate was 0.204.

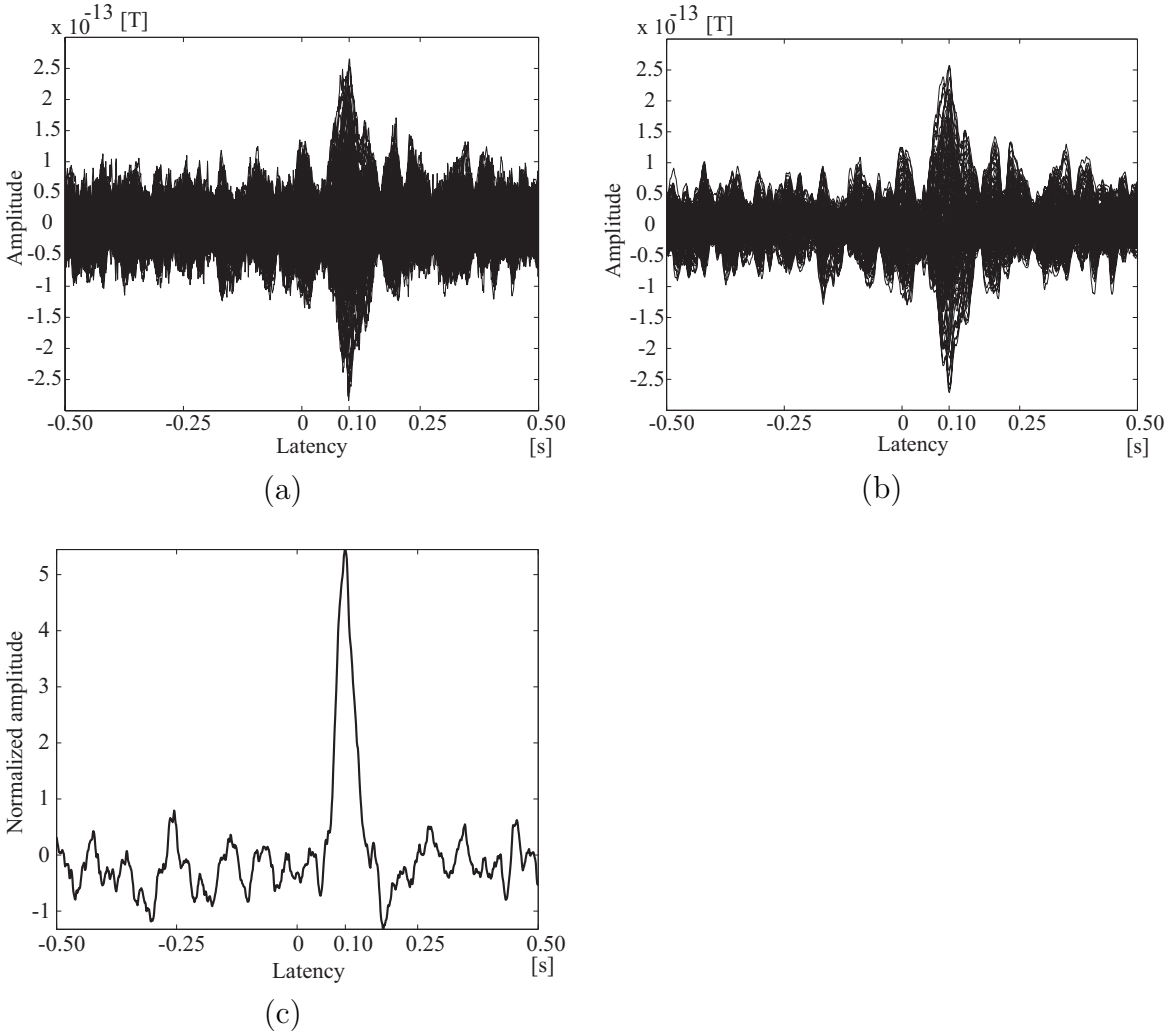

Figure 4.51: MEG data in the analysis of the real AEF averaged over 80 trials: (a) the AEF signals averaged across 80 trials, (b) the FA-processed Kalman filtered signals with 40 common factors and (c) the extracted IC with the peak due to N1m.

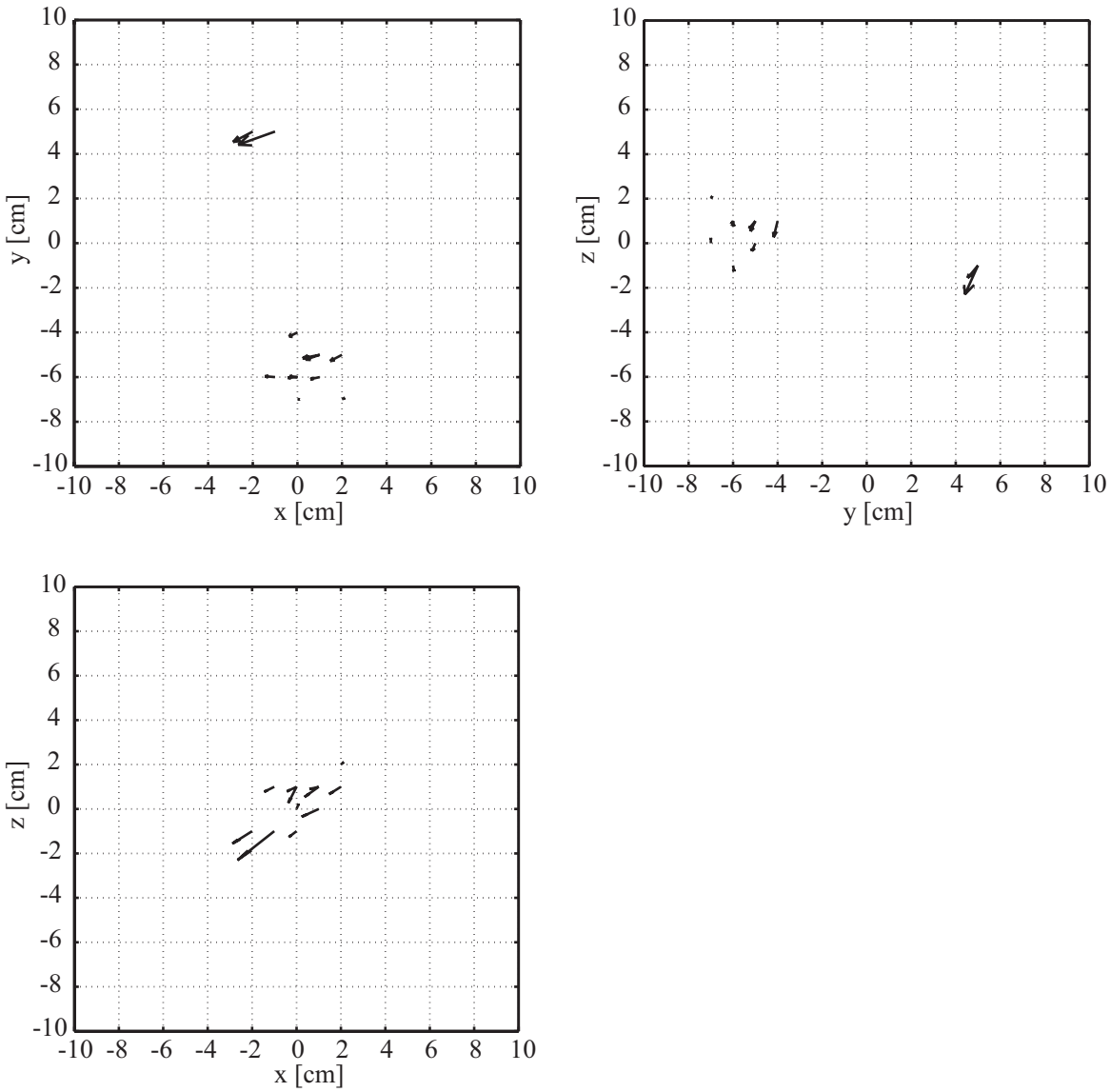

Figure 4.52: Dipoles reconstructed by the combination of the FA-processed Kalman filter, ICA and the SFR in the analysis of the real AEF data averaged 40 trials. The initial number of the dipoles were 20 and 12 dipoles remained. The error rate was 0.115.

Chapter 5

Conclusion

In this paper, a noise reduction method and an estimation of brain activity in MEG measurement are proposed.

In the signal processing in MEG analysis, the imposition of the burden to the patients due to the noise reduction with averaging across many trials is the issue. Though the MEG analysis with ICA, which extracts the independent signals from the data contaminated by the noises and artifacts, may resolve the issue, it is slightly problematic by the influence of the independent sensor noise.

A sensor-noise reduction method, which is a combination of a Kalman filter and factor analysis (FA-processed Kalman filter), is proposed. The Kalman filter powerfully eliminates the sensor noise in MEG data: the state-space model for the Kalman filter is constructed with the forward solution of the MEG measurement. The approximations of the noise covariance matrices are provided by factor analysis. Some numerical experiments show that the FA-processed Kalman filter effectively eliminates the sensor noise, and it is robust to the error in the number of the common factors in factor analysis. These features relieve the issues in the preprocessing step in ICA. It makes the decision of the number of the independent components easier, and the orthognalization of the signals with PCA becomes more successful with less independent additive noises. In addition, the noise reduction can be conducted without concerning the frequency range of the signals required in usual band-pass filtering, and the FA-processed Kalman filter can get along with band-pass filtering.

It was illustrated through the numerical experiments that the FA-processed Kalman filter greatly supports ICA. The independent components had higher signal-to-noise ratios (SNRs) in ICA following the FA-processed Kalman filtering. The FA-processed Kalman filter and ICA succeeded to extract AEF signal from the unaveraged single-trial MEG data.

In the inverse analysis, i.e. the estimation of the current density distribution in a brain, the dependence on prior information such as the number of the dipoles and on temporal information, the covariance of the MEG data is the issue to be addressed.

In the studies of the neuroscience, it is preferable not to depend on prior information to obtain fair results. The reasonable localization of the current distribution is necessary especially in the clinical applications also. In the inverse problems, the redundant expansion, ambiguity of the solution appears due to the nature of the problems. The use of temporal information in the LCMV beamformer and the SAM aggravates the issue in the cases where the some activities in the brain have correlations; the spatial resolution declines in such cases.

The spatial filter without using temporal information is proposed. The current dipoles are regarded as random variables, and the characteristic functions of their probability density functions are introduced into the design of the spatial filter. In the actual objective function to optimize the spatial filter, the cumulants of the second and fourth orders are employed. As the result of the consideration of the higher order statistics, the dipoles estimated by the spatial filter possess the characteristics of non-Gaussianity, i.e. independence and smaller entropy, and the current density distribution constructed with them indicates the higher localization, as shown in the numerical experiments.

The reconstruction of the current distribution estimated by the spatial filter with multiple linear regression (spatial filtered reconstruction: SFR) assists the spatial filtering. With the C_p statistic which is a criterion to select the regression model fitting the data better with fewer variables, the redundant dipoles in the distribution are removed. Moreover, it even corrects the error in the current distribution. In the

numerical experiments, the current density distribution was localized effectively and reasonably by the reconstruction with the objective criterion. The reconstruction showed its ability in the real MEG analysis. The current dipoles localized in the auditory cortexes precisely in the averaged-AEF data analysis.

Furthermore, the combination of the FA-processed Kalman filter and the SFR was performed in the single-trial AEF analysis. The activities in the brain were successfully estimated by the combination.

The proposals for solutions of the issues in MEG analysis are shown in this paper. They achieve to alleviate the issues of low SNR and of the inverse problem. The implementation of them will gain the usability and reliability of MEG for uses in the clinical applications and researches. They will make a deep impact on MEG analyses, and consequently contribute to the further progress of the neuroscience and to all of the societies hope understanding the human brain functions and making good use of it in the future.

Acknowledgments

This thesis is the compilation of the author's researches at the School of Fundamental Science and Technology, Graduate school of Keio University.

I would like to express my sincere thanks to my adviser, Professor Satoshi Honda, for his patient and tolerant guidance. I would also like to express my thanks to Professor Eitarou Aiyoshi and Associate Professor Eiji Okada at Keio University, and Professor Tsunehiro Takeda at Tokyo University. Their comments and suggestions have improved the thesis.

I wish to thank Mr. Atsushi Aoyama at Keio for offering the real MEG data. This study was partly supported by the Keio Leading-edge Laboratory of Science and Technology and by the 21st Century COE Program at Keio: Integrative Mathematical Sciences.

Finally, this thesis is dedicated to my mother, Kazuko Okawa, for her affectionate support and encouragement.

References

[1] M. Hämäläinen, R. Hari, R. J. llmoniemi, J. Knuutilia, and O. V. Lounasmaa, "Magnetoencephalography-theory, instrumentation, and applications to non-invasive studies of the working human brain", Rev. Mod. Phys., Vol.65, No.2, pp.413-497, Apr., 1993.

[2] S. Baillet, J. C. Mosher, R. M. Leahy, "Electromagnetic Brain Mapping", IEEE Sig. Proc. Mag., Vol.18, pp.14-30, Nov., 2001.

[3] H. Walter, R. Kristeva, et al., "Individual Somatotopy of Primary Sensorimotor Cortex Revealed by Intermodal Matching of MEG, PET, and MRI", Brain Tomogr., Vol.5, No.2, pp.183-187, 1992.

[4] A. Babajanim M.-H. Nekooei,et al., "Integrated MEG and fMRI Model: Synthesis and Analysis", Brain Topogr., Vol.18. No.2, pp.101-113, Winter 2005.

[5] P. L. Nunez, R. B. Silberstein, "On the Relationship of Synaptic Activity to Macroscopic Measurements: Does Co-Registration of EEG with fMRI Make Sense", Brain Topogr., Vol.13, No.2, pp.79-96, 2000.

[6] T. Ebrahimi, J.-M. Vesin, G. Garcia, "Brain-Computater Interface in Multimedia Communication", IEEE Signal Process. Mag., Vol.20, No.1, pp.14-24, January,2003.

[7] T. Hinterberger, N. Weiskopf, "An EEG-Driven Brain-Computer Interface Combined With Functional Magnetic Resonance Imaging (fMRI)", IEEE Trans. Biomed. Eng., Vol.51, No.6, pp.971-974, June, 2004.

[8] T. N. Lal, M. Schröder, et al., "Support Vector Channel Selection in BCI", IEEE Trans. Biomed. Eng., Vol.51, No.6, pp.1003-1010, June, 2004.

[9] H. Ramoser, et al., "Optimal Spatial Filtering of Single Trial EEG During Imagined Hand Movement", IEEE Trans. Rehabil. Eng., Vol.8, No.4, December, 2000.

[10] D. J. McFarland, W. A. Sarnacki, et al., "Brain-computer interface (BCI) operation: signal and noise during early training sessions", Clinic. Neurophysiol., Vol.116, pp.56-62, 2005.

[11] P. S. Lewis, J. S. George, "Magnetoencephalography", IEEE Potentials, Vol.9, 4, pp.9-13, December, 1990.

[12] A. I. Ahonen, M. S. Hämäläinen, et al., "MULTICHANNEL SQUID SYSTEM FOR BRAIN RESEARCH", IEEE Trans. Magn., Vol.27, No.2, pp.2786-2792, March, 1991.

[13] J. Vrba, S. E. Robinson, et al., "Fetal MEG Redistribution by Projection Operators", IEEE Trans. Biomed. Eng., Vol.51, No.7, pp.1207-1218, July, 2004.

[14] R. Kleiner, D. Koelle, et al., "Superconducting QUantum Interference Divices: State of the Art and Application", Proceedings of the IEEE, Vol.92, No.10, pp.1534-1548.

[15] E. Pataraia, C. Baumgartner, et al., "Magnetoencephalography in presurgical epilepsy evaluation", Neurosurg. Rev. Vol.25, pp.141-159, 2002.

[16] L. Timmermann, J. Gross, "The cerebral oscillatory network of parkinson resting tremor", Brain, Vol.126, No.1, pp.199-212, January, 2002.

[17] E. Püregger, P. Walla, et al., "Magnetoencephalographic-Features related to mild cognitive impairment", NeuroImage, Vol.20, pp.2235-2244, 2003.

[18] A. Tarkiainen, P. Helenius, R. Salmerin, "Category-specific occipitotemporal activation during face perception in dyslexic individuals: an MEG study", NeuroImage, Nol.19, pp.1194-1204, 2003.

[19] D. Cohen, B. N. Cuffin, "EEG Versus MEG Localization Accuracy: Theory and Experiment", Brain Tomogr., Vol.4, No.2, pp.95-103, 1991.

[20] J. C. de Munckm F. Bijma, et al., "A Maximum-Likelihood Estimator for Trial-to-Trial Variations in Noisy MEG/EEG Data Sets", IEEE Trans. Biomed. Eng., Vol.51, No.12, pp.2123-2128, 2004.

[21] N. A. Laskaris, S. Fotopoulos and A. A. Ioannides, "Mining Information from Event-Related Recordings", IEEE Signal Process. Mag., pp.66-77, May,2004.

[22] T. Tominaga, H. Endo, S. Honda, T. Takeda, "Current Dipole Localization with Fewre Average of Evoked Fields through Wavelet Based Time Varying Filter", Recent Advance in Biomagnetism, pp.314-317, Tohoku University Press, 1999.

[23] S. Taulu, J. Simola, M. Kajola, "Application of the Signal Space Separation Method", IEEE Trans. Sig. Proc., Vol.53, No.9, pp.3359-3372, September, 2005.

[24] R. Vigário, V. Jousmaäki, M. Hämäläinen, R. Hari, and E. Oja, "Independent Component Analysis for identification of artifacts in Magnetoencephalographic recordings", Advance in Neural Information Processing Systems 10 (*Pro. NIPS '97*), pp.229-235, 1997.

[25] R. Vigário, J. Särelä, V. Jousmäki, M. Hämäläinen, and E. Oja, "Independent Component Approach to Analysis of EEG and MEG Recordings.", IEEE Trans. Biomed. Eng., 47, pp.589-593, 2000.

[26] S. Ikeda, K. Toyama, "ICA for noisy neurobiological data", Proc. Int. Joint Conf. of Neural Networks(IJCNN2000), Como, Italy, 2000.

[27] R. N. Vigário, "Eatraction of ocular artefacts from EEG using independent component analysis", Electroencephalogr. clinic. Neurophysiol., Vol.102, pp.395-404, 1997.

[28] R. Vigário, J. Särelä, E. Oja, "Independent Component Analysis in Wave Decomposition of Auditory Evoked Fields", International Cocnference on Artificial Neural Networks (ICANN'98), Skövde, Sweden, 1998.

[29] A. Cichocki, S. L. Shishkin, et al., "EEG filtering based on blind source separation (BSS) for early detection of Alzheimer's disease", Clinic. Neurophysiol., Vol.116, pp.729-737, 2005.

[30] J. Cao, N. Murata, S. Amari, A. Cichocki and T. Takeda, "Independent component analysis for unaveraged single-trial MEG data decomposition and single-dipole source localization", Neurocomput., 49, pp.255-277, 2002.

[31] J. Cao, N. Murata, S. Amari, A. Cichocki, T. Takeda, H. Endo, and N. Harada, "Single-Trial Magnetoencephalographic Data Decomposition and Localization Based on Independent Component Analysis Approach", IEICE Trans. Fundamentals, E83-A, pp.1757-1766, 2000.

[32] A. Cichocki, S. Amari, "Adaptive Blind Signal and Image Processing Learning Algorithms and Applications", John Wiley & Sons, Ltd., 2002.

[33] A. Hyvärinen, J. Karhunen, E. Oja, "Independent Component Analysis", John Wiley & Sons, Inc., 2001.

[34] J.-F. Cardoso, B.H.Laheld, "Equivariant Adaptive Source Separation", IEEE Trans. Signal Process., Vol.44, No.12, pp.3017-3030, December, 1996.

[35] J.-F. Cardoso, "High-Order Contrasts for Independent Component Analysis", Neural Comput., Vol.11, pp.157-192, 1999.

[36] C. R. Vogel, "Computational Methods for Inverse Problems", the Society for Industrial and Applied Mathematics, 2002.

[37] D. W. Oldenburg, "An Introduction to Linear Inverse Theory", IEEE Trans. on Geosci. Remote Sens., Vol.GE-22, No.6, pp. 665-674, November, 1984.

[38] S. Ueno, K. Iramina, "Modeling and Source Localization of MEG Activities", Brain Topogr., Vol.3, No.1, pp.151-165,1990.

[39] J. C. Mosher, R. M. Leahy, and P. S. Lewis, (1999): "EEG and MEG: Forward Solutions for Inverse Methods", IEEE Trans., Biomed. Eng., 46, pp.245-259, 1999.

[40] M. S. Hämäläinen, J. Sarvas, "Realistic Conductivity Geometry Model of the Human Head for Interpretation of Neuromagnetic Data", IEEE Trans., Biomed., Eng., 36, no.2, Feb. 1989.

[41] J. Sarvas, "Basic mathematical and electromagnetic concept of the bio magnetic inverse problem", Phys. Med. Biol., Vol.32, No.1, pp.11-22, 1987.

[42] O. Hauk, "Keep it simple: a case for using classical minimum norm estimation in the analysis of EEG and MEG data", NeuroImage, No.21, pp.1612-1621, 2004.

[43] C. Philips, M. D. Rugg, "Systematic Regularization of Linear Inverse Solutions of the EEG Source Localization problem", NeuroImage, Vol.17, pp.287-301, 2002.

[44] M. Sato, T. Yoshioka, S. Kajihara, et al., "Hierarchical Bayesian estimation for MEG inverse problem", NeuroImage, 23, pp.806-826, 2004.

[45] C. Amblard, E. Lapalme, et al., "Biomagnetic Source Detection by Maximum Entropy and Graphical Models", IEEE Trans. Biomed. Eng., Vol.51, No.3, pp. 427-442, March, 2004.

[46] J. C. Mosher, S. Baillet, R. M. Leahy, "Equivalence of linear approach in bioelectromagnetic inverse solution", Statistical Signal Processing, 2003 IEEE Workshop on, pp.294-297, 28 September - 1 October, 2003.

[47] K. Jerbi, S. baillet, et al., "Localization of realistic cortical activity in MEG using current multipoles", NeuroImage, Vol.22, pp. 779-793, 2004.

[48] B. V. Baryshnikov, B. D. Been, R. T. Wakai, "Maximum-Likelihood Estimation of Low-Rank Signals for Multiepoch MEG/EEG Analysis", IEEE Trans. Biomed. Eng., Vol.51, No.11, pp.1981-1993, Nov., 2004.

[49] C. Bertrand, M. Ohmi, et al., "A Probabilistic Solution to the MEG Inverse Problem via MCMC Mehods: The Reversible Jump and Parallel Tempering Algorithms", IEEE Trans. Biomed. Eng., Vol.48, No.5, pp.533-541, May, 2001.

[50] C. Bertrand, Y. Hamada, H. Kado, "MRI Prior Computation and Parallel Tempering Algorithm: A Probabilistic Resolution of the MEG/EEG Inverse Problem", Brain Tomogr., Vol.14, No.1, pp.57-61, Fall, 2001.

[51] J. C. Mosher, P. S. Lewis, R. E. Leahy, "Multiple Dipole Modeling and Localization from Spatio-Temporal MEG Data", IEEE Trans. Biomed. Eng., Vol.39, No.6, pp.514-557, Jun., 1992.

[52] J. C. Mosher and R. M. Leahy, "Source Localization Using Recursively Applied and Projected (RAP) MUSIC", IEEE Trans. Signal Process., Vol.47, No.2, pp.332-340, Feb., 1999.

[53] J. C. Mosher, S. Baillet, et al., "MEG multipolar modeling of distributed sources Using RAP-MUSIC", Conference Record of the Thirty-Fourth Asilomar Conference on Signals, Systems and Computers, 2000, Vol.1, pp. 318-322, 29 Oct.-1 Nov., 2000.

[54] B. D. van Veen and K. M. Buckley, "Beamforming: A Versatile Approach to Spatial Filtering", IEEE ASSP Mag., Vol.5, pp.4-23, Apr., 1988.

[55] B. D. van Veen, W. van Dronglen, M. Yuchtman, A. Suzuki, "Localization of Brain Electrical Activity via Linearly Constrained Minimum Variance Spatial Filter", IEEE Trans. Biomed. Eng., Vol.44, No.9, pp.867-880, Spt., 1997.

[56] S. E. Robinson, J. Vrba, "Functional Neuroimaging by Synthetic Aperture Magnetometry (SAM)", Recent Advances in Biomagnetism, Tohoku university press, Sendai, pp. 302-305, 1999.

[57] J. Vrba and S. E. Robinson, "Difference between Synthetic Aperture Magnetometry (SAM) and Linear Beamformers", Biomag 2000, 12th International Conference on Biomagnetism, Aug. 13-17, 2000, Helsinki Univ. of Technology, Espoo, Finland.

[58] J. Vrba, S. E. Robinson, "Linear constrained minimum variance beamformers, synthetic aperture magnetometry, and MUSIC in MEG applications", Signal, System, and Computers, 2002. Conference Record of the Thirty-Fourth Asilomar Conference on, Vol.1, pp.331-337, 2000.

[59] S. D. Hall, I. E. Holliday, et al., "Distinct contrast response function in striate and extra-striate regions of visual cortex revealed with magnetoencephalography (MEG)", Clinic. Neurophysiol., Vol.116, pp. 1716-1722, 2005.

[60] K. Sekihara, S. S. Nagarajan, et al., "Performance of an MEG Adaptive-Beamformer Source Reconstruction Technique in the Presence of Additive Low-Rank Interference", IEEE Trans. Biomed. Eng., Vol.51, No.1, pp.90-99, Jan., 2004.

[61] K. Sekihara, S. S. Nagarajan, et al., "Reconstructing Spatio-Temporal Activities of Neural Sources Using an MEG Vector Beamformer Technique", IEEE Trans. Biomed. Eng., Vol.48, No.7, pp.760-771, July, 2001.

[62] W. Chau, A. R. McIntosh, et al., "Improving permutation test power for group analysis of spatially filtered MEG data", NeuroImage, Vol.23, pp.983-996, 2004.

[63] M. J. Brooks, A. M. Gibson, "A general linear method for MEG beamformer imaging", NeuroImage, Vol.23, pp.936-946, 2004.

[64] S. E. Robinson, D. F. Rose, "Current source image estimation by spatial filtered MEG", Biomagnetism: Clinical aspects, pp.761-765, 1992.

[65] K. Toyam, K. Yoshikawa, et al., "A NEW METHOD FOR MAGNETOENCEPHALOGRAPHY: A THREE-DIMENSIONAL MAGNETOMETER-SPATIAL FILTER SYSTEM", Neurosci., Vol.91, No.2, pp.405-415, 1999.

[66] R. E. Kalman, "A New Approach to linear Filtering and Prediction Problems", Trans., ASME, Ser.D, J., Basic Eng., 82, pp.35-45, 1960.

[67] R. E. Kalman, R. S. Bucy, "New Results in Linear Filtering and Prediction Theory", Trans., ASME, Ser.D, J., Basic Eng., 83, pp.95-108, 1961.

[68] P. J. Hargrave, "A tutorial introduction to Kalman filtering", IEEE Colloquium on Kalman Filters: Introduction, Application and Future Developments, pp.1/1-1/6, 21 February, 1989.

[69] R. Mehra, "On the identification of variance and adaptive Kalman filtering", IEEE Trans. Autom. Control, Vol. 15, No.2, pp.175-184, April 1970.

[70] I. Rhodes, "A tutorial introduction to estimation and filtering", IEEE Trans. Autom. Control, Vol.16, No.6, pp.688-706, December, 1971.

[71] T. H. Lee, W. S. Ra, et al, "Robust Kalman filtering via Krein space estimation", IEE Proceedings Control Theory and Applications, Vol.151, No.1, pp.59-63, January, 2004.

[72] M. P. Tarvainen, J. K. Hiltunen, et al., "Estimation of Nonstationary EEG with Kalman Smoother Approach: An Application to Event-Related Synchronization(ERS)", IEEE Trans. Biomed. Eng., 51, pp.516-524, 2004.

[73] G. Beligiannis, L. Skarlas, S. Likothanassis, "A Generic Applied Evolutionary Hybrid Technique", IEEE Signal Process. Mag., Vol.21, No.3, pp.28-38, May, 2004.

[74] K. L. Berrier, D. C. Sorensen, D. Khoury, "Solving the Inverse Problem of Electrocardiography Using a Duncan and Horn Formulation of the Kalman Filter", IEEE Trans. Biomed. Eng., Vol.51, No.3, pp.507-515, March, 2004.

[75] J. M. Mendel, "Tutorial on Higher-Order Statistics (Spectra) in Signal Processing and System Theory: Theoretical Results and Some Applications", Proceedings of The IEEE, Vol.79, No.3, pp.278-305, March, 1991.

[76] M. C. Dogan, M. Mendel, "INTERPRETRATION OF CUMULANTS FOR ARRAY PROCESSING", Signals, Systems and Computers, 1993. 1993 Conference Record of The Twenty-Seventh Asilomar Conference on, pp.1260-1264, 1-3, Nov., 1993

[77] C. L. Mallows, "Some Comments on C_p", Technometrics, Vol.15, No.4, pp.661-675, 1973.

[78] C. L. Mallows, "More Comments on C_p", Technometrics, Vol.37, No.4, pp.362-372, 1995.

[79] F. D. Ridder, R. Pintelon, et al., "Modified AIC and MDL Model Selection Criteria for Short Data Records", IEEE Trans. Instrum. Meas., Vol.54, No.1, Feb., 2005.

[80] R. Hari, K. Kaila, T. Katila, T. Tuomisto, T. Varpula, Interstimulus interval dependence of the auditory vertex response and its magnetic counterpart: implications for their neural generation, Electroencephalogr. Clin. Neurophysiol. Vol.54, pp.561-569, 1982.

[81] T. Rosburg, J. Haueisen, I. Kreitschmann-Andermahr, "The dipole location shift within the auditory evoked neuromagnetic field components N100m and mismatch negativity (MMNm)", Clin. Neurophysiol. Vol.115, pp. 906-913, 2004.